Development and investigation of CO_2 heat pump for domestic buildings

A Thesis Submitted for the
Degree of Doctor of Philosophy

By

Usman Qayyum

Department of Mechanical and
Aerospace Engineering,

Brunel University London

2025

Abstract

The residential building sector in the UK, is responsible for 25% of energy consumption and 17% of CO_2 emissions, with space heating accounting for 65% of this. More than 80% of existing dwellings use gas boilers for space heating and domestic hot water and to decarbonise this energy input, heat pumps are considered to be a key technology. Despite this potential, heat pumps have so far failed to gain wide market penetration in the UK due to high capital and installation costs, inability to provide high enough temperatures to be used with existing radiators in retrofit applications and requirement for thermal energy storage.

This project makes a contribution to addressing this challenge by investigating the development of a CO_2 high-temperature heat pump and its integration with thermal energy storage. to satisfy space heating requirements for existing and new dwellings, facilitate the use of low tariff electricity and provide demand services to the grid. The investigations involved: i) dynamic simulations of 2 and 3 bedroom semi-detached dwellings to establish space and domestic hot water energy demand; ii) extensive experimental investigations on a CO_2 heat pump developed at Brunel to establish operating characteristics; iii) simulation of the heat pump to enable design optimisation; iv) investigations on the performance and integration of the heat pump with a Phase Change Material (PCM) thermal energy storage system.

The work has demonstrated that: i) The CO_2 heat pump can provide significant flexibility in the provision of different water delivery temperatures from 40 ºC to 80 ºC to satisfy both domestic hot water and space heating demand and the requirement of different types of heat emitter in existing and new dwellings; ii) Using the performance characteristics of the heat pump, the optimum hot water storage tank size for the 4 bedroom domestic dwelling was determined to be between 200 and 300 litres: iii) Using current domestic electricity and gas prices and CO_2 emission factors, the annual running cost of the heat pump was found to be approximately double that of the gas boiler due to the large difference between gas and electricity prices, but offering 40% reduction in CO_2 emissions; iv) Heat pump design and optimisation work using a simulation model developed for this purpose is expected to lead to an increase in increase the seasonal COP of the heat pump and its cost effectiveness over gas boilers; v) Integration of the heat pump with a PCM storage tank designed and using Rubitherm RT70HC PCM has shown that the heat pump can charge the storage tank effectively, leading to a 50% reduction in the storage volume required for the same thermal energy storage capacity compared to hot water storage.

Acknowledgment

Firstly, I would like to express my sincere gratitude and respect to my supervisor, Professor Savvas Tassou, for his continuous support, guidance, knowledge and expertise throughout my PhD journey. It has been a privilege to develop this technology under his supervision. His encouragement and active involvement in my studies over the past four years have significantly contributed to my growth as an engineer. I am truly grateful for the opportunity to work with him, and his guidance has always struck the perfect balance between providing me with the freedom to develop my research and ensuring I remained focused on my goals.

I would also like to extend my thanks to Professor Harjit Singh and Dr. Debarati Torrens for their invaluable support throughout my PhD progress. Their advice and insights have been much appreciated.

My heartfelt thanks to Maureen Senatore for her dedication and hard work in coordinating the components of the CO_2 heat pump and procuring the necessary software for me.

I would like to extend my special thanks to Dr. Liang Li for his unwavering support throughout the final year of my PhD.

I would like to thank Jose Tavares for his assistance in the continuous construction and development of the CO_2 heat pump, which has been essential to the success of my project.

Special thanks to my lab colleagues, particularly Dr. Alok Kumar, for their encouragement and motivation during this research journey.

I would also like to express my gratitude to my parents, sisters and brother for their unwavering love, support, and prayers, which have been instrumental in my success.

Finally, I would like to acknowledge and thank the Centre for Sustainable Energy Use in Food Chains (CSEF) for their financial support, which made this research possible.

Table of Content

List of Figures

List of Tables

Chapter 1 Introduction

Numerous countries and organisations are making substantial efforts to achieve net-zero carbon emissions by 2050 (Nastasi et al., 2022). Over a third of all greenhouse gas emissions originate from the housing sector, with half of these emissions attributed to domestic space heating and hot water requirements (Hamilton et al., 2020). Emissions reduction goals have been adopted as an integral part of national policy in some nations as a direct response to rising climate change concerns (IEA, 2021).

The UK Government has set a target to achieve carbon neutrality by 2050, with a more immediate objective of reducing emissions by 78% from the 1990 baseline by 2035. These goals imply a quick change in residential heating. About 25% of the country's total energy usage and 17% of CO_2 equivalent emissions are attributable to the provision of household space heating and hot water (BEIS, 2021). More than 85% of building heat in the UK comes from gas and oil boilers; approximately 75% of heating and hot water demand is met by natural gas, while 10% is supplied by liquid petroleum oil (Watson et al., 2023). Only 5% of the UK's domestic heating demand is met by low-carbon heating systems at the moment; thus, by 2050, the vast majority of UK houses will need to switch to a decarbonised heat solution (Rosenow et al., 2020).

A variety of methods can be employed to provide low-carbon residential heating, such as electric resistive heating, district heating (assuming the heat source is low-carbon), and the utilisation of hydrogen or biomethane to decarbonise the gas grid. Improving the thermal efficiency of existing and new homes can also substantially contribute to the reduction of building emissions. In the present scenario, there exist considerable uncertainties pertaining to the prospective trajectory of hydrogen production via steam methane reformation or electrolysis, particularly in terms of achieving zero-carbon emissions and cost-effectiveness. Presently, the UK lacks both widespread electrolysis-based hydrogen production and significant demonstration programmes meant to grasp the scope of hydrogen availability in the country (Scamman et al., 2020). It is difficult and subjective to draw assumptions regarding the availability, affordability and priority use of hydrogen across the economy in the absence of a UK hydrogen policy.

Extensive electrification of heating systems is the principal strategy for decarbonising the heat supply in residential buildings in the UK (Broad et al., 2020). Heat pumps are the most promising technology currently available because they have the potential to be more cost-effective than gas boilers (Wang and He, 2021).

The operating characteristics and the performance of a heat pump are largely determined by the characteristics of the heat source and the lift. The main heat source for heat pumps providing space heating and hot water is likely to be air, water, or ground.

Based on the heat source, which can be the air, ground, or water, HPs are divided into Ground Source Heat Pumps (GSHPs), Water Source Heat Pumps (WSHPs), and Air Source Heat Pumps (ASHPs), respectively. In addition, they are further divided into Air-to-Air-Heat-Pumps (AAHPs), Air to Water Heat Pumps (AWHPs), Ground to Water Heat Pumps (GWHPs), etc., depending on the type of heat sink used.

Ground Source Heat Pumps (GSHPs): Ground Source Heat Pumps (GSHPs) and Geothermal Heat Pumps (GHPs) have higher thermal efficiency than conventional Air Source Heat Pumps (ASHPs) because the temperature of the ground remains constant independent of climate conditions or seasonal variation above the earth(Nikitin et al., 2021). GSHPs and GHPs both harness the thermal energy naturally stored beneath the earth as a power source. The terms "ground source" and "geothermal" are sometimes used as synonymously. In urban and metropolitan locations, the land footprint requirement prevents them from being adapted (Gaur et al., 2021).

Water Source Heat Pumps (WSHPs): Water Source Heat Pumps (WSHPs) use water bodies such as lakes, ponds, rivers or ground water as a source of heat. They extract low grade heat from water and convert to useful heat. Compared to Air Source Heat Pumps, WSHPs generate less carbon emissions and result in substantial cost savings. As opposed to ASHPs, ambient temperature conditions do not significantly influence the performances of WSHPs. This is due to the fact that a waterbody possesses enough heat to enable WSHPs to operate even during wintry weather conditions and also the temperature of the waterbody fluctuates less than that of air (Gaur et al., 2021). WSHPs are known for their great efficacy, but their use is constrained by the necessity of large waterbodies or storage tanks close to residences for their implementation. Moreover, the need to adhere to certain environmental regulations may further result in a low uptake rate of WSHPs.

Air Source Heat Pumps (ASHPs): Air Source Heat Pump (ASHP) has been divided into Air-to-Air Heat Pump (AAHP) and Air to Water Heat pump (AWHP). AWHPs are by far the most common type of HP used for domestic applications in the UK. AWHP uses an electrically powered fan to pull in external air. In the evaporator, this air passes over and heats a coil containing liquid refrigerant, turning it into a gas. The gas is then pressurised by a compressor (the heat pump's biggest electricity consumer) to raise its temperature. This high-temperature refrigerant gas then travels to a second heat exchanger (the condenser or gas cooler) where the heat is transferred from the refrigerant to a separate closed water loop and used for space heating and/or hot water preparation. This now-cooled refrigerant then passes through an expansion valve and back to the evaporator. This process is continuously repeated (O'Hegarty et al., 2022).

Both ASHPs and GSHPs come in two main types: indoor or outdoor single-packaged (monobloc) and split-system HP. Monoblocs, where the entire circuit is installed outdoors, require insulated water pipes running between the HP and the building. Single-packaged HPs installed indoors usually require a ducted air inlet and/or outlet if the source is air and refrigerant pipework running between the HP unit and the collector if the source is the ground. Split systems have both an indoor (condenser) and an outdoor unit (evaporator, expansion valve, compressor), connected with refrigerant pipework (Roy et al., 2010).

HPs can provide SH and/or DHW, with SH usually being their main application. There are several categories of water heat emitters available, such as underfloor pipework, radiators, and fan coils, all of which can be combined in a single installation. Underfloor heating (UFH) can operate at the lowest temperatures, i.e., 30-45°C, fan coils at 35-55°C, low-temperature radiators at 45-60 °C and high-temperature radiators at 60-75 °C. Air room heaters can operate at temperatures even lower than those required by UFH, i.e., 25-35°C (Hu et al., 2019).

DHW is usually heated at around 50-60°C but can be as high as 65°C, depending on the HP model. No direct electric top-up is needed for a HP able to take DHW up to temperatures of 60-65°C. Even if pasteurisation temperatures cannot be reached by the HP alone, the HP should still be set to provide the bulk of water heating. Reversible HPs can also provide space cooling in the summer by passing cooled water through fan coils or underfloor heating pipes, in which case flow temperature is limited to approximately 18°C to avoid the risk of condensation (EST, 2008).

The main benefits and considerations around the installation of ASHPs and GSHPs are presented in Table 1. Both present longer lifetimes than traditional boiler systems and require minimal maintenance, e.g., once in 3-5 years, mainly due to performance loss relating to refrigerant leakage. The lifecycle of the compressor is around 15-20 years and ground collectors are expected to last approximately 50 years (Staffell et al., 2010).

Table 1. Benefits and considerations for domestic air-to-water (ASHP) and ground-to-water (GSHP) heat pumps

	ASHP	**GSHP**
Capital cost	Relatively low, more expensive than the traditional heating systems they usually replace	Relatively high, more expensive than the traditional heating systems they usually replace
Running cost	Low, if installed and operated appropriately	Low, if installed and operated appropriately
Installation	Easy; possible adverse impact on building's appearance	Disruptive installation; unobstructive once installed
Heat source installation and operational requirements	HP operational at external temperatures as low as -15 °C; a backup resistance heater steps in for temperatures lower than that	Land area (horizontal loop ground collectors); access for drilling equipment (vertical closedloop ground collectors); water quality and minimum flow (vertical open-loop ground collector)
Operative conditions	A short interruption of operation may be required in cold weather to allow defrosting of the evaporator	Less prone to efficiency fluctuations in cold weather due to thermal inertia of the ground
Efficiency	High; influenced by external temperature fluctuations and defrost cycles	High
Energy consumption	Low	Low
Noise disturbance	Possible	Relatively low; less noisy than ASHP and boilers
Supplementary heating	Use of resistance heaters should be carefully controlled to avoid efficiency reduction, e.g., through appropriate sizing	Use of resistance heaters use should be carefully controlled to avoid efficiency reduction, e.g., through appropriate sizing
Heat source maintenance	Possible air intake fouling; possible freezing of outdoor unit	Possible thermal depletion of the ground, gradually over decades of use; long life of ground collector (50+ years);
Durability and system maintenance	Long lifetime, high reliability, low maintenance	Long lifetime, high reliability, low maintenance

The performance of heat pumps is critically dependent on the selection of the working fluid, commonly referred to as the refrigerant. As such, it is imperative to choose the appropriate refrigerant in alignment with the system design and specific temperature requirements to optimise efficiency and functionality (Yıldız and Yıldırım, 2021). The utilisation of hydrochlorofluorocarbon (HFC) refrigerants with relatively high Global Warming Potential (GWP), such as R410A (GWP = 2,088), R134a (GWP = 1,430), and R407C (GWP = 1,774), has raised considerable concerns, particularly with respect to refrigerant leakage into the environment during installation and servicing. This issue has gained increasing prominence alongside the widespread adoption of heat pumps (UNEP, 2020). In recent years, the use of R410A refrigerant, with a high Global Warming Potential (GWP = 2088), has become prevalent in the UK. Simultaneously, there has been an increase in the consumption of R134a (GWP = 1300) and R32 (GWP = 675) (BEIS, 2021). The Montreal Protocol is a globally recognised treaty that established the requirement for the gradual reduction of synthetic chemical manufacturing, specifically chlorofluorocarbons (CFCs) in 1991 and hydrochlorofluorocarbons (HCFCs) in 1996. Additionally, it stipulated the future reduction of hydrofluorocarbon (HFC) imports, commencing in 2019 (Goyal et al., 2019). As an alternative to synthetic refrigerants, natural refrigerants derived from biological or chemical cycles in nature have been chosen for use in heat pumps, air conditioning, and refrigeration systems (Abas et al., 2018). The natural refrigerants commonly utilised in refrigeration systems are carbon dioxide, ammonia, butane, isobutane, and propylene (Chaichana et al., 2003). These refrigerants have demonstrated competitive energy performance when employed under suitable operating conditions. The CO_2 (R744) has a number of benefits over the others, such as being inexpensive, non-flammable, non-toxic, having a high thermal conductivity, a low dynamic viscosity and a large thermal capacity (Wang et al., 2022).

As of March 2020, there were 28.5 million households in the UK, with 92.6% of dwellings in England relying on gas for their heating. There are some of the oldest homes in Europe in the UK, with 23% of private sector dwellings constructed before 1919 and 72% of social housing stock constructed between 1945 and 1980. Consequently, a large proportion of the existing housing stock is inefficient. The average SAP rating of homes in England was 65 points in 2019, equivalent to an EPC B and rating of D. For reference, buildings are assessed on their efficiency with an EPC Rating from A (most efficient) to EPC rating G (least energy efficient). Research suggests that to maximise the effectiveness of heat pumps, they should be used in buildings with a minimum EPC rating of C. For this reason, the decarbonisation of heating is vital in the UK meeting its net-zero carbon commitments (BEIS, 2021).

1.1 Worldwide deployment of heat pumps

Based on the statistics provided by the International Energy Agency (IEA), as illustrated in Figure 1, the global installation of heat pumps reached a cumulative count of 177 million by the year 2020. The majority of heat pumps were installed in China, accounting for 33% of the total, with North America and Europe following closely at 23% and 12%, respectively. In recent times, the growth of the heat pump sector has been insufficient in meeting the decarbonization scenarios outlined by the IEA and the UK's Committee on Climate Change (IEA, 2021). According to the IEA global heat pump stock statistics, the lack of heat pump installations worldwide by 2030 is evident. The projected number of heat pumps to be installed by that year, based on present rates, is only 253 million. However, the IEA's net-zero scenario requires 600 million units to be built by 2030, resulting in a deficit of 58% (refer to Figure 1). This includes air-to-air, air-to-water and ground-to-water heat pumps.

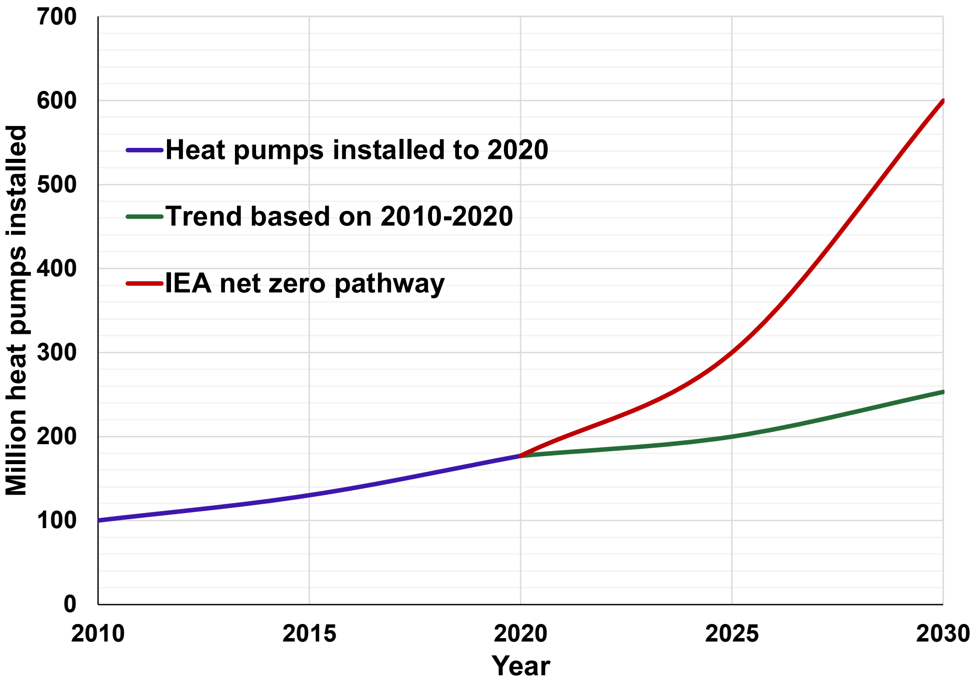

Figure 1. Global historic heat pump sales and IEA net zero 2050 pathway; Source: (IEA, 2021)

Even though the heat pump market keeps growing, heat pumps met only 7% of the heating demands of homes around the world in 2020. The growth is uneven, with most installations happening in newly built homes (IEA, 2021). One major obstacle is the slow adoption rate in pre-existing buildings, where inefficient heating systems fueled by fossil fuels must be replaced. Despite heat pumps' superiority over traditional, carbon-based heating systems in terms of both efficiency and environmental impact, they are not widely adopted. To meet the climate goals of 2030 and 2050, it is clear that heat pump adoption in existing buildings must increase (IEA, 2021).

Heat pumps are extensively sold in Europe and other regions for both commercial and residential heating applications. As depicted in Figure 2, the European Heat Pump Association (EHPA) projected a market growth rate of over 34% in 2021 in Europe. This expansion resulted in annual sales of over 2.85 million units of heat pumps (EHPA, 2022). According to the numbers, there are now approximately 20 million heat pumps across Europe. As per association data, the aforementioned entity is responsible for supplying heating to around 16% of Europe's residential and commercial buildings, hence resulting in the avoidance of 54 million metric tons of CO_2 emissions. Among them, a majority of 94% use air to water and 6% use the ground source heat pumps. In the European market, France, Italy, and Germany collectively constituted 50% of the market share in the year 2021 (EHPA, 2022).

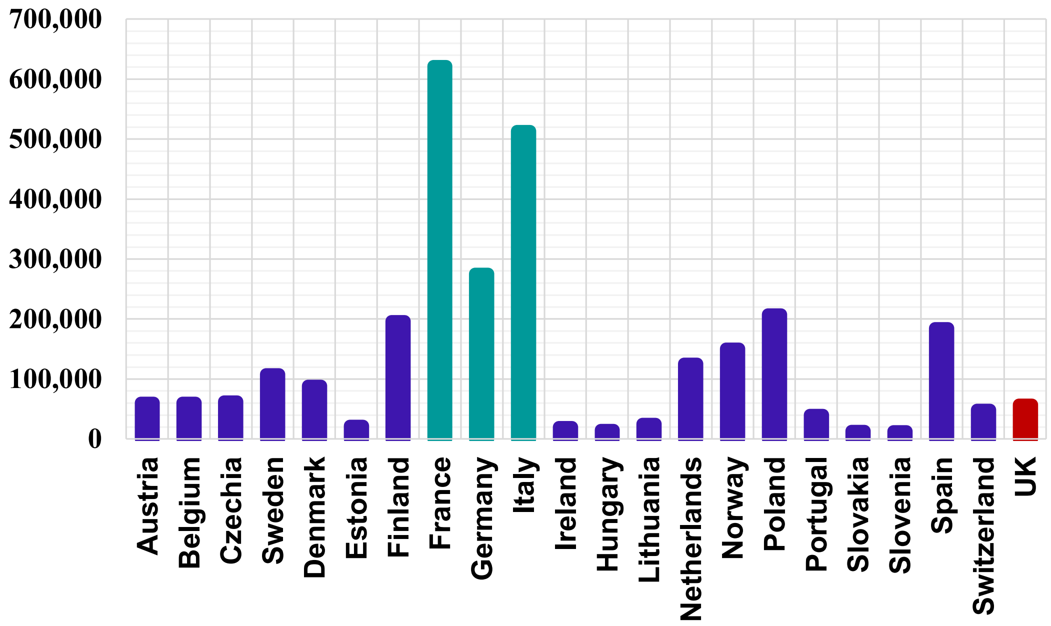

Figure 2. Heat pump sales in 2021 in Europe; Source: (EHPA, 2022)

There were more heat pumps sold in France (621,776), Italy (513,535), Spain (184,950), Sweden (108,000), Norway (150,004), Finland (196,359), Poland (209,992), and Germany (275,697 units) in 2021 than in any of the other 21 European nations assessed by EHPA.

In China, the world's largest market for air-to-water heat pumps (AWHPs), sales rose by around 7% in 2021, reaching a total of 12.5 million units (China IOL, 2022). The implementation of policy regulations that mandate the adoption of specific technologies has been the primary factor driving the development of sustainable heating technologies in China. The Electric Heating Policy and the Clean Winter Heat Plan in Northern China are two notable examples that necessitate the replacement of coal-fired heating systems with electric alternatives (Wang et al., 2020). These efforts have been further supported by local financial incentives, such as those in Beijing, which promote the installation of heat pumps (Zhou et al., 2022). Furthermore, the heat pump market received support from China's Clean Air Act, which aimed to enhance air quality by addressing air pollution (Yang Lingyan and Xu Wei, 2021). Figure 3 illustrates the worldwide sales of air source heat pumps (ASHP) in the year 2021.

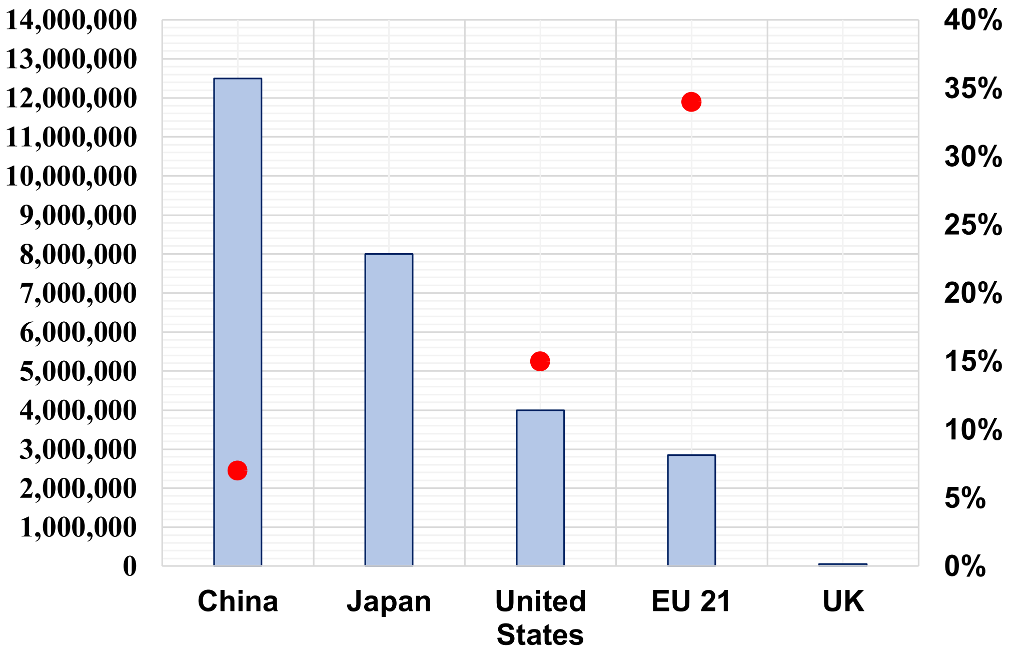

Figure 3. Global Air-source heat pump sales and market growth in 2021; Source:(IEA,2022)

In the United States, ASHPs experienced larger sales than gas furnaces for the first time in 2020, solidifying their position as a significant market contender. The aforementioned pattern persisted in the year 2021, when the market experienced a growth rate of 15%, concluding a series of consecutive year growth rates surpassing 5% since 2015 (AHRI, 2022), as illustrated in Figure 3. The installation of heat pumps as the primary heating equipment in new buildings varies depending on the kind of building, with approximately 40-50% of new structures opting for this technology. (Ed Vineyard and Van Baxter, 2021).

1.2 Heat pumps in the UK

Despite the government's commitment to positioning the United Kingdom as a global frontrunner in the heat pump sector, the country now exhibits one of the lowest rates of heat pump installation in Europe. The UK ranked 11th out of 21 adjacent nations for the overall volume of heat pump installations in 2021 and last for the number of heat pumps installed per capita. The Climate Change Committee (CCC) stated in its last annual report that heat pump installations in the UK were significantly below the anticipated trajectory necessary to meet the government's net-zero objectives, including a 68% decrease in carbon emissions by 2030 compared to 1990. In 2022, around 72,000 heat pumps were installed, with 69,000 in residential properties, markedly behind the CCC's forecast of 130,000 installations (Lowe, 2017) under 1% of homes. Approximately 87% of the aforementioned heating systems consist of air-to-water heat pumps (AWHPs). These AWHPs are particularly suitable for the prevalent housing stock in the UK, characterised by older structures with inadequate insulation. This is due to the AWHPs' ability to offer greater inertia and radiant heat compared to the more commonly favoured air-to-air units found in other regions worldwide, (mainly because they are reversible) (BEIS, 2021).

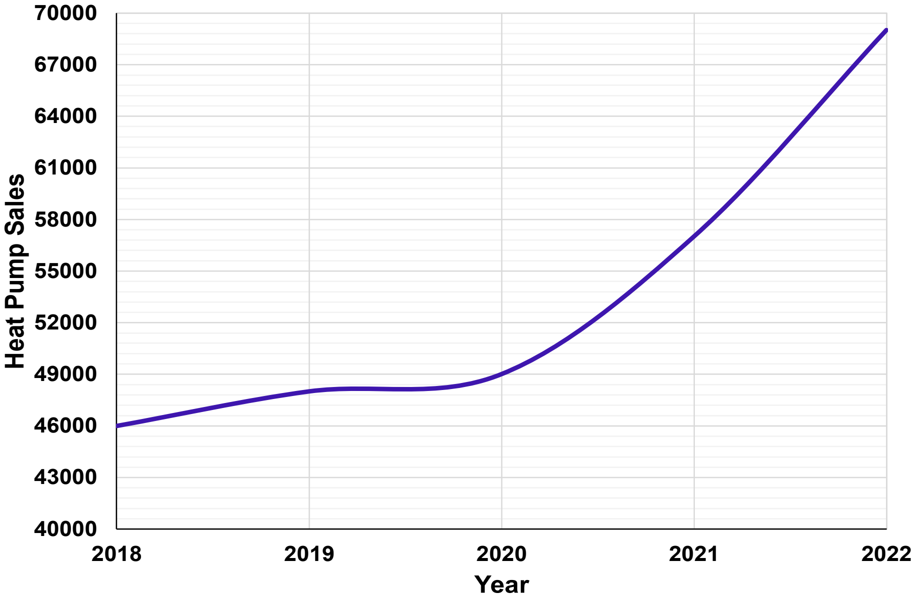

Figure 4. Heat Pump Sales in the UK

Sales of AWHPs in the UK during the past five years are shown in Figure 4. In comparison, it is estimated that there are already 26 million gas boilers in use, with 1.7 million replacement gas boilers installed each year in the UK (Rosenow et al., 2020), or more than 6,000 every working day. In other words, heat pumps only make up 2% of sales of gas boiler replacements (BEIS, 2021) and over 120 gas boilers are being installed for every new low-carbon heating system (Rosenow et al., 2020).

1.3 Heat pump forecast for new build housing

The UK Climate Change Committee's (CCC) 2025 assessment positions new housing as a central lever in the transition to low-carbon residential heating, with heat pumps identified as the default technology required to align the housing sector with the UK's statutory carbon budgets and net zero target. The CCC's pathway indicates that the majority of heating systems installed in new dwellings should be low-carbon by the mid-2030s, highlighting the strategic importance of embedding heat-pump-ready design within new-build standards. Consequently, the decarbonisation of new housing is not only a technical necessity but also a critical policy instrument for avoiding future retrofit burdens and ensuring the long-term sustainability of the UK residential building stock (CCC,2025)..

The CCC further notes that although annual installation rates have reached tens of thousands of units per year, with approximately 60,000 installations recorded in 2023/24, this scale of deployment is markedly insufficient for the latter half of the decade. Modelling undertaken by the CCC in support of the Seventh Carbon Budget demonstrates that heat pump deployment must accelerate rapidly, reaching several hundred thousand installations annually by 2030 to remain consistent with the UK's legally binding carbon reduction pathway. Related assessments suggest that approximately 450,000 heat pump installations per year will be required by 2030 to decarbonise residential heating at the pace necessary, with further increases anticipated throughout the 2030s as the transition away from fossil-fuel heating intensifies (CCC, 2025)..

1.4 Factors affecting the uptake of heat pumps in the UK

There is a widespread consensus regarding the considerable potential of heat pumps in effectively reducing greenhouse gas emissions and their overall positive impact on the sustainable growth of the heating and cooling industries (Fischer and Madani, 2017). Heat pumps have a promising future in the marketplace, which could lead to a number of positive social and economic outcomes (Gaigalis et al., 2016). However, the widespread adoption of heat pump technology faces numerous challenges, including technological, economic, regulatory, policy, and public acceptance issues.

1.4.1 Policy

The primary obstacles to the widespread use of heat pumps are commonly attributed to the presence of policy uncertainties, as well as the absence of well-defined pathways for decarbonizing heat and limited technical adoption (Chaudry et al., 2015). Insufficient allocation of financial resources towards research and development in the field of heat pumps might be considered as an additional policy obstacle that impacts the competitive advantages of these technologies, consequently influencing their adoption rates.

1.4.2 Upfront and running costs

According to the evidence, high capital and installation costs are significant barriers to the adoption of heat pumps in the UK. The upfront costs for heat pumps include the price of the unit and installation. The price varies based on the system's kW capacity. The larger the home's floor area, the larger the heating system must be to adequately heat it. Typically, heat pumps have significantly higher initial costs than boiler systems. Among heat pumps, GSHPs are more expensive than AWHPs (Ahmed, 2023).

The upfront cost for an AWHP ranges from £7,000 to £13,000, whereas for a GSHP, the range is £14,500 to £45,000 (Vekony, 2023). In contrast, the unit and installation costs of gas boilers are £2000 to £4500 (Ahmed, 2023). The upfront cost presents a substantial barrier to the widespread use of heat pumps.

Numerous variables make it challenging to estimate the operating costs of heat pump systems. The Coefficient of Performance (COP), varies according to the type of heat pump employed and the operational conditions under which it is used, while building characteristics and patterns of use further affect energy demand.. Additional variables that determine the seasonal performance factor (SPF) include the electricity tariff and user behaviour, as well as the heating system's specification and commissioning. Maintenance is also recognised as an issue with the running cost.

The existing disparity in energy taxes and levies undermines the economic viability of heat pumps inside the UK. At present, taxes and levies constitute a substantial proportion of electricity and gas prices, thereby impacting household energy expenditures. The cost of electricity per kilowatt-hour (kWh) is higher compared to that of gas or oil. The UK has some of the highest electricity prices in Europe and some of the lowest gas prices, making it difficult for consumers seeking to replace an existing gas system. As a result, the cost to operate an electric boiler in the same home would be higher than that of a gas or oil boiler. Heat pumps have a COP of between 2 and 3, meaning they consume significantly less energy than a boiler would to generate the same quantity of heat. As of right now, for consumers on a fixed tariff, an AWHP does not achieve running-cost parity with a gas boiler because of the significantly higher cost of electricity per kWh compared to gas (McMillan, 2022).

1.4.3 Public attitudes towards heat pumps

The adoption of heat pump technology is hindered by substantial hurdles related to public acceptance and understanding. These concerns arise due to unfounded anxiety, misunderstandings, inaccurate information, and/or past encounters with the effectiveness of heat pumps, specifically in terms of their technological limitations. The prevalence of limited public awareness of the environmental and economic advantages associated with heat pumps is not infrequent, even within highly developed societies (Hughes, 2008). Heat pumps can generate noise pollution, giving rise to public concerns and perhaps diminishing their acceptance levels. Nevertheless, noise levels emitted by these entities are frequently regulated through noise baffles, which mitigate noise-related disturbances within the surrounding community (Chassein et al., 2017).

Research from numerous field trials shows that heat pump adoption is slowed by a lack of reliable information about microgeneration (Toke, 2022). The interaction between specific technologies, architectural forms, and user characteristics is a significant aspect to consider. Hence, the level of operational complexity exhibits substantial variation when a single variable is altered inside the system. For example, elderly homeowners encounter more challenges when it comes to managing the maintenance demands of emerging technologies, potentially impacting the overall effectiveness of the system.

Several studies have also identified usability difficulties, namely related to the control interface and hardware. However, it is important to note that these challenges do not directly indicate a barrier, but rather pose prospective obstacles to the eventual acceptability of such systems. Some individuals propose that the installation of heat pumps and associated demand side control may lead to the disturbance of family routines (Sweetnam et al., 2019). Recently, a demand-side response trial was conducted in social housing units in Barnsley, England. Residents' lives were disrupted, but only to a tolerable level (Goyal et al., 2019).

There is evidence that knowledge sharing within communities can result in large increases in uptake of energy efficiency measures (Owen et al., 2023) and heat pumps (Hyysalo et al., 2018). Industry and academic stakeholders argue that media focus on adverse experiences contributes to diminishing public trust in heat pump technology (Lowes et al., 2020). Negative experiences often relate to poor installation, leading to lower performance and higher running costs than expected (Burns et al., 2021).

1.4.4 Manufacturing and sourcing

A significant proportion of heat pumps installed in the UK are sourced from foreign manufacturers, constituting over two-thirds of the total. In contrast, half of the boilers utilised in the UK are domestically built. Historically, the gas boiler industry has a few larger players, such as British Gas, alongside many small firms and sole traders; there are over 78,000 firms approved to install gas equipment, employing over 130,000 registered engineers (MCS, 2020). In comparison, there are only 1134 heat pump installers registered with the microgeneration certification scheme (MCS 2022) in the UK. Major installers and manufacturers of heat pumps are active in the UK, and the UK Heat Pump Federation has 100 members; this is comparable to the larger European Heat Pump Association (170 members). However, the number of skilled technicians is still low. Compared to the 1.7 million gas boiler installations each year in the UK, the European Heat Pump Association estimates that total annual installations of AWHP and GSHP only increased from 18,500 in 2014 to around 40,000 (37,000 AWHP) in 2021. Within this the Renewable Heat Incentive was supporting the installation of around 15,000 AWHP and 1,700 GSHP units per year by February 2022 (ofgem, 2023).

1.4.5 Installer skills gaps

The significance of installers in facilitating the shift towards low-carbon heating is of utmost importance, as they serve as the crucial element for the process of decarbonising heat. Installers serve as the primary point of contact between homeowners and play a pivotal role in the engagement process within the industry. As per the Department for Business, Energy and Industrial Strategy (BEIS), installers or tradespeople are regarded as the most reliable cohort for dispensing guidance pertaining to the selection of a heating system for residential premises (BEIS, 2021). The absence of a rise in the number of installers will impede the capacity to effectively and adequately deploy heat pumps. Furthermore, it will hinder the essential engagement and promotion with families required to generate the necessary increase in demand for net-zero heating. Consequently, there is a need for an increase in the quantity of heat pump installers (refer to Figure 5). The attainment of these figures is contingent upon the implementation of a comprehensive decarbonization policy framework by the government, with concerted endeavours from the industry to involve and educate small and medium-sized enterprises specialising in heat pump installations. With a definitive dedication from both the private sector and the public sector, this expansion will be initiated. The objective set by the UK government is to have a total of 50,200 installers by the year 2030 (Branford and Roberts, 2022).

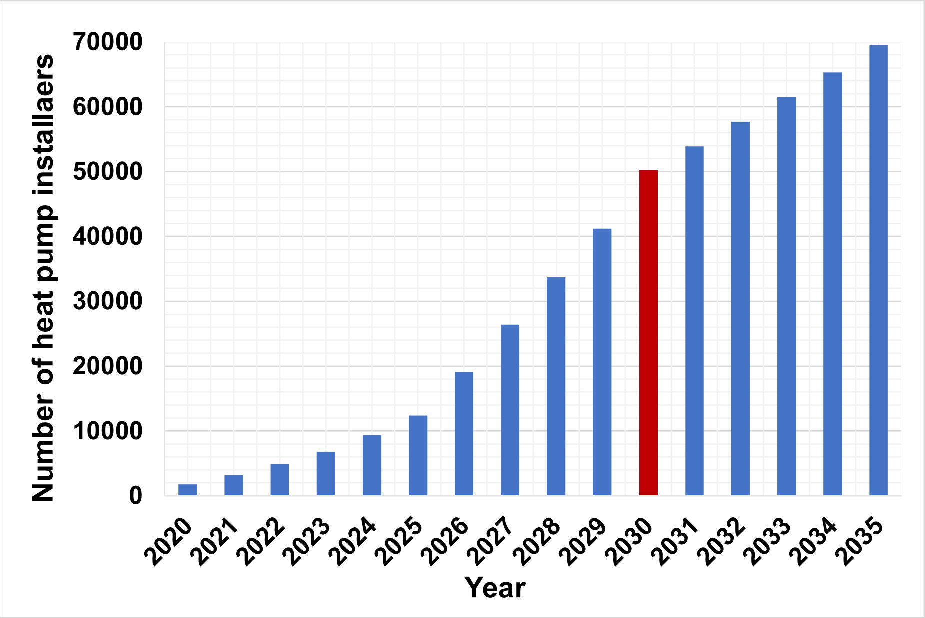

Figure 5. Potential total number of installers needed; Source:(BEIS, 2021)

1.4.6 Advanced technological features of heat pumps

One significant impediment to the widespread use of heat pumps is the constraint imposed by the electrical grid, a factor that is not frequently acknowledged. The utilisation of heat pumps has the potential to increase electricity consumption during peak periods, thereby requiring additional investments in electrical grid infrastructure to meet the increased demand (Fawcett et al., 2015). Electrical distribution systems, which have historically been designed to accommodate lower electrical loads, are expected to experience the most significant impact from the widespread adoption of electrification in the heating sector. An increase in peak winter load could have serious financial and environmental consequences (Fawcett et al., 2015). Heat pump installation, for instance, has the potential to boost UK peak electricity demand by 14% (Love et al., 2017). The observed rise in peak demand may necessitate the implementation of network reinforcement, which could potentially have adverse effects on the economic feasibility of integrating heat pumps. According to Protopapadaki and Saelens (2017), an increase in the use of heat pumps may cause problems with overloading and power stability. Some estimates suggest that annual electricity demand could increase by 25-50% and peak demand by 50-100% in a scenario where 80-90% of households install heat pumps (Watson et al., 2023). This would require significant investment in electricity infrastructure to deliver more power to households, particularly during peak times (Lawton and Abeysinghe, 2022). Further study and research are required to examine the correlation between heat pump penetration levels and peak power demand. Additionally, exploring novel approaches to decrease the peak-to-average demand ratio may be necessary (Fawcett et al., 2015).

1.5 Overcoming barriers to increase the uptake of heat pump

By addressing these performance and cost-related factors, the uptake of heat pumps in the UK can be significantly increased, leading to a more sustainable and cost-effective heating solution for homes.

1.5.1 Compressor cycling

The frequent on/off cycling of the compressor is a contributing element that leads to heightened electricity consumption, mostly as a result of the substantial energy demand during the compressor's start-up phase. Compressor cycling may manifest as a symptom of two underlying problems, namely low heat loads or high flow temperatures. Human actions, including opening windows, contribute to cycling by rapidly releasing the building's interior heat. This can happen if the temperature range between when the heat pump turns on and when it turns off (the hysteresis setting) is too small. Compressor and other component lifetimes can be shortened, and system efficiency can drop due to short cycling. Increased cycling is indicative of either bad initial specification or installation or persistently poor operation due to user knowledge gaps and will have varying effects on overall efficiency. Additionally, the surge in consumption at compressor start-up raises grid demand, which may necessitate management when heat and transportation become electrified. Inverter-driven variable-speed compressors are designed to reduce on/off cycling by matching compressor speed with heating load. A fixed-speed compressor has a constant operating speed and either turns on or off depending on the temperature requirements. To lessen the frequency of cycling, a fixed-speed compressor coupled with a thermal storage tank is recommended (Burns et al., 2021).

1.5.2 Flow temperature

Heat pumps operate most efficiently when the flow temperature is maintained at a low level. However, at lower flow temperatures, heat emitters transfer less heat to the room, necessitating the use of larger heat emitters to maintain thermal comfort. Fabric efficiency also plays a critical role in ensuring thermal comfort, as the rate at which heat emitters deliver heat to a room must align with the rate at which heat is lost. Therefore, achieving optimal system performance requires a careful balance between flow temperatures, heat emitter sizing, and fabric efficiency in the design of heat pump systems (Burns et al., 2021).

1.5.3 Load factor

The percentage of the heating load that is satisfied by the heat pump is known as the load factor. The seasonal performance factor (SPF) of a heat pump can be negatively affected by both an excessive load factor (under-sizing) and a low load factor (over-sizing).

In the UK, manufacturers and the Microgeneration Certification Scheme (MCS) offer guidelines for the proper sizing of heat pumps, including fixed inside temperatures and fluctuating exterior temperatures that differ by location. The suggested temperatures are intended to guarantee that the heat pump can fulfil heating requirements throughout the season, excluding a few occurrences of severe weather. The design external temperature aims to reconcile the necessity for effective heat delivery in cold conditions with the objective of preventing the over-sizing of the heat pump for milder temperatures. If the design exterior temperatures were established below current norms, the heat pump would be excessively large for most of the year's performance demands (Lowe et al., 2017).

1.5.4 Installation and retrofitting costs

Gas boiler replacements for 3 to 4 bedrooms typically cost £3,000 - 4,500. Depending on the extent of the retrofitting necessary, the cost of a heat pump retrofit can vary significantly, frequently surpassing £10,000. Future heat pump replacement costs are anticipated to be more comparable to those associated with boiler replacements, as retrofitting is a one-time expense. The government’s Boiler Upgrade Scheme is designed to reduce the cost barrier for new heat pump installations. On Thursday, September 21, 2023, the Department for Energy Security and Net Zero announced an increase in the grant level for the Boiler Upgrade Scheme (BUS) in relation to AWHP and ground source heat pumps (GSHP). As part of this update, installers will now be eligible to receive a grant of £7,500 for both AWHP and GSHP installations (ofgem, 2023). The Boiler Upgrade Scheme (BUS) is a relatively long-term initiative that provides an upfront grant. It has been extended until 2028 as part of the government's "Green Day" collection of policy announcements. Building on the lessons learnt from previous financial schemes in the UK, the BUS has the potential to serve as a significant instrument in supporting the deployment of heat pumps in the future, thanks to its streamlined administration.

1.5.5 Heat pump running costs

According to research by Watson et al. (2021), heat pumps' ability to compete economically hinges heavily on their SPF. Heat pumps with a higher SPF are more cost-effective than gas boilers when comparing annual fuel expenditures. Therefore, research implies that lowering electricity taxes and levies while increasing taxes on fossil fuels can lower the total cost of ownership of heat pumps. Under the existing system, governments can levy a tax on pollutants whose environmental damages are estimated. One such system is the Emissions Trading System (ETS), which employs a 'cap and trade' strategy in which a maximum permitted level of emissions is established and businesses must hold an emission allowance for each tonne of CO_2 they release in a given year. Watson et al. (2023) noted that the electricity demand associated with running heat pumps is unlikely to yield running cost reductions in comparison to gas boilers, which could exacerbate the fuel poverty problem in Scotland. They propose many alternate methods for recovering the price of energy levies, such as charging a flat rate per home or dividing the price of levies between gas and electricity rates. The UK government has acknowledged that the current energy tax and levy mechanism does not encourage consumers to make environmentally friendly choices like switching from gas boilers to electric heat pumps, and so it plans to lower electricity costs by shifting or rebalancing energy levies or obligations away from electricity over the next decade (BEIS, 2021).

1.5.6 Other strategies for reducing running costs

Solar photovoltaic (PV) was chosen as an upgrade measure in early optimisation runs due to high power prices offsetting PV's capital expenses and lowering overall running costs. According to these preliminary findings, solar photovoltaics are currently economically viable for households who can afford them, and they may also be a technique to ensure lower running costs in fuel-poor homes, provided these households are helped to meet capital expenses. Time of Use Tariffs incentivize consumers to use power during low-demand times and to cut back during peak-demand times. This has the potential to lower energy costs, ease grid pressure, and increase the use of renewable energy sources. These tariffs and a heat pump would have been cost-effective before the energy price increases in 2021/22. The heat pump in a well-insulated home can be turned up before peak pricing hours (usually 4-7 p.m.) and turned down during those hours to save money. Since many energy providers have temporarily pulled time-of-use tariffs from the market in response to the current volatility of energy prices, there are currently very few options for consumers to choose from. The remaining ones are currently less desirable than regular tariffs. As more households switch to cleaner electric heating, however, Time of Use (TOU) Tariffs may become more widespread, with energy providers likely making them more appealing to assist in addressing periods of very high demand without making substantial investments in power networks. Heat pumps may have lower operating costs in the future if they are able to take advantage of lower low-demand power rates (BEIS, 2021), however, the future of conventional and TOU tariffs is still unclear.

1.5.7 Improving consumer awareness

Another significant barrier to decarbonising heat is a general low-level consumer awareness of low-carbon heating options. Research by the think tank Bright Blue revealed that only 42% of British people have heard of heat pumps. Worryingly, this is the highest scoring system in terms of familiarity. Government, industry and wider stakeholders need to do more to improve consumer awareness and understanding of the opportunities and benefits of zero-emission heating systems. Unless this issue is addressed, it is unclear how the UK will meet its ambitious decarbonisation targets for heat. A consumer campaign and a strategy for improving consumer awareness should be a priority within the Scottish and UK Government's approach to rapidly increasing zero-emission heat system uptake (BEIS, 2021).

1.6 Aims and Objectives

The main aim of the project is to investigate the feasibility of domestic heat pumps using CO_2 as the working fluid to satisfy the space heating and hot water requirements of domestic dwellings in the UK. Potential advantages offered by CO_2 heat pumps compared to conventional heat pump technologies are the use of a near zero global warming refrigerant, small footprint and ability to deliver hot water at higher temperatures than that possible with other heat pump technologies.

Specific Objectives include:

1. Investigation of the current state of the art of CO_2 heat pumps for domestic heating applications through literature review and experimental investigations in the laboratory of commercially available systems for domestic space and water heating applications.
2. Use outcomes from Objective 2 to design and/or select individual components and build a CO_2 pilot domestic heat pump for testing and development in the laboratory.
3. Undertake a comprehensive experimental programme to investigate and optimise the performance of the heat pump and its integration with thermal energy storage. Both hot water and Phase Change Material storage to be considered.
4. Investigate through modelling the energy and environmental performance of the developed heat pump in domestic dwellings, draw conclusions from the work and identify further research and development opportunities.

1.7 Thesis structure

This thesis is divided into eight chapters as follows

Chapter 1 provides an overview of the UK residential heating sector. The characteristics of the housing stock and the fuel composition of energy consumption. After that, the tendencies of the global and UK heat-pump markets and the low rate of heat-pump adoption in the UK and the steps that will improve both efficiency and affordability in this market are considered.

Chapter 2 presents the current state of the art on CO_2 transcritical air to water heat pump (AWHP) research and development. More emphasis is given to specific aspects of CO_2 heat pump technology, including system design and performance.

Chapter 3 offers a comprehensive evaluation of the performance of a commercially available 2.3 kW CO_2 domestic heat pump. Through a series of experiments conducted under various operating conditions. This chapter aims to provide a detailed understanding of the heat pump's behaviour, efficiency, and effectiveness in real-world scenarios. The results of these experiments are presented, and discussed.

Chapter 4 focuses on simulating the energy demand for space heating and domestic hot water (DHW) in new domestic dwellings within the UK by using the TRNSYS software, a dynamic energy simulation tool

Chapter 5 includes the modeling of the transcritical CO_2 air-to-water heat pump (AWHP) and the thermodynamic equations governing the operation of its various components. It also introduces the Engineering Equation Solver (EES) software tool employed for the analysis. Finally, the section outlines the input parameters, presents the simulation results, and provides a discussion of the findings.

Chapter 6. Integration of heat pump with thermal storage system and optimisation of design and operation of the integrated system to minimise energy demand from the grid.

Chapter 7. The research findings are scrutinised in the final chapter, which also presents the primary conclusions. It also provides suggestions for future research, emphasising areas that require additional investigation.

Chapter 2 Literature Review

This chapter presents a comprehensive literature review covering refrigerants and in particular, the characteristics of CO_2 as a refrigerant, CO_2 heat pump cycles and approaches to improve energy performance and studies on individual components and their optimisation.

2.1 Working fluids for heat pumps

Choosing the right refrigerant is crucial when developing a heat pump. The ideal refrigerant must first meet all the cycle's requirements, including density, thermal conductivity, critical temperature, and pressure, to mention a few. However, the detrimental effects that conventional refrigerants have had and continue to have on our atmosphere have come to light due to increased consciousness of climate change and its effects on the environment. Leaks happen, harming the atmosphere even though refrigerants should remain inside the refrigeration cycle. Furthermore, there is a lot of room for improvement in the way those compounds are treated after their useful lives.

2.2 CO_2 (R744) thermodynamic properties

CO_2 concentration in air is roughly 0.04 % (v/v) (Emerson, 2016). In CO_2 (R744) refrigeration and heat pump systems, two thermodynamic states of critical importance, as highlighted by Cavallini and Zilio (2007), are illustrated in Figure 6. The triple point, occurring at approximately 5.2 bar (0.52MPa) and −56.6°C, represents the condition at which the solid, liquid, and vapour phases coexist; operation near this point poses a risk of dry ice formation, which can obstruct flow and damage system components. The critical point, at 31.1°C and 73.8 bar (7.38 MPa), is comparatively low relative to typical ambient temperatures, thereby necessitating transcritical operation in many practical applications. Under transcritical conditions, the refrigerant does not undergo condensation but instead behaves as a supercritical fluid, which has fundamental implications for system design and control strategies.

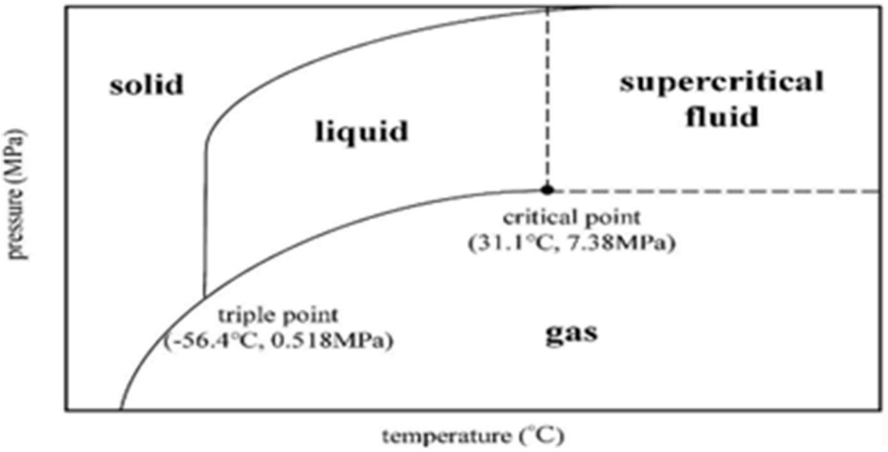

Figure 6. Schematic representation of carbon dioxide phase diagram

At pressures below a specific threshold, a liquid phase is absent, demonstrating that solid carbon dioxide (CO_2) transitions directly to the gaseous state via sublimation at ambient pressure. A significant factor to consider is the critical point, which occurs at 73.8 bar (7.38 MPa) and 31°C. At this juncture, the liquid and gaseous phases display analogous properties, leading to an indistinct boundary between them. Past this critical point, the refrigerant becomes a supercritical fluid, making the notion of latent heat of vaporisation irrelevant. The behaviour of supercritical fluids markedly differs from that of subcritical fluids. When heat is removed from a fluid that is above its critical pressure and temperature, no phase transition takes place; rather, the temperature of the fluid decreases. A subcritical fluid exhibits a constant temperature during a phase change while exchanging latent heat. The unique characteristic of refrigerant fluids is beneficial in refrigeration systems, as supercritical CO_2 can cool without undergoing condensation. CO_2 is distinguished among commonly used refrigerants due to its low critical temperature, which renders it advantageous for specific applications (Cavallini and Zilio, 2007).

2.3 Comparison between refrigerants

The finalisation of the working fluid is vital for the efficiency and effectiveness of the heat pump system. Additionally, various factors need to be thoroughly examined to identify sustainable long-lasting solutions. To facilitate this process, Danfoss implemented the 7 Force Model, which categorises these factors into three primary criteria: cost-effectiveness, environmental impact, and safety. It is important to define the characteristics that a refrigerant must possess to achieve a balance among these three considerations (Danfoss, 2018). To begin with, it is essential that the fluid has a low life cycle capital and a medium to high availability to ensure easy access. From a chemical standpoint, the fluid should exhibit stability, be dissolved with lubricants, and be feasible with the materials used in construction. This compatibility minimizes wear on components, thereby enhancing long-term reliability, and it is crucial that the fluid is neither toxic nor flammable. Lastly, as previously mentioned, regulations governing refrigerant usage have become significantly stricter to mitigate environmental effects. Consequently, the fluid must demonstrate a low ODP and a GWP (Hundy et al., 2016; Poongavanam et al., 2021).

To enhance the efficiency of heat pump operation, it is essential to carefully evaluate the transport and thermodynamic characteristics of the selected refrigerant. The refrigerant should possess suitable critical and boiling points, along with a low vapor heat capacity. To mitigate the risk of leakage and air infiltration, the evaporation pressure must exceed ambient pressure. Additionally, low viscosity and high thermal conductivity contribute to the design of small heat exchangers due to an increased transfer coefficient. A higher latent heat of vaporisation significantly reduces the necessity for a high mass flow rate of the refrigerant, which in turn minimises compressor displacement and decreases power usage. Ideally, a low-pressure ratio is preferred, as it enhances the volumetric efficiency of the compressor, thereby reducing the work required. Lastly, achieving a low-pressure drop is advantageous, which can be accomplished by selecting a low viscosity refrigerant (Thonon, 2007). The categorisation of toxicity and in flammability holds considerable importance, as outlined in ASHRAE Standard 34, which pertains to the safety and designation aspect of refrigerants. ASHRAE designates an identifying reference letter to indicate the toxicity class and a corresponding number to indicate the refrigerant’s flammability. In terms of toxicity, refrigerants are classified into either class A or B (Gupta et al., 2018):

- **Class A** refrigerants are those that do not demonstrate toxicity at 400 ppm (v/v) or lower. In contrast,
- **Class B** refrigerants are characterized by their toxicity at < 400 ppm (v/v).

For flammability, refrigerants are classified into four distinct classes:

- **Class 1** represents refrigerants which do not transfer flames in air at a temperature of 21°C and 101 kPa pressure.
- **Class 2** comprises refrigerants having a lesser flammability limit beyond 0.10 kg/m3 at 101 kPa and 21°C, along with combustion heat of less than 19 kJ.
- **Class 2L** is a subclass that denotes refrigerants with lower flammability, characterized by a very slow burning velocity of less than 10 cm/s.
- **Class 3** consists of extremely flammable refrigerants, that either have a lower flammability limit of 0.10 kg/m3 or less at 21°C and 101 kPa, or a combustion heat equal to or greater than 19 kJ/kg.

The refrigerant must not be flammable or toxic. This results in an ideal classification of A1, indicating the absence of flame propagation and low toxicity. Figure 7 illustrates the distribution of the majority of available refrigerants.

Flammability	**Higher**	**A3**	R290, R1270, R601, R600, R600a, E170	**B3**	
	Lower	**A2**	R142b, R152A, R365mfc, R1234ze (Z)	**B2**	
		A2L	R1234ze (E), R1234yf	**B2L**	R717
	No flame propagation	**A1**	**R744**, R113, R114, R124, R134a, R236fa, R227ea, R1336mzz(Z), R1336mzz€, R718	**B1**	R123, R21, R245ca, R245fa
		Lower		**Higher**	
		Toxicity			

Figure 7. Refrigerant flammability classes

In light of the aforementioned considerations, it is crucial to recognise that no single refrigerant can possess all the desired properties. Consequently, selecting a refrigerant necessitates a compromise that aims to fulfil the intended function of the fluid as effectively as possible. Refrigerants are primarily classified based on their composition, which is split into six prevalent types:

Chlorofluorocarbons (CFCs): The CFCs emerged as 2nd-generation refrigerants, addressing issues such as material mismatch, toxicity, and flammability. But, due to environmental concerns related to ODP and GWP, their production and commercialization were prohibited after dominating the market for 60 years. Notable examples include R12, R114, and R502 (Gupta et al., 2018).

Hydrochlorofluorocarbons (HCFCs), primarily exemplified by R22, were introduced with the incorporation of hydrogen atoms. Although they have a relatively brief atmospheric lifespan of approximately 13 years, the presence of chlorine atoms continues to endanger the ozone layer. Consequently, efforts are underway to gradually eliminate their production (Elkins, 1999).

Hydrofluorocarbons (HFCs) represent the third generation of fluorine-based gases. Due to the absence of chlorine in their composition, these refrigerants are classified as having a zero-ozone depletion potential (ODP), making them strong candidates for use. However, HFCs are associated with a relatively high GWP, being approximately one hundred times greater than CO_2. As a result, despite being the fastest-growing greenhouse gases at present, numerous countries have agreed to implement measures to reduce HFC emissions. appropriate refrigerants in this category include R134a, R410A, R152a, R32 and R245fa (Gupta et al., 2018).

HCs are organic compounds, including R1270, R290, and R600. They have a brief atmospheric lifespan, leading to a minimal Global Warming Potential (GWP), and are typically available at a lower cost owing to reduced energy consumption. However, their significant flammability poses challenges, restricting their application in low-power settings like household refrigeration (Razzaq et al., 907).

Hydrofluoro-olefins (HFOs) represent the 4th generation of fluorine-based refrigerants, emerging in 2010s. The primary distinction from hydrofluorocarbons (HFCs) lies in the occurrence of a double bond between C-atoms, that contributes to a significantly shorter atmospheric lifespan. The first HFO introduced was R1234yf, designed to replace R134a & R114 in applications such as mobile and domestic refrigeration. This compound boasts a low GWP and has a zero-ODP. But its mild flammability and considerably higher production costs pose challenges to its widespread adoption. Another notable HFO that has been developed is R1234ze (Hafner, 2019).

Inorganic natural refrigerants consist of substances such as water (R718), ammonia (R717), and CO_2 (R744), all of which are produced through natural biochemical processes. As a result, these refrigerants do not harm the ozone layer and possess an almost negligible GWP. Additionally, their high efficiency further enhances their reputation as environmentally friendly options (Carvalho et al., 2014).

Given the environmental issues and existing regulations, the primary factors to consider are the ODP and GWP. Many refrigerants in use today have an ODP of zero, which does not serve as a distinguishing factor. However, the GWP can vary significantly depending on the selected refrigerant. Carbon dioxide (CO_2), with an ODP of 0 and a GWP of 1, is recognized among most environmentally benign refrigerants. Additionally, newer hydrofluoro-olefins (HFOs) and hydrocarbons (HCs) exhibit nearly negligible GWP values. Although their high GWP does not eliminate their current application, the utilization of hydrofluorocarbons (HFCs) is being curtailed (Hafner, 2019).

Due to safety, the flammability of the HCs (R290 or R600a), restricts its usage, as compared to nontoxic and non-flammable CO_2 (A1). CO_2 and R134a similarly come with excellent safety grades.

As discussed, the significantly lesser critical temperature of CO_2 serves as the primary distinguishing factor, enabling heat rejection to occur as a single-phase procedure. Additionally, various thermophysical properties enhance the advantages of CO_2:

- The high density of CO_2, which is 30 times greater than R717 and three times that of R410A, typically leads to reduced size requirements for heat pumps and lowers the work input needed by compressors.
- The increased specific heats enhance heat transfer coefficients and the efficiency of heat exchangers.
- CO_2 has a higher latent heat of vaporisation than other refrigerants, resulting in a reduced flow rate for specific cooling and heating capacities.

Despite the fact that the differences in suction and discharge pressures are considerably larger—fourteen times greater than R134a & five times more than R410A.CO_2 compressors generally function with lesser pressure ratios (PR) than those utilising HFC. The PR in a transcritical cycle typically ranges between 2-4, whereas HFC cycles can exhibit PR as high as 8. This suggests that CO_2 compressors could, in theory, operate with greater efficiency.

However, it is essential to consider other factors, such as increased leakage and diminished volumetric efficiency, before concluding this. These challenges primarily arise from elevated pressure and heat loss. Furthermore, CO_2 demonstrates compatibility with common construction materials like copper and stainless steel, and standard lubricants can be utilized in CO_2 systems. These characteristics help mitigate excessive wear on heat pump components (Mastrowski et al., 2019).

As depicted in Figure 8, CO_2 shows significantly higher volumetric refrigerating capacity compared to conventional refrigerants and other common refrigerants due to its high vapor density. The volumetric refrigeration capacity of CO_2 increases with temperature, reaching a maximum at approximately 22 °C, before decreasing at higher temperatures. By definition, this capacity reduces to zero at the critical point(Kim et al., 2004).

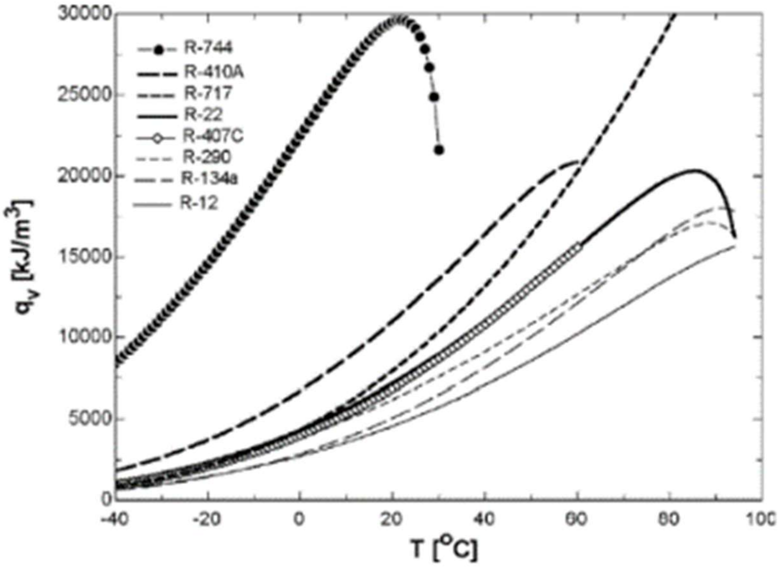

Figure 8. R744 volumetric refrigerating capacity comparison with other refrigerants

2.4 CO_2 Air-to-Water Heat Pump (AWHP)

CO_2 refrigerant in an AWHP is gaining popularity due to its superior operating performance and less impact on the environment as compared to AWHPs using more conventional hydrofluorocarbon (HFC) refrigerants. In addition, AWHP using CO_2 as a refrigerant is capable of obtaining a high-water outlet temperature of more than 80°C by running in the transcritical area (Carroll et al., 2020) .

2.4.1 Basics of transcritical CO_2 cycle

The fundamental transcritical CO_2 heat pump is represented schematically in Figure 9 (a), while Figure 9 (b) illustrates the cycle process via a P-h diagram. The system comprises four essential components: a gas cooler, a compressor, an evaporator, and a throttling valve. The CO_2 transcritical cycle comprises four fundamental processes similar to those in the conventional vapour compression cycle (VCC), which serves as the foundation for HCFCs and CFCs. Compression occurs from state 1 to state 2, followed by heat rejection from state 2 to state 3, expansion from state 3 to state 4, and heat absorption from state 4 back to state 1. The low critical temperature of CO_2 (31.1°C) necessitates that the evaporator functions in subcritical regimes while heat rejection occurs in the supercritical zone, resulting in the designation of the cycle as a transcritical cycle. The supercritical heat rejection process is the sole process that diverges from the established standard vapour compression cycle (VCC). In a transcritical cycle, the evaporator continues to perform the heat absorption function; however, heat rejection is not achieved via condensation. The refrigerant pressure is elevated to supercritical levels, and heat rejection is achieved through sensible cooling. Consequently, most of the time, a CO_2 system operates in a transcritical CO_2 cycle.

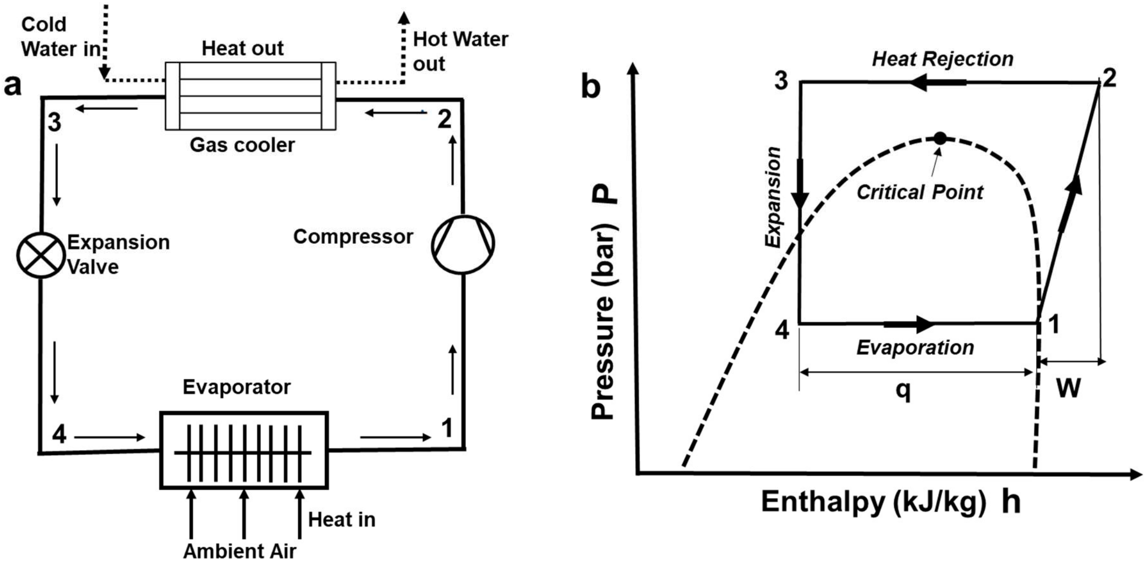

Figure 9. Basic Transcritical cycle of CO_2 (a) Schematic CO_2 cycle, (b) P-h diagram

The fluid exhibits vapor-like characteristics, such as low density and low viscosity, when temperatures exceed the critical point, while it displays liquid-like attributes, including high density and high viscosity, at temperatures below this threshold. At the critical pressure, a notable increase in the specific heat of CO_2 is observed as supercritical CO_2 approaches the critical temperature. As the pressure surpasses the critical level, the temperature at which this increase occurs also rises, although the intensity of the increase diminishes. This temperature is known as the pseudo-critical temperature. Consequently, the heat released during the cooling of the gas can be used for different heating purposes, like domestic water heating, space heating, dehumidification, and food preparation (Yu et al., 2019).

In contrast, the entire cycle in a conventional heat pump (subcritical vapour-compression) runs below the critical point of the utilised refrigerant, as seen in Figure 10. The refrigerant absorbs heat at low pressure through evaporation and rejects heat at high pressure through condensation, undergoing a phase change between the vapour and liquid states (from state 2′ to state 3). Under such operating conditions, the discharge temperature following compression typically remains below 80°C, which is generally insufficient for high-temperature water heating applications. Normally, water heating up to 60°C is essential in domestic hot water (DHW) applications. As a result, heat rejected from CO_2 is substantially less for a subcritical cycle, resulting in a low heat capacity and low heating efficiency. (Bellos and Tzivanidis, 2019).

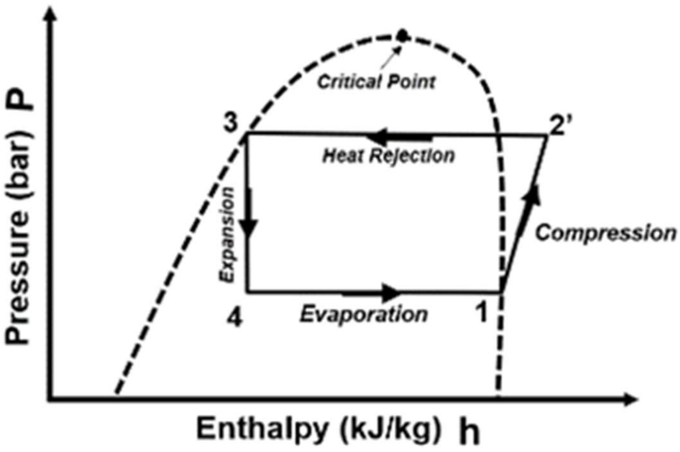

Figure 10. P-h diagram of Subcritical cycle

To utilise the transcritical cycle effectively, it is essential to consider the significant pressure differential and the unique characteristics of gas cooling process. The evaluation of the transcritical cycle relies on parts and operational parameters that differ from those found in conventional cycles. The distinctive features of the transcritical cycle render it particularly suitable for certain heating applications. Since the gas cooler dissipates heat through sensible cooling, the temperature difference for the outlet and inlet (temperature glide) is considerably more than that observed in a condensing operation. Consequently, the transcritical cycle offers greater benefits for applications like heating that necessitate a swift rise in temperature (Austin and Sumathy, 2011).

2.5 CO_2 transcritical cycle characteristics

In comparison to traditional refrigerants, carbon dioxide (CO_2) exhibits a notable characteristic: a low critical temperature (31.1°C). Consequently, heat rejection typically occurs at supercritical pressure, resulting in a "transcritical" cycle, which consists of a supercritical high-pressure and subcritical low-pressure side. Within a transcritical VCRS, the high-pressure side operates independently of temperature, making the choice and directive of this side a new capricious that influences both capacity and coefficient of performance (COP). The subsequent discussion will address additional aspects of the single stage transcritical CO_2 cycle, including the high-pressure side, optimal pressure, and refrigerant temperature glide.

2.5.1 High pressure side

Pressure and temperature function as distinct variables in the supercritical phase of the CO_2 transcritical cycle. When the exit temperature of the gas cooler is maintained constant, the system's increased pressure affects the enthalpy of the fluid. With an increase in high pressure, the isotherm exhibits a progressively steeper gradient, influencing specific heating capacity (q), specific compressor work (w), and coefficient of performance (COP), while the evaporating temperature (T1) and exit temperature of the gas cooler (T3) remain constant. The pressure of heat rejection influences both the work of the compressor and the heat absorption capacity of the evaporator. When the heat rejection pressure exceeds the critical threshold for the gas cooler exit temperature, the heat absorption capacity of the evaporator increases. This occurs as the specific enthalpy of the refrigerant exiting the gas cooler decreases, leading to a lower specific enthalpy entering the evaporator. As the heat rejection pressure nears the critical level, the operational work required for the compressor increases. As the heat rejection pressure increases, the rate of heat absorption by the evaporator increases more significantly than the work required by the compressor, resulting in an enhancement of the COP. A specific heat rejection pressure exists at which the COP attains its maximum before beginning to decrease. The optimal gas cooler pressure, primarily influenced by the exit temperature of the gas cooler (T3), aligns with the maximum coefficient of performance (COP), as demonstrated in Figure 11 (Shao et al., 2018).

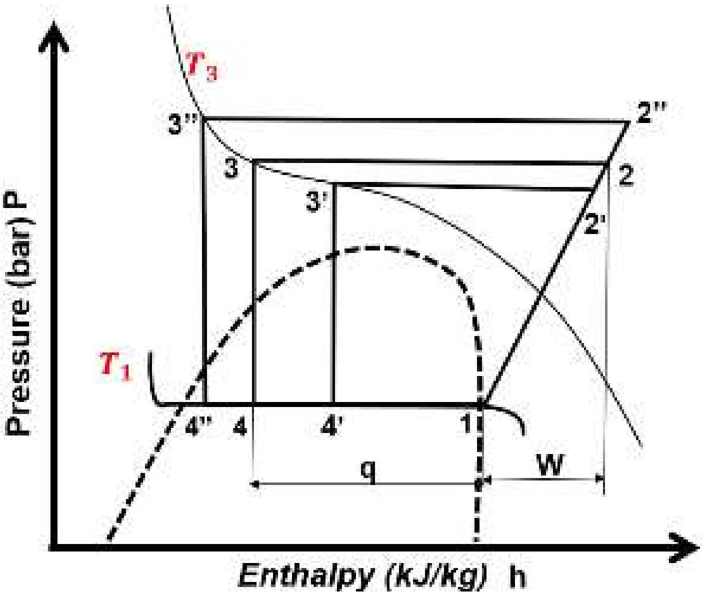

Figure 11. Effect of high-pressure side

2.5.2 Optimal pressure studies

The investigation into performance enhancement of CO_2 systems has focused on identifying the optimal discharge pressure. The optimal discharge pressure for maximising the COP is identified in the operation of transcritical CO_2 cycles, considering the properties of supercritical CO_2.

Initially, research primarily relied on numerical simulations, exemplified by Kauf's (1999) study on a CO_2 transcritical cycle that omitted the integrated heat exchanger applicable to automobile air conditioning. The study analysed the performance of constant gas cooler and evaporator systems, revealing that the influence of evaporator pressure and compressor operating parameters on ideal pressure was minimal compared to the effect of refrigerant exit temperature. They established a relationship between the ideal pressure and the temperature at the gas cooler exit, correlating it with ambient temperature.

$$P_{opt}\,(bar) = 2.6\,\cdot\,T_{amb} = 2.6 = 2.6\,T_{gc} + 7.54 \tag{2}$$

Where: $35°\mathrm{C}\ <\ T_{amb}\ < 50°\mathrm{C}, and\ 91\ bar <\ P_{opt}\ < 130\ bar$

Based on the work of Kauf (1999), numerous studies on optimised pressure have been conducted, with various correlations proposed. For instance, Liao et al. (2000) performed a steady-state simulation to examine several practical examples featuring an IHX. Their findings indicated that, alongside evaporation temperature, gas cooler output temperature, and compressor efficiency, all significantly influenced the ideal pressure. A streamlined relationship was proposed, focusing exclusively on the evaporation temperature and the outlet temperature of the gas cooler.

$$P_{opt}\,(bar) = \left(2.778 - 0.0157\cdot\,T_{evap}\right)\,\cdot\,T_{gc} + 0.381\cdot\,T_{evap} - 9.34 \tag{3}$$

Where: $-10°\mathrm{C}\ <\ T_{gc}\ < 20°\mathrm{C}, 30°\mathrm{C} <\ T_{gc}\ < 60°\mathrm{C}, and\ 71 < P_{opt} < 120\ bar$

Sarkar et al. (2004) suggested correlation for simultaneous heating and cooling applications by considering outlet temperatures of gas cooler and evaporation.

$$P_{opt}\,(bar) = 4.9 + 2.256\cdot\,T_{gc} - 0.17\,\cdot\,T_{evap} + 0.002\,\cdot T_{gc}^2 \tag{4}$$

Where: $-10°\mathrm{C}\ <\ T_{evap}\ <\ 10°\mathrm{C}, and\ 35°\mathrm{C} < T_{evap} < 50°\mathrm{C}$

Sarkar et al. (2006) enhanced another transcritical cycle developed for concurrent heating and cooling applications by incorporating an IHX and established a simplified correlation that relies on the inlet temperature of water in the gas cooler. Furthermore, they created computer programs to theoretically analyse the ideal delivery pressures for transcritical & subcritical high-temperature heat pumps utilizing various natural refrigerants, including CO_2.

$P_{opt}\,(bar) = 85.45 + 0.774 \cdot\ T_{gc\,win}$ (5)

Where: $20°\mathrm{C}\ <\ T_{win}\ <\ 40°\mathrm{C}$

Chen & Gu (2005) used simulation data to determine two optimal pressure correlations for the evaporator and IHX quality.

With no IHX present and the evaporator quality is 1.0:

$P_{opt}\,(bar) = 2.304 \cdot\ T_{amb}\ + 19.29$ (6)

If the temperature reaches 2.9 °C at the gas cooler exit:

$P_{opt}\,(bar) = 2.68 \cdot T_{amb} + 0.975 = 2.68 \cdot\ T_{gc} - 6.797$ (7)

Where: $-10°\mathrm{C}\ <\ T_{evap}\ <\ 10°\mathrm{C}, and\ 35°\mathrm{C} < T_{gc} < 50°\mathrm{C}, and\ 80\ bar\ <\ P_{opt} < 135\ bar$

Various research and papers described experimental research in which they established optimal pressure correlations.

Wang et al. (2013) developed two optimal pressure correlations for an experimental AWHP operating at a constant inlet water temperature. This study analysed the impact of water ambient and outlet temperatures on the coefficient of performance (COP) and the optimal discharge pressure. The results indicated that the optimal discharge pressure increased with higher ambient and water outlet temperatures. Additionally, simulations were conducted using a variety of plausible assumptions.

$P_{opt}\,(bar) = 23.08391 + 1.22379 \cdot\ T_{gc} - 0.004707 \cdot T_{wo}^2\ + 0.16207 \cdot T_{amb}$
(8)

Where: $-15°\mathrm{C}\ \leq\ T_{amb}\ \leq\ 5°\mathrm{C}$

$P_{opt}\,(bar) = 10.98 + 1.06442 \cdot\ T_{wo} - 0.01216 \cdot T_{amb}^2\ + 1.01404 \cdot T_{amb}$ (9)

Where: T_{wo}, is water outlet temperature, in the range: $55°\mathrm{C}\ \leq\ T_{wo}\ \leq\ 80°\mathrm{C}$

Previous studies have focused on creating an approximation equation designed to produce a reference setpoint that can be adhered to through a Proportional-Integral-Derivative (PID) feedback loop. Around 2010, Cecchinato et al. (2010) suggested that computational intelligence algorithms might provide the most effective approach for managing optimal pressure. Since that time, numerous studies have been undertaken in which researchers strive to maintain the system's operation at optimal pressure levels without depending on a pre-established method for determining optimum pressure. Zhang and Zhang (2011) devised a correlation-less online optimum control method that relies on the continuous computation and adjustment of the ideal pressure value tailored to the current operating conditions. Minetto (2011) utilised a logic control system capable of executing real-time calculations of the coefficient of performance (COP) by incorporating the suction and discharge pressures of the compressor, along with the inlet and outlet temperatures of the gas cooler as input parameters. Cecchinato et al. (2012) developed an advanced control system by employing an online ANN system identification method, which tackled the development challenge using a particle swarm optimisation technique. Liu et al. (2017; 2018) developed an optimisation model-based approach utilising a genetic algorithm to improve the transient coefficient of performance (COP). This was achieved by adjusting controlled variables, including compressor frequency, expansion valve position, and mass flow rates of cold and hot water ($\dot{m}_w$), while maintaining set points within acceptable limits. Yin et al. (2019) and Song et al. (2019) established a Group Method of Data Handling (GMDH) to examine the relationship between operating parameters and optimal pressure, employing a Particle Swarm Optimization-Back Propagation (PSO-BP) neural network to determine the optimal discharge pressure under different operating conditions. Peñarrocha et al. (2014) applied a Perturb and Observe (P&O) method to reduce the sensor count by prioritising the minimisation of compressor usage rather than improving the COP. Eventually, Hu et al. (2015) and Rampazzo et al. (2019) implemented a perturbation-based extremum seeking control scheme (ESC). This algorithm is a self-optimizing control method aimed at identifying an unknown or gradually changing optimal input, specifically the ideal discharge pressure, in relation to a defined performance index, which is the system's COP. The control mechanism introduces perturbations to the system, observes its response in terms of variations in COP, and subsequently adjusts the discharge pressure.

Stene (2005) investigated the influence of the touch point on the optimal performance and discharge pressure of a CO_2 heat pump water heater (HPWH). Recently, Chen (2016; 2019) investigated how the pinch point influences the design of the gas cooler and the ideal pressure for CO_2 high-pressure water heaters (HPWH). It also provided a correlation that relates the optimal pressure to the difference in temperature at the touch point, the evaporation and water temperature, at both the entry and exit of the gas cooler. He et al. (2020) employed RSM to determine the dynamic effects of various influencing factors on the optimal pressure. The findings suggest that, in refrigeration units, the refrigerant temperature at the outlet of the gas cooler is the most significant factor influencing optimal pressure. In HPWH, the optimal pressure is primarily influenced by the water entry and exit temperatures, evaporation, and the temperature differential at the touch point. The authors identified a correlation closely resembling that of Chen (2019).

The literature review reveals multiple methods for achieving optimal pressure control. Model-based techniques can be applied using standard PID controllers; however, they may produce suboptimal results if the model parameters are not precisely calibrated. An online model-based control can be implemented to address this issue. This system replicates the process and identifies the appropriate pressure; however, it necessitates considerable effort for model development and updates, as well as computational resources that are generally not accessible in refrigerant systems (Rampazzo et al., 2019). Finally, several authors have developed model-free techniques, such as (Peñarrocha et al., 2014; Rampazzo et al., 2019; Hu et al., 2015) although these algorithms also have limitations. To achieve optimal control performance, it is essential to select the control parameters carefully. Under different operating conditions, these parameters may respond slowly or even move in an undesirable direction until the allowable pressure threshold is attained, at which point the control adjusts back to the ideal value.

2.5.3 Refrigerant temperature glide

The heat transfer mechanism in a gas cooler is distinctly different from the condensation process seen in conventional refrigerants, as shown in Figure 12. In this scenario, heat transfer is primarily attributed to sensible cooling, resulting in a temperature differential between the CO_2 entering and exiting the gas cooler, which frequently exceeds that observed during heat rejection through condensation. This phenomenon is referred to as refrigerant temperature glide.

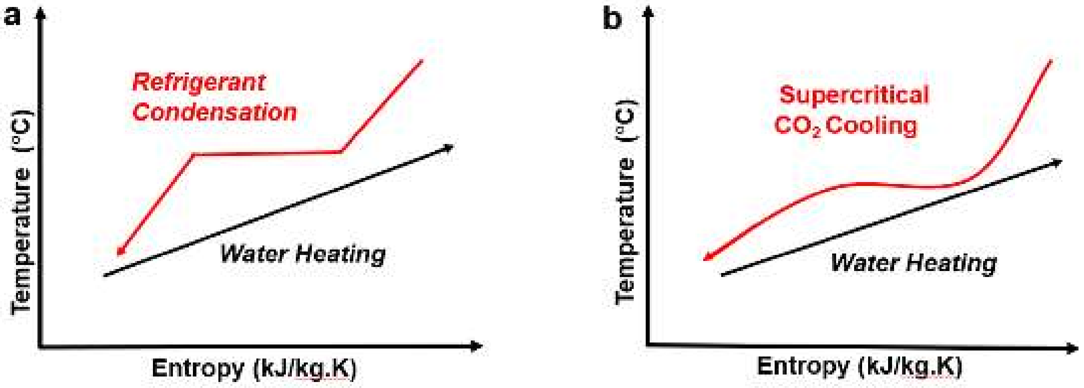

Figure 12. Temperature plot for heat rejection by:(a) condensation and (b) supercritical gas cooling

Researchers have documented the influence of refrigerant temperature glide on the essential performance of transcritical systems. Cecchinato et al. (2005) found that the coefficient of performance (COP) of a standard transcritical heat pump system increased significantly with an elevation in water temperature glide. A study was conducted on an air-source CO_2 heat pump water heater, focussing on its ability to heat water from 15 °C to 45 °C and from 40 °C to 45 °C. The COP increased by 56–84 percent with a temperature rise ranging from 15 °C to 45 °C.

Similarly, Song and Cao (2018) observed that a decrease in water inlet temperature resulted in an improvement in COP. A decrease in water entry temperature leads to a reduction in the refrigerant temperature at the gas cooler outlet, resulting in an increased refrigerant temperature glide.

Additionally, Fernandez et al. (2010) examined the operation of a CO_2 system connected to a storage tank under different heating conditions. The conditions encompass initial heating from 15°C to 57.2°C; subsequent reheating to 57.2°C following cooling due to standby losses; and reheating to 57.2°C upon the introduction of low-temperature make-up water into the tank. The entire tank experiences a temperature increase from 15°C to 57.2°C, yielding the most significant temperature variation. The second scenario involves maintaining the tank at 42.2°C, demonstrating a negligible vertical temperature gradient, indicative of the least detectable temperature variation. In the third case, despite the average temperature being 42.2°C, the water exhibits significant stratification, as the cooler make-up water accumulates at the bottom, resulting in a marked temperature differential. The initial heating process exhibited optimal performance, whereas reheating following standby losses demonstrated the lowest efficiency. The COP during standby loss reheating was observed to be 30–40% lower compared to the initial heating.

2.6 CO_2 Transcritical cycle improvements

While utilizing a natural refrigerant like CO_2, the normal transcritical cycle might not fully leverage the advantageous thermodynamics and heat transfer properties of the working fluid. Therefore, instead of seeking an alternative fluid that aligns with the established cycle, it is possible to implement certain modifications to the conventional cycle. The objective of these adjustments is to enhance, capacity, performance efficiency, and sizing of components by tailoring the unit to meet its specific needs. In particular, the modifications for the analysed cycle primarily aim to minimize exergy losses during the gas cooling and throttling stages. Numerous researchers have proposed and examined a wide array of technological enhancements for the conventional CO_2 cycle.

Many ways have been offered over the years to address this issue, including the use of an IHX to lower the refrigerant temperature at the throttling device's inlet (Zhang et al., 2018; Cao et al., 2019). An expander was used to retain the work of expansion and decrease the losses in throttling (Ferrara et al., 2016; Vutukuru et al., 2019), energy regulation with the use of a flexible ejector (Liu et al., 2016; Brodal and Eiksund, 2020), the technology of dedicated mechanical subcooling for lowering the exit temperature of gas cooler and lowering the work input to the compressor (Llopis et al., 2018). Furthermore, both multistage compression and parallel compression can successfully offset the loss in single-stage CO_2 systems' performance at high rejection temperatures. (Chen et al., 1996; Khan et al., 1998).

2.6.1 Internal heat exchanger (IHX)

The IHX is frequently incorporated into fundamental systems. As illustrated in Figure 13, the IHX serves as a crucial element in refrigeration systems, facilitating the transfer of heat from a liquid to a vapor refrigerant. This process enhances system efficiency and raises the delivery temperature, thereby fulfilling the requirements for hot water.

Lorentzen and Pettersen pioneered the concept of IHX for automobile air conditioning (Lorentzen & Pettersen, 1993). Following that, other reports show that IHX was helpful to system functioning, and as a result, IHX has become an integral component of the transcritical CO_2 cycle system. Tao et al. (2010) evaluated the transcritical CO_2 system with an internal heat exchanger experimentally and discussed the impact of throttling loss on the COP. According to his findings, the COP of the system increased by 13% compared to the system without IHX. Using IHX and real-time control analysis, Kim et al. (2017) examined and confirmed the optimal high-side pressure control method in a CO2-based transcritical system with varying volumes of charged refrigerant. The IHX's CO_2 transient behaviour was numerically investigated under a variety of input parameters, and it was discovered that increasing the inlet temperature decreases the COP. (Ituna-Yudonago et al., 2017).

The majority of studies have confirmed that adding IHX to the transcritical CO_2 cycle system improves system COP, however, the extent of improvement depends on the specific working conditions (Cao et al., 2019). It is proposed in literature that IHX impact is significant on the overall system COP, making it hard to evaluate IHX's contribution as a primary component to system COP enhancement. Although some literature has given ways for calculating IHX efficiency, such methods represent the potential of IHX for heat transfer and do not consider its influence on system working (Purohit et al., 2018). Additionally, the effect of IHX on the exergy efficiency of the system is thoroughly investigated and assessed under various conditions. The research may deliver scientific assistance for the optimisation and design of CO_2 transcritical heat pump systems.The potential of an IHX is to remove the need for subcooling and superheating in a typical system.

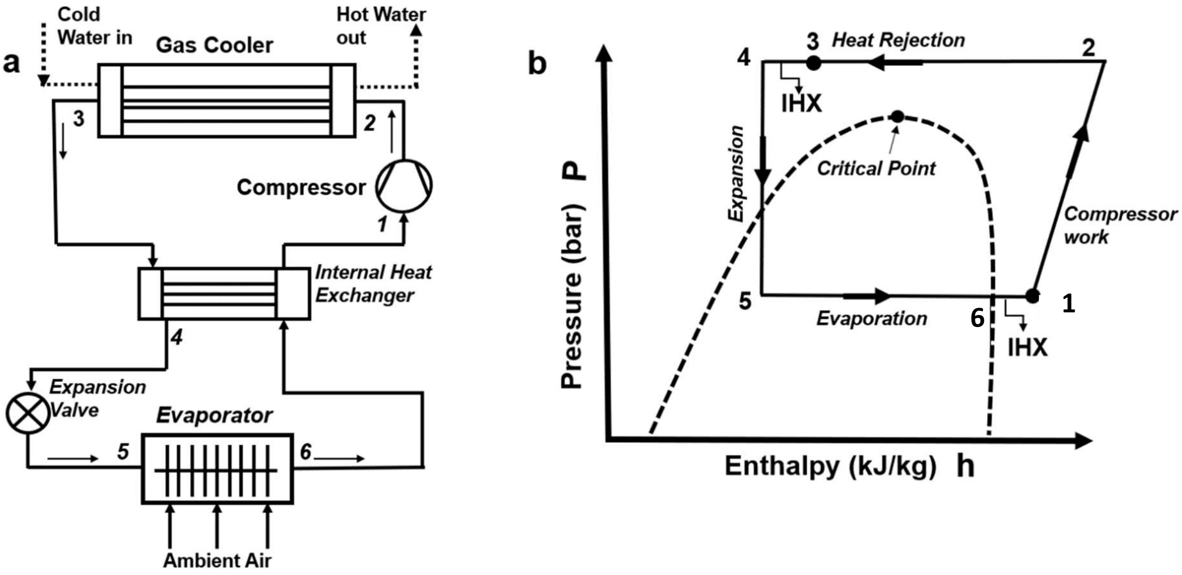

Figure 13. (a) Schematic of CO_2 heat pump with internal heat exchanger, (b) P-h diagram of CO_2 heat pump with internal heat exchanger

The IHX, commonly referred to as (suction line gas heat exchanger) SGHX, is typically located near outlet of the gas cooler and within the inlet of compressor. Its positioning is illustrated in the schematic presented in Figure 13. The heat exchange that occurs in between the discharge vapor from gas cooler and that from the evaporator facilitates the subcooling of the fluid prior to its entry into the expansion valve, while simultaneously superheating the fluid destined for the compressor. Consequently, the extra heat imparted to the fluid due to prolonged residence in the evaporator becomes unnecessary (Liao and Zhao, 2002).

In summary, the incorporation of this heat exchanger enhances the efficiency of the heat pump in three significant ways: first, it elevates the enthalpy at the compressor's inlet, thereby decreasing the workload on the compressor; second, it ensures that the working fluid is fully vaporized prior to compressor entry; and third, it amplifies the heat expelled from the high-pressure side, which in turn diminishes the heat input required by the evaporator.

2.6.2 Ejector expansion transcritical CO_2 system

Heat rejection is a cooling mechanism in a CO_2 transcritical cycle that takes a temperature glide, which improves the system's heat capacity and performance (Y. Ma et al., 2013). In the context of thermodynamics related to a CO_2 compression cycle, a transcritical cycle exhibits lower efficiency compared to a subcritical cycle. This inefficiency arises from significant expansion losses associated with the isenthalpic throttling process, which happens when a refrigerant transitions from a supercritical to the subcritical zone. Within the various devices designed for recovering work of expansion, the ejector stands out as a particularly effective solution, as it facilitates the use of environmentally friendly refrigerants like CO_2. The implementation of an ejector is among the strategies identified to harness part of the kinetic energy generated during the expansion. By increasing the pressure of the superheated CO_2 at the compressor's inlet, the ejector reduces the pressure ratio, thereby conserving input power for the compressor. Furthermore, by appropriately lowering the inlet pressure during expansion, throttle losses can be minimised, leading to an enhancement in the COP (Besagni et al., 2016; Elbel & Lawrence, 2016). The basic transcritical CO_2 ejector cycle schematic is depicted in Figure 14.

The ejector comprises four fundamental components: the suction chamber, diffuser, primary nozzle, and mixing chamber. The most direct techniques of understanding the flow inside the transcritical CO_2 ejector and primary nozzle are experimental measurement and visualization.

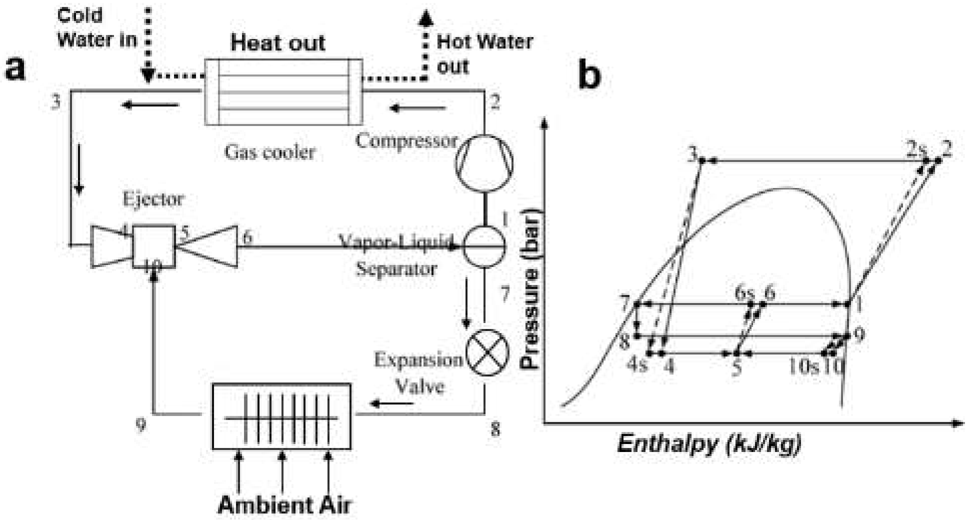

Figure 14. (a) Basic schematic of Transcritical CO2 ejector cycle, (b) And its P-h diagram

Xu et al. (2012) conducted a study that provides valuable insights into the subject matter. The experimental analysis of a transcritical CO_2 heat pump with an ejector revealed that extending the needle into the throat of the motive nozzle improved both the COP and heating capacity. Minetto et al. (2013) assessed the performance of a CO_2 heat pump incorporating an ejector, contrasting it with systems utilising an expansion valve. The findings indicated that the benefit of the ejector on the COP of the heat pumps increased in relation to the increase in throttling exergy losses linked to the isenthalpic process. Sarkar (2008) employed modelling outcomes to improve the efficiency of an ejector expansion CO_2 transcritical heat pump cycle intended for simultaneous cooling and heating applications. The findings indicate that the gas cooler exit temperature has a significant impact on the operation of ejector-expansion CO_2 transcritical heat pump cycles, surpassing the influence of the evaporator temperature.

Chen et al. (2009) conducted an experimental study on a CO_2 heat pump water heater equipped with a modifiable ejector nozzle throat, concluding that optimal conditions could be maintained by utilising an adjustable ejector. Zhu et al. (2018) recently conducted experimental testing on transcritical CO_2 ejector-expansion heat pump water heater systems. The ejector and overall system performance were evaluated for tap water temperatures from 50°C to 90°C. At a temperature of 70°C, the outlet temperature of the tap water resulted in a COP of 4.6, indicating a 10.3% improvement compared to the conventional cycle. Existing literature indicates that research on CO_2 transcritical heat pumps employing an ejector as an expander is limited. Theoretical analyses often exhibit better performance than experimental results, likely due to the simplified modelling of the cycle and ejector, which are rarely validated in these studies.

2.6.3 Mechanical subcooling

The supercritical CO_2 stream that exits the gas cooler is directed immediately to the expansion component within the basic CO_2 system, where it undergoes throttling. The output temperature of the CO_2 gas cooler is theoretically constrained by the ambient conditions, where follows an approach temperature that varies based on the effectiveness of the gas cooler. Due to the restricted outlet temperature of the gas cooler following throttling, the quality of the evaporator entry, specifically the vapor fraction, is difficult to diminish further, thereby limiting the specific cooling capacity. Consequently, studies have developed subcooling techniques at the outlet of the gas cooler, which have demonstrated improved efficiency despite the increased energy requirements associated with the subcooling system (Yu et al., 2019). Figure 15 depicts the relationship between subcooling and the primary CO_2 cycle. Recently, mechanical subcooling (MS) has garnered significant interest. To enhance the efficiency of the system, MS can be implemented to decrease the outlet temperature of the gas cooler through the use of a straightforward vapor compression cooling system.

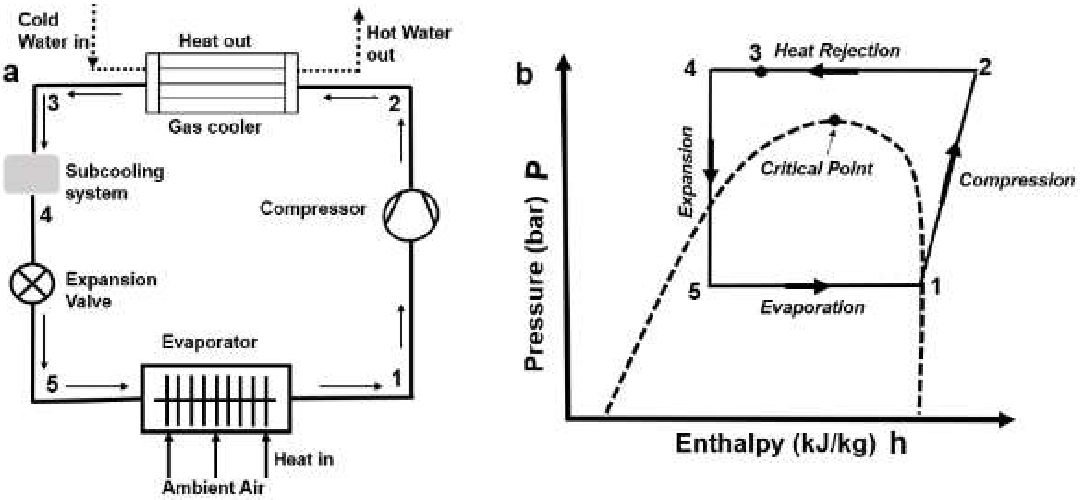

Figure 15. (a) Schematic of the CO2 subcooling system, (b) and its P-h diagram

several studies have been reported on the application of heating. Wang et al. (2019) examined how to enhance the efficiency of transcritical CO_2 systems by incorporating subcooling with MS, an internal heat exchanger, a cooling tower, and a dry cooler. Cao et al. (2019) developed an innovative transcritical CO_2 HP combination system. Comparatively, the COP is 15.3% higher than in a regular plant. Song et al. (2017) observed that a greater water temperature differential between the entry and exit of the gas cooler helps to improve the efficiency of clubbed and cascade R134a/CO_2 system for space heating. After that, they examined and improved the CO2 transcritical system with an MS in conjunction.

Dai et al. (2017) employed MS to report a thermodynamic study of the CO_2 transcritical refrigeration system. The findings indicated that the highest COP is associated with a specific combination of discharge and subcooling pressure. Furthermore, they examined the CO_2 refrigeration cycle alongside MS utilising a zeotropic mixture and obtained that the COP could be enhanced even more. According to Sarkar (2010) installing a sub-cooler next to the gas-cooler can lower the optimum temperature of heat rejection and the CR of the main cycle, resulting in further benefits.

Finally, it has been noticed that MS plants have been found to be a successful strategy to increase the efficiency of CO_2 transcritical systems. However, it should be noted that most of the studies are theoretical in nature and that experimental studies are required to precisely measure the benefits that can be accomplished.

2.6.4 Mechanical expander

A notable drawback of the CO_2 cycle is the considerable loss associated with expansion. The throttling process is irreversible, resulting in two main drawbacks: a decrease in the refrigerating effect and an increase in the work input necessary for compression. Employing a mechanical expander in a CO_2 transcritical system can mitigate throttling losses, facilitating energy recovery for mechanical power generation. In thermodynamics, the addition of a work-generating component, like an expander, improves system efficiency by converting the isenthalpic process into a more isentropic process. Figure 16 presents schematic configurations of a CO_2 refrigeration system with a mechanical expander. In particular, Figure 16(b) illustrates the corresponding pressure–enthalpy (p–h) diagram for the CO_2 cycle, where the solid lines represent operation with a mechanical expander and the dotted lines denote the conventional configuration without an expander. The use of a mechanical expander rather than an expansion valve improves the cooling effect by making the expansion process more isentropic (B. Yu et al., 2019).

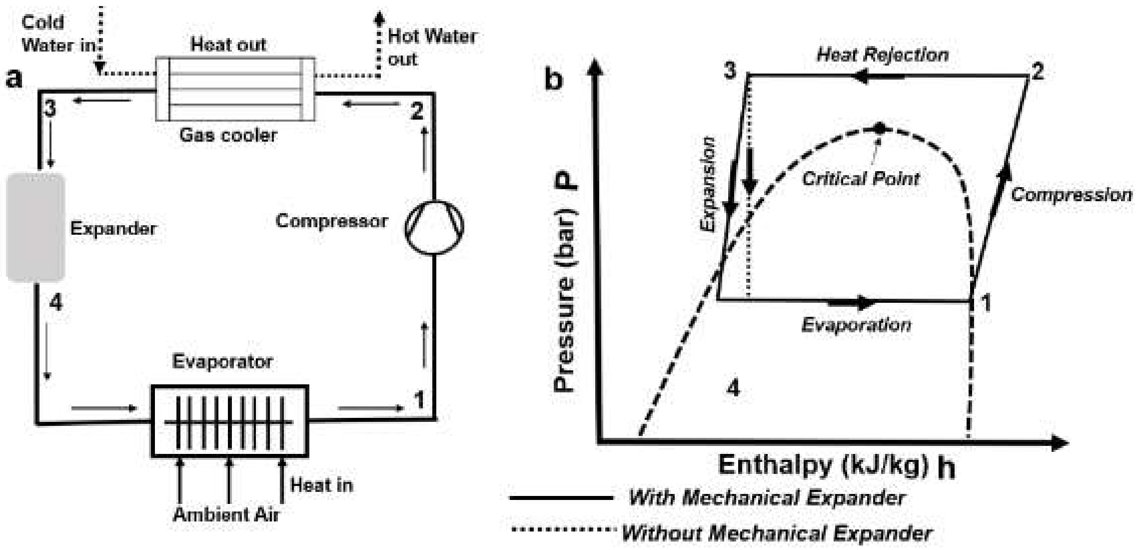

Figure 16. (a) Schematic of CO2 cycle with mechanical expander, (b) A P-h diagram of CO2 system with mechanical expander

Tian et al. (2010) theoretically estimated the coefficient of performance (COP) of a CO2 transcritical cycle with an expander, revealing a 6–10% increase in COP compared to the basic system. Yang et al. (2005) performed a thermodynamic analysis of the expander system, finding that it mitigated a 50% decrease in exergy loss during the expansion process and enhanced the overall exergy efficiency of the system by 30%, leading to a 33% rise in COP.

Robinson and Groll (1998), assert that an expander enhances the coefficient of performance (COP) of a conventional CO2 system by reducing exergy loss throughout the process. The enhanced benefits of an expander will be negated by the placement of an IHX within the system, leading to a reduced COP. This can be attributed to two factors: The implementation of an IHX reduces the temperature of the fluid exiting the gas cooler, thereby constraining the potential work that can be extracted by an expander.

2.6.5 Multistage compression

The objective of employing two-stage or multi-stage compression is to decrease the energy contribution required by the compressor. This can be achieved through methods such as flash gas intercooling, intercooling, and flash gas bypass. The configuration of two-stage compression along with intercooling is illustrated in Figure 17. In this setup, the CO_2 refrigerant is cooled by an external fluid as it passes through the intercooler following the 1st stage compressor, also known as the low-pressure compressor (LP). The cooled CO2 gas is then compressed and heated in the second stage compressor, or high-pressure compressor, until it attains a supercritical state at point 4. Prior to entering the evaporator, the gas is further cooled to state 5 in the gas cooler, and its pressure is reduced to state 6. To guarantee that the gas entering the suction line of the low-pressure compressor is dry, the gas exiting the evaporator is generally superheated by absorbing heat from the outlet of the gas cooler via an internal heat exchanger (IHX).

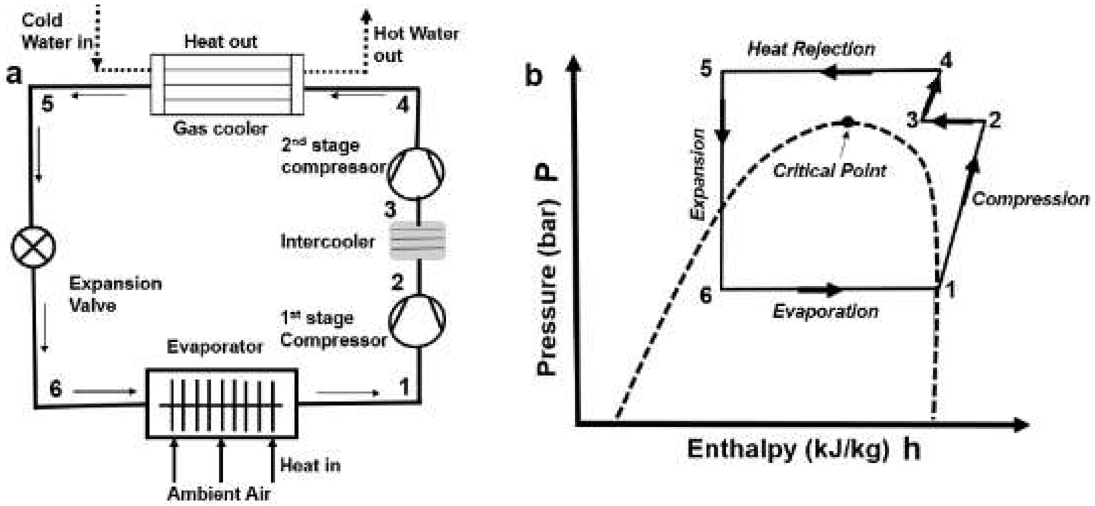

Figure 17. (a) Schematic of CO2 cycle with multi-stage compression with intercooling, (b) multi-stage CO2 cycle with intercooling in a P-h diagram

It is evident from Figure 17 that the second stage of the compression process swiftly transitions to the supercritical region once the intermediate pressure surpasses the critical pressure. In this phase, the isentropic slope is notably steeper compared to those in the traditional superheated area. Actually, the 2nd stage of compression operates at a lower enthalpy compared to critical enthalpy, as the slopes of the isotherms approach zero within the supercritical zone. Consequently, when the midway pressure exceeds the critical pressure, the increase in enthalpy through the second stage compressor diminishes significantly. The COP reaches its peak just prior to the isotherm slopes returning to lower enthalpies, which minimises the required compression work. The intercooler, operating at intermediate pressure, functions as the key heat exchanger in the complete cycle, as the enthalpy change across the intercooler (at high-side pressure) is considerably more than that across the gas cooler (at intermediate pressure) when the COP is at its maximum. A two-stage CO_2 transcritical cycle, along with intercooling, can achieve up to a 24% increase in performance compared to a standard transcritical cycle, depending on the operational conditions and other factors affecting the cycle (Baek et al., 2005; Agrawal et al., 2007).

2.6.6 Parallel compression

Multiple strategies exist to enhance the COP of a transcritical CO_2 cycle, one of which involves parallel compression economization. To optimise the efficiency of the transcritical CO_2 refrigeration cycle, two separate streams of refrigerant vapor—one sourced through an economizer (flash tank) and the different from the primary evaporator—are compressed to a supercritical discharge pressure without mixing. The main aim of this approach is to decrease throttling losses. Figure 18 depicts a parallel compression system; the dotted line indicates that corresponding compression can be achieved not only through the use of two distinct compressors but also via a single connected compressor, such as a dual compressor with a common shaft.

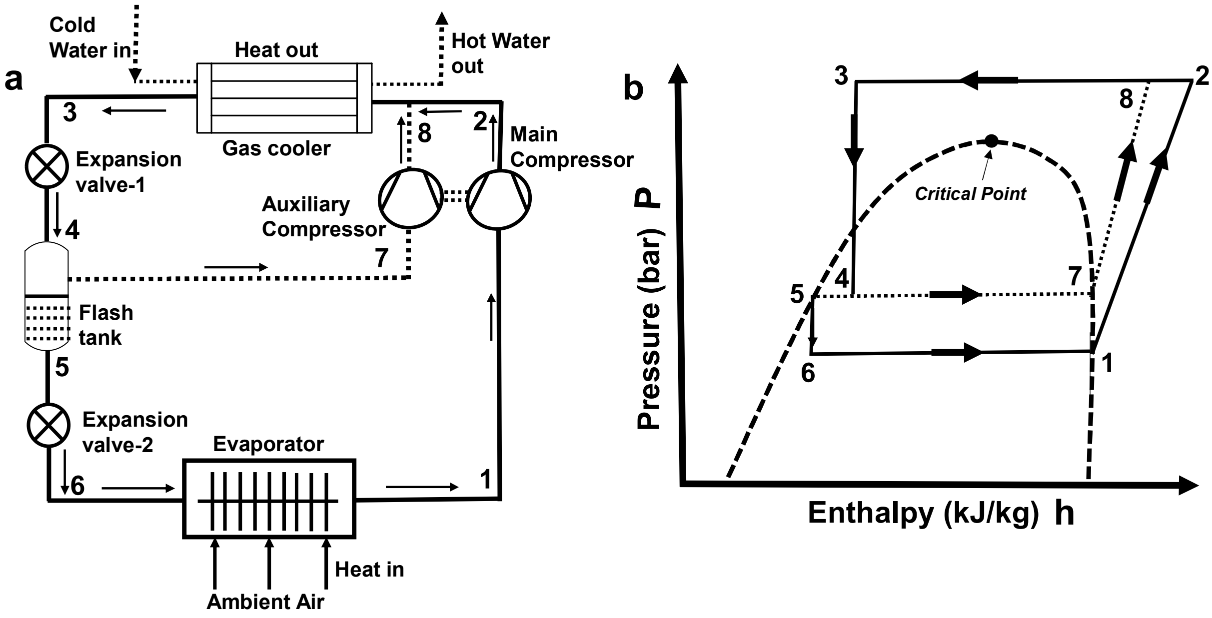

Figure 18. (a) Schematic of CO2 cycle with parallel compression system, (b) P-h diagram of CO2 cycle with parallel compression system

By using parallel compression, Sarkar & Agrawal (2010) found that it is possible to achieve both a rise in cooling performance and a lowering in delivery pressure. The parallel compression is particularly advantageous for low-temperature usage since it achieves a 47.3% increase in COP compared to the conventional system under the specified operating parameters, with the optimum intermediate pressure fluctuating just slightly.

Chesi et al. (2014) showed both theoretical and experimental studies on parallel compression, comparing the findings to the fundamental CO_2 system. The thermodynamic model indicated that an ideal cycle could enhance the COP by over 30% and surge cooling capacity by more than 65%. Although the experimental results align with the anticipated trend, the actual values are lower due to the pressure losses and performance of the separator throughout the system's piping. It was depicted that a rise in the flow rate at the entrance of the separator leads to a decrease in its efficiency.

When Song et al. (2022) analysed the performance of a parallel compression systems, they discovered that under certain conditions, considerable increases in efficiency of at least 10% are possible, if the following requirements are met: The gas cooler outlet temperature must exceed 27.5°C; the evaporation temperature must be less than 7°C; and midway pressures up to 45 bar are conceivable.

2.7 Refrigerant injection technique

As previously mentioned, working compressors at elevated CR may lead to significantly high ejection temperatures. This condition can chemically deteriorate refrigerant oil and potentially cause mechanical failures. The technique of refrigerant injection has been shown to effectively maintain dependable cycle operation and enhance the working of VCRS.

Refrigerant intake is widely employed to mitigate the excessively high discharge temperatures of compressors, thereby ensuring dependable system working and enhancing heating or cooling capacity while maintaining the same swape volume in compressor. The methods of refrigerant injection are classified into vapour injection (VI), liquid injection (LI), and 2-phase injection (TPI), according to the properties of the injected fluid. Song et al. (2021) demonstrated that employing liquid and vapour injections results in improvements in both COP and the reliability of heat pumps. Lee (2018) assessed the cooling efficiency of an R-22-based system employing both liquid and vapour injections in high CR conditions.

2.7.1 Liquid injection

From research conduction on liquid injection to improve the compressor's reliability in extreme weather conditions. Additionally, it serves as an effective method to prevent excessively high discharge temperatures. The purpose of liquid injection is to safeguard the compressor by ensuring sufficient cooling. Yin et al. (2019)conducted both theoretical and experimental research to examine the effect of liquid refrigerant on the operation of an R-22 high-side scroll compressor. His findings indicated that as the injection ratio increased, the oil temperature decreased, resulting in a modest enhancement in working. Kim et al. (2018) investigated the impact of liquid injection on the discharge temperature of an R-22 compressor, and the findings indicated a linear decrease in discharge temperature corresponding to the injection ratio. Specifically, for each percentage increase in liquid injection, the discharge temperature was reduced by roughly 1.2°C. Cui et al. (2021) investigated the impact of liquid injection on a low-side scroll compressor driven by an inverter, examining various compressor frequencies. The findings indicated that liquid injection at high frequencies significantly enhances the compressor's performance and reliability. In contrast, liquid injection at low frequencies presents certain drawbacks concerning the compressor's capacity, power, and adiabatic performance, primarily due to increased seepage through the breach in the scroll covering.

2.7.2 Two-phase injection

A two-phase injection system is recognized as more effective in reducing ejection temperature linked to vapor injection, primarily due to its utilization of latent heat. This method provides superior cooling during the compression process relative to vapor injection. Nevertheless, the implementation of two-phase injection raises concerns, particularly regarding the issue of wet compression and the challenges associated with accurately measuring injection quality in experimental settings (Kim et al., 2018). Peng et al. (2020) analysed the ejection temperature of a low-side R-22 compressor during 2-phase injection and compared it to the scenario without injection. His findings indicated that the ejection temperature could be decreased by 10 to 20 °C when the class of the inoculated refrigerant was 0.9. Zhang et al. (2018) evaluated the effectiveness of 2-phase suction, fluid injection, and 2-phase injection on the reduction of release temperature in an R32-based scroll compressor. Wang et al. (2008)demonstrated that the energy input of the compressor in a two-phase injection system was 22.6% lower than that of the vapor-injection cycle when functioning at reduced external temperatures in heating mode. However, the influence of injection quality and injection pressure on the efficiency of a two-phase injection heat pump under varying operating conditions remains inadequately explored. Kim et al. (2018) compared two-phase, liquid, and vapour injection heat pumps that utilise a scroll compressor with R-410A as the refrigerant. The study aimed to identify the optimal injection quality in a two-phase injection heat pump to enhance the COP, considering variables such as compressor frequency, intermediate pressure, and outdoor temperature. The findings indicate that the fluid injection heat pump exhibits a more pronounced reduction in ejection temperature relative to both the vapour injection and 2-phase injection heat optimum injection quality.

However, as outdoor temperatures drop, the two-phase injection heat pump with optimal injection quality proves to be more effective in enhancing the COP and lowering the discharge temperature. Despite these advantages, the use of two-phase injection is constrained by the challenges associated with wet compression.

2.7.3 Vapour-injection

Previous research primarily concentrated on vapor injection utilising rotary and scroll compressors to improve the reliability and performance of domestic heat pumps in low-temperature environments (Kim et al., 2018).

Heat capacity and COP can be improved using the vapor-injection technique. Wang et al. (2021) examined the impact of midway pressure, intermediate wet injection, and gas superheat on the performance of a scroll compressor utilising vapour injection. They analysed the effects of vapour injection versus liquid injection on its working. The findings indicated that vapour injection markedly enhances system efficiency, while liquid injection has a minimal impact. Several works on vapour injection demonstrated that it leads to substantial improvements in both capacity and

COP. Vapour injection results in a reduction of the ejection temperature, limiting the refrigeration effect produced by the vapour refrigerant. Peng et al. (2020) investigated the effect of injection enthalpy on a scroll compressor utilising R-22. The analysis demonstrated that efficacy increases with a decrease in injection enthalpy, a phenomenon associated with diminished internal leakage and its impact on losses resulting from under-compression or over-compression. They also examined the optimisation of a vapor-injection heat pump. The flash tank variant of the vapor-injection heat pump exhibits enhanced performance capabilities relative to the economizer-type vapor-injection heat pump. Research on the application of vapor-injection heat pumps in electric automobiles is currently being actively pursued.

2.8 Finned tube heat exchanger

Various heat exchanger designs are employed in heat pumps, with finned tube heat exchangers being the predominant selection for the outdoor coil in air-source heat pumps (ASHPs). This heat exchanger consists of a coiled tube for refrigerant circulation, along with multiple fins attached to the pipes. The fins are optimally placed within the airflow path to augment the heat transfer surface area, consequently improving the heat transfer rate. Tubes designed for refrigerant transport can be configured in various arrangements to enhance heat transfer efficiency. Excessive rows can result in a greater pressure drop on the air side and may increase noise generated by the airflow. The optimal number of rows is contingent upon the specific application and the dimensions of the heat pump. Additionally, alterations in fin design may improve heat transfer efficiency (L. Gu et al., 2017).

Surface frost accumulation of the evaporator with finned tube is an unwelcome yet frequent occurrence in an ASHP system. Presence of frost on the evaporator hinders air passage and diminishes the area of heat exchange, significantly increasing air flow resistance. If not addressed promptly, this situation can severely impair the efficiency of heat exchange and may ultimately lead to system failure (Wang et al., 2012).

2.8.1 Frost growth

AWHPs operating in moderate to low temperature environments, generally between -15 °C and 6 °C, encounter issues associated with frost formation. When the fins' body temperature falls below the dew point, vapour in the air starts to condense. When the surface temperature drops below zero, the condensed vapour freezes, resulting in the formation of frost. The frost layer acts as an insulator on the heat exchange surface, obstructing heat transfer from the air to the refrigerant. Ye & Lee (2013) demonstrated that thicker frost layers result in increased obstruction to heat transfer. The accumulation of frost between the fins obstructs airflow, leading to a decrease in convective heat transfer. This phenomenon reduces the operational efficiency of the heat pump, increases energy consumption, and ultimately decreases the COP. Elevated humidity, air and surface temperatures, and ambient air velocity are all factors that contribute to frost formation (Zhang et al., 2018).

The issue of frost accumulation on air-sourced heat exchangers is being thoroughly investigated, as frost can reduce efficiency and potentially lead to heat pump malfunctions if not addressed. Widespread study has been reported on the process of frost deposition on flat surfaces, identifying it as a multi-stage phenomenon (Patil et al., 2017; Song & Dang, 2018). The stages are provided specific names by individual authors, but concept is same.

Frost deposition on a cold surface occurs in three distinct phases: crystal growth, the development of the frost layer, and the completion of the frost layer. The process of frost nucleation marks the onset of the frost growth phase. Initially, crystals begin to form independently, exhibiting a more rapid vertical growth compared to horizontal expansion. However, this vertical growth is impeded when frost crystals make contact and collide with one another. In the frost layer growth phase, a porous structure emerges as the height and density of the crystals increase significantly in comparison to the earlier crystal growth phase. This porous formation arises from the accelerated vertical growth of the crystals relative to their horizontal counterparts. As the frost layer reaches its full development, the elevated portions of the frost structure start to melt and fall into the porous matrix, where they subsequently freeze again, contributing to the formation of an ice layer. This cycle of melting and refreezing results in a deeper and denser frost layer (Patil et al., 2017).

The surface temperature heavily influences both the height and growth rate of frost. In colder conditions, ice crystals form more rapidly and attain greater sizes compared to warmer temperatures. Leoni et al. (2017) investigated the frost layer under various ambient temperature concerning thermal conductivity. They found that density plays a crucial role in conductivity, with higher density correlating to increased conductivity. Moreover, elevated ambient air temperatures and reduced plate surface temperatures facilitated densification.

The process of frost growth can similarly be observed in finned tube heat exchangers, where condensation occurs on the fins and tubes, leading to the development of ice crystals. This branching of frost contributes to the development of a porous frost layer, ultimately resulting in a thicker frost layer. Due to the vertical orientation of the fin surfaces, gravity affects the initial growth phase. Furthermore, frost tends to accumulate more rapidly between the fins than on a cold, flat surface following the starting condensation phase (Song et al., 2018). In heat exchangers featuring multiple rows of tubes, the front row tends to accumulate a greater amount of ice compared to the subsequent rows, with the frost accumulation diminishing progressively towards the rear row, which exhibits the least frost (Yao et al., 2004).

The literature on frosting in finned tube heat exchangers indicates an initial rise in the heat transfer coefficient, with some studies proposing that the rough surface of the initial ice layer enhances the heat exchange surface. Huang et al. (2008) reported the influence of surface nature on heat transfer and suggested that it only proved effective under conditions of turbulent flow. Finned tube heat exchangers function within a laminar flow setting, and further examination of the initial heat transfer surge is necessary to ascertain its underlying causes.

Accurately predicting frost formation is crucial for preventing efficiency losses and optimizing heat pump performance. However, due to the challenges in monitoring the density and precise conductivity of the entire frost layer as it develops, many models fall short in their ability to accurately represent frost behaviour. The early stages of droplet formation and crystallization are characterized by unpredictability and irregularity, making the creation of a precise model challenging. Once this initial phase is complete, frost growth becomes more uniform and can be predicted more reliably based on initial conditions, with (K. S. Lee et al., 2003) achieving a modelling error of 10% in the later stages.

The operational efficiency of heat pumps under frosting conditions has been analysed by various researchers to enhance the understanding of how frost impacts the parameters of heat pumps. Ma et al. (2018) created a computational model to find frost formation on a wavy-surfaced plate. They concluded that a lower cooling surface temperature accelerates frost layer growth due to a heightened driving force for phase change. The mass flow of vapour, influenced by air velocity and the concentration of water vapour in the air, facilitates the rapid expansion of the frost surface. Chung et al. (2019) employed an adapted ε-NTU technique to model an AWHP for heat transfer estimation. Their findings indicated that a heat pump's performance was most significantly affected during the later stages of frosting, with heating capacity being more sensitive to frost accumulation than the COP. A model examining airflow blockage, validated against experimental data, revealed that the decline in performance during the further stages of frosting was primarily due to reduced convective heat transfer as airflow through the evaporator diminished, rather than an increase in thermal boundary from the frost surface (Silva et al., 2011). The surface temperatures of the fins and tubes in the heat exchanger exhibit a gradient, with lower temperatures at the refrigerant entry and higher temperatures at the exit. As a result, frost formation on the evaporator exhibits non-uniformity, which contradicts the assumptions of numerous models.

Padhmanabhan et al. (2011) conducted simulations of non-uniform frost development by segmenting the heat exchanger tubes and varying the refrigeration temperatures from the inlet to the outlet. To balance the air pressure drops transversely the heat exchanger, they calculated the pressure drop caused by frost for each segment. As frost built up, airflow was readdressed to areas with less obstruction. This model achieved a 20-50% improvement in predicting frost formation compared to a model assuming uniform airflow.

The results indicate that frost growth occurs most rapidly during the initial stages and diminishes over time. Additionally, it was frequently noted that increases in air temperature, air velocity, and humidity corresponded with a rise in frost accumulation. Furthermore, lower temperatures of the refrigerant or evaporator surfaces also contributed to this phenomenon.

2.8.2 Defrosting

The presence of frost accumulation on heat pumps leads to diminished operational efficiency, making defrosting essential for restoring normal functionality. Various defrosting methods and operational strategies are available, which can be categorised into passive and active approaches. Passive defrosting emphasises preventive measures such as specialised coatings, fin designs, and adjustments to inlet conditions. In contrast, active defrosting techniques involve the use of external energy to actively eliminate or mitigate ice formation. Examples of these techniques include electric heaters, ultrasonic vibrations, and reverse cycle hot gas defrosting (Rahman & Jacobi, 2012; Liu et al., 2018; Qu et al., 2019).

In colder climates, periodic defrosting is crucial for heat pumps, as frost tends to form on the heat exchanger through heating operations. During the defrosting process, the heat pump does not transfer heat to the heat sink, and in the situation of active defrosting methods, the heat exchanger's temperature is raised using an external energy source to facilitate ice melting. This process requires considerable energy and time, during which the heat pump is unable to provide any beneficial heat to heat sink. Consequently, minimising the duration of defrosting is vital to restore normal operation and maintain thermal comfort (Jang et al., 2013).

Three methods of system defrost are electric heating, on-off, and reverse cycle.

1. The on-off defrosting technique is straightforward and cost-effective as it involves halting the heating process to allow frost to naturally melt. However, since no external heat is introduced to the heat exchanger, the duration of defrosting is extended, causing a lack of heat given to the system during this period. This prolonged defrosting can negatively impact the thermal comfort within the building. Furthermore, this method is only applicable in outdoor conditions where temperatures remain above freezing.
2. Electric resistive heaters are integrated into the heat exchanger to shorten the defrosting duration. While this method is effective and relatively easy to install, it requires significant electrical power, which can reduce the heat pump's COP. The increased electricity usage may also lead to higher operational costs.

3. The reverse cycle hot gas defrost is the most commonly utilised method. While installation costs are higher than those of electric resistive heaters, the system functions by reversing the refrigerant flow in the heat pump cycle. This process channels hot gas from the compressor into the heat exchanger, thereby facilitating the melting of ice. This method accelerates the defrosting process, rendering it more efficient than both the electric resistive heater and the on-off defrost method, while also achieving a superior coefficient of performance compared to the other two approaches (Amer & Wang, 2017).

Numerous studies in the literature examine defrosting techniques aimed at enhancing the efficiency of heat pumps. Liang et al. (2020) introduced an innovative design for an ASHP that incorporates a frost suppression method, resulting in a COP that is 21-37% higher than that of conventional AWHPs. Similarly, Tang et al. (2020) established a model featuring an additional electric heater to mitigate frost buildup. By inhibiting frost formation, the operational efficiency of the heat pump can be significantly improved, as this delays frost development and optimize heating capacity for cold conditions, thus enhancing the COP. Qiao et al. (2018) analysed an ASHP utilizing converse cycle defrosting and found that 17.7% of the power supplied by the refrigerant was required to remove the frost, with the remainder dissipated into the surrounding air or retained within the tubes and fins. Additionally, Song et al. (2020) examined an ASHP with opposite cycle defrosting and investigated two methods for managing melted frost: downward flow and local drainage. Their findings indicated that local drainage was more effective than downward flow, as it transferred less heat to the melted frost descending along the fins.

It is essential to recognize that not only the defrosting method itself contributes to improved control strategy, but also the operational performance employed during the defrosting process. The primary objective of defrost control is to ensure a high COP while minimizing operational costs. Other factors that may trigger defrost initiation include reduced heating capacity and airflow obstruction. Determining the optimal approach is challenging, as it varies based on the specific ambient conditions associated with each heat pump and is also motivated by the design of the evaporator.

2.9 Gas-cooler performance studies

Given the importance of gas cooler performance in this study, a variety of articles on several class of gas coolers have been reviewed. This examination includes a range of designs, from basic tube-in-tube coolers to particularly developed microchannel coolers, brazed plate gas coolers, and fluted tube-in-tube gas coolers.

The gas cooler plays a crucial role in the CO_2 transcritical cycle by facilitating a consistent temperature reduction of CO_2. Its flow configurations and characteristics significantly influence the optimal operating pressure and overall system efficiency. During the heat rejection phase, the CO_2 fluid within the gas cooler exists in a supercritical state, experiencing a substantial temperature decrease. The thermophysical characteristics of CO_2 vary considerably along temperature fluctuations, particularly in pseudocritical zone. Therefore, it is essential to examine the heat transfer process of CO_2 within the gas cooler to enhance system working (Yang et al., 2016).

Wang et al. (2013) numerically studied gas cooler with tube-in-tube designed focused on geometry, optimum ejection pressure, and system working, as the primary research objectives. Gas coolers featuring larger heat transfer surfaces and reduced discharge pressures exhibit higher coefficients of performance (COP), a finding corroborated by experimental data. An increased rate of mass flow enhances the heat transfer within the gas cooler; however, this improvement comes with the trade-off of elevated pressure drop and discharge pressure. Simulations conducted at various mass flow rates identified the optimal flow rate at which the COP approaches its maximum, indicating that adjustments to the gas cooler's design are necessary.

Yu et al. (2014) reported a numerical analysis of heat transfer performance dynamics of a supercritical CO_2 liquid-cooled gas cooler configured in a tube-in-tube counterflow arrangement, integrated within a CO_2 based heat pump that includes an inbuilt heat exchanger. To validate their model, they matched the outcome with experiments. Under conditions of minimum water flow rate and maximum inlet water temperature, the predicted heating capacity deviated by no more than 20% from the experimental results. The experimental findings reaffirmed earlier conclusions that higher evaporator water entry temperatures and increased water flow rates enhance the COP. This improvement is corresponding to the thermal resistance of water is generally 40% to 60% greater than that of CO_2. Additionally, CO_2's specific heat approached its highest at the pseudocritical point, which leads to an increase in the local heat transfer coefficient for CO_2 at that location. Consequently, during transcritical operation, a significant portion of thermal resistance shifts from the water to CO2 side. This shift results in a reduction of local refrigerant-side thermal resistance, thereby increasing the local rate of heat transfer at the pseudocritical point. The findings also indicated that as the discharge pressure nears the critical pressure, characteristics of pseudocritical region become increasingly pronounced.

Chen (2016) performed the touch point analysis on a smooth tube-in-tube gas cooler and identified the essential water-to-CO_2 flow ratios (m_w/m_c) that influence the temperature gradient at the pinch point. The heat transfer limit factor and the approach temperature differential vary based on the location of the pinch points. Consequently, expanding the area of heat transfer may not often cause a substantial drop in the approach temperature differences. The temperature of inlet water plays a significant role in establishing the position of the pinch point and the critical mass flow ratios. As the inlet water temperature decreases, there is a marked reduction in the critical mass flow ratio.

Sánchez et al. (2012) developed a model for a liquid-based CO_2 heat exchanger featuring refrigerant circulation through a tube bundle arrangement within the system. This model was created utilizing a finite volume method along with correlations for the convective coefficient of CO_2. Their findings indicated that thermal efficiency rises with higher refrigerant pressure and mass flow rate of water, while it declines with elevated evaporator pressure and water entry temperature.

Zhang et al. (2018) presented an optimisation method employing temperature glide for a CO_2 heat pump featuring a tube-in-tube gas cooler, specifically for water heating applications. Peng et al. (2020) developed numerical models for a CO_2 transcritical vapor-injection heat pump device, incorporating tube-in-tube gas coolers and evaporators to examine the impact of different operating parameters on heating performance. Furthermore, certain researchers have explored the application of multi-twisted and corrugated inner tubes to improve the efficiency of heat exchangers featuring a tube-in-tube design. The fluted tube is frequently utilised in the design of tubular heat exchangers.

Yang et al. (2016) conducted a series of studies and executed a theoretical analysis to assess the efficiency of a CO_2-based heat pump utilising a multi-twisted tube gas cooler. The research demonstrated that improving the water side heat transfer coefficient is crucial for elevating both the coefficient of performance (COP) of the system and the water exit temperature from the gas cooler. Furthermore, it was noted that the heat transfer efficiency of the finned gas cooler with four tubes surpasses that of the configuration with three tubes; however, a considerable increase in pressure drop is observed when the number of inner tubes exceeds four. He observed that increasing the refrigeration flow rate and inlet water temperature, while decreasing the cooling water flow rate, can raise the water outlet temperature of the gas cooler; however, these modifications may lead to a reduced COP.

Yu et al. (2020) performed a quantitative analysis of supercritical CO_2 cooling in a fluted tube, determining an optimal geometric configuration under defined conditions. Zhu et al. (2019) analysed the heat transfer performance of a fluted heat exchanger featuring a tube-in-tube arrangement and developed a new correlation for these parameters. The influence of the specified heat exchanger configuration on the operation of the CO_2 heat pump system remains unexamined.

Sarkar et al. (2006) simulated a CO_2 heat pump for the heating and cooling of a dairy plant. The gas cooler was constructed using a tube-in-tube arrangement. A mathematical model was developed to analyse the cooling process to 4°C and the heating process to 73°C, including an integrated heat exchanger. Researchers determined the heat transfer coefficient as a function of the refrigerant's bulk temperature in the gas cooler. The variation in heat transfer coefficients was most significant near the pseudocritical zone, where the Nusselt number demonstrated a threefold change in the gas cooler. The maximum heat transfer coefficient was observed in the pseudocritical zone. Furthermore, it was observed that the optimal pressure rose with elevated water entry temperatures and mass flow rates, resulting in increased compressor utilisation and a decrease in the system's COP.

Helical spiral gas coolers, which an important components of Eco-cute heat pumps, was investigated by Xu et al. (2011). A model was employed to predict the heat transfer and pressure reductions in the gas cooler. This device was designed with a reduced refrigerant diameter to improve heat transfer efficiency, resulting in enhanced overall performance. In response to the insufficient performance of a single helical tube, the number of helical tubes was increased from one to three.

Fronk and Garimella reported the efficiency of a CO_2 gas cooler with microchannels used in a heat pump water heater. The initial paper presented their experimental results (Fronk & Garimella, 2011a), while the subsequent paper focused on their modelling approach and its validation (Fronk & Garimella, 2011b). This study analysed a system that utilised microchannel gas coolers rather than the conventional tube-in-tube configuration. This design facilitated improved operational capabilities by systematically increasing heat transfer coefficients and reducing pressure drops. The experimental study examined three distinct designs of microchannel gas coolers. A five-plate gas cooler and a seven-plate arrangement were tested in the laboratory, while a twelve-plate cooler was developed using a computer model. In these gas coolers, water traverses the plates, while the refrigerant circulates through the plates via microchannels (Fronk and Garimella, 2011b).

Experimental computations were conducted to determine approach temperatures, capacity, and total heat transfer coefficient (UA) values across various mass flow rates of refrigerant. The findings indicated that a rise in the refrigerant flow within the gas cooler enhanced heat transfer efficiency. The seven-plate heat exchanger exhibited a more significant performance improvement compared to the five-plate variant. Furthermore, the heat pump's efficiency was augmented by reducing the approach temperature, defined as the temperature change between the fluid inlet and the CO_2 outlet streams in the gas cooler and by minimizing pressure drop through the use of larger heat exchangers, which feature more plates. It was observed that smaller heat exchangers had a more pronounced effect on heating capacity when the water flow was altered. As the refrigerant mass flow rate increased, the UA value also rose, suggesting that the refrigerant side became the limiting factor in capacitance rates as water flow was enhanced. Additionally, the temperature and flow rate drop crosswise the gas cooler were found to affect pressure drop measurements. Elevated temperatures resulted in decreased densities and increased velocities, leading to a rise in pressure drop. The pressure loss in the gas cooler was calculated between 40-100 kPa for heat transfer between 2-4 kW & UA values between 0.05-0.13 kW/°C. Moreover, an increase in plate numbers corresponded with a rise in both pressure drop and UA value for CO_2 and water (Fronk and Garimella, 2011b).

Several common features emerged from a survey of the study on gas coolers. To begin, Sarkar et al. (2006), Xu et al (2010), Wang et al. (2013), and Yu et al. (2014) all observed that heat transfer coefficients were greatest in the pseudocritical zone. Further, it was observed by Fronk and Garimella (2011a) and Wang et al. (2013) that increasing the mass flux enhanced the amount of heat transferred in the gas cooler, with higher pressure drop and delivery pressure. Also, both authors focused on the need for having a gas cooler that was properly constructed and scaled in order to get the best outcomes.

2.10 Thermal energy storage (TES)

TES is the process of capturing thermal energy for later use in both residential and industrial thermal applications. This energy storage can be performed in three ways: sensible storage, latent form, and thermochemical form. Sensible TES involves the accumulation of heat within a storage medium, such as rock or water, based on temperature variations. Latent heat storage pertains to the retention of thermal energy during phase changes of materials, such as water or salt hydrates, transitioning between solid, liquid, and gas states. Finally, thermochemical heat storage depends on energy that is stored through a reversible chemical reaction (Cunha & Eames, 2016). In all instances, the storage material is housed within designated containers, like tanks, which is fitted with the required entry and exit devices.

This section aims to describe sensible thermal energy storage (TES) and to examine prior research that integrates AWHPs with water tanks, specifically as a heating solution for residential buildings in the United Kingdom.

2.10.1 Sensible TES

The amount of heat stored by a sensible TES system is calculated as follows:

$$Q = m\, C_P\, \Delta T \quad \text{(Joules)} \tag{1}$$

where m is mass (kg) and C_p is specific heat capacity (J/kgK) of the storage material, and ΔT is the temperature difference of inlet and outlet of the heat transfer medium. Gases are generally not suitable for sensible TES applications because of the lesser density. An essential consideration in the development of a TES device is the use of robust and properly insulated tanks, which are necessary to sustain the water weight and restrict heat losses. The heat loss rate through the TES devise can be obtained using the following formula:

$$q = U\,A\,\Delta T \qquad \text{(Watts)} \qquad (2)$$

where U-value represents thermal transmittance in W/m^2K (of storage tank), A is the area of the tank in m^2 and ΔT is the temperature difference of the storage devise. Water is one of the most recognized mediums for TES. Its ability to retain a significant amount of heat per unit weight is attributed to its greater specific heat capacity. Furthermore, water is typically free and readily accessible, can be easily pumped, is non-toxic, non-flammable, and exhibits mild corrosiveness when oxygen is absent (Han et al., 2009).

The most common sensible TES systems designed for residential use, where the thermal demand is met through electric means (for space heating and domestic hot water), typically consist of mixed or stratified water tanks. Thermally stratified storage tanks are designed with distinct volumes of medium at varying temperatures, specifically engineered to reduce the mixing of these layers. Water, when utilised as a storage medium, exhibits natural stratification owing to its increased density at lower temperatures: colder water sinks to the bottom, whereas warmer water rises to the surface, resulting in an intermediate layer referred to as the thermocline, as illustrated in Figure 19. Thermal stratification of water is influenced by various factors, including the dimensions of the tank, the design and placement of entry and exit points, as well as the flow rate and temperatures during storage and recovery processes. Multiple approaches have been employed to improve the thermal stratification of water (Pinel et al., 2011). Storage tanks operate using either indirect or direct heating methods. In a direct TES unit, the storage unit functions as the main mechanism for energy storage. In contrast, indirect systems utilise supplementary heat exchangers that provide additional heating as needed (Arteconi et al., 2012).

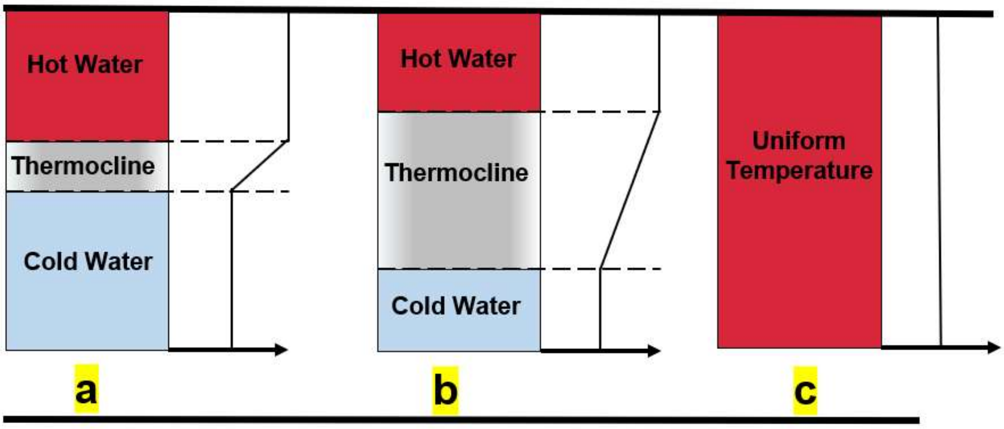

Figure 19: Stratification zone of a water TES tank: (a) Highly stratified; (b) Moderately stratified; (c) Fully mixed

2.10.2 ASHP coupling with TES

The coupling of TES with heat pumps in residential settings offers significant advantages for grid management and enhances consumer flexibility regarding energy consumption. This synergy between TES and renewable or low-carbon technologies is recognized as an effective Demand-Side Management (DSM) approach. It promotes demand flexibility by redistributing electricity usage from peak demand times to periods of lower demand, thereby aiding in grid stabilization and reducing electricity costs for consumers who capitalize on favorable electricity tariffs (Arteconi et al., 2012). Additionally, it is also possible to enhance the energy efficiency of buildings by using together TES and heat pumps.

Numerous prior studies have concentrated on determining the necessary storage capacity to efficiently transfer heating loads from periods of high electricity tariffs to those with lower rates, as defined by the electricity pricing structure in the UK. However, load-shifting has not consistently proven to be a feasible option for two primary reasons. First, the substantial storage capacity required for efficient load-shifting poses a challenge, particularly for many existing homes in the UK, which often have limited space for water storage tanks. Furthermore, the most commonly observed electricity tariffs, such as E7 & E10, primarily provide reduced rates during nighttime hours. However, operating an AWHP at night, when ambient temperatures are typically lower than during the day, leads to a decrease in the COP, resulting in higher energy consumption and costs.

Eames et al. (2014) investigated into the necessary thermal energy storage (TES) volume required to manage peak heating demands during the morning and evening hours (7-9 am and 4-7 pm) for a big, detached residence in Derby, UK. The findings indicated that a water tank with a capacity of 560 litres was essential for a house built in compliance with the 2010 Building Regulations. Conversely, for homes constructed prior to 1980, the essential storage volume was determined more than 2,500 litters. Similar conclusions were reached by Kelly et al. (2014), who evaluated the load-shuffling capabilities of an AWHP paired with a phase-change improved tank for a detached house in UK, utilizing the low-tariff hours offered by the E10 tariff. Here, energy consumption was observed to rise by 60.0%, with a necessary storage volume ranging from 500.0 litters to 1,000.0 litters, contingent upon the amount of phase-change material employed. In this regard, the adoption of variable Time-of-Use (ToU) tariffs, which are becoming more specific in the UK electricity market, could provide a solution to the challenges posed by traditional electricity tariffs, thereby facilitating the integration of AWHPs with TES as a feasible and economically competitive domestic heating option (Renaldi et al., 2017).

2.11 Summary

A comprehensive literature review has been conducted on the recent advancements in the use of CO_2 as a refrigerant in transcritical cycle heat pumps, with the key findings summarized as follows:

i. When properly designed and installed, heat pumps can provide low-carbon, cost-effective heating.
ii. The CO_2 heat pump cycle typically operates as a transcritical cycle due to the low critical temperature of CO_2 (31.1 °C) and its high critical pressure (73.8 bar).
iii. It has been observed that thermodynamic analysis and cycle optimization across the broad temperature range at which domestic heat pumps operate still require further investigation to ensure that the return water temperature to the heat pump remains as low as possible, thereby improving performance.
iv. Further research is needed on the integration of heat pumps and thermal energy storage within the overall heating system of domestic dwellings to enhance seasonal performance.

Chapter 3 2.3 kW CO_2 heat pump experiments and two-bedroom house energy modelling

3.1 Introduction

This chapter outlines the assessment of a commercially installed 2.3 kW CO_2 air-to-water heat pump (AWHP) at Brunel University London. The objective is to evaluate its performance and assess its potential as an effective solution for meeting the heating energy demands of typical houses in the UK. The SANDEN AWHP was meticulously monitored within the Centre for Sustainable Energy Future (CSEF) to characterise its operational behavior and efficiency using existing facilities. The experimental findings from this investigation serve as the basis for developing a heat pump performance map. This map is subsequently utilised to construct a new TRNSYS heat pump model, enabling the evaluation of the AWHP's performance in a standard 2-bedroom house in the UK. The chapter commences with a comprehensive overview and schematics of the experimental setup, followed by a detailed examination of the major components integrated into the system. Subsequently, the chapter delves into the presentation and analysis of experimental results. Additionally, it offers insights into the data acquisition system, the installed sensors within the setup, and a thorough analysis of uncertainties associated with the study.

3.2 CO_2 heat pump and thermodynamic analysis

Figure 20 (a) illustrates the configuration of the CO_2 heat pump water heating system investigated in this study. The heat pump consists of a compressor, gas cooler, electronic expansion valve (EEV), evaporator, and internal heat exchanger (IHX). The system's thermodynamic cycle is represented in the pressure-enthalpy (p-h) diagram shown in Figure 20 (b). The operational process is as follows: Initially, the low-pressure and low-temperature superheated CO_2 gas exiting the IHX is compressed by the compressor, raising its pressure and temperature (process 1–2). The high-temperature, high-pressure CO_2 gas then undergoes cooling in the gas cooler, where it transfers heat to the return water (process 2–3), followed by additional cooling in the internal heat exchanger (IHX) (process 3–4). Subsequently, the high-pressure CO_2 gas flows through the EEV, where it undergoes isenthalpic expansion, resulting in a low-pressure, low-temperature CO_2 gas-liquid mixture (process 4–5). This mixture then absorbs heat from the ambient air in the evaporator (process 5–6), which is supplied through an outdoor air handling unit (AHU) to maintain controlled airflow conditions. Finally, the CO_2 undergoes superheating in the IHX (process 6–1), completing the cycle. The primary function of the IHX in this system is to cool the CO_2 gas discharged from the gas cooler while simultaneously enhancing the suction temperature of the compressor by heating the gas. This process serves to minimise flash evaporation within the electronic expansion valve (EEV) and prevent liquid shock in the compressor. As a result, the system achieves a higher discharge temperature at a given discharge pressure, contributing to improved operational stability of the CO_2 heat pump cycle (Ge et al., 2023). Detailed specifications of the main system components are provided in Table 1.

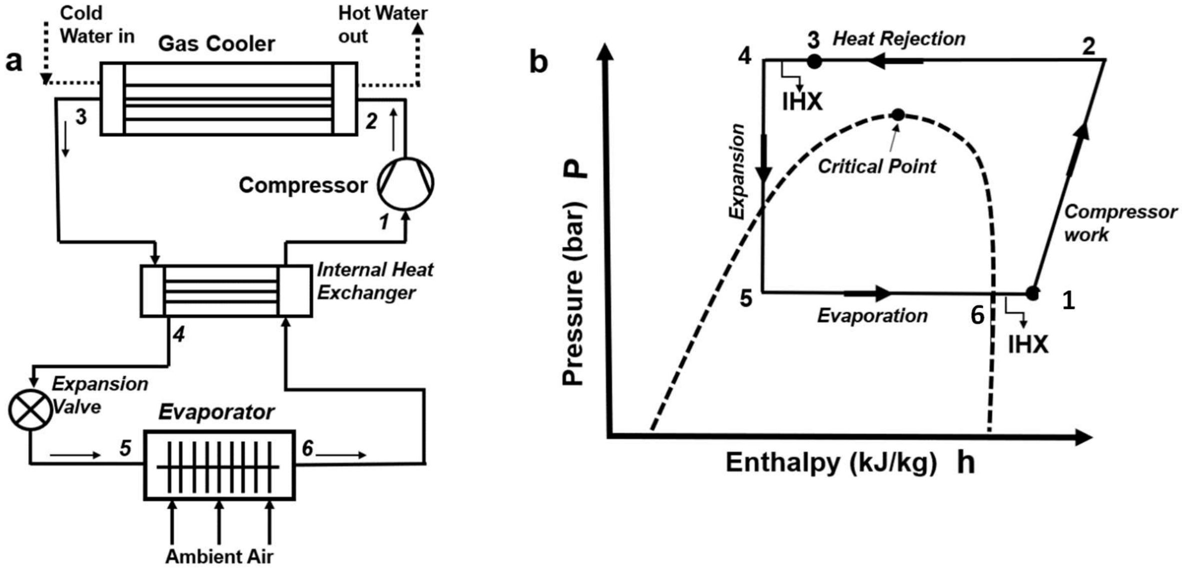

Figure 20. (a) Configuration of CO2 heat pump, (b) p-h diagram for CO2 heat pump

Table 2. Main components of the CO2 heat pump

Name of components	Type	Description
CO_2 compressor	Hermetic-scroll type 4.0 cc	Nominal heating capacity: 2.3 kW Nominal electric input: 1.8 kW Speed range: 2040 RPM to 5220 RPM
Gas cooler	Tube-in-tube type	Outside tube diameter: 12.7 mm; thickness: 0.8 mm Inside tube 1 diameter: 5.3 mm; thickness: 0.6 mm Inside tube 2 diameter: 3.1 mm; thickness: 0.5 mm
Evaporator	Fin-and-tube	Copper tube (CO2) Outer diameter: 5 mm Wall thickness: 0.45 mm H x W x D: 588 x 800 x 36.4 mm
Expansion device	Electronic type	Maximum temperature: 60 °C Maximum flow rate: 0.048 kg/s
Centrifugal blower	Fan	Flow rate: 800 m^3/h

3.3 Experimental setup and testing procedure

The experimental setup comprises four main components: A heat pump system, an air supply system, a water supply system and a data collection system. The heat pump and water storage tank are located in the pump room at ambient temperature, while three radiators are set up in the environmental chamber for use as space heating. In order to accurately regulate the input conditions and evaluate the heat pump system's performance, real-time measurements were taken on both the water and air sides. The air supply system, comprising an outdoor air handling unit (AHU) and a humidifier, ensured the maintenance of the specified temperature and humidity conditions for each experimental operating scenario. A controlled valve on the experimental platform controlled the flow rate of the hot water supplied by the heat pump.

A schematic diagram and picture of the experimental setup are presented in Figure 21 and Figure 22, respectively. The primary objective of these experiments was to analyse the heat pump's performance and track the state points under varying conditions. Since the study exclusively focused on the heat pump's response to increasing water inlet temperatures, no hot water draws were conducted, and no cold water was introduced into the hot water storage tank during testing. Initially, the hot water tank was filled with cold water from the cold water supply system. Once filled, the valves connecting the hot water tank and storage tank were closed. The heat pump was then activated, drawing water from the bottom of the hot water tank and circulating it through the gas cooler, where it was heated before returning to the top of the hot water tank. The heat pump continued operating until the entering water temperature reached 50 °C, at which point it automatically deactivated. Across all tests, the ambient air temperature remained constant, whereas the water inlet temperature varied dynamically between 20 °C and 50 °C. This process was repeated for different ambient air temperatures, enabling performance evaluations across a wide range of operating conditions. Throughout the testing phase, temperature, flow rate, and power consumption were continuously recorded at 5-second intervals using a data acquisition system, ensuring high-resolution data collection for comprehensive performance analysis.

The start-up and shutdown of the experimental platform, along with the set water temperature of the water tank manually controlled and compressor speed and EEV opening, are all controlled by the control system. The experiment uses a variable-speed compressor that is controlled by a frequency converter to generate hot water. During start-up, the compressor speed is increased to reach the target water temperature as fast as possible. After reaching its maximum speed, the compressor continues to operate at full load. As the system water temperature approaches the set target, the frequency is gradually reduced until the compressor shuts down.

The experimental system is equipped with four pressure sensors, six temperature sensors and two flow meters to facilitate comprehensive data acquisition and analysis. These sensors are strategically positioned at key locations within the system to monitor the thermodynamic parameters of the CO_2 heat pump cycle. Specifically, pressure and temperature sensors are installed at the compressor inlet and outlet (P-01, T-01; P-02, T-02), the gas cooler outlet (P-03, T-03), and the outlet of the expansion valve (P-04, T-04). Additionally, on the waterside, two temperature sensors and one flow meter are positioned to monitor water flow conditions. The temperature sensors are placed at the water inlet and outlet of the gas cooler (T-05, T-06). The sensor positions within the experimental setup are illustrated in Figure 23. This arrangement ensures precise monitoring of system performance, enabling accurate evaluation of heat transfer characteristics and overall efficiency. The refrigerant pressures at various state points within the heat pump system were measured using pressure transducers with an uncertainty of ±0.5%. The refrigerant and water temperatures at key locations were recorded using K-type thermocouples, which have an uncertainty of ±1.5°C. The refrigerant mass flow rate was measured using a Coriolis effect flow meter, ensuring high accuracy with an uncertainty of ±0.2%. On the waterside, the volume flow rate was measured using a magnetic flow meter, which has an uncertainty of ±3%. The total system power consumption was monitored using a power meter, with an uncertainty of ±2.5%. The measurement deviation of the heating capacity between the refrigerant side and air side was maintained within ±2.0% throughout the tests, ensuring reliable performance evaluation. The instrumentation and propagated uncertainties are further detailed in the following sections. The specifications of the measurement instruments are summarized in Table 2.

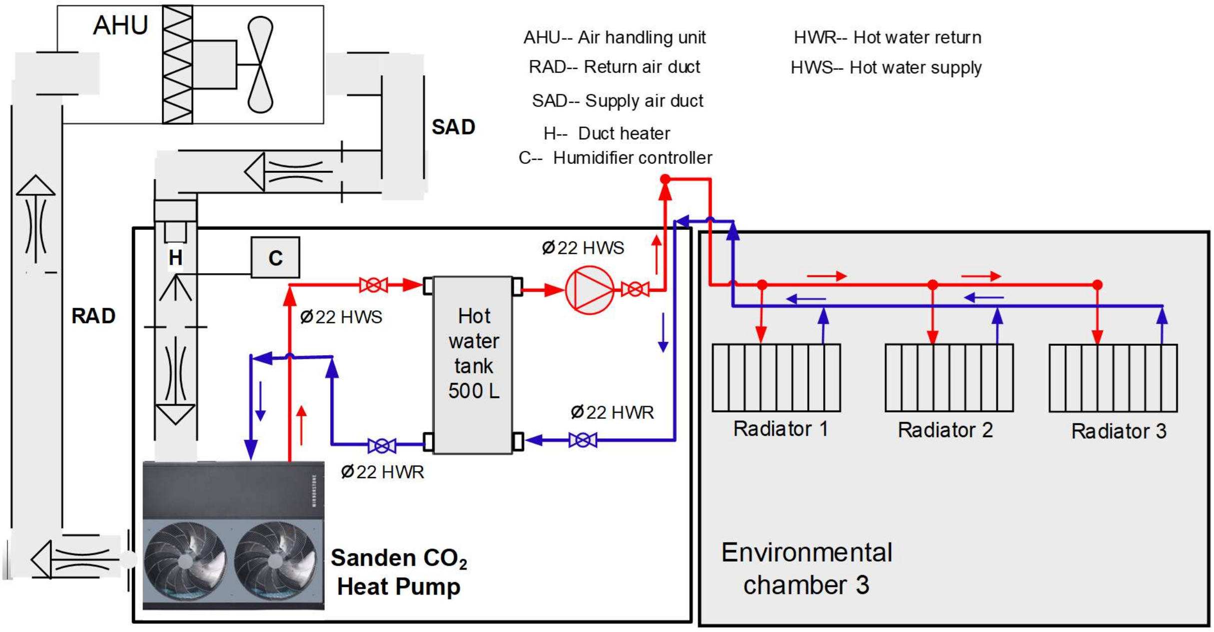

Figure 21. Schematic diagram of the experimental setup

Figure 22. A picture of the experiment setup

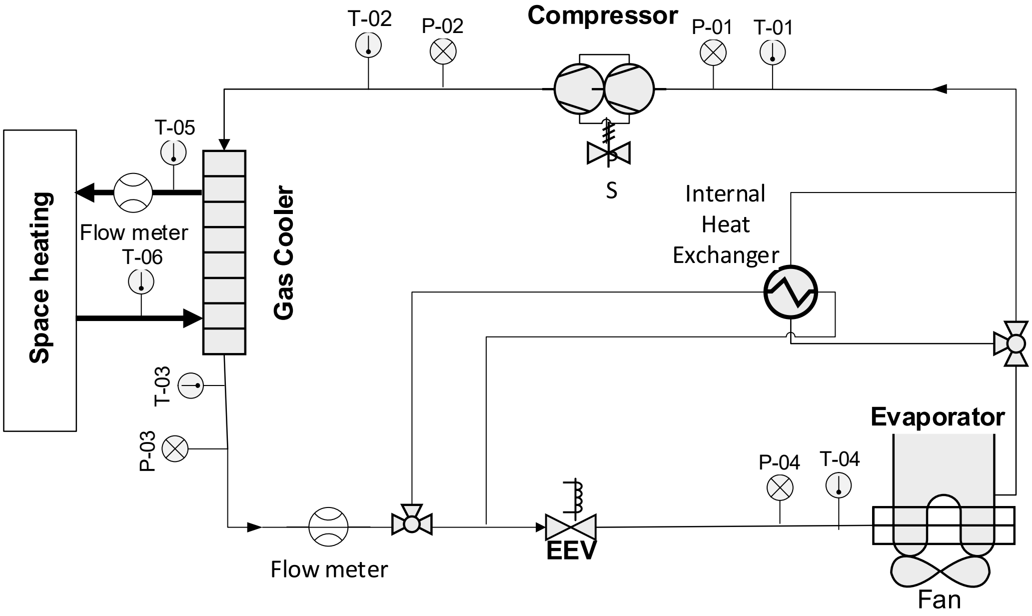

Figure 23. Pressure and temperature sensors positions.

3.4 Data monitoring and collection

To characterize the performance of the commercial CO_2 heat pump unit, a data monitoring and acquisition system was implemented. The collected data was essential for developing a performance map, which was subsequently used to analyse the system's efficiency and operational behavior under varying conditions. To achieve this, a compact data acquisition (DAQ) system, control cards, and LabVIEW software were integrated to establish a computer interface capable of both monitoring and controlling the experimental apparatus. This setup enabled real-time data collection, facilitating precise performance evaluation and ensuring the system operated within the desired parameters.

3.4.1 Data acquisition system

A compact NI cDAQ-9133 chassis was employed as a communication interface between different equipment components and the external computer system through input/output (I/O) modules. This communication was managed by multiple timing engines, allowing the simultaneous control of up to eight different hardware modules, each operating at independent sampling rates. To ensure reliable and efficient data transmission, the data acquisition (DAQ) system was connected to the laboratory computer via an Ethernet cable, providing a stable and high-speed communication link. The selection of this DAQ system was primarily driven by its intuitive graphical interface in LabVIEW, which allows seamless real-time control and monitoring of the I/O modules. Unlike traditional DAQ chassis, which often require additional configuration steps to set up virtual inputs and outputs, the NI cDAQ-9133 provides a streamlined and user-friendly integration process, allowing for direct data acquisition and efficient system control. As shown in Figure 24, the complete assembly of the NI cDAQ-9133 chassis and its associated NI-9214 and NI-9203 modules is illustrated.

A variety of I/O modules were employed to facilitate essential control functions and data acquisition for the experiments. The I/O modules integrated into this setup included binary input, binary output, analog input (AI), analog output (AO) and a thermocouple module. The binary input signals were collected from the power monitoring system and pulse-generating devices, such as the water flow meter or refrigerant mass flow meter. These pulse signals were processed within LabVIEW, where they were converted into power readings or flow rate measurements using device-specific conversion equations. Meanwhile, binary output signals were generated by the DAQ module and distributed to various system components and instruments, primarily serving on/off control functions. The AI signals were acquired from various sensors via current or voltage signals, which were then communicated to the DAQ system. These signals were utilised in Proportional-Integral (PI) control loops for real-time data collection and system regulation. The AI channels were responsible for collecting data from all installed sensors, with the exception of thermocouples, which were measured separately using a dedicated thermocouple module to assure accurate temperature monitoring.

The NI 9203 is a versatile combination voltage and current input module, featuring eight channels for ±20 mA current input and eight channels for ±10 V voltage input. This module is primarily used for high-accuracy data acquisition, particularly in industrial and laboratory applications where precise analog signal measurement is required. In this study, the NI 9203 was utilised to measure the flow rate through its current AI channels, which are commonly used for 4–20 mA industrial flow sensors. The module's high resolution and fast sampling capabilities ensured accurate and reliable data collection, facilitating real-time monitoring and control of the system's flow dynamics. Temperature readings were acquired using the NI 9214 AI module, which offers eight input channels and a 24-bit resolution designed for K-type and T-type thermocouples.

Figure 24. National Instrument DAQ chassis and modules

The NI 9214 is equipped with a built-in cold junction compensation (CJC), which was utilised to ensure accurate temperature measurements. The cold junction compensates for the voltage generated by the two dissimilar metals of the thermocouple, which varies with temperature. By comparing this voltage difference to the known reference at the cold junction, precise temperature readings were obtained. In this setup, the AO signals were used exclusively for control purposes. The Proportional-Integral (PI) controller processed the measured temperature data and generated a control signal to regulate the system based on the predefined set-point. This feedback mechanism ensured the stable and efficient operation of the equipment, maintaining the desired thermal conditions throughout the experiment. As shown in Figure 25, the complete installation and wiring configuration of the data acquisition (DAQ) system is presented.

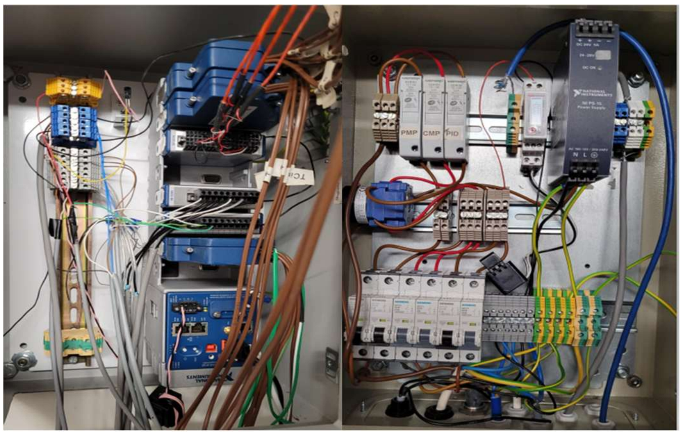

Figure 25. Data acquisition system.

3.4.2 LabVIEW

LabVIEW is a software platform designed to develop visual programming using graphical language created by National Instruments. It employs a graphical user interface (GUI) known as a Virtual Interface (VI), which enables users to develop control and data acquisition programs through a workflow-based approach resembling block diagrams. This visual programming method enhances user interaction and facilitates real-time monitoring during control programming. The GUI for the experimental apparatus was developed using LabVIEW VI in this work. This allowed for efficient data gathering, system control, and visualisation. In order to create the performance map and test the CO_2 heat pump, the following sections will explain the control tactics used to set up the necessary test circumstances.

3.4.3 Performance map virtual interference

A performance mapping virtual interface (VI) was developed to continuously monitor the heat pump's operational performance under varying conditions, including different supply air temperature and return water temperature. The system's performance was evaluated by tracking fluctuations in water temperature, which directly reflected the heat dissipation from the gas cooler and the energy consumption of the compressor.

The evaporator's performance was evaluated by monitoring the temperature variation of air passing through the external air handling unit (AHU). The LabVIEW VI facilitated data acquisition and exported the collected data to an Excel sheet. Additionally, the incoming air conditions in the AHU were dynamically adjusted based on the VI and real-time measured parameters. This process involved a proportional-integral (PI) control loop, which regulated the temperature and humidity of the supply air, as well as the return water temperature in the storage tank. To initiate a new test, the water in the storage tank was preheated to 63 °C to ensure a uniform temperature distribution before being supplied to the radiators in chamber room 3. During testing, data were recorded at 5-second intervals across a return temperature range of 20 °C to 50 °C. The process was then repeated for the next air supply temperature to construct a comprehensive performance map. Figure 26 illustrates the layout of the performance map VI.

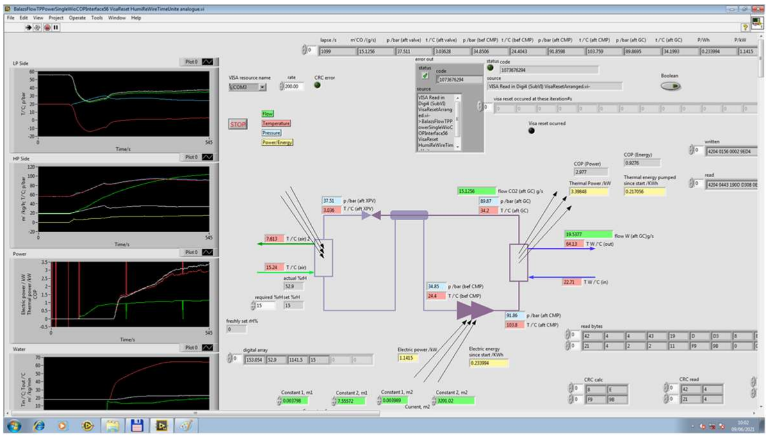

Figure 26. Data monitoring performance

3.5 Uncertainty analysis

An uncertainty analysis was performed to evaluate the potential experimental errors arising from the experimental setup and the associated measurement sensors, such as thermocouples and flowmeters. Experimental errors and uncertainties may arise due to instrument selection, calibration status, operational conditions, as well as environmental factors and reading inaccuracies. Conducting an uncertainty analysis is essential to validate the accuracy and reliability of the experimental results (Ozgener and Hepbasli, 2005).

The objective of this section is to determine the uncertainty of COP. Initially, Equation (1) is introduced, defining COP and identifying heating capacity (Q) as the primary parameter of interest. The parameter Q is determined using a combination of variables specified in Equation (2), all of which are continuously monitored through flow meters and sensors. Given the dynamic nature of the AWHP system, fluid properties are influenced by temperature fluctuations. To accurately estimate the overall uncertainty in Q, it is crucial to account for errors associated with temperature and flow sensors. The multiple sources of measurement uncertainty were systematically combined using the uncertainty propagation methodology proposed by Taylor (1997) to determine the uncertainty range associated with the calculated COP. This study employed high-precision instruments to gather measurements of temperature, flow rate, and power, as detailed in the subsequent sections.

a) Measurement of mass flow rates of water mixture by a Magnetic-Inductive Flow Meter (ifm SM 7000)
b) The temperature of the water at the inlet and outlet of the gas cooler was measured using K-type thermocouples, which were installed on the water inlet and outlet lines to ensure precise temperature monitoring.
c) Measurement of the outdoor air temperatures K- type thermocouples.
d) Measurement of the instantaneous power consumptions of the compressor by a clamp power meter (Fluke 345).

Table 3. Specifications for measurement instruments.

Nos.	Variable	Measuring Device/ Manufacture	Accuracy
1	Temperature (Water side)	K-Type Thermocouple NiCr-Ni (TC)	± 1.5 ℃
2	Flow meter (Water Side)	Magnetic-Inductive Flow Meter (ifm SM 7000)	± 3% of reading
3	Electric Power	Clamp Power Meter (Fluke 345)	± 2.5% of reading

$$COP = \frac{\mathrm{Q}}{\mathrm{P}} \tag{1}$$

Where,

COP - Coefficient of Performance

Q - Heating capacity (kW)

P - Compressor Work (kW)

$$Q = m_w \times Cp_w \times \Delta \mathrm{T} \quad (2)$$

Where,

Q - Heating capacity (kW)

m_w - mass flow rate of water (kg/sec)

Cp_w - Specific heat of water (kJ/kgK)

ΔT - Water temperature difference across the gas cooler (°C)

Here,

$\Delta \mathrm{T} = T_{Wout} - T_{Win}$

3.5.1 Total uncertainty

The total uncertainty is estimated by systematically combining the uncertainties associated with each identified source of error. These sources of error are derived from the heat transfer and coefficient of performance (COP) equations. For equations involving addition or subtraction, the total uncertainty is determined by first summing the squares of the individual uncertainties and then taking the square root of the resulting sum. In this section, the uncertainty in heat transfer is quantified first, followed by the uncertainty estimation for COP, ensuring a comprehensive evaluation of measurement accuracy.

3.5.2 Uncertainty for heat transfer

As previously stated in Equation (2), the heating capacity (Q) is a function of the mass flow rate, specific heat capacity, and the temperature difference. These parameters collectively determine the amount of heat energy transferred within the system, directly influencing its thermal performance. But, the specific heat of water is constant and its effect on uncertainty is negligible. Therefore, the uncertainty of Q can be determined by summing the squares of the individual uncertainties and subsequently calculating the square root of the resultant sum, as illustrated in Equation (3).

$$\frac{\partial \mathrm{Q}}{\mathrm{Q}} = \sqrt{\left[\frac{\partial \mathrm{m}}{\mathrm{m}}\right]^2 + \left[\frac{\partial \Delta \mathrm{T}}{\Delta \mathrm{T}}\right]^2 + \left[\frac{\partial \mathrm{C_P}}{\mathrm{C_P}}\right]^2} \quad (3)$$

$\partial \triangle \mathrm{T}$ - Error range for temperature difference (℃)

∂m - Error range for mass flow rate (kg/s)

∂Q - Error range for heat transfer rate (kW)

m - Reference mass flow rate (kg/s)

$\triangle \mathrm{T}$ - Reference temperature difference (℃)

Q - Reference heat transfer rate (kW)

The error in the calculated temperature difference is influenced by the measurement uncertainties of the individual temperature sensors. These individual errors are systematically combined to determine the overall uncertainty in the temperature difference.

$$\partial \triangle \mathrm{T} = \sqrt{{T_{Wout}}^{2} + {T_{Win}}^{2}}$$

As from Table -1, the K-type sensor error is ± **1.5** ℃

$$\partial \triangle \mathrm{T} = \sqrt{1.5^{2} + 1.5^{2}}$$

$$\partial \triangle \mathrm{T} = \pm \mathbf{2.1}\ ℃$$

For 1st reading, At 0 ℃ ambient temperature and 20 ℃ return water temperature

$\triangle \mathrm{T} = 43$ ℃ and m = 0.019 kg/sec

Put values in Eq.3

$$\frac{\partial Q}{\mathrm{Q}} = \sqrt{\left[\frac{0.0006}{0.019}\right]^{2} + \left[\frac{2.1}{43}\right]^{2}}$$

(Assuming negligible uncertainty in C_P)

$$\frac{\boldsymbol{\partial Q}}{\mathbf{Q}} = \pm \mathbf{0.058}$$

$$\frac{\boldsymbol{\partial Q}}{\mathbf{Q}} = \pm \mathbf{5.8}\%$$

$$\partial \mathrm{Q} = 3.44 \times 0.058$$

$$\partial \mathrm{Q} = \pm 0.2 \text{ kW}$$

3.5.4 Uncertainty for COP

As previously stated in Equation (1), the COP is dependent on the heating capacity and the compressor power consumption. Consequently, the uncertainty in COP can be determined by summing the squares of the individual uncertainties and subsequently computing the square root of the total sum, as expressed in Equation (4).

$$\frac{\partial COP}{\mathrm{COP}} = \sqrt{\left[\frac{\partial Q}{Q}\right]^2 + \left[\frac{\partial \mathrm{P}}{\mathrm{P}}\right]^2} \tag{4}$$

$\partial\mathrm{COP}$	-	Error range for COP
∂P	-	Error range for Power (kW)
∂Q	-	Error range for heating capacity (kW)
COP	-	Coefficient of performance
P	-	Reference Power (kW)
Q	-	Reference heating capacity (kW)

At 0 °C ambient temperature,

P = 1.47 kW

$$\frac{\partial COP}{\mathrm{COP}} = \sqrt{\left[\frac{0.2}{3.44}\right]^2 + \left[\frac{0.037}{1.47}\right]^2}$$

$$\frac{\partial COP}{COP} = \pm 0.0643$$

$$\frac{\partial COP}{COP} = \pm 06.43\%$$

$$\partial COP = 2.33 \times 0.0643$$

$$\partial COP = \pm 0.15$$

Tables 3 to 6 summarize the uncertainty analysis results for the COP and heating capacity of the heat pump. The estimated average uncertainty in COP during heating operation ranges between ±6.0% and ±15%, emphasizing the variability in measurement accuracy.

Table 4. Ambient air 0 °C

Nos.	T_{Win}	T_{Wout}	ΔT	∂ΔT	m (kg/s)	∂m	P (kW)	∂P	Q (kW)	∂Q (kW)	%∂Q	COP	∂COP	%∂COP
1	20	63	43	±2.1	0.019	0.0006	1.47	0.037	3.44	±0.20	5.81	2.33	±0.15	6.43
2	25	63	38	±2.1	0.021	0.0006	1.52	0.038	3.38	±0.21	6.21	2.22	±0.15	6.81
3	30	63	33	±2.1	0.023	0.0007	1.56	0.039	3.24	±0.23	7.09	2.08	±0.16	7.45
4	35	63	28	±2.1	0.025	0.0007	1.57	0.039	2.98	±0.24	8.04	1.90	±0.16	8.33
5	40	63	23	±2.1	0.030	0.0009	1.56	0.039	2.87	±0.27	9.40	1.80	±0.18	10.00
6	45	63	18	±2.1	0.034	0.0010	1.53	0.038	2.67	±0.31	11.60	1.74	±0.21	12.06
7	50	63	13	±2.1	0.041	0.0012	1.55	0.039	2.51	±0.38	15.14	1.62	±0.25	15.43

Table 5. Ambient air 10 °C

Nos.	T_{Win}	T_{Wout}	ΔT	∂ΔT	m (kg/s)	∂m	P (kW)	∂P	Q (kW)	∂Q (kW)	%∂Q	COP	∂COP	%∂COP
1	20	63	43	± 2.1	0.020	0.0006	1.23	0.031	3.54	± 0.20	5.65	2.89	±0.18	6.37
2	25	63	38	± 2.1	0.021	0.0006	1.27	0.032	3.44	± 0.21	6.11	2.70	±0.18	6.66
3	30	63	33	± 2.1	0.024	0.0007	1.31	0.033	3.34	± 0.23	6.88	2.55	±0.19	7.46
4	35	63	28	± 2.1	0.027	0.0008	1.33	0.033	3.17	± 0.25	8.00	2.38	±0.20	8.40
5	40	63	23	± 2.1	0.030	0.0009	1.37	0.034	2.96	± 0.28	9.37	2.16	±0.21	9.71
6	45	63	18	± 2.1	0.033	0.0010	1.31	0.033	2.61	± 0.31	11.87	2.00	±0.24	12.00
7	50	63	13	± 2.1	0.040	0.0012	1.31	0.033	2.39	± 0.36	15.08	1.82	±0.28	15.29

Table 6. Ambient air 15 °C

Nos.	T_{Win}	T_{Wout}	ΔT	∂ΔT	m (kg/s)	∂m	P (kW)	∂P	Q (kW)	∂Q (kW)	% ∂Q	COP	∂COP	% ∂COP
1	20	63	43	± 2.1	0.019	0.0006	1.07	0.027	3.41	± 0.20	5.87	3.18	±0.20	7.03
2	25	63	38	± 2.1	0.020	0.0006	1.11	0.028	3.29	± 0.21	6.39	2.97	±0.20	7.40
3	30	63	33	± 2.1	0.023	0.0007	1.11	0.028	3.14	± 0.22	7.10	2.83	±0.21	8.36
4	35	63	28	± 2.1	0.025	0.0008	1.15	0.029	2.99	± 0.24	8.12	2.60	±0.22	9.24
5	40	63	23	± 2.1	0.028	0.0008	1.19	0.030	2.78	± 0.26	9.36	2.34	±0.23	10.64
6	45	63	18	± 2.1	0.032	0.0010	1.20	0.030	2.53	± 0.30	11.75	2.11	±0.25	12.70
7	50	63	13	± 2.1	0.038	0.0012	1.23	0.031	2.31	± 0.35	15.16	1.88	±0.29	15.79

Table 7. Ambient air 20 °C

Nos.	T_{Win}	T_{Wout}	ΔT	∂ΔT	m (kg/s)	∂m	P (kW)	∂P	Q (kW)	∂Q (kW)	% ∂Q	COP	∂COP	% ∂COP
1	20	63	43	± 2.1	0.019	0.0006	0.97	0.024	3.30	± 0.20	6.06	3.40	±0.21	6.18
2	25	63	38	± 2.1	0.020	0.0006	0.98	0.024	3.18	± 0.20	6.30	3.25	±0.22	6.78
3	30	63	33	± 2.1	0.022	0.0007	1.01	0.025	3.09	± 0.22	7.08	3.07	±0.23	7.49
4	35	63	28	± 2.1	0.025	0.0007	1.03	0.026	2.96	± 0.23	7.95	2.88	±0.24	8.35
5	40	63	23	± 2.1	0.028	0.0008	1.05	0.026	2.76	± 0.26	9.39	2.62	±0.26	9.71
6	45	63	18	± 2.1	0.032	0.0010	1.08	0.027	2.52	± 0.30	11.78	2.34	±0.28	11.97
7	50	63	13	± 2.1	0.038	0.0011	1.10	0.027	2.28	± 0.34	14.94	2.08	±0.32	15.42

3.6 Experimental conditions

This study investigates the influence of inlet water temperature and ambient air temperature on heat pump performance parameters through a series of controlled experiments. The parameters analysed include COP, heating capacity, power consumption, compressor discharge and suction pressures, as well as discharge and suction temperatures. The ambient air temperature is varied between 0 °C and 20 °C, while the inlet water temperature ranges from 20 °C to 50 °C. A summary of the experimental conditions is provided in Table 7.

Table 8. Experimental conditions

Nos.	Ambient air Dry Bulb (DB) /Wet Bulb (WB) (°C)	Equivalent relative humidity (%)	Water Inlet temperature (°C)	Water outlet temperature (°C)
1	$0 / -0.5$	90	20	63
2			25	
3			30	
4			35	
5			40	
6			45	
7			50	
8	10 / 8.7	85	20	63
9			25	
10			30	

11			35	
12			40	
13			45	
14			50	
15	15 / 13	80	20	63
16			25	
17			30	
18			35	
19			40	
20			45	
21			50	
22	**20 / 17**	**75**	**20**	**63**
23			**25**	
24			30	
25			35	
26			40	
27			45	
28			50	

3.7 Results and discussion

The variation in heating capacity, power consumption and COP of the CO_2 AWHP was experimentally investigated under the range of operating conditions described below.

3.7.1 Heating capacity

As the inlet water temperature rises, the heating capacity decreases at a constant ambient temperature, as depicted in Figure 27. This reduction in heating capacity with increasing return water temperature is mainly due to the reduced temperature gradient between the refrigerant and circulating water, which lowers the overall heat exchange efficiency. Furthermore, as the ambient temperature increases, the evaporation pressure also rises, resulting in a higher refrigerant mass flow rate at the compressor suction, thereby enhancing the heating capacity. However, despite the increase in CO_2 refrigerant mass flow rate at a fixed ambient temperature, the dominant factor influencing heating capacity remains the enthalpy difference. A higher inlet water temperature reduces this enthalpy difference, leading to a gradual decline in heating capacity under constant flow conditions, as shown in Figure 27. In contrast, the heating capacity declines at lower ambient temperatures as the heat pump struggles to extract heat from the colder air and vice versa.

At an ambient temperature of 10 °C, when the inlet water temperature increases from 35 °C to 50 °C, the heating capacity decreases from 2.9 kW to 2.2 kW, showing a reduction of 24%. Conversely, when the ambient temperature decreases from 10 °C to 0 °C at an inlet water temperature of 50 °C, the heating capacity declines from 2.2 kW to 2 kW, representing a reduction of 9%. These results indicate that heating capacity is more strongly influenced by inlet water temperature than by ambient temperature.

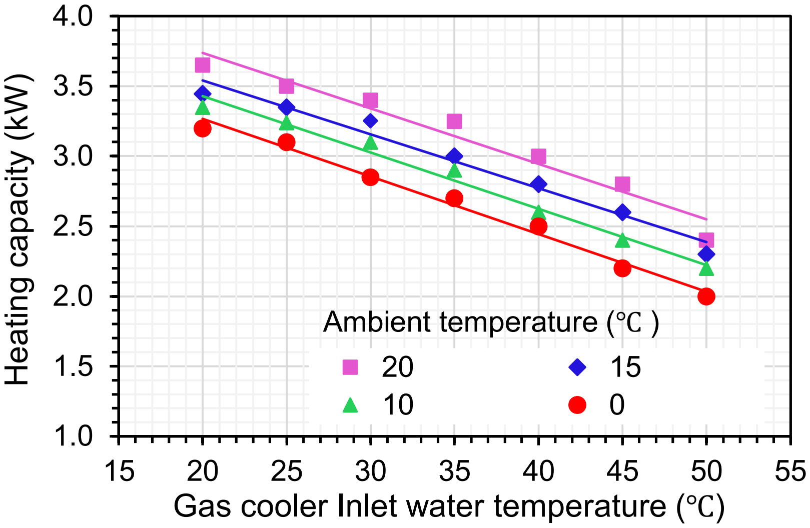

Figure 27. Heating capacity vs inlet water temperature

3.7.2 Power input

The variation in compressor power consumption with different ambient temperatures and return water temperatures in the gas cooler is illustrated in Figure 28. As the ambient temperature increases, the pressure ratio decreases, as shown in Figure 29, typically resulting in lower compressor power consumption. However, the suction pressure decreases at lower ambient temperatures, reducing the refrigerant mass flow rate. This decrease in mass flow rate increases the compression process, ultimately increasing compressor power consumption. At an ambient temperature of 10 °C, when the inlet water temperature increases from 35 °C to 50 °C, the electric power consumption rises from 1.36 kW to 1.41 kW, representing a 6% increase. Conversely, when the ambient temperature decreases from 10 °C to 0 °C at an inlet water temperature of 50 °C, the electric power increases from 1.41 kW to 1.64 kW, indicating a 16% rise. These results suggest that the increase in power consumption is more strongly influenced by ambient temperature rather than return water temperature. This trend is further illustrated in Figures 29 and 30.

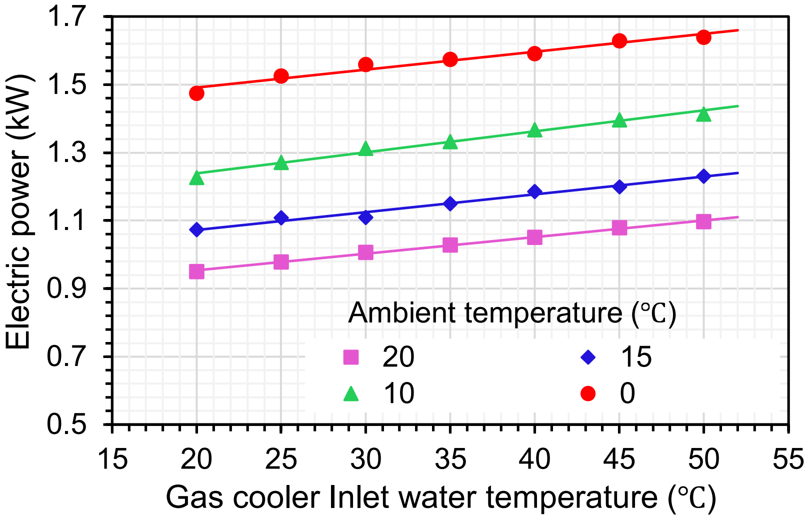

Figure 28. Electric power vs inlet water temperature

Figure 29 presents the variation of the pressure ratio with different gas cooler inlet water temperatures under varying ambient conditions. As the inlet water temperature increases from 20 °C to 50 °C, the pressure ratio exhibits a steady rise across all ambient temperatures. This behavior is attributed to the elevated gas cooler outlet temperature at higher inlet water temperatures, which increases the discharge pressure, additionally, at lower ambient temperatures (e.g., 0°C), the pressure ratio is significantly higher over the entire range of inlet water temperatures compared to higher ambient conditions. This is due to the reduction in evaporating (suction) pressure at lower ambient temperatures, as shown in Figure 30, which amplifies the difference between discharge and suction pressures, thereby increasing the pressure ratio. Conversely, at higher ambient temperatures (e.g., 20°C), the suction pressure rises due to the warmer air, leading to a lower overall pressure ratio.

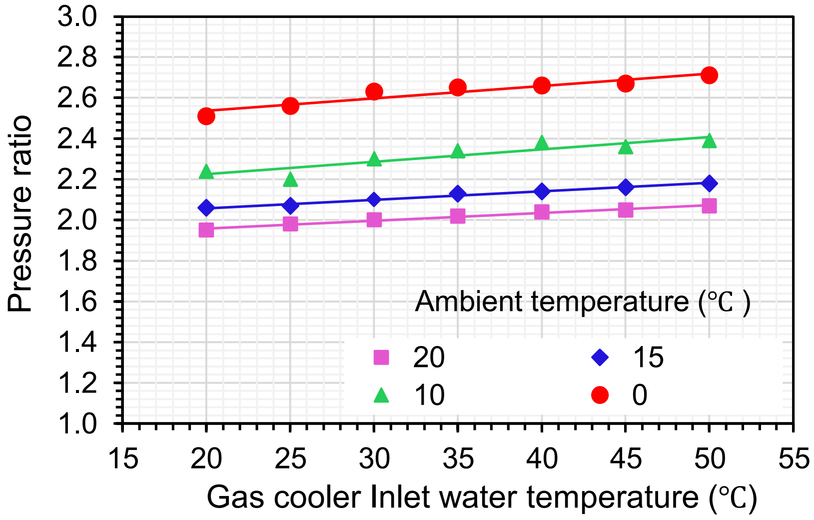

Figure 29. Pressure ratio vs inlet water temperature

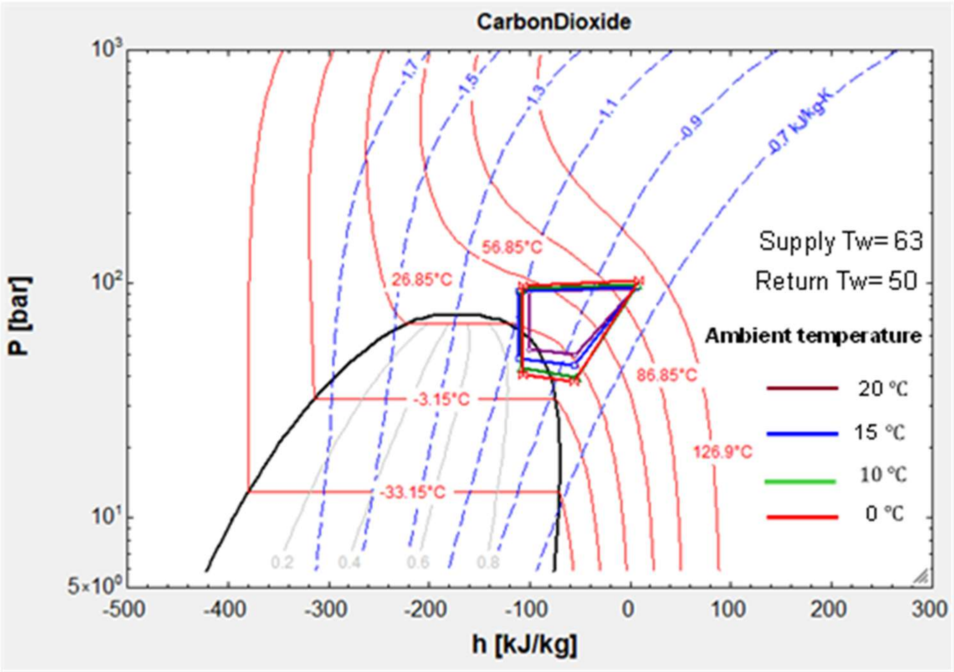

Figure 30. P-h diagram under different outdoor air temperatures

3.7.3 Coefficient of Performance (COP)

Figure 31 illustrates the variations in the COP at different inlet water temperatures in the gas cooler and under varying ambient temperatures. The figure demonstrates that, for a constant supply of water temperature, an increase in return water temperature leads to a gradual decline in COP. Moreover, the higher the return water temperature, the more rapidly the COP decreases.

Conversely, the heat pump system operates more efficiently when the return water temperature is lower and the outdoor temperature is higher. This trend can be attributed to the combined effect of ambient temperature and return water temperature on system performance.

As the ambient temperature decreases, both the evaporation and discharge temperatures also decrease, reducing the enthalpy difference between the CO_2 refrigerant and the circulating water. Additionally, the mass flow rate of the CO_2 refrigerant decreases, leading to a reduction in heat capacity at a constant water flow rate. Simultaneously, the compression ratio increases, resulting in a rise in power consumption. Since the rise in power consumption is more significant than the increase in heating capacity at a higher compression ratio, the COP exhibits a downward trend.

On the other hand, with an increase in ambient temperature, both the evaporation temperature and the corresponding evaporation pressure rise, as the temperature difference between the air and refrigerant side remains nearly constant. Consequently, the pressure ratio decreases as ambient temperature increases, as illustrated in Figure 29, even when the discharge temperature remains unchanged. Under optimal conditions, where variations in the CO_2 gas cooler outlet temperature are minimal, as shown in Figure 30, a reduction in pressure ratio results in a decrease in input power consumption. As a result, the system COP improves with rising ambient temperature, as depicted in Figure 31.

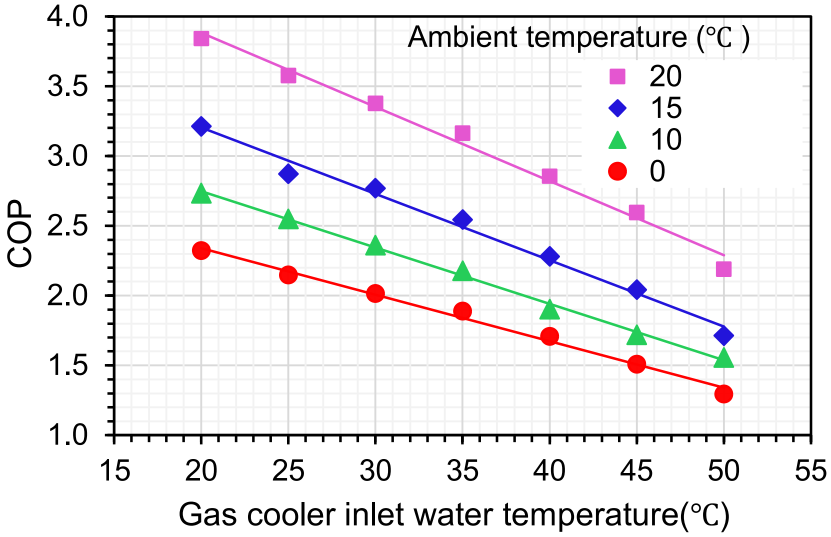

Figure 31. COP vs water inlet temperature in the gas cooler

Increasing the inlet water temperature from 40 °C to 50 °C while keeping the water outlet temperature at 63 °C leads to a decrease of the measured COP from 1.9 to 1.5 at the given ambient temperature of 10 °C, as can be seen in Figure 31.

In general, ambient temperatures are also the critical factor influencing the system COP of heat pumps. When the ambient temperature increases from 0 °C to 10 °C at an inlet water temperature of 50 °C, the COP increases by about 20%. The heating capacity was observed to increase at a greater rate than the total power consumption, resulting in a higher system COP, which aligns with common practice.

Discharge temperature and pressure under different working condition

Figure 32 presents the variation in compressor discharge temperature with the return water temperature at different ambient temperatures. As the return water temperature increases, the discharge temperature also rises. This trend is primarily attributed to the rapid increase in pressure ratios, which intensifies the compression process and leads to higher discharge temperatures.

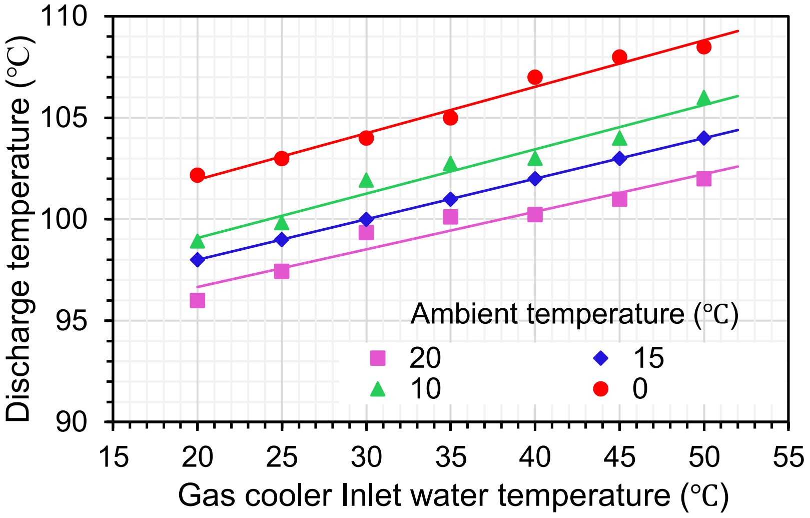

Figure 32. Discharge temperature vs water inlet temperature in the gas cooler

As shown in Figure 33, the discharge pressure increases linearly with the rise in inlet water temperature. This trend is primarily attributed to the rapid increase in gas cooler temperature, as depicted in Figure 30.

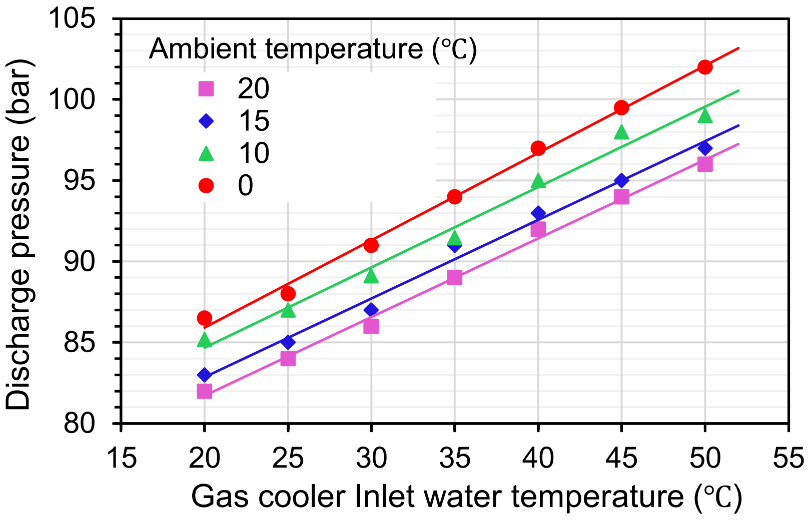

Figure 33. Compressor discharge pressure vs water inlet temperature in the gas cooler

3.8 Building Energy Modelling of Two-Bedroom House

3.8.1 Introduction

This chapter will report the investigation of energy demand for space heating and domestic hot water (DHW) systems and the resulting electric power requirements for an air-to-water heat pump (AWHP) in a two bedroom semi-detached house in London (UK). Energy demand and power requirements in new, well-insulated buildings are considered. Using simulation results, the heating energy and electric power requirements for the heat pump in the semi-detached house will be computed. The effect of a thermal energy storage tank (TES) on indoor temperature, heat pump control settings and heat pump thermal capacity for economic and CO_2 emission analysis in the residential house is investigated.

3.8.2 Methodology

The research aims to integrate the AWHP system into a typical semi-detached house and to investigate the seasonal energy performance and indoor comfort condition of different thermal energy storage tanks when coupled with AWHP. A dynamic simulation model was required to determine the building's thermal load as well as the energy demand for space heating and domestic hot water. The building considered in this study was a single-family home located in London, UK; the heating system was composed of an inverter-driven air-to-water heat pump with two-pipe radiators as terminal units. Results from four simulations carried out for varying tank capacities are presented in this chapter.

3.8.3 Energy Modelling of a 2-Bedroom Semi-Detached House

The building modelled in this study is a two-bedroom, semi-detached, single-family house with a total heated floor area of 78 m^2. It is a typical UK single-family house construction. The building has two floors and an unheated attic. It was assumed that 4 people were living in this house. Figure 34 (a) shows the planning layout of the proposed building, including the schematic of the proposed house and the floor plans. Figure 34 (b) displays the building geometry, which was created in Sketchup 2022/TRNSYS 3d plug-in. The wall with no windows represents the shared wall with the adjacent semi-detached house, which was assumed to be adiabatic. The building comprises eight thermal zones namely the kitchen, living room, hall, toilet, bedroom 1, bedroom 2, bathroom, and landing, respectively. Both air volume and thermal capacitance vary between zones. The thermal zones are naturally ventilated. The temperature is maintained at 20 ± 1 °C all year round in each zone that is heated. The assessment of the building heating load was the first step to be carried out in a detailed building energy simulation analysis. For each building's thermal zone, the calculation procedure starts with the analysis of the related heat flows. These flows were determined by heat conduction through the walls, convection and radiation both internally and externally, radiation from the sun entering through the windows, and heat loss due to infiltration and ventilation. In order to determine the building's energy balance, dynamic modelling techniques often calculate the envelope's heat loss and gain (Tang et al., 2020).

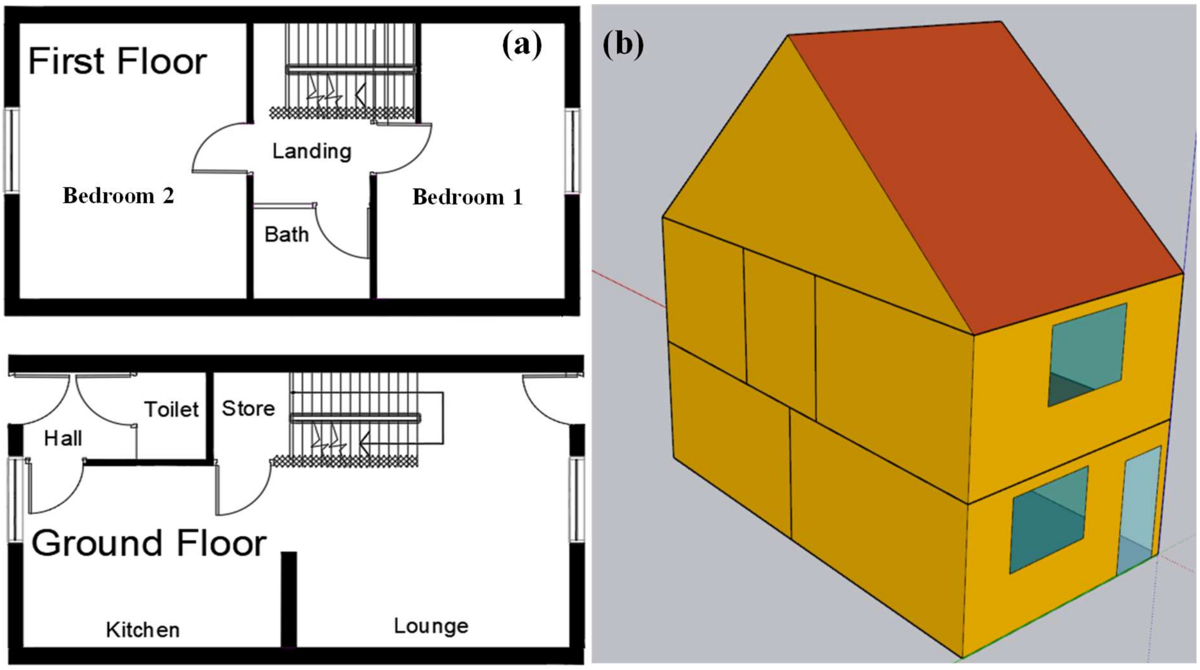

Figure 34. (a) layout of the studied semi-detached 2 bed-room house, (b) the schematic of the studied semi-detached 2-bedroom house

TRNSYS is a graphical simulation environment for transient systems. The objective of the TRNSYS building project was to assess the thermal energy demand and calculate the thermal peak loads of buildings. TRNSYS 18, a popular dynamic simulation programme, was used to create the model of this system. The tool is highly precise and reliable for assessing the energy demand of buildings and the scientific community considers it a standard tool for validating in-house building simulation models. TRNSYS 18's extensive library of components can properly replicate the energy performance of the building-plant system's components. The types within the TRNSYS environment are regarded as reliable and have been verified (Calise et al., 2020). In the energy model designed here, the house is assumed to be located in the center of London. Therefore, the weather station located in London central (Latitude: 51.51 - Longitude: -0.09) is selected in TRNSYS with the data obtained from the Meteonorm database (Remund et al., 2020).

3.8.4 Thermal Construction of the Building

The construction details employed in the studied building were selected from the CIBSE guide A – Part F: Environmental Design (Chapter 3-Thermal properties of building structures) (CIBSE Guide A, 2019). The constructions were presented in the CIBSE guide based on the Government's Standard Assessment Procedure for Energy Rating of Dwellings (SAP 10) **Error! Reference source not found.** presents the details of the construction material. The properties of all the employed materials were obtained from the CIBSE guide including density, thermal conductivity and specific heat. It should be noted that among many different types of construction as the typical wall construction in the CIBSE guide (Appendix 3. A8), the most insulated constructions (lowest u-value) were selected due to being closer to the future standards of the building.

Table 9. Details of the construction in different parts of the building

Unit	Description	U-value (W/m^2K)
External walls (Brick/lightweight aggregate concrete block cavity walls)	105 mm brick, 100 mm blown fibre insulation, 100 mm lightweight aggregate concrete block, 13 mm dense plaster	0.30
Internal wall (Party wall)	12 mm plasterboard, 22 mm airspace/battens, 100 mm lightweight aggregate concrete block, 75 mm airspace, 100 mm lightweight aggregate concrete block, 22 mm airspace/battens, 12.5 mm plasterboard	0.56
Pitched roof (insulated at ceiling level)	Waterproof roof covering, 100 mm polyurethane insulation, vapour control layer, 19 mm timber decking, unventilated airspace, 12.5 mm plasterboard	0.17
Ground floor	10 mm carpet/underlay, 19 mm timber or chipboard on 100 mm joists, ventilated underfloor cavity	0.76
Internal floor/Ceiling	19 mm timber flooring or chipboard on 100 mm joists, 12.5 mm plasterboard ceiling	1.64

Semi-exposed ceiling	12 mm plasterboard, airspace, 150 mm mineral wool quilt on 100 mm joists, 19 mm timber flooring or chipboard	0.2
Door	52 mm Hardwood	2.18

The windows for the proposed building were selected from CIBSE guide A, part F (chapter 3-Table 3.30) as a triple-glazed window with a 16 mm air gap with wood or PVC frame considering 30% window frame fraction presented with details in Table 9.

Table 10. Details of the glazing units used in the proposed building

Unit	type	Air layer thickness	U-value (W/m^2K)
External windows	Triple glazed (air filled-Low emissivity)	16 mm	1.4

3.8.5 Infiltration and natural ventilation

Infiltration and natural ventilation are the other important parameters that affect the heating load of the building noticeably. The equation from Building Research Establishment (BRE) (BRE, 2012) was used to calculate the air changes per hour by both fabric (infiltration) and deliberate ventilation as follow.

$$L_{sub} = (L_{fab} + L_{DV}) \times Sh_E \times Sh_D \times V_{wind}/4 \qquad (5)$$

where L_{fab} is the infiltration rate of building fabric (ACH-air changes per hour), L_{DV} is the deliberate ventilation (ACH), Sh_E is the site exposure factor, is the dwelling exposure factor and V_{wind} is the wind speed. The value of Sh_E is considered 0.95 as the proposed building is placed in the average exposure category, which includes partially sheltered urban and rural sites where there is some geographical reduction in local wind speed. According to the building's local shielding class, Sh_D is roughly 0.925 for the proposed structure. L_{fab} is determined aby the rea-weighted average of different building components. For the filled cavity wall, L_{fab} is 0.3 ACH. As most of the exposed building structure is the walls, the value of 0.3 is considered as the mean value. Natural ventilation is considered due to openable windows, flow through cracks or vents due to wind and buoyancy pressure. To model this, an open flue is considered for the main rooms, including the lounge, kitchen, toilet, bathroom and bedrooms, in which the airflow is 20 m^3/hour, according to the BRE report (BRE, 2012). The L_{DV} is then calculated by dividing the amount of airflow by the volume of the room.

The average wind speed in London, placed in the southeast of England, is 4.04 m/s according to BREDEM, and thus, the average infiltration rate from the fabric according to Eq. (5) is 0.27 ACH. Based on CIBSE guide A (Environmental design, Chapter 4: Ventilation and air infiltration), the empirical value for air infiltration for rooms in buildings on normally exposed sites in winter for dwellings with 2 floors is 0.25 for new dwellings considering the air permeability of 5 m^3/m^2h at 50 Pa showing a good agreement with the calculated data from BREDEM method.

3.8.6 CO_2 heat pump model

There are two main types of heat pump models found in the official TRNSYS library: performance-map models and thermodynamic models. In the first, the user specifies a finite number of working points at which the heat pump performance is estimated by the interpolation of experimental data; in the second, the model for the heat pump is derived from the simulation of the entire refrigeration cycle. In this study, the performance-map approach was adopted to assess the dynamic behavior of a heat pump system, utilising TRNSYS 18 for model development and simulation.

In order to evaluate the dynamic behavior of a heat pump system, the performance map of commercially available CO_2 AWHP was developed at Brunel University (CSEF laboratory) by executing a series of experiments at steady state conditions as shown in Figure 35. The nominal heating capacity and coefficient of performance (COP) were 2.3 kW and 1.5, respectively. TRNSYS was used to simulate the AWHP (Type 941) using the performance map that included heating capacity and power consumption data, which were functions of the ambient temperature ($T_{ambient}$) and return water temperature T_{return_water}) in the gas cooler. The heat pump supplied water to the radiators at a temperature of 57 °C to 60 °C.

A performance map approach is used to determine the energy performance of the black-box system, which is the Type 941 heat pump. The experimentally derived heating capacity and electrical power input of the heat pump are inserted in a look-up table as a function of ambient air temperature and the return water temperature in this approach. The model calculates the heating capacity and electrical power input needed by the system at each simulation timestep by performing linear interpolation inside the look-up tables using the input parameters ($T_{ambient}$, T_{return_water}). The operating mode of the heat pump is controlled by the input signal for heating operation (HS). When HS is active, the heat pump operates, whereas when HS is off, the unit remains inactive

The control technique of a heat pump, in addition to the temperatures of the source and sink, influences the energy performance of the system. Since the experimental arrangement used a variable speed compressor, this modelling technique assumes that the AWHP control logic is based on continuous compressor speed modulation to match the instantaneous thermal load demand, thereby maintaining stable supply temperatures.

With just two possible states in which the heat pump compressor can operate, the on-off controller is the most straightforward and suitable choice for controlling this system. Furthermore, because of this operational restriction, the heat pump can only match the building's thermal load requirements by performing a series of on-off cycles.

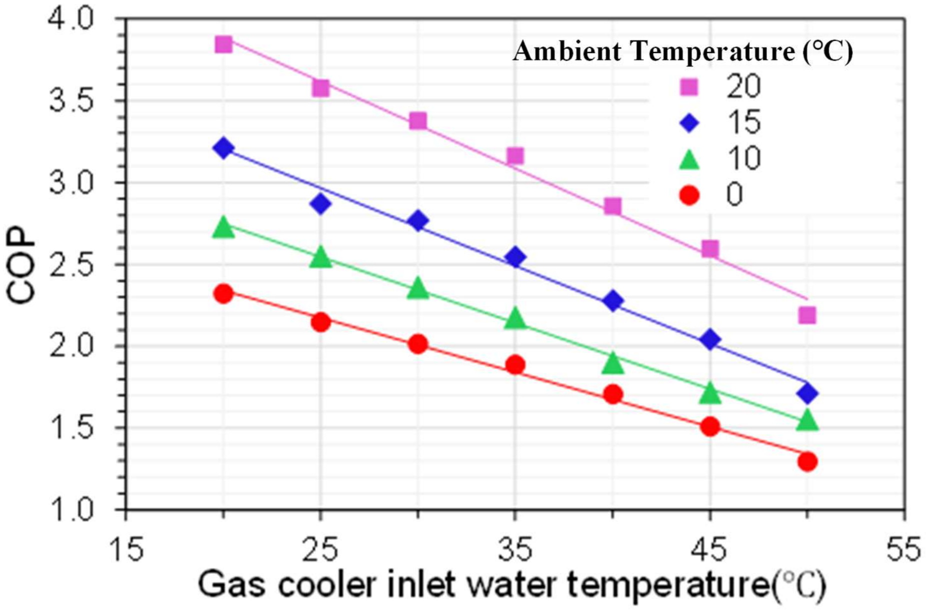

Figure 35. Performance map of CO2 AWHP

3.8.7 Domestic hot water demand profile

AWHPs are recognised as an efficient solution for domestic hot water (DHW) production in the building sector. In order to reduce the risk of Legionella spp., DHW must be heated to 60 °C to 65 °C in accordance with European regulations (Lee, 2018) and World Health Organisation (WHO) guidelines (Bartram, 2007). An average temperature increase of 45°C to 55 °C is necessary throughout the year, excluding seasonal variations, due to the fact that the inlet water temperature typically varies between 10 °C and 15 °C (EST, 2008). To guarantee hygienic safety, the DHW storage tank must be consistently maintained at 60 °C, particularly during standby mode (no flow conditions). At the end user's side, flowing DHW is generally consumed at 40 °C to

45 °C. Hot water daily use in residential buildings has been widely investigated and characterised in many research studies. Daily domestic hot water patterns typically present two prominent consumption peaks that occur in the morning and the evening and, less frequently, a peak in the afternoon (EST, 2008). This pattern is driven by higher water demand during specific times of the day, particularly in the morning when people wake up, in the afternoon when they return home from work or school, and in the evening before going to sleep. These peak usage periods contrast with the lower demand observed during other times of the day.

In most households, DHW usage exhibits both random and routine-based characteristics. Although individual water uses may occur unpredictably, overall demand is concentrated during periods of peak household activity, particularly in the morning and evening. The majority of DHW consumption is associated with sink use, which typically involves short-duration, low-to-moderate flow rates and often occurs in closely spaced intervals(Hendron et al., 2010). In terms of duration, the longest hot water extractions are typically associated with showers and baths, which predominantly occur in the morning and evening. Meanwhile, the most frequent category of draw events, lasting approximately 2–3 minutes, accounts for nearly 30% of all extractions. Regarding the distribution of hot water consumption across household appliances, field studies conducted in the UK indicate that approximately 70% of the total hot water volume is utilised for baths and showers, followed by consumption at bathroom basins and kitchen sinks (EST, 2008).

To calculate the hot water demand of the proposed building with 4 occupants, first, the hot water consumption profile is required. This data is gathered from the LEEDR project home energy dataset 24/04/18, which includes the measurement data for hot water consumption profiles for different types of buildings in the UK (Marini et al., 2019). The data was measured for 2 years, from 2012 to 2014, every one second. Based on the LEEDR monitoring dataset, the average hourly domestic hot water demand profile was derived from 12 months of recorded data. The 24-hour profile, illustrated in Figure 36, represents the mean hourly demand aggregated across four monitored dwellings, each occupied by four residents. The individual dwellings exhibited broadly similar temporal patterns, with comparable peak periods and demand distributions throughout the day, thereby justifying the use of an averaged representative profile. According to the measured data, the yearly average volume of hot water consumed in one day is 119.7 litres. This profile is used in the TRNSYS simulation for annual dynamic analysis to calculate the amount of required heat for domestic hot water demand in the proposed building.

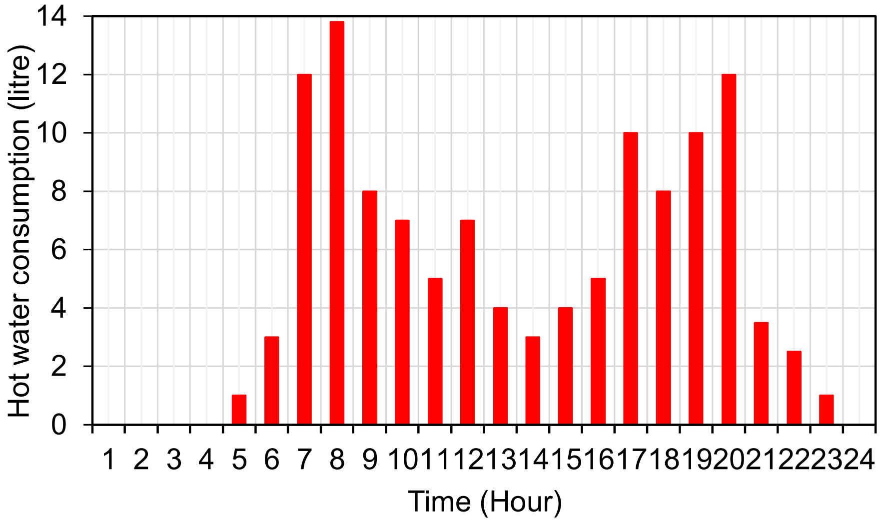

Figure 36. Average hourly hot water demand profiles derived from 12 months of measured data in LEEDR for 24 hours

3.8.8 Space heating plan

For space heating, the system is programmed to maintain an indoor air temperature of 20 ± 1 °C during the occupied periods of 05:00–09:00 and 15:00–23:00. This heating schedule is implemented exclusively during the winter season. Figure 37 shows the daily space-heating schedule used in the simulation model.

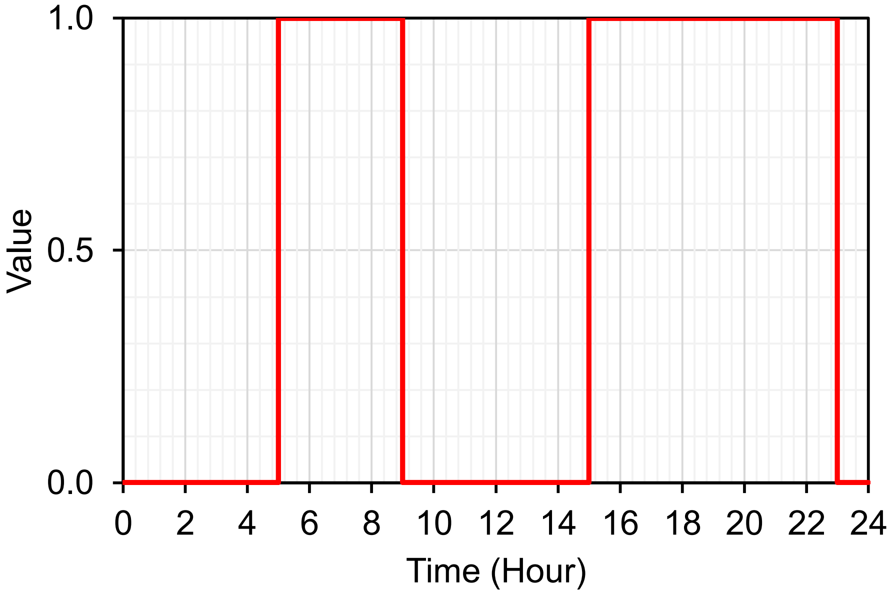

Figure 37. Schedule for space heating plan during the day

3.8.9 TRNSYS Model Development and Simulation Methodology

Figure 38 displays a schematic diagram of the whole system including the CO_2 heat pump, thermal energy storage (TES) tank, radiators, valves, and hot water system (shower and tap).

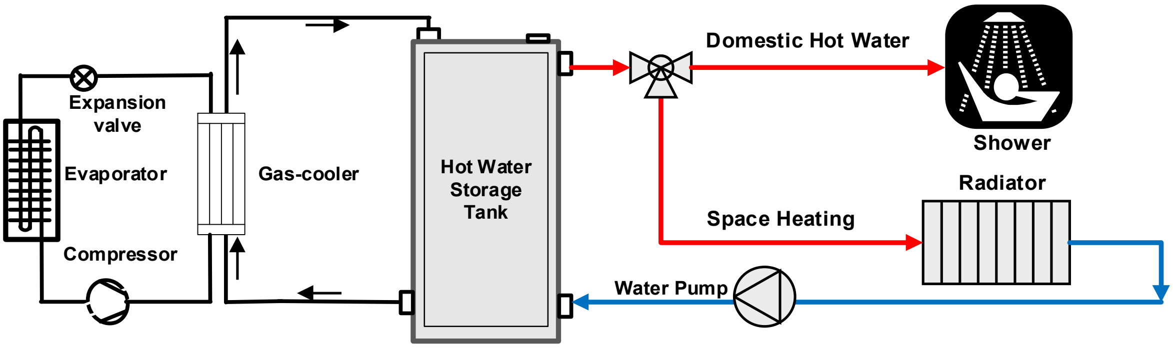

Figure 38. The schematic of the whole system

Figure 39 displays the TRNSYS model to calculate the required heating load demand for both space heating and hot water. It includes different components for space heating and hot water demands and also controllers and equations to control the system as well as printers and plotters to present the results. The hydronic circuit starts in the CO_2 AWHP, which distributes hot water to the space heating system (radiators) and to the domestic hot water (DHW) system through the storage tank. In the simulation, a hot-water radiator heating system (Type 1231) was evaluated for the central heating system. In the system, the heat was generated in CO_2 AWHP (Type 941) and distributed via heated water (heat carrier) to the radiators.

The Type 534 (cylindrical storage tank) component from the TRNSYS library was employed with a total storage volume of 200 litres (L), incorporating two inlet and two outlet flow ports. Specifically, the inlet ports were assigned for domestic cold water (DCW) supply and the return flow from the space heating radiators, while the outlet ports were configured for the delivery of domestic hot water (DHW) to the dwelling and the supply of heated water to the radiator circuit. The tank was modelled as a vertically stratified storage unit to accurately capture thermal layering effects and transient temperature variations within the storage volume. According to the data, the thermal loss coefficient of the tank is equal to 0.85 W/m^2K. The supply water temperature of the CO_2 AWHP unit was set at 60 °C. Two water circulating pumps (Type 114) were installed, with a supply flow rate of 0.4 kg/sec and a return flow rate of 0.06 kg/sec, to transfer hot water from the storage tank to the radiators and the heat pump. To regulate the system, two on / off differential temperature controllers (Type 1502 and Type 106) were used. The temperature in the room was monitored by one controller (Type 1502), while the hot water tank temperature was tracked by a second controller (Type 106). When the water temperature in the water tank reaches the pre-set temperature of 60 °C, the water pump 1 (Type-3) and CO_2 AWHP unit will shut off and restart when the temperature drops by 5 °C. Additionally, the upper dead band and the lower dead band were both set to 1 °C, and the room temperature was maintained at 20 °C. When the temperature in the room was between 20 ± 1 °C, water pump-2 was switched off; when the temperature dropped 1 °C below the setting room temperature, the pump was turned back on.

Moreover, the control logic of the DHW system, including signal controls and activation timespans, was modelled by employing the equation/calculator unit, the schedule (Type 14). Furthermore, for the DHW (showers and wash basins) the Type 709 model was employed and tee piece (Type11) and diverting valve (Type 647) were adopted for mixing and diverting valves, respectively also it was assumed in the simulation the piping network friction losses were zero. In order to ensure the simulation's stability and convergence, a time step of 4 minutes was employed in this modelling. All these simulation parameters are emulated from original experiments.

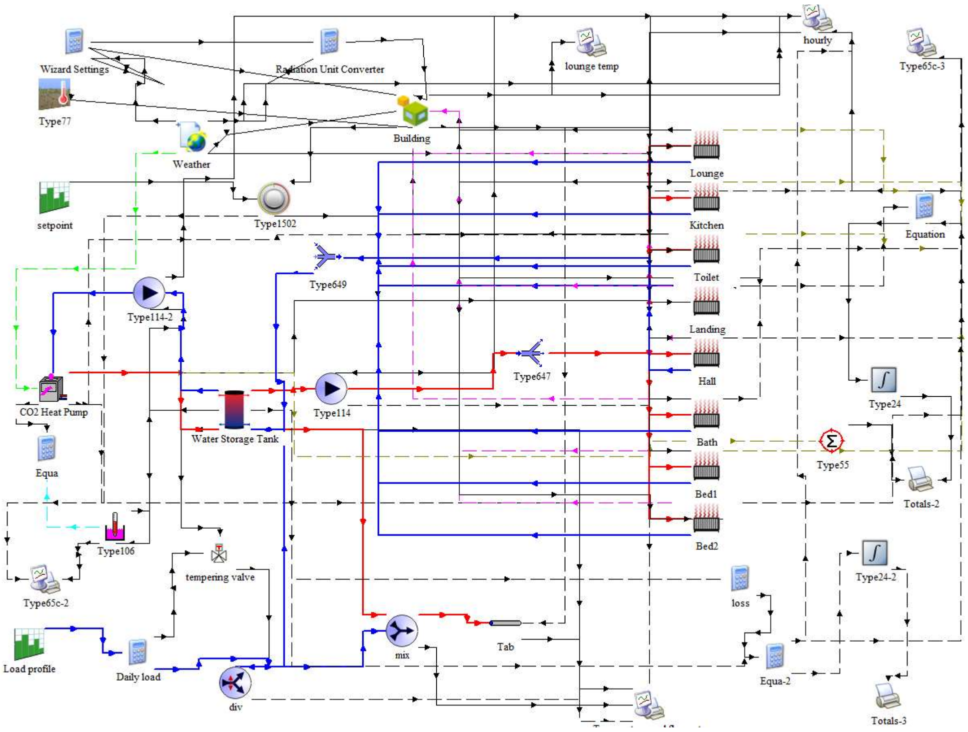

Figure 39. TRNSYS simulation model

3.9 Simulation results and discussion

3.9.1 Yearly evaluation of the system

During the heating season, the system's performance is evaluated in terms of its DHW load coverage over the entire operating season and its space heating (SH) contribution.

For the space heating and thermal energy storage (TES) tank, ten radiators are defined for different rooms of the building, including the living room, kitchen, bedrooms, toilet, hall, landing, and bathroom. The design temperature of the radiator's surface is also set to 55°C. The flow rate of 0.2 kg/s is chosen for the flow rate of water from the TES tank to the radiators through a single-speed pump. This flow is divided for the eight employed radiators by the fluid-diverting valve after the pump. As the areas of the living room and kitchen are higher than the other rooms, the fraction of the flow to the living room and kitchen is considered 0.15 kg/sec, while it is 0.1 kg/sec for the other rooms. For example, the flow rate of hot water to the radiators in the living room and bedroom 1 is determined at 0.045 kg/sec and 0.03 kg/sec, respectively. The water returned from the radiators is mixed by a mixing valve, which is then returned to the storage tank to heat up again.

SH demand is determined by the temperature of the house's internal space. SH is implemented in this configuration by employing a thermostat to activate the heating system when the internal space temperature falls below 19 °C and to deactivate it when the internal space temperature exceeds 21 °C (20 °C is recommended by Public Health England for comfort and minimising health risks in winter (Wookey et al., 2014)). A thermostat (Type 1502) is placed in the living room as the main room of the building to control the behaviour of the storage tank through the pump. The setpoint temperature of the thermostat is set to 20 °C as the thermal comfort temperature with the temperature dead band of ±1 °C. This means that when the temperature reaches below 19 °C, the pump is turned on and circulates hot water into the radiators. When the room temperature reaches 21 °C, the pump is turned off. The controller signal does not change until the room temperature reaches the setpoint plus or minus half of the dead band again. The thermostat has a lockout signal, which enables the definition of a schedule for the heating system. The schedule for space heating is defined previously in Figure 37.

The design capacities of the radiators are obtained based on heat load demand calculations when the heat setpoint temperature of 20 °C is enabled for 12 hours a day based on the defined schedule (from 5.00 to 9.00 and 15.00 to 23.00). The capacity of the radiators equals the maximum heat load demand during the year. Note that the internal heat gains are ignored when selecting the capacities of the radiators. The peak design heat loss was 7.34 kW. Also, the domestic hot water (DHW) heating load was calculated, and it was constant throughout the year at 2 kW, as shown in Figure 40. Table 10 presents the design capacity of different radiators inside the house.

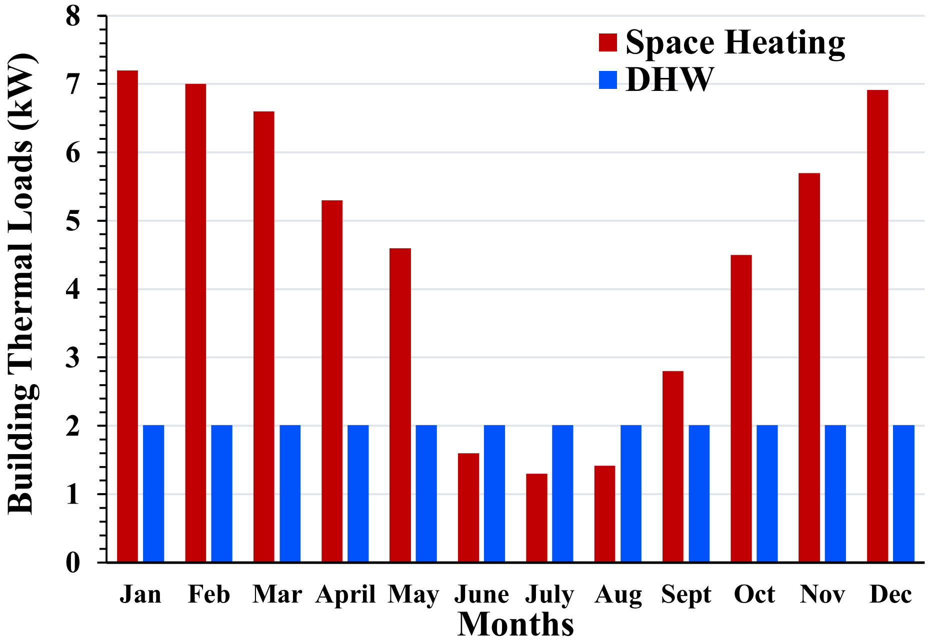

Figure 40. A monthly basis building loads (space heating and DHW)

Table 11. Design capacity of different radiators inside the building

Room	**Design capacity (W)**
Living room	2300
Kitchen	1400
Toilet	500
Hall	530
Bed 1	1100
Bed 2	1000
Bath	510
Total	**7340**

A 200-litre TES tank is used for space heating and domestic hot water. The setpoint temperature for the TES tank is 60 °C. A thermostat is placed at 2/3 height of the storage tank, and its temperature is connected to the controller with a dead band of ±5 °C. This means that when the thermostat's temperature reduces to less than 55 °C, the pump starts working until the temperature reaches 65 °C.

A tempering valve is used to control the hot water temperature for the tap. The tempering valve mixes the hot water outlet of the tank and cold water through a mixing valve to adjust the temperature to 45 °C during the hot water usage. Note that the heat loss from the pipes is not considered in the calculations and the temperature of hot water after the mixing valve and tab are similar. The temperature of cold water draw-off is considered 10 °C. The domestic hot water (DHW) load was calculated to be 1.78 kW, as specified in Table 11. The hourly DHW demand profile previously illustrated in Figure 36 was subsequently implemented as an input to the simulation model in order to determine the corresponding hot water mass flow rate through the thermal energy storage (TES) tank and the tap outlet under dynamic operating conditions..

Table 12. The characteristics of hot water demand calculation

Characteristics	**Value**
Domestic hot water load	1780 W (1.78 kW)
Setpoint temperature	60 °C

Figure 41 illustrates the temperature in the living room compared with the ambient temperature during the year. As previously mentioned, the indoor air temperature is maintained within a comfort range of 19°C to 21°C during the space heating system's scheduled operating hours. This temperature range is maintained by thermostatic control, which activates the heating system when the room temperature falls below 19 °C and deactivates it or reduces it when it approaches 21 °C, thereby ensuring thermal comfort while minimising unnecessary energy consumption. During the unheated hours, it drops to lower temperatures during winter. As shown, the minimum temperature inside the room is 13°C while the room’s temperature is usually not less than 16°C. During the summer, when the ambient temperature is higher than the pre-defined temperatures as the thermal comfort temperature, the maximum room’s temperature is around 27 °C while it is usually less than 25 °C.

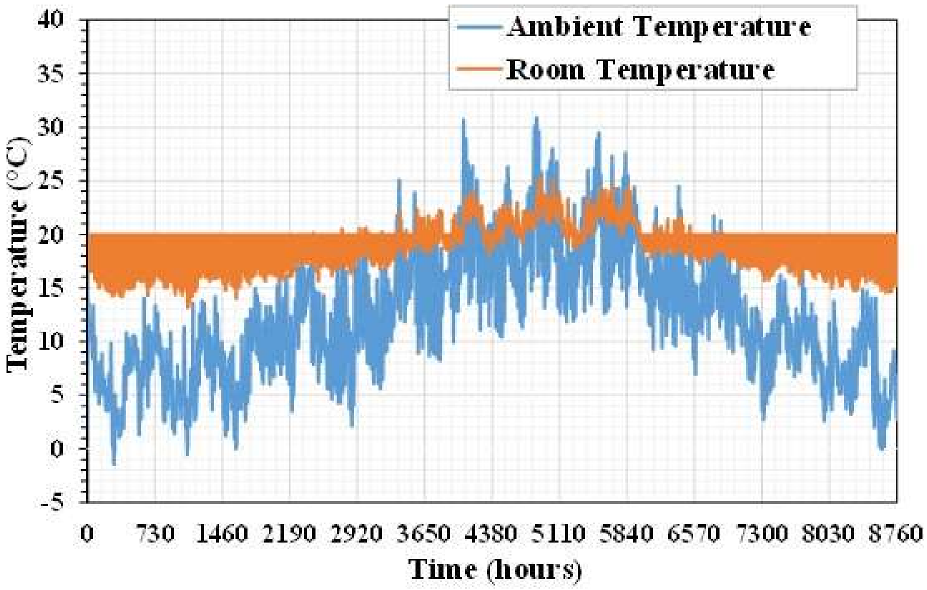

Figure 41. The variation of room's temperature as well as ambient temperature during a year

Table 12 shows the annual heating demand for different rooms of the building as well as the input energy from the heat pump to the TES tank and the heat lost from the tank. Note that a little difference between the heat pump energy input and the sum of heat loss and heat required for the radiators still remains as the stored heat in the tank. According to the data, almost 6.75% of the energy delivered from the heat pump is lost during the year.

Table 13. Annual heating demand for different rooms of the building and domestic hot water

Room	Annual heating load (kWh)
Living room	1200
Kitchen	1000
Toilet	210
Hall	255
Bed 1	958
Bed 2	970
Bath	297
Landing	240
Total heat required in the radiators	5130
Hot water demand	1780
Heat lost from the tank	500
Heat pump energy to the tank	7410

Table 13 presents the total heat produced by the heat pump, heat pump power, compressor power, and maximum and average COP of the heat pump. The maximum COP of the system was 2.80 while the average annual COP, which was calculated by dividing the total generated heat by the heat pump power, was 1.80.

Table 14. Annual thermal energy and power as well as maximum and mean COP of the heat pump

	Value
Total generated heat (kWh)	7410
Compressor power (kWh)	3818
Heat pump power (kWh)	4100
COP (maximum)	2.80
COP (average)	1.80

3.9.2 CO_2 emission and operating cost analysis

The electricity required to operate the heat pump was provided from the national grid. According to the UK government report on greenhouse gas emissions, the CO_2 emissions for domestic energy usage in 2023 are 0.205 kg of CO_2e per kWh of electricity and 0.183 kg of CO_2e per kWh of gas (Bramwell et al., 2023). Therefore, considering the current carbon footprint of electricity generation, Table 5 presents a comparison of the heat pump employed in this study and a conventional boiler as the heat source. It should be noted that to provide 7410 kWh of thermal energy by a conventional boiler with an efficiency of even 90%, 8233 kWh of energy should be provided. As shown in Table 14, the CO2 emission produced by the heat pump system is around 44 % less than that produced by the conventional boiler system.

Table 15. Annual CO_2 emission of the proposed CO_2 heat pump compared with a conventional boiler system

	Required energy (kWh)	CO_2 emission (kg)	Annual operating cost (£)
CO_2 heat pump	4100 (electricity)	841	1361
Boiler	8233 (gas)	1507	848

Table 14 also presents the annual operating cost for the CO_2 heat pump compared with the conventional boiler system based on the current tariffs in the UK. The average net selling value of gas and electricity for the domestic sector in the UK in 2023 is 10.3 pence/kWh and 33.2 pence/kWh, respectively (Bramwell et al., 2023). According to the current tariffs, the annual operating cost of the CO_2 heat pump is £513 higher than that of the conventional gas boiler.

3.9.3 Optimum sizing of thermal energy storage tank

The thermal energy storage (TES) included in this study is a typical domestic hot water tank with a 150-litre (L) to 300-litre (L) volume range. In this comprehensive analysis, the focus was on investigating the impact of a TES tank on a heat pump system. The simulations were conducted by keeping the capacity of the heat pump unit constant at 2.3 kW while systematically changing the volume of the TES tank. Four different thermal storage systems, each with volumes of 150, 200, 250, and 300 L, were scrutinised to assess their influence on space heating (SH), domestic hot water (DHW) systems. A ±5 °C dead band was applied around the TES tank, allowing for a range of temperatures before the system triggered actions. Additionally, a ±1 °C range was set around the desired indoor thermal temperature, providing a tolerance level for the system's performance.

The findings, presented in Figure 42, provided a detailed insight into the annual values associated with the AWHP-generated heat, TES tank heat loss and the energy delivered from the heat pump to both radiators and DHW. As the storage tank's capacity increased, the energy required for the DHW system remained constant. However, it was noted that heat loss from the TES tank experienced an anticipated escalationfrom 500 kWh for a 150 L tank to 750 kWh for a 300 L tank capacity. This was attributed to the larger tank capacity demanding more heat to attain a temperature of 60 °C within the storage tank.

The total heat required in the thermal energy storage system fluctuated from 7410 kWh for a 150 L storage tank to 7930 kWh for a 300 L storage capacity. Consequently, the heat generated by the heat pump for space heating exhibited an increase from 5130 kWh to 5400 kWh when transitioning from a 150 L to a 300 L storage tank. This underscores the direct correlation between TES tank capacity and the heat pump's performance.

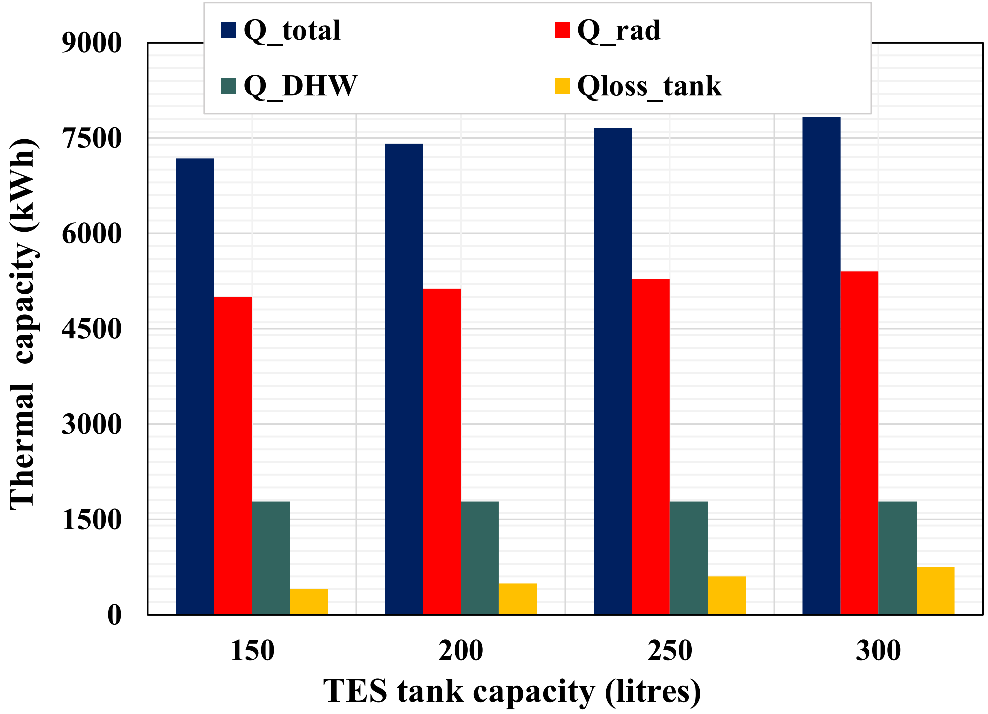

Figure 42. The total annual heat generated by the AWHP (SH & DHW) and the heat loss in the storage tanks for different storage tank

To assess the system's ability to maintain thermal comfort within the building, the fluctuation of room temperature in the living room was selected as the criterion over a specific period — 10 days from January 10th to January 20th, spanning from 240 hours to 480 hours. It is noteworthy that, as depicted in Figure 43, these 10 days represent the coldest period of the year, as identified from the Test Reference Year (TRY) weather file used in the simulation.

Figure 43 illustrates the variation in the living room's temperature over the 10-day period for different capacities of thermal energy storage (TES) tanks, along with the ambient temperature. For the system with a 150 L capacity, the room temperature falls below 20 °C throughout the 10 days. However, for systems with TES capacities of 200, 250, and 300 L, the temperature consistently fluctuates between 19 °C to 21 °C throughout the scheduled space heating periods.

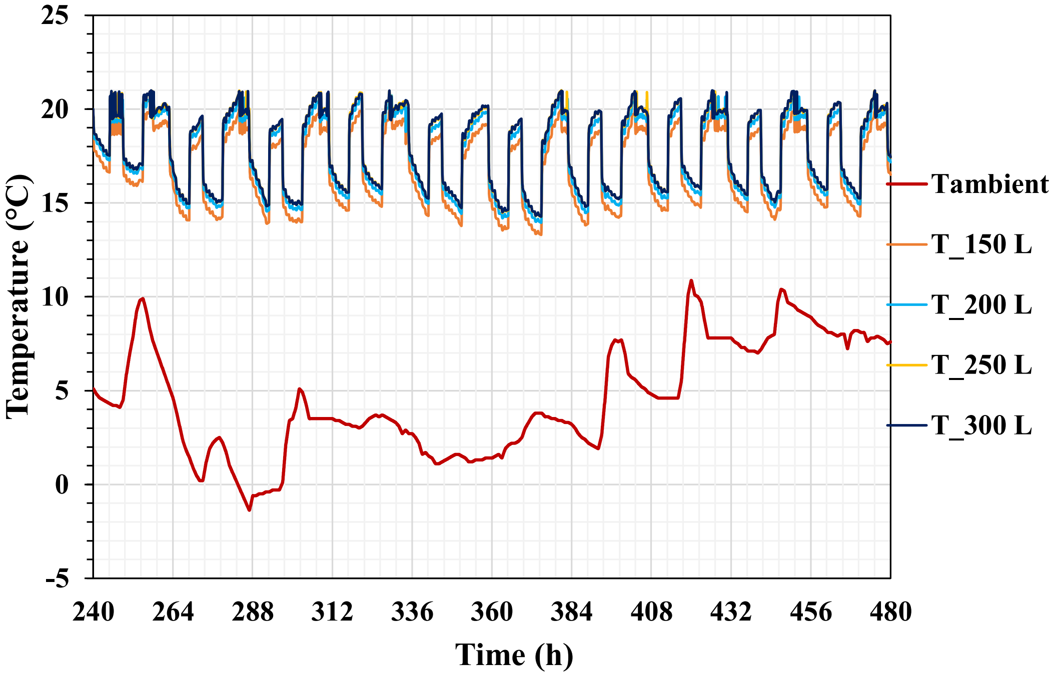

Figure 43. The variation of living room's temperature for different storage tank

The storage tank 150 L found it challenging to maintain the living room's temperature even at 19 °C, indicating that this system was incapable of maintaining the required thermal comfort temperature within the building. This was a result of the lower outdoor temperature and higher heating demands of the house. It should be noted that the 200, 250 and 300 L storage tanks always maintained the living room's temperature between 21 °C and 19 °C during the coldest time and the scheduled space heating operation. Considering the lower cost of the system and the smaller volume of the storage tank, thereby saving more space, the system with a 200 L storage tank is recommended. This choice is optimal as it meets the thermal comfort requirements while being more cost-effective and space-efficient using the minimum volume suggested by the heat pump manufacturer. The proposed operating savings, however, are likely to grow in significance relative to the equipment acquisition costs in light of the worldwide trend in energy prices.

Conclusions

This research involved studying the performance of a commercially available transcritical CO_2 air-to-water heat pump (AWHP). A wide range of performance data was experimentally measured, such as the COP, heating capacity, electrical power consumption, compressor discharge pressure, compressor discharge temperature, and refrigerant mass flow rate through the compressor. The performance data for the heat pumps were collated for the ambient air temperatures of 0 °C, 10 °C, 15 °C and 20 °C at different return water temperatures ranging from 20 °C to 50 °C. From the above experimental results, the following conclusions can be derived. The evaporator side air inlet parameters have little effect on COP. The gas cooler side water inlet temperature is the main influencing factor.

In this modelling, transcritical CO_2 AWHP was investigated and integrated with a thermal storage tank to provide the heating demand for both space heating and hot water in a two-bedroom house with 4 occupants. The whole system was modelled using TRNSYS 18 software on a daily and yearly basis, comprehensively. The following results were the key outcomes of this study: (a) Comparing different volumes of thermal heating storage tanks with the heat pump capacity of 2.3 kW it was observed that a 200 L storage tank was capable of meeting the heating demand and comfort temperature required inside the house. (b) The annual thermal energies required for space heating and domestic hot water demands were 5130 kWh and 1780 kWh, respectively, while the energy obtained from the 2.3 kW heat pump with 300 L tank for space heating and domestic hot water were 5400 kWh and 1780 kWh respectively. Also the heat loss from the tank was 750 kWh . (c) The heat pump required electrical power of 4100 kWh and the maximum and mean COP obtained were 2.80 and 1.80 respectively. (d) Compared with a boiler system with an efficiency of 0.9 and based on the current tariffs for the CO_2 emission and operating cost; the heat pump system produced around 44.2 % less CO_2 emissions annually; however, the operating cost of the heat pump system was £513 per year higher than that for the boiler system. (e) The performance evaluation presented in this study for an integrated CO_2 heat pump with thermal storage might help towards heat electrification in the near future as the main pathway for different countries to achieve heat decarbonisation and thereby net-zero goals.

Chapter 4 4.5 kW CO_2 heat pump experiments and four bedroom house simulation

4.1 Introduction

This chapter focuses on a 4.5 kW air-to-water heat pump (AWHP) employing CO_2 as a natural refrigerant, developed within the CSEF. This heat pump aims to contribute to energy savings in both new and existing homes in the UK, serving as a replacement for traditional boilers. Like the 2.3 kW heat pump, the experimental results from this system were employed to generate a heat pump performance map. This map is then used to create a new TRNSYS heat pump model, facilitating the assessment of the 4.5 kW AWHP's performance for space heating and domestic hot water in a four-bedroom house in the UK.

The chapter commences with a comprehensive overview and schematics of the experimental setup, followed by a detailed examination of the major components integrated into the system. The heating performance, electric power and COP of the transcritical CO_2 heat pump were measured by varying the return water temperature, ambient air temperature and compressor speed (RPM). Subsequently, the chapter delves into the presentation and analysis of experimental results. Additionally, it offers insights into the data acquisition system, the installed sensors within the setup, and a thorough analysis of uncertainties associated with the study.

4.2 Description of CO_2 air-to-water heat pump (AWHP)

Figure 44 illustrates the piping and instrumentation (P & I) diagram of the 4.5 kW transcritical CO_2 air-to-water heat pump (AWHP), designed and developed at the Centre for Sustainable Energy Future (CSEF) laboratory at Brunel University London. The transcritical CO2 AWHP incorporates a two-stage rotary hermetic compressor, a flash tank, two electronic expansion valves (EEVs), a needle valve, two 3-way reversing valves, a brazed plate heat exchanger (gas cooler), a fin-and-tube outdoor heat exchanger (evaporator), an oil separator, and an internal heat exchanger (brazed plate). The needle valve, located in the vapor injection line, facilitates on/off control of the injection stream entering the compressor. The heat pump system can operate in either a vapor injection cycle or a non-injection cycle, depending on the system's requirements (the conventional cycle). The system functions in a non-injection cycle referred to as the conventional heat pump cycle when the needle valve is closed and the compressor engages in single-stage compression. Additionally, the two 3-way valves are strategically positioned to enable the system to operate in both conventional cycles, with or without the internal heat exchanger (IHX). The experimental plant was specially protected by setting the limits for the compressor discharge pressure (P ≤120 bar) and temperature (T ≤130 ◦C). The lubricant that was carried by the CO_2 refrigerant was reintroduced into the compressor via an oil separator. Table 15 provides the specifications of the main components.

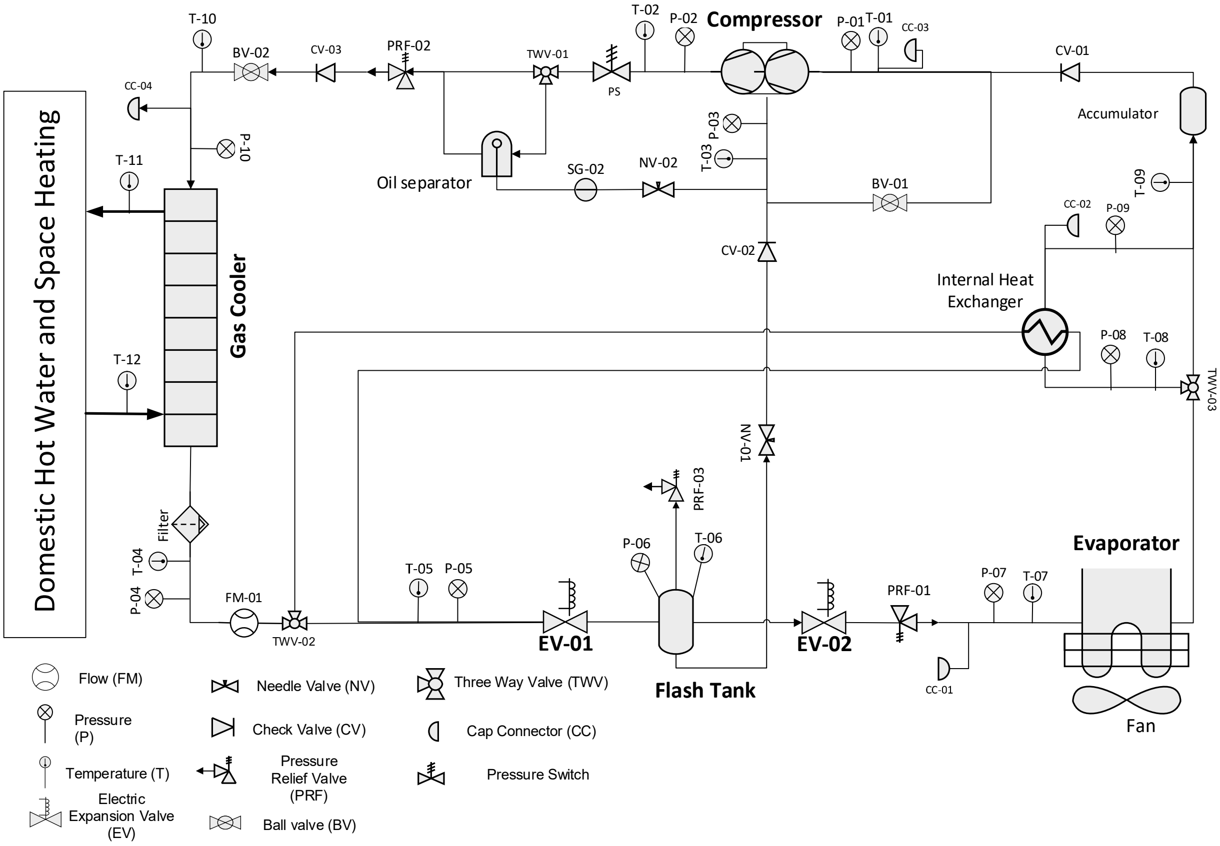

Figure 44. Schematic of the 4.5 kW CO2 heat pump

Table 16. Detailed parameters of system components

Name of components	Type	Description
CO_2 compressor	Rolling piston 2-stage hermetic	Nominal heating capacity: 6.42 kW Nominal electric input: 2.27 kW Speed range: 2400 RPM to 4800 RPM
Gas cooler	Brazed plate	Material: Stainless Steel Maximum numbers of plates: 60 Maximum flow: 2.5 m^3/hmm
Evaporator	Fin-and-tube	Copper tube (CO_2) Tube diameter: 5 mm Maximum row: 74 H x W x D: 588 x 800 x 36.4 mm
Expansion device	Electronic type	Maximum temperature: 70 °C
Centrifugal blower	Fan	Flow rate: 1800 m^3/h

4.3 Experimental setup and test procedure

The experimental plant was primarily composed of four main sections: the transcritical CO_2 air-to-water heat pump (AWHP) cycle, the water loop, the environmental chamber, and the outdoor heat rejection fan, along with the control and data acquisition system. The transcritical CO_2 AWHP cycle consisted of a two-stage rotary compressor, a gas cooler, an electronic expansion valve (EEV), an evaporator, an oil separator, and a flash tank. In the water loop, a variable outdoor air-cooled heat exchanger, controlled by a PI controller, regulates the fan speed to maintain the inlet water temperature at the gas cooler across varying conditions. The water flow rate was controlled by adjusting the variable frequency water pump and gate valve. The water inlet temperature was maintained within the range of 25 °C to 50 °C, while the ambient temperature in the environmental chamber was kept between 0 °C and 30 °C. Finally, the measuring instruments are marked in Figure 44, and the detailed uncertainties of the experimental parameters used in this study are shown in Table 16. Furthermore, a computer-based data acquisition system was utilized to collect data during the heating performance test. Table 17 shows the test conditions used in the experiments.

The thermocouples and pressure transducers were employed to measure the necessary pressure and temperature for the system's control and performance evaluation. The thermocouples employed in the experiment had an accuracy of ±0.5 °C, while the pressure transducers demonstrated an accuracy of ±0.25% of full scale. The Coriolis effect flow meter was used to measure the refrigerant mass flow rate, resulting in a high level of accuracy with an uncertainty of 0.2%. The volume flow rate was determined on the water side by employing a magnetic flow meter with an uncertainty of 3%. Inverters were employed to regulate the speeds of the compressor and evaporator fan. A digital power meter was used to measure the actual power input to the compressor's inverter over a period of time in order to calculate the COP. Relative humidity, temperature, and volumetric flow rate were employed to determine the air's heating capacity. Use of a manometer was implemented to quantify the airflow rate. Heat rejection on the high-pressure side was determined by analysing the temperature difference and flow rate of the cooling water that circulated through the gas cooler. All experimental tests were performed at steady state conditions at a fixed water outlet water temperature of 60 °C.

A schematic diagram and picture of the experimental setup are presented in Figure 45 and Figure 46, respectively. The main goal of these tests was to observe the state points under different settings and evaluate the heat pump's performance. No cold water was added to the system during testing, and no hot water withdrawals were conducted because the study was limited to the heat pump's response to increasing water inlet temperatures. Initially, cold water was filled into the system (piping and outdoor heat exchanger) from the cold water supply. Once the system was filled, the valves connecting the main water line were closed, and the valve at the gas cooler inlet was opened. The heat pump was then activated, followed by the activation of the water pump, with the flow rate measured after air was purged from the vent valve. The heat pump subsequently drew water from the outdoor heat rejection fan, circulating it through the gas cooler where it was heated before returning to the outdoor fan, where the heat was rejected. The heat pump continued operating until the entering water temperature reached 50 °C, at which point it automatically deactivated. Across all tests, the ambient air temperature remained constant, whereas the water inlet temperature varied dynamically between 20 °C and 50 °C. This process was repeated for different ambient air temperatures, enabling performance evaluations across a wide range of operating conditions. Throughout the testing phase, temperature, flow rate, and power consumption were continuously recorded at 5-second intervals using a data acquisition system, ensuring high-resolution data collection for comprehensive performance analysis.

The start-up and shutdown of the experimental platform, along with the set water temperature of the water tank manually controlled and compressor speed and EEV opening, are all controlled by the control system. The experiment uses a variable-speed compressor that is controlled by a frequency converter to generate hot water. During start-up, the compressor speed is increased to reach the target water temperature as fast as possible. After reaching its maximum speed, the compressor continues to operate at full load. As the system water temperature approaches the set target, the frequency is gradually reduced until the compressor shuts down.

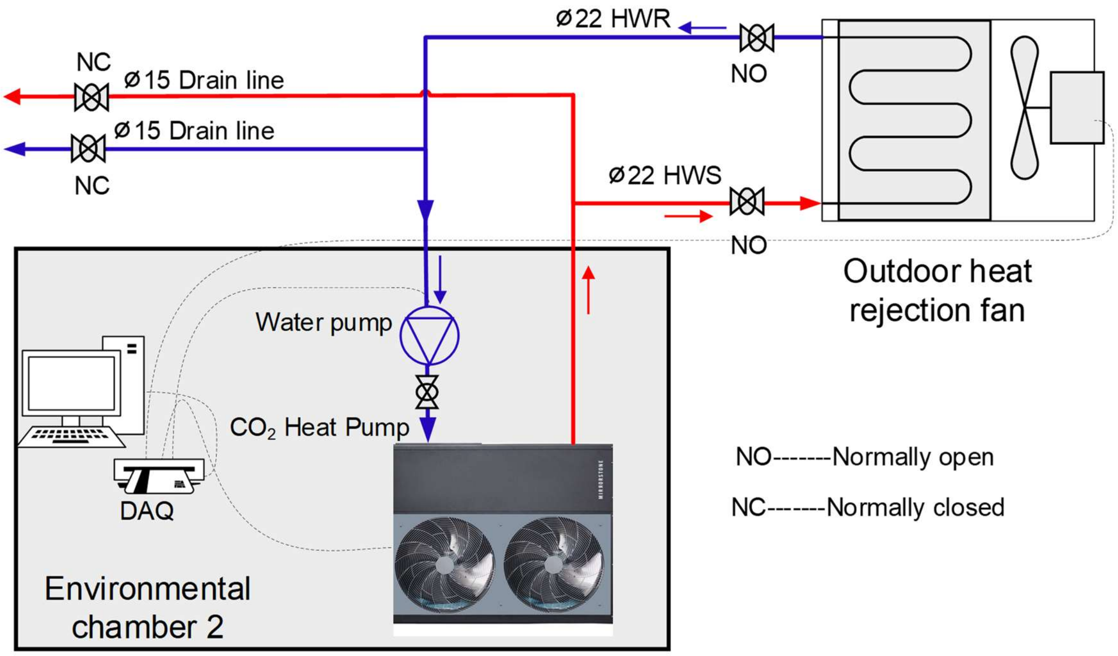

Figure 45. Experimental schematic

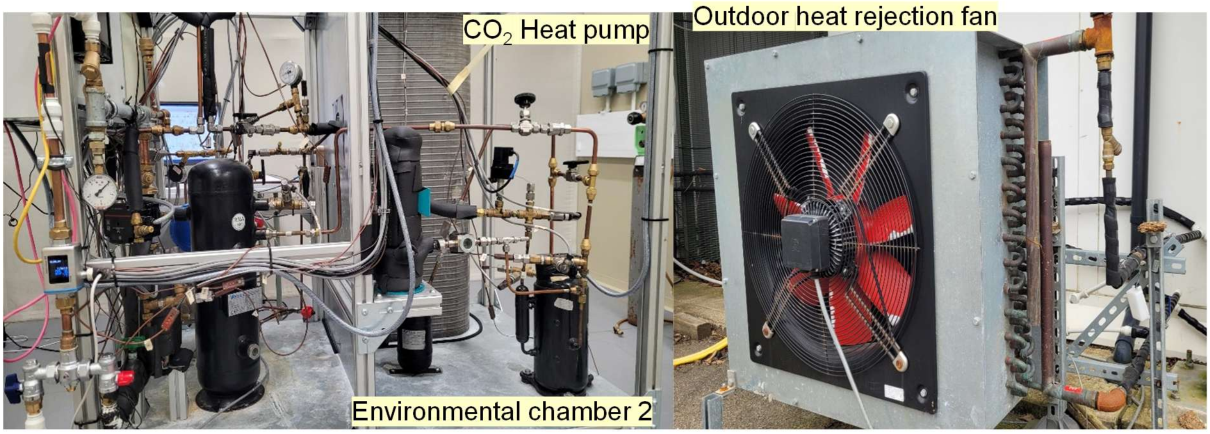

Figure 46. Picture of experimental setup

Table 16. Data Input Signals

	Components	Quantity	Type
1	Pressure Sensors	10	4-20 mA
2	Temperature Sensors	20	Thermocouples
3	CO_2 mass flow meter	1	4-20 mA
4	Water flow meter	2	4-20 mA
5	Fan speed	2	0-10 V
6	Power consumption	3	-
7	Air velocity meter	1	4-20 mA
8	Compressor Run signal	1	Digital
9	Compressor inverter ready	1	Digital

4.4 Data Monitoring and Collection

To characterise the performance of the commercial CO_2 heat pump unit, a data monitoring and acquisition system was implemented. The collected data was essential for developing a performance map, which was subsequently used to analyse the system's efficiency and operational behavior under varying conditions. To achieve this, a compact data acquisition (DAQ) system, control cards, and LabVIEW software were integrated to establish a computer interface capable of both monitoring and controlling the experimental apparatus. This setup enabled real-time data collection, facilitating precise performance evaluation and ensuring the system operated within the desired parameters.

4.4.1 Data acquisition devices

A compact NI cDAQ-9133 chassis was employed as a communication interface between different equipment components and the external computer system through input/output (I/O) modules. This communication was managed by multiple timing engines, allowing the simultaneous control of up to eight different hardware modules, each operating at independent sampling rates. To ensure reliable and efficient data transmission, the data acquisition (DAQ) system was connected to the laboratory computer via an Ethernet cable, providing a stable and high-speed communication link. The selection of this DAQ system was primarily driven by its intuitive graphical interface in LabVIEW, which allows seamless real-time control and monitoring of the I/O modules. Unlike traditional DAQ chassis, which often require additional configuration steps to set up virtual inputs and outputs, the NI cDAQ-9133 provides a streamlined and user-friendly integration process, allowing for direct data acquisition and efficient system control.

A variety of I/O modules were employed to facilitate essential control functions and data acquisition for the experiments. The I/O modules integrated into this setup included binary input, binary output, analogue input (AI), analogue output (AO) and a thermocouple module. The binary input signals were collected from the power monitoring system and pulse-generating devices, such as the water flow meter or refrigerant mass flow meter. These pulse signals were processed within LabVIEW, where they were converted into power readings or flow rate measurements using device-specific conversion equations. Meanwhile, binary output signals were generated by the DAQ module and distributed to various system components and instruments, primarily serving on/off control functions. The AI signals were acquired from various sensors via current or voltage signals, which were then communicated to the DAQ system. These signals were utilised in Proportional-Integral (PI) control loops for real-time data collection and system regulation. The AI channels were responsible for collecting data from all installed sensors, with the exception of thermocouples, which were measured separately using a dedicated thermocouple module to ensure accurate temperature monitoring.

The NI 9203 is a versatile combination voltage and current input module, featuring eight channels for ±20 mA current input and eight channels for ±10 V voltage input. This module is primarily used for high-accuracy data acquisition, particularly in industrial and laboratory applications where precise analog signal measurement is required. In this study, the NI 9203 was utilised to measure the flow rate through its current AI channels, which are commonly used for 4–20 mA industrial flow sensors. The module’s high resolution and fast sampling capabilities ensured accurate and reliable data collection, facilitating real-time monitoring and control of the system’s flow dynamics. Temperature readings were acquired using the NI 9214 AI module, which offers eight input channels and a 24-bit resolution, specifically designed for K-type and T-type thermocouples. These devices are shown in Figure 47. The installation details of the DAQ system are also presented in Figure 48. The output signals, both digital and analogue, are presented in Table 17, while the specifications of the National Instruments (NI) modules used for data acquisition are provided in Table 18.

Figure 47. Data acquisition devices

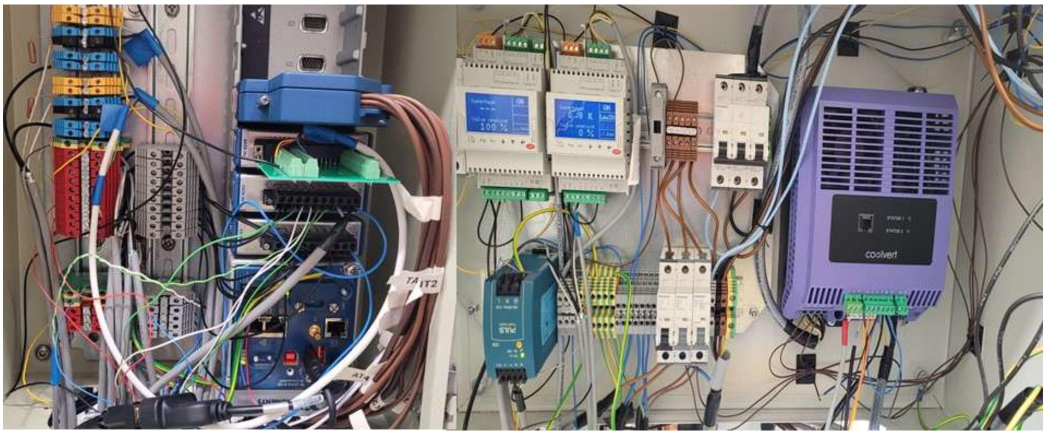

Figure 48. Data acquisition system

Table 17. Output Signals Digital and Analogue

	Components	**No.**	**Digital and Analogy**
1	Compressor (on/off)	1	Digital (D)
2	Compressor (speed)	1	Analogue (A)
3	Expansion valve	2	Analogue (A)
4	Solenoid valve (on/off)	1	Digital (D)
5	Fans (on/off)	2	Digital (D)
6	Fans (speed)	2	Analogue (A)
7	Water pumps (on/off)	2	Digital (D)
8	Water Pumps (speed)	2	Digital (D)

Table 18. Specifications of NI Modules Used for Data Acquisition

	Part ID	**No.**	**Application**	**No.of Channels**	**Type**
1	NI 9375	1	DI and DO	16 (DI)/16 (OD)	24 V
2	NI 9226	1	RTD Analogy Input	8	250 Vrms CAT
3	NI 9209 with DSUB	1	Analogy Input	32	± 10 V
4	NI 9203	1	Analogy Input	8	± 20 mA
5	NI 9264	1	Analogy Output	16	± 10 V
6	NI 9214	2	Thermocouple Input	16	250 Vrms CAT
7	NI TB-9214	2	-	-	250 V CAT
8	NI 9207	1	Analogy Input	8 and 8	± 10 V and ± 20 mA

4.5 Uncertainty analysis

An uncertainty analysis was conducted to assess potential experimental errors associated with the measurement instruments and operating conditions. This analysis follows the same methodology described in Section 3.5. The primary objective was to evaluate the uncertainty of the COP, which is calculated based on the heating capacity (Q) and electrical power input. Since Q is determined from measured temperature differences and mass flow rates, uncertainties arising from temperature sensors and flow meters were considered. The individual measurement uncertainties were combined using the error propagation method proposed by Taylor (1997) to estimate the overall uncertainty in COP. High-precision instruments were used to minimise measurement deviations.

4.6 Experimental conditions

The testing protocol for the CO_2 AWHP system, as outlined in BS EN14511-2:2022, was strictly followed regarding methodology, sensor specifications, number, and measurement accuracy standards. The environmental chamber's ambient conditions were regulated by a specialised outdoor air handling unit (AHU), with test conditions established at 2 °C, 7 °C, 12 °C, and 18 °C, while the inlet water temperature ranged from 25 °C to 50 °C. A summary of the experimental conditions is provided in Table 19. This study investigates the influence of inlet water temperature and ambient air temperature on heat pump performance parameters through a series of controlled experiments. The parameters analysed include COP, heating capacity, power consumption, compressor discharge and suction pressures, as well as discharge and suction temperatures.

Table 19. Experimental conditions

Nos.	**Ambient Temperature ℃**	**Water Out Temperature ℃**	**Water Return Temperature ℃**	**IHX**	**Heat Pump Cycle**	**Compressor RPM**
			Experimental Configuration 1			
1	18	60	25, 30, 35, 40, 45, 50	No	Single Stage	2400
2	12	60	25, 30, 35, 40, 45, 50	No	Single Stage	2400
3	7	60	25, 30, 35, 40, 45, 50	No	Single Stage	2400
4	2	60	25, 30, 35, 40, 45, 50	No	Single Stage	2400
5	7	60	25, 30, 35, 40, 45, 50	Yes	Single Stage	2400
			Experimental Configuration 2			
6	15	Changed (42 ℃ to 27 ℃)	Changed (18 ℃ to 15 ℃)	Yes	Single Stage	2400, 2700, 3000, 3300, 3600, 3900,4200
7	2	Changed (33 ℃ to 20 ℃)	Changed (16 ℃ to 12 ℃)	Yes	Single Stage	2400, 2700, 3000, 3300, 3600, 3900, 4200
			Experimental Configuration 3			

8	18	73	14	No	Single Stage	2400
9	18	80	17	Yes	Single Stage	2400
10	18	72	16	No	Single Stage	2400
			Experimental Configuration 4			
11	12	50	27	No	Single Stage	Maximum 4700
12	12	47	23	No	Single Stage	Maximum 4700
13	2	44	24	No	Single Stage	Maximum 4700
14	2	43	24	No	Single Stage	Maximum 4700
15	12	80	20	No	Single Stage	2400
			Experimental Configuration 5			
16	18	60	17	Yes	Single Stage	4000
17	12	60	15	Yes	Single Stage	4000

4.7 Results and discussion

The CO_2 AWHP's performance data was gathered from a variety of air and water intake temperatures. The measured parameters include heating capacity, compressor power and COP. By employing linear interpolation between the data points, performance maps were created using this dataset. Data is plotted as functions of the two key temperatures in the performance maps influencing the unit's performance and heating capacity: ambient air temperature and water inlet temperature. This section will describe the effects of these temperatures on the system's performance. Data were collected for four ambient air temperatures (2 °C, 7 °C, 12 °C, and 18 °C) and varying the water inlet temperatures from 25 °C to 50 °C. The performance maps are presented, and the observed trends are discussed.

4.7.1 Heating capacity

Figure 49 illustrates the heating capacity in relation to the temperatures of the air and water inlets. The heating capacity is more significantly influenced by the water inlet temperature than by the ambient air temperature. The heating capacity decreases significantly as the water inlet temperature rises, as illustrated in Figure 49. For example, the heating capacity decreases by 13% as the water inlet temperature increases from 25 °C to 50 °C at an ambient temperature of 7 °C. The primary cause of this decrease in heating capacity is the reduction in the temperature difference between the inlet and discharge water across the gas cooler. The heat transfer required to raise the water temperature to the intended setpoint for the outlet decreases as the water inlet temperature increases.

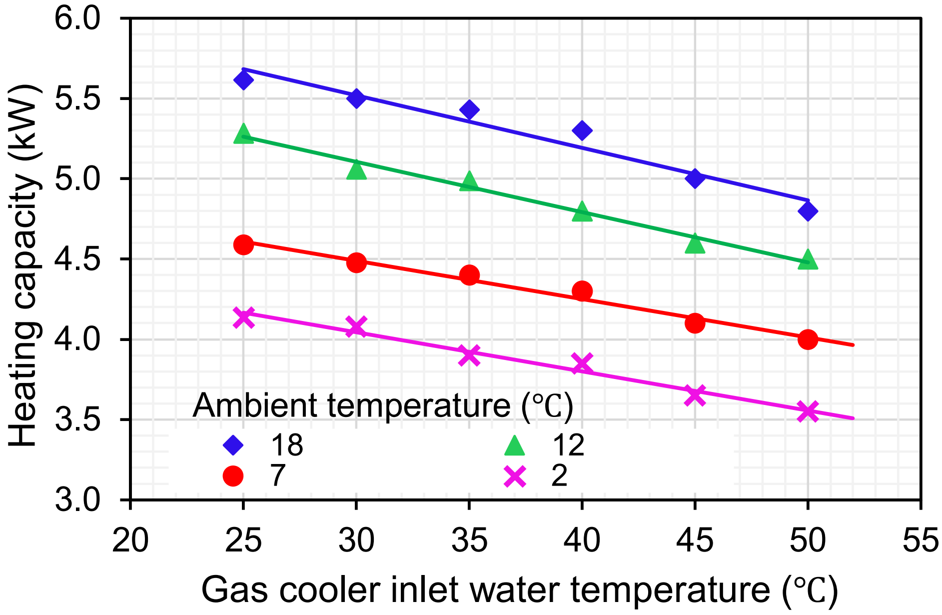

Figure 49. Heating capacity vs water inlet temperature in the gas cooler

4.7.2 Power input

Figure 50 illustrates that the electric power consumption is influenced by both ambient air temperature and water inlet temperature. Furthermore, Figure 50 illustrates the compressor power corresponding to the four air temperatures recorded. At an ambient temperature of 12 °C, the electric power consumption escalates from 1.92 kW to 2.56 kW when the inlet water temperature goes from 25 °C to 50 °C, indicating a 33% increase. Conversely, at an ambient temperature of 2 °C, when inlet water temperature increases from 25 °C to 50 °C, the electric power increases from 2.05 kW to 2.7 kW, indicating a 35% rise. These results suggest that the increase in power consumption is more strongly influenced by ambient temperature rather than return water temperature. This is because the suction pressure decreases at lower ambient temperatures, reducing the refrigerant mass flow rate. This decrease in mass flow rate increases the compression process, as shown in Figure 51, ultimately increasing compressor power consumption. Another important factor is the water inlet temperature. The discharge pressure is directly proportional to the temperature of the water entering the gas cooler. The compressor's power consumption goes up as a consequence of the greater pressure ratio caused by the increased pressure.

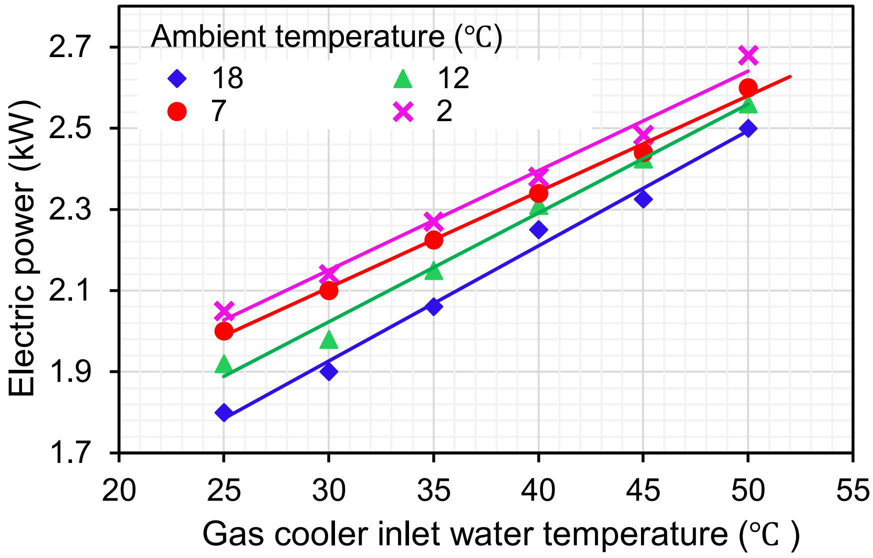

Figure 50. Electric power vs water inlet temperature in the gas cooler

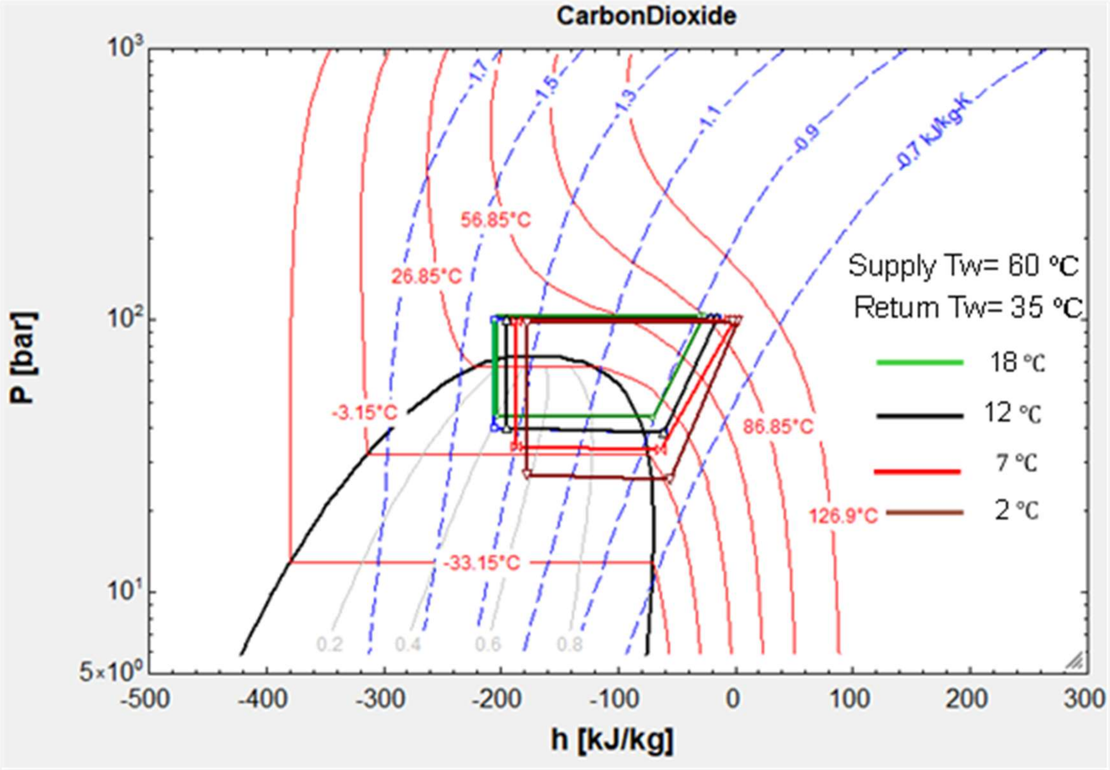

Figure 51. P-h diagram under different outdoor air temperatures

4.7.3 COP

Figure 52 shows the variations in the COP at different inlet water temperatures in the gas cooler and under varying ambient temperatures. The figure demonstrates that, for a constant supply of water temperature and for a constant ambient temperature, an increase in return water temperature leads to a gradual decline in COP. Moreover, the higher the return water temperature, the more rapidly the COP decreases. The heat pump system functions more efficiently with a lower return water temperature and a higher outside temperature. This trend can be attributed to the combined effect of ambient temperature and return water temperature on system performance.

The enthalpy difference between the CO_2 refrigerant and the circulating water diminishes as the ambient temperature falls because the evaporation and discharge temperatures also decrease. Additionally, the mass flow rate of the CO_2 refrigerant decreases, reducing heat capacity at a constant water flow rate. Simultaneously, the compression ratio increases, resulting in a rise in power consumption. Since the rise in power consumption is more significant than the increase in heating capacity at a higher compression ratio, the COP exhibits a downward trend.

The measured COP is reduced from 2.27 to 1.5 at an ambient temperature of 7 °C when the inlet water temperature is raised from 25 °C to 50 °C while the water discharge temperature remains at 60 °C, as illustrated in Figure 52. In general, the COP of heat pump systems is significantly influenced by the ambient temperature. The COP increases by approximately 34% when the ambient temperature rises from 2 °C to 12 °C at an inlet water temperature of 50 °C. This increase in COP is due to the heating capacity increasing at a rate that exceeds the total power consumption, resulting in an overall improvement in system efficiency, as is consistent with established practice.

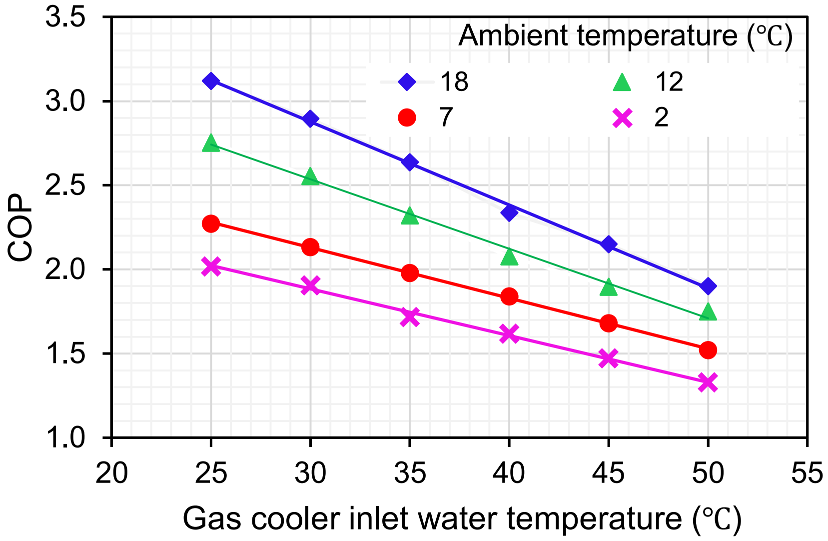

Figure 51. COP vs water inlet temperature in the gas cooler

4.7.4 Discharge temperature and pressure under different working conditions

Figure 53 presents the variation in compressor discharge temperature with the return water temperature at different ambient temperatures. As the return water temperature increases, the discharge temperature also rises. This trend is primarily attributed to the rapid increase in pressure ratios, which intensifies the compression process and leads to higher discharge temperatures.

As shown in Figure 54, the discharge pressure increases linearly with the rise in inlet water temperature. This trend is primarily attributed to the rapid increase in gas cooler temperature, as depicted in Figure 51.

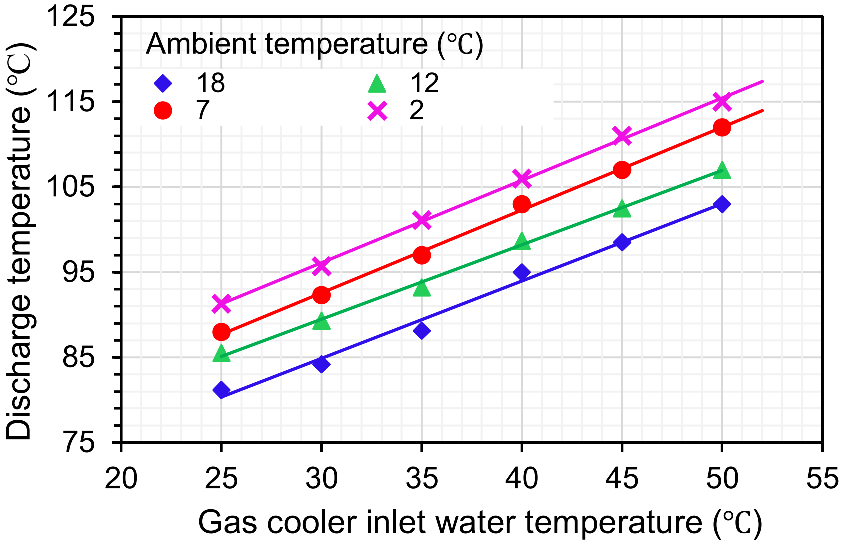

Figure 52. Discharge temperature vs inlet water temperature

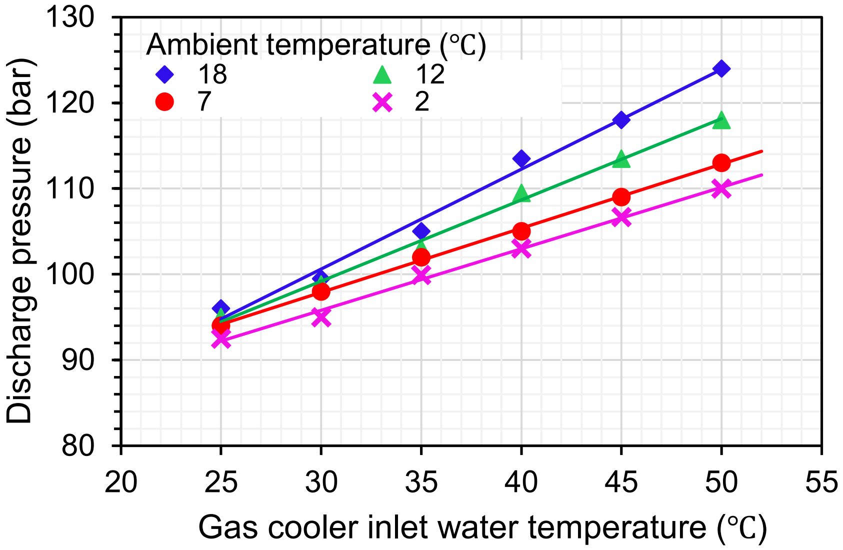

Figure 53. Discharge pressure vs inlet water temperature

4.8 Influence of IHX on the transcritical CO_2 air to water heat pump (AWHP)

This section uses experimental data to examine the impact of the internal heat exchanger (IHX) on the transcritical CO_2 AWHP cycle. Figures 55 and 56 illustrate the transcritical CO_2 AWHP cycles with and without an internal heat exchanger at a discharge pressure of 104 bar in the P-H diagram. The cycle without IHX is denoted as 1-2-3-4-5-1, but the cycle with IHX is denoted as 1-2-3-4-5-6-7-1. As the refrigerant quality at the evaporator input cannot be determined from direct temperature and pressure measurements, it was presumed that the throttling process in the expansion valve is isenthalpic.

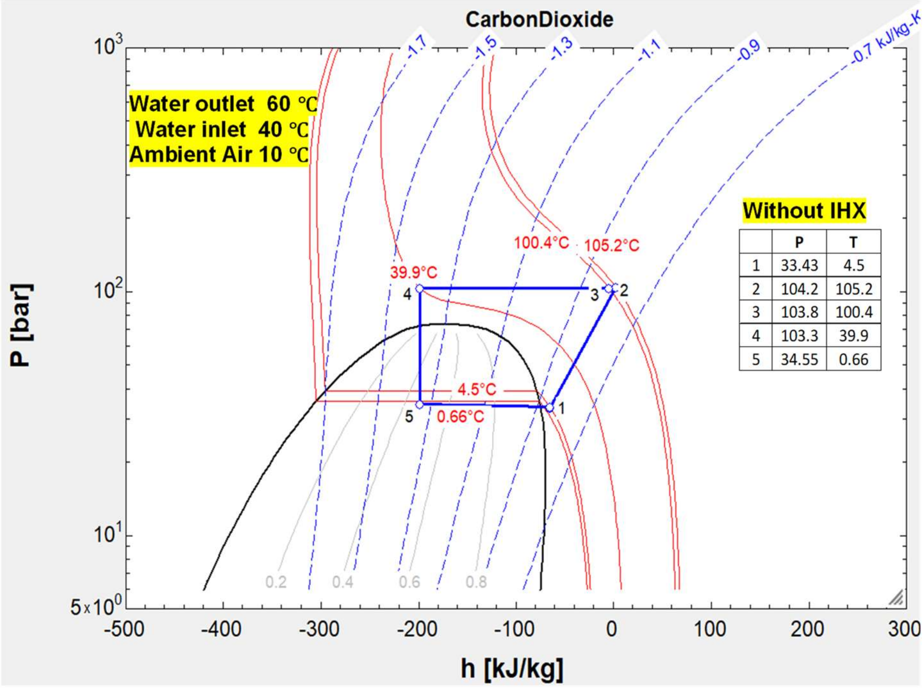

	P	T
1	33.43	4.5
2	104.2	105.2
3	103.8	100.4
4	103.3	39.9
5	34.55	0.66

Figure 54. Pressure-enthalpy without IHX

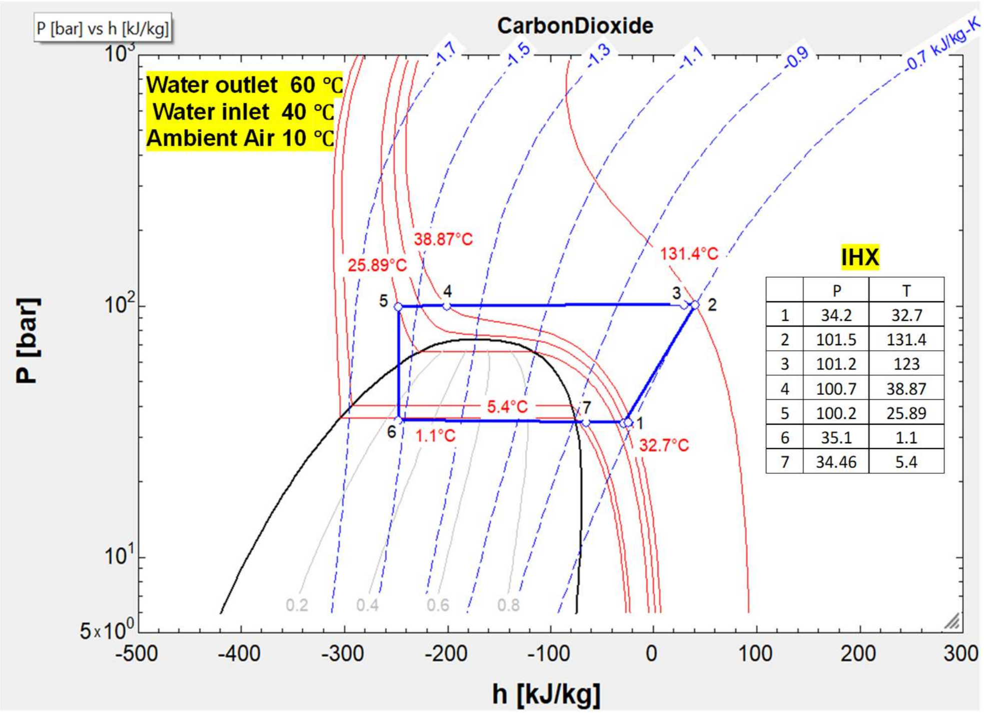

	P	T
1	34.2	32.7
2	101.5	131.4
3	101.2	123
4	100.7	38.87
5	100.2	25.89
6	35.1	1.1
7	34.46	5.4

Figure 55. Pressure-enthalpy with IHX

The steps involved in the heat pump cycle are as follows:

- Process 1-2: Compression within the compressor
- Process 3-4: Heat release in the gas cooler without a phase change
- Process 4-5: The expansion valve throttling process
- Process 5-1: Heat absorption with phase change in the evaporator (without IHX)
- Process 7-1 and 4-5: Heat transfer occurring within the IHX

The impact of the IHX on cycle pressure is predominantly evident on the high-pressure side. Figure 56 illustrates that the gas cooler pressure in cycles incorporating an IHX is marginally lower than in cycles without an IHX. The illustration indicates that the evaporator pressure on the low-pressure side is only marginally influenced by the implementation of the IHX.

The temperature of the cycle is affected by heat transfer in the IHX. In particular, compressor suction and discharge temperatures are higher in IHX cycles than without IHX cycles. Lubricating oil can be cooked at very high discharge temperatures. Because the evaporation temperature drops and the compressor pressure ratio rises in an IHX heat pump cycle, the discharge temperature rises as the ambient temperature falls. Moreover, the increase in discharge temperature is more pronounced when the water inlet temperature is higher. Therefore, to prevent the detrimental effects of excessively high discharge temperatures, careful consideration must be given when applying the IHX under operating conditions with low ambient temperatures and high water inlet temperatures in the gas cooler.

Secondly, the use of the IHX has only a marginal impact on the refrigerant condition at the evaporator's outlet. This is apparent from the conditions at points 7 and 1 in Figure 56. The evaporator inlet enthalpy decreases as a result of the subcooling and superheating effects produced by the IHX while the vacuum temperature increases. Consequently, the refrigerant mass flow rate decreases as the suction temperature increases. Under these circumstances, the enthalpy difference between the evaporator inlet and outlet increases as the refrigerant mass flow rate decreases, with the evaporator's heat transfer area remaining constant. As a consequence, the refrigerant condition at the evaporator outlet does not vary significantly.

Thirdly, the gas cooler outlet temperature is influenced by using IHX. When the water inlet temperature is 40 °C or higher, the gas cooler outlet temperature decreases with the application of IHX. At low water inlet temperatures, the heat transfer area is sufficient; at high temperatures, it becomes too large. The usage of the IHX reduces the refrigerant mass flow rate, which in turn increases heat release and decreases the temperature approach at the gas cooler outlet at a water inlet temperature of 40 °C. The reduction in refrigerant mass flow rate with the use of an internal heat exchanger (IHX) is primarily associated with changes in the thermodynamic state of the refrigerant at the compressor inlet and the resulting impact on compressor operation. In a transcritical CO_2 system, the IHX transfers heat from the high-pressure refrigerant leaving the gas cooler to the low-pressure refrigerant exiting the evaporator. As a result, the suction vapour is further superheated before entering the compressor.The discharge-side refrigerant is subcooled before expansion.The additional superheating at the compressor inlet increases the specific volume of the suction vapour (i.e., reduces its density). Since the compressor has a fixed volumetric displacement (or limited speed range in variable-speed systems), the mass flow rate is proportional to suction density. Because suction density decreases due to superheating, the refrigerant mass flow rate correspondingly decreases.

The cycle temperature is influenced by the IHX, as illustrated in Figure 56. This results in heightened enthalpy differences between the compressor inlet and outlet, as well as between the gas cooler inlet and outlet. The heating capacity and compressor power consumption are typically improved by these increased enthalpy differences, whereas the refrigerant mass flow rate is reduced, which tends to diminish them. Furthermore, a decrease in the optimal discharge pressure results in a decrease in compressor power consumption. Consequently, the combined effects are the primary cause of the observed fluctuations in compressor power consumption and thermal capacity.

4.8.1 Comparison of heating capacity

Figure 57 compares the heating capacity of the CO_2 AWHP at varying inlet water temperatures, with an ambient temperature of 7 °C, with and without IHX. Under similar experimental conditions, the thermal capacity of the AWHP with IHX is found to be greater than that of the AWHP without IHX. This difference is primarily attributed to the presence of the IHX.

In the AWHP system incorporating an IHX, when the water inlet temperature reaches 40 °C or higher, the outlet temperature of the gas cooler is reduced due to the effect of the IHX, as illustrated in Figure 56. The reduction in refrigerant mass flow rate resulting from the application of the IHX enhances the heat rejection process and lowers the temperature approach at the gas cooler outlet. Consequently, the refrigerant exiting the gas cooler is sub-cooled via heat exchange with the refrigerant vapor from the evaporator within the IHX. This sub-cooling effect decreases the refrigerant enthalpy at the evaporator inlet, thereby increasing the enthalpy difference across the evaporator. As a result, the cooling capacity is improved, which subsequently leads to an increase in the heating capacity of the system. Figure 57 illustrates that when the water inlet temperature increases from 20 °C to 50 °C, the heating capacity of the AWHP without the IHX diminishes from 4.6 kW to 4.2 kW, but the AWHP with the IHX shows a reduction from 4.75 kW to 4.35 kW. The results indicate that the enhancement in heating capacity provided by the IHX rises from 3.3% to 3.6% relative to the AWHP without the IHX at an ambient temperature of 7 °C.

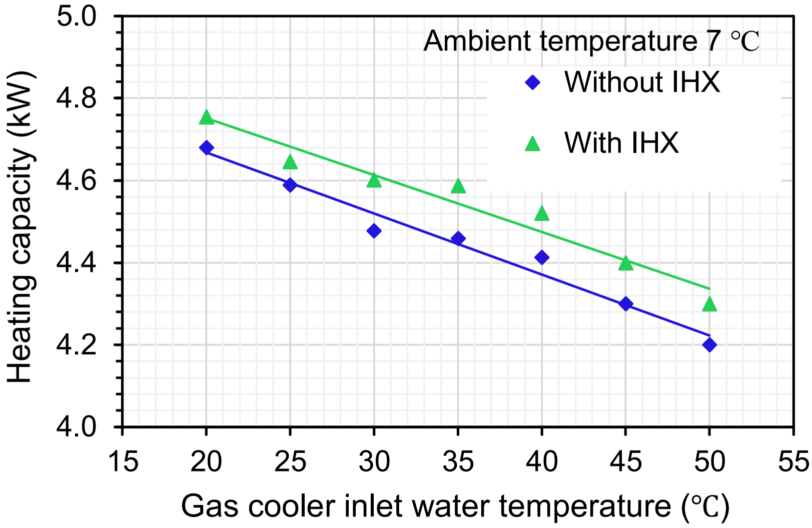

Figure 56. Heating capacity vs water inlet temperature

4.8.2 Comparison of electric power

The power consumption of the CO_2 AWHP system is compared in Figure 58 at an ambient temperature of 7 °C, with variable return water temperatures at the gas cooler, with and without an IHX. The inlet water temperature increases linearly, resulting in a linear increase in power consumption for both configurations. The reason for this trend is the rise in refrigerant mass flow rate, which is correlated with higher return water temperatures. The power consumption of the AWHP system with an IHX is consistently lower than that of the system without an IHX at the same inlet water temperatures. The combined effects of the refrigerant mass flow rate and pressure ratio can account for this decrease. In the AWHP system with an IHX, the IHX induces a slight increase in the compressor's power consumption and a small pressure decrease at the compressor suction. Nevertheless, this increase is counterbalanced by a concurrent decrease in the refrigerant mass flow rate. In particular, the superheating of refrigerant vapour within the IHX leads to a reduction in refrigerant density at the compressor inlet, which in turn reduces the refrigerant mass flow rate and, as a result, the compressor power necessity. The power consumption of the AWHP without the IHX increases from 1.87 kW to 2.58 kW when the inlet water temperature increases from 20 °C to 50 °C, as illustrated in Figure 58. Similarly, the power consumption of the AWHP with the IHX increases from 1.74 kW to 2.42 kW. The AWHP with the IHX utilises approximately 7.7% less power than the system without the IHX at an inlet water temperature of 50 °C.

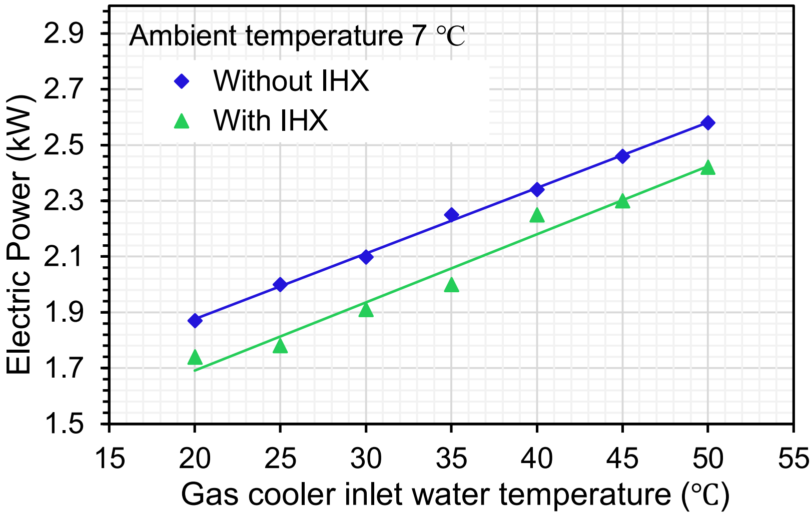

Figure 57. Electric power vs water inlet temperature

4.8.3 Comparison of COP

Figure 59 illustrates a comparison of the COP for the CO_2 AWHP system with and without IHX in relation to the gas cooler inlet water temperature. The experimental results indicate that the COP of the AWHP without the IHX decreases from 2.5 to 1.63 as the return water temperature increases from 20 °C to 50 °C, which is achieved while maintaining a constant ambient temperature of 7 °C. Conversely, the COP of the AWHP with the IHX decreases from 2.73 to 1.77 within the same temperature span. It is important to note that the COP of the AWHP with the IHX is approximately 10% higher than that of the system without the IHX at a return water temperature of 50 °C. Reduced power consumption and higher thermal capacity, as mentioned earlier, are the combined impacts that lead to this improvement in COP. To be more specific, the AWHP system that incorporates the IHX improves system efficiency by offering a higher heating capacity with lower power consumption.

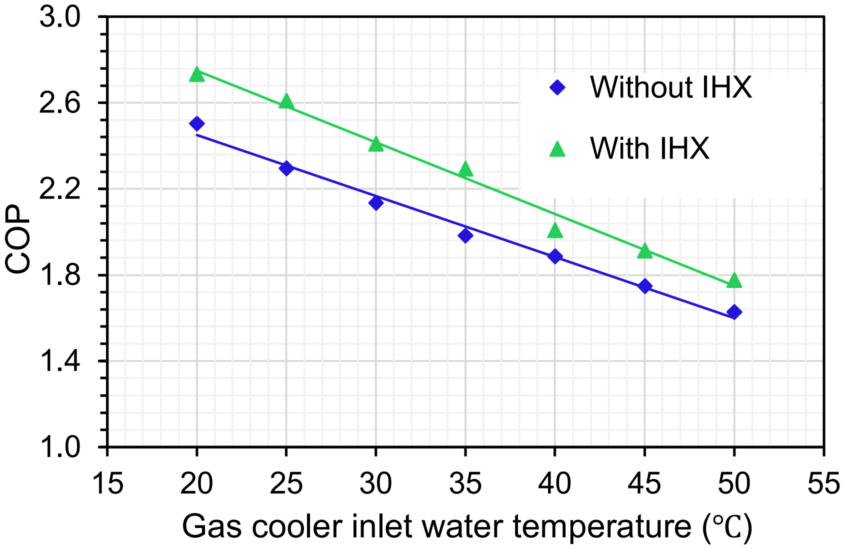

Figure 58. COP vs water inlet temperature

4.8.4 Comparison of mass flow rate

Figure 60 indicates that the refrigerant mass flow rate of CO_2 is lower in the system incorporating an IHX compared to the system without an IHX. This behaviour is primarily attributed to the additional superheating of the suction vapour caused by the IHX. The increased suction superheat reduces the refrigerant density at the compressor inlet, thereby decreasing the mass flow rate for a given compressor displacement and operating speed.

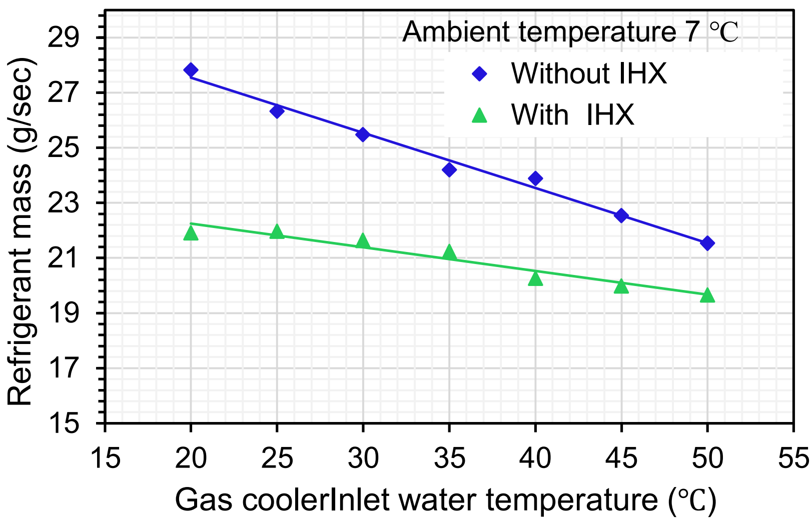

Figure 59. Refrigerant mass vs water inlet temperature

4.8.5 Comparison of compressor temperature

The discharge temperature for the AWHP system with and without IHX is shown in Figure 61, with different return water temperatures at the gas cooler. Remember that the superheating effect from the vaporised refrigerant causes the compressor discharge temperature to rise dramatically when using the IHX. The IHX system causes the compressor discharge temperature to rise with increasing return water temperature, eventually reaching 138 °C at 50 °C water inlet temperature. Such increased discharge temperatures can present operational challenges for the refrigeration system, including potential degradation of the lubricant oil and reduced lifespan of components exposed to high temperatures at the compressor discharge. In contrast, the AWHP system without the IHX exhibits a lower maximum discharge temperature of 113 °C under the same inlet water temperature conditions.

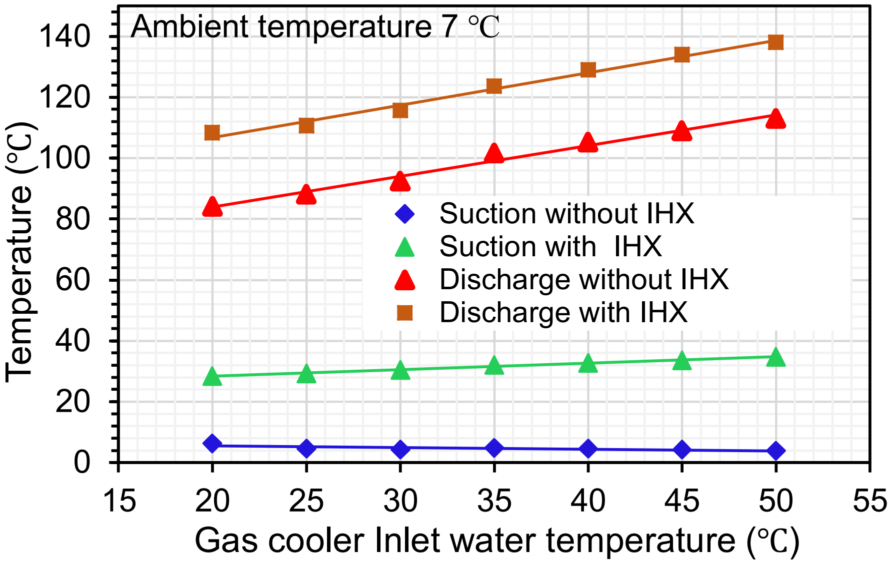

Figure 60. Suction and discharge temperature vs water inlet temperature

4.8.6 Comparison of compressor pressure

Figure 62 illustrates a comparison of the suction and discharge pressures for the AWHP with and without IHX across different return water temperatures at the gas cooler. The impact of the IHX on cycle pressure is only seen on the discharge pressure side. Figure 62 shows that the compressor discharge pressure with IHX is slightly lower than in those without an IHX, particularly at high return water temperatures. The figure also demonstrates that the compressor suction pressure remains unaffected by the presence of the IHX.

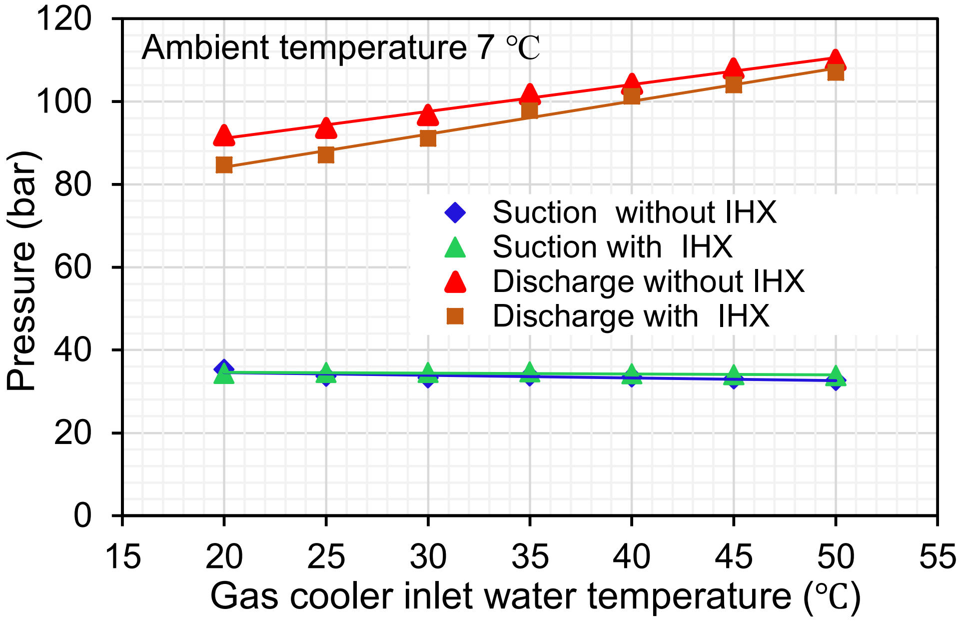

Figure 61. Suction and discharge pressure vs water inlet temperature

4.9 Effect of compressor speed

Compressor frequency, often referred to as compressor speed, is a key parameter in the operation of heat pump systems. Modulating the rotating speed (RPM) directly impacts the discharge volume, thereby changing the system's heating performance. Experimental results demonstrate that an increase in compressor speed leads to corresponding increases in heating capacity, power consumption, compressor discharge pressure and temperature, outlet water temperature and refrigerant mass flow rate, as shown in Figures 63 to 66. Conversely, the COP exhibits a declining trend with higher compressor speeds. Experiments were carried out at the ambient temperature of 12 °C, return water temperature of 26 °C and supply water temperature of 40 °C to 60 °C.

The effect of compressor speed on the CO_2 AWHP's heating capacity, power consumption and COP is depicted in Figure 63. At a fixed water flow rate of 4.4 L/min, the heating capacity rises from 5.4 kW to 10.8 kW, representing a 100% increase when the compressor speed increases from 2400 RPM to 4500 RPM. Despite the substantial increase in heating capacity, there are also significant changes in compressor power. There is a noticeable rise in compressor power consumption. This indicates an approximate 188% augmentation in compressor output, rising from 1.32 kW to 3.75 kW. The reason for this trend is that an increase in compressor speed leads to a higher compression ratio and increased power consumption by increasing the mass flow rate of the CO_2 refrigerant and the discharge pressure. Additionally, the compressor speed affects the system's COP. Figure 63 illustrates that increased compressor speed results in lower COP values. The COP decreases from 4 to 2.8, representing a 30% reduction, when the compressor speed increases from 2400 RPM to 4500 RPM. This phenomenon is primarily caused by the high discharge temperature which increases the enthalpy difference between the gas cooler inlet and outlet temperatures, thereby increasing the system's heating capacity. Hence, as power consumption increases at a faster rate than heating capacity, the COP gradually falls.

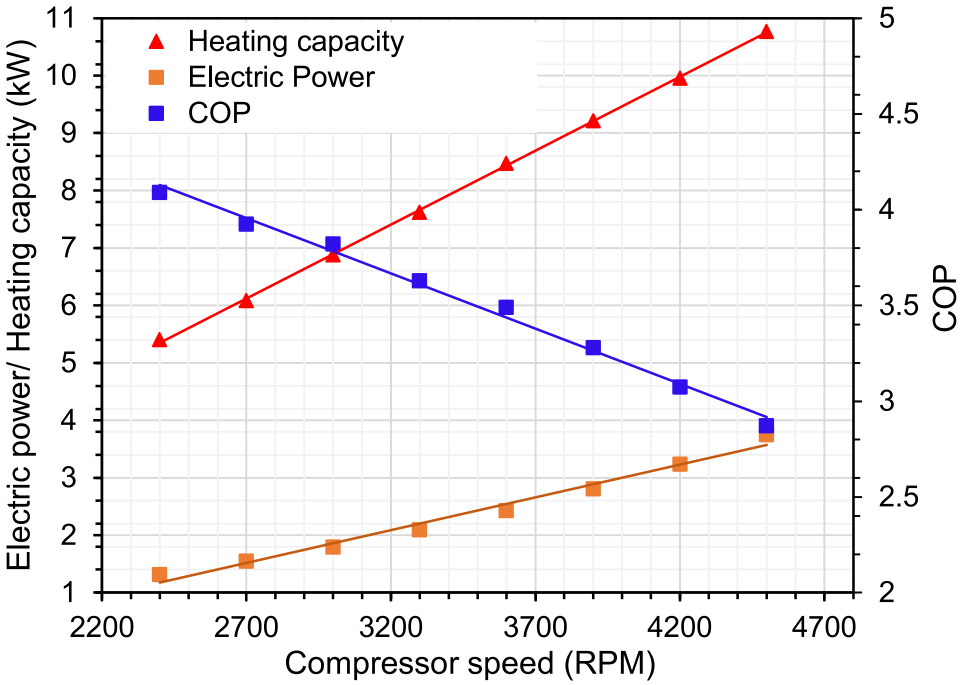

Figure 62. COP, heating and electric power vs compressor speed

Furthermore, as illustrated in Figure 64, at a fixed water flow rate of 4.4 L/min, the outlet water temperature increases from 41 °C to 58 °C, representing a 41.5% rise, while the mass flow rate increases from 0.028 kg/s to 0.047 kg/s, a 68% increase. This trend can be attributed to the increase in compressor speed, which raises both the discharge volume and discharge pressure, resulting in a higher compression ratio and, consequently, greater power consumption.

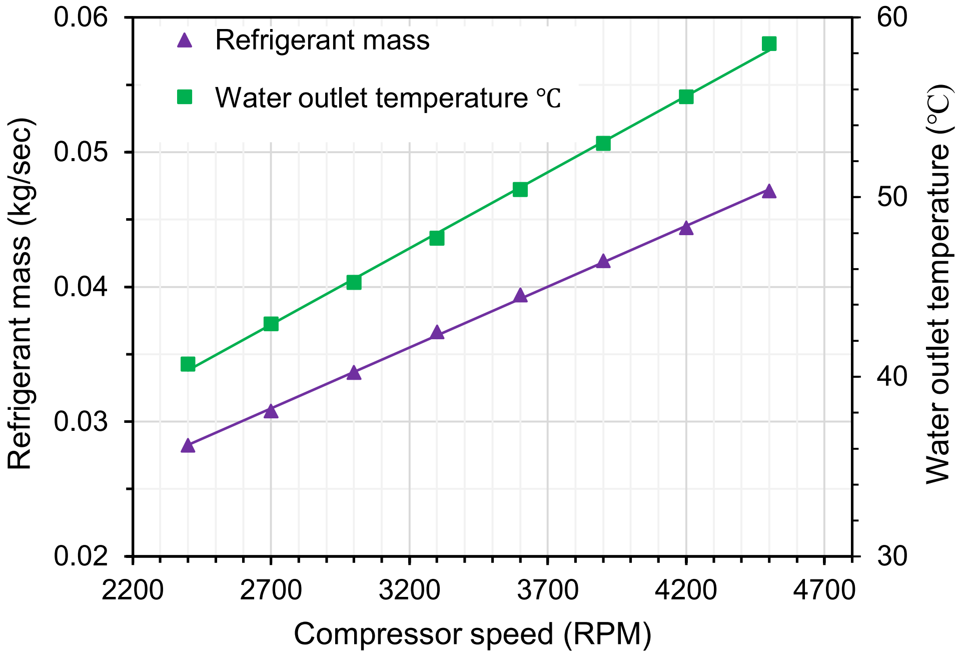

Figure 63. Refrigerant mass and water outlet temperature vs compressor speed

Figure 65 shows that the discharge temperature rises with increasing compressor speed. At a compressor speed of 4500 RPM, the discharge temperature reaches 112 °C, indicating that the compressor can still operate effectively at high speeds under cold conditions. This behavior can be primarily attributed to the fact that as compressor speed increases, the refrigerant mass flow rate relative to the maximum heating capacity decreases, which diminishes the intercooling effect within the compressor. Consequently, under these conditions, the discharge temperature increases.

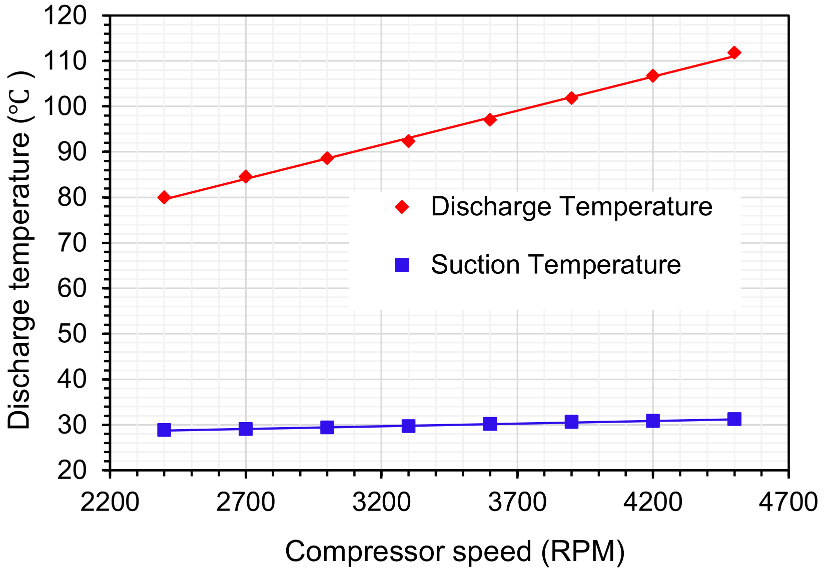

Figure 64. Compressor discharge temperature vs compressor speed

Figure 66 demonstrates a steady rise in discharge pressure corresponding to an increase in compressor speed. Conversely, the suction pressure remains very stable irrespective of the compressor speed, signifying that the evaporator pressure undergoes negligible fluctuation. This indicates that the experimental AWHP system and testing conditions were adequately regulated. The discharge pressure linearly increases by 18% as the compressor speed increases from 2400 RPM to 4500 RPM. An increase in both the discharge temperature and the refrigerant mass flow rate through the gas cooler is the consequence of a rise in the discharge pressure. Figures 64 and 65 show how the heating capacity increases subsequently.

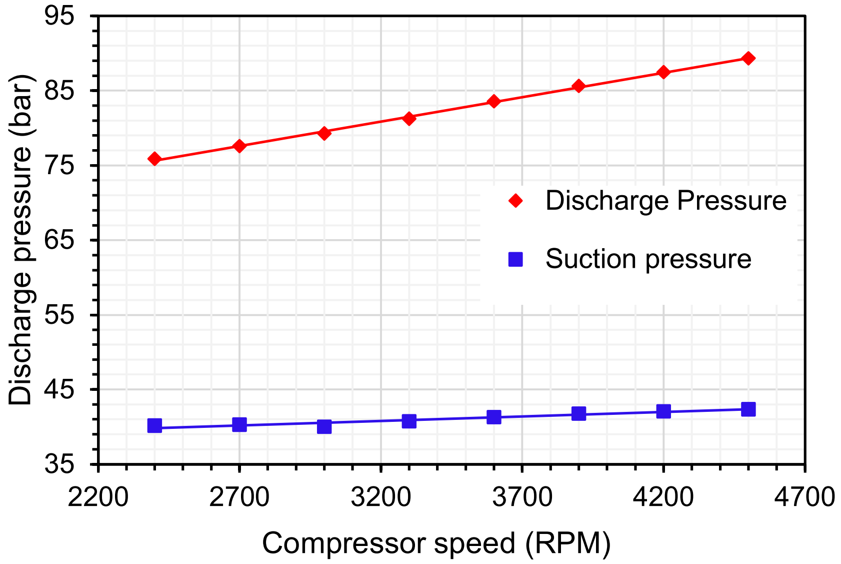

Figure 65. Compressor discharge pressure vs compressor speed

4.10 Four-bedroom house dynamic simulation

This chapter contributes to this challenge by addressing the optimum sizing of a CO_2 heat pump and thermal storage for a four-bedroom, semi-detached domestic dwelling in the London area of the UK. This chapter presents the characteristics of the newly constructed, well insulated UK dwelling and hourly simulation of the thermal loads for space heating and domestic hot water. Results of the influence of the thermal energy storage tank (TES) on the indoor temperature are presented alongside the optimum tank size to maintain indoor temperatures in the house within comfort limits during the occupied period (5:00 to 9:00 and 15:00 to 23:00). Carbon emissions and economic analysis are also given to identify areas for further investigation and performance improvement.

4.11 Building Characteristics and Thermal Loads

4.11.1 Characteristics of a four-bedroom semi-detached dwelling

The simulated dwelling was a four-bedroom, semi-detached, single-family home with two floors and a total heated floor area of 102 m^2. The location was presumed to be within the Greater London area, and the meteorological data for the simulation was obtained from the London weather station (Latitude: 51.51; Longitude: -0.09) in the Meteonorm database (Remund et al., 2020). The occupancy level was assumed to be 4 persons, including 2 adults and 2 children. Figure 67 (a) shows the floor plan of the building and Figure 67 (b) a 3D view created in Sketchup (2022/TRNSYS 3d plug-in) (Mazzeo et al., 2020).

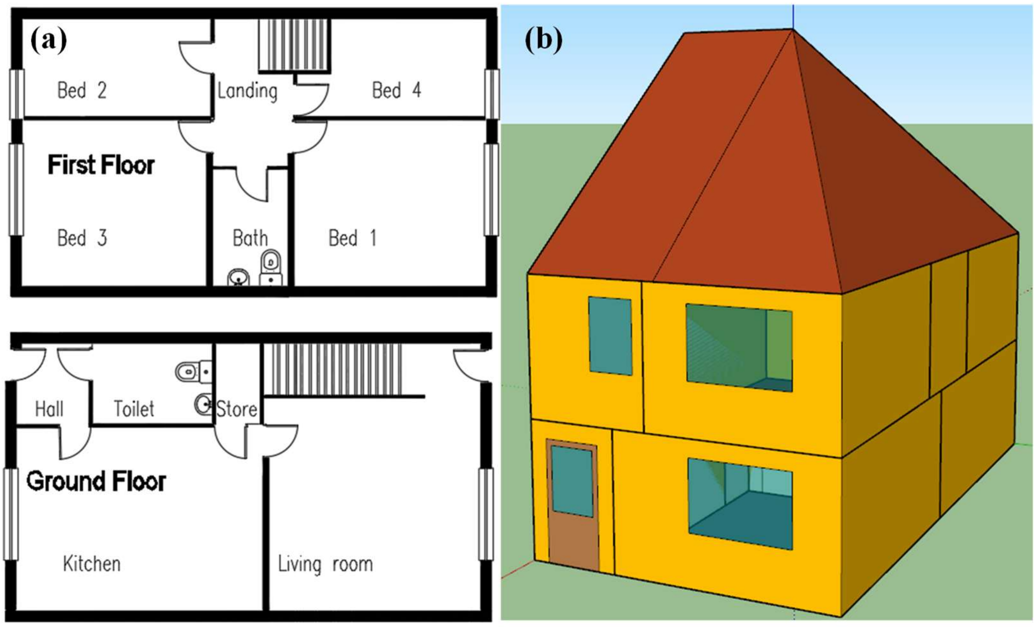

Figure 66. (a) Floor plan of the studied semi-detached four-bedroom house, (b) 3D model of the dwelling

The U values of the main building elements, used in the simulations and presented in Table 25, were selected to comply with Part L1A of the current Building Regulations (Conservation of Fuel and Power: Approved Document L Volume 1, 2023).

Table 19. Maximum overall heat transfer coefficient for the new-build UK homes

Description	U-value (W/m^2K)
External walls	0.18
Pitched roof (insulated at ceiling level)	0.16
Ground floor	0.13
Door	1.2
Windows (Triple-glazed low emissivity 16 mm air layer thickness)	1.4

Infiltration was assumed to be 0.15 air changes per hour and ventilation 37 litres per second for the whole house. These were apportioned to the various spaces in the dwelling according to their floor area (Approved Document F Volume 1,2023).

4.12 Domestic hot water demand profile

The hot water demand of the dwelling was calculated using data from the LEEDR project, which provided measurements of hot water consumption profiles for different types and sizes of domestic dwellings in the UK (Marini et al., 2019). The average hourly hot water demand profile for a four-bedroom dwelling with four occupants over a 24-hour period is shown in Figure 68. From this, the average daily demand was determined to be 119.7 litres per day.

4.13 CO_2 heat pump

The heat pump model was based on experimental data from tests performed on a CO_2 air-to-water heat pump (AWHP) developed in the laboratory at Brunel University. The heat pump is a single stage air-to-water system that can deliver hot water at temperatures up to 80 ºC. The tests were carried out in an environmental chamber across a range of ambient temperatures from 0 ºC to 20 ºC and water return temperatures to the heat pump from 17.5 °C to 47.5 °C. Measurements of heat delivered and electrical power consumption were used to calculate the Coefficient of Performance (COP) of the heat pump, which was plotted in a performance map as shown in Figure 69. It can be seen that an increase in the ambient temperature leads to an increase in the COP, whilst an increase in the water return temperature leads to a reduction in the COP. This is because it reduces the heat transfer that can be affected in the gas cooler of the heat pump and, hence, its heating capacity (Cui et al., 2019). A performance map was used to simulate the heat pump's performance within the TRNSYS simulation environment.

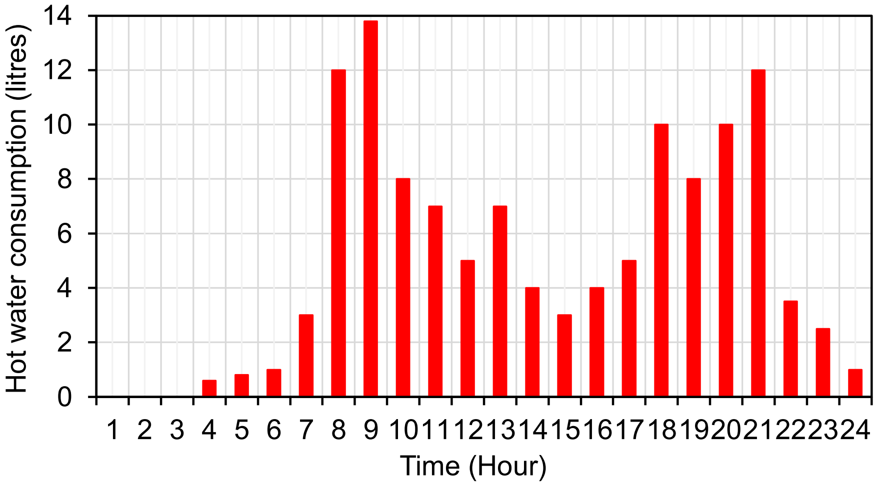

Figure 67. Average hourly hot water demand profiles derived from 12 months of measured data in LEEDR for 24 hours

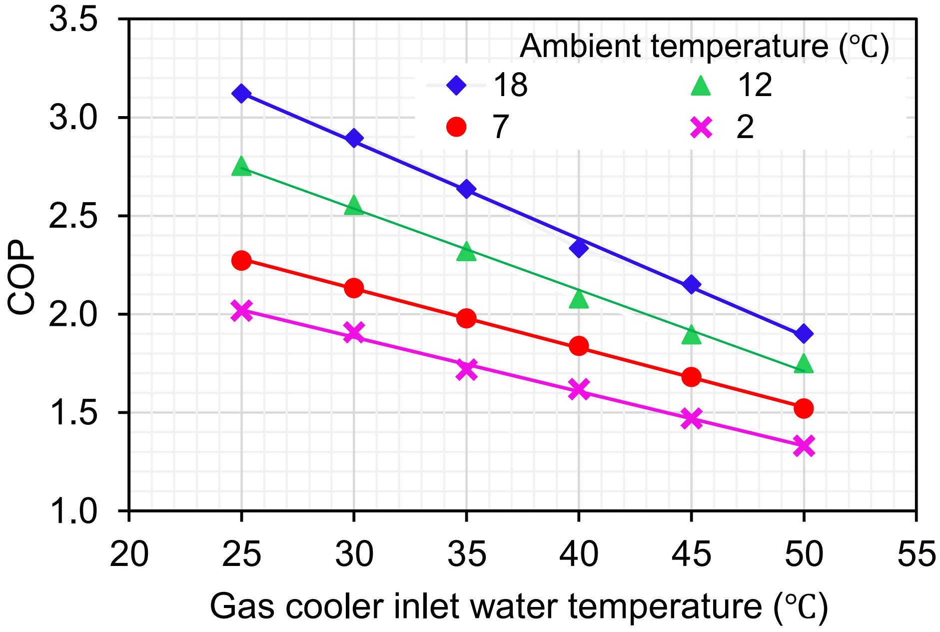

Figure 68. Performance map of the CO_2 AWHP

4.14 Integrated heating system

Figure 70 shows a schematic diagram of the heating system, which includes a CO_2 heat pump, thermal energy storage (TES) tank, heat distribution system, and domestic hot water supply.

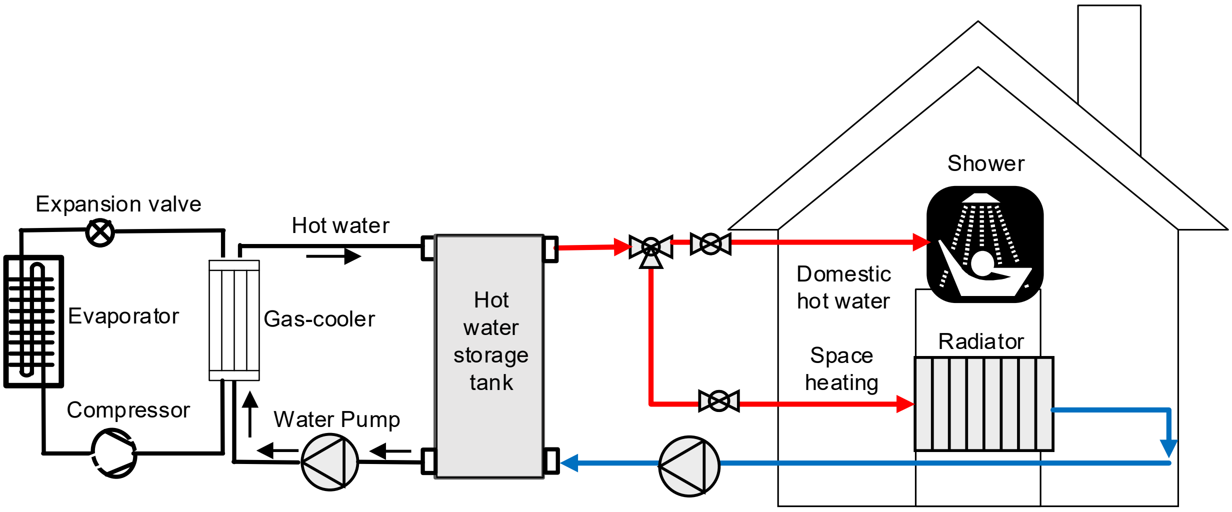

Figure 69. The schematic of the whole system

The system uses 9 radiators in total to heat the various spaces in the dwelling, with a flow rate of 0.2 kg/s apportioned to the radiators in proportion to the design thermal loads, presented in Table 15.

4.15 Simulation results and discussion

The hourly simulation of the heating system was performed using the TRNSYS 18 software platform (Klein et al., 2010). The simulation flow diagram is shown in Figure 71 and the components and data flows are illustrated in Figure 72. A thermostat in the living room controls space heating (SH). For the simulations, the thermostat was set at 20 °C with a dead band of ± 1.0 °C. This dead band is fairly standard in most domestic thermostats to provide reasonable control of internal space temperature without excessive cycling of the heating system that can lead to a reduction in efficiency and lifetime of the heating system (boiler or heat pump). The set-point temperature was selected based on thermal comfort requirements and a recommendation by Public Health England to minimise health risks in winter (Wookey et al., 2014)). The space heating schedule, shown in Figure 73, was chosen for an initial base case based on the occupancy pattern of the dwelling during the week. The temperature in the storage tank was assumed to be maintained constant by the heat pump at 60 °C with a ± 3 °C dead band.

Heating systems in the London area of the UK are normally designed to meet the heating requirements at an ambient temperature of −3 °C (CIBSE, 2019). Based on this external temperature, the building characteristics and the indoor design temperature, the thermal load at design conditions was determined for every space in the dwelling without including internal or external heat gains. This gave the thermal capacity of the radiators and a maximum space heating load of 8.34 kW, as presented in Table 26. The domestic hot water (DHW) load was determined to be approximately 2.0 kW based on the average hot water consumption of 119.7 litres per day, at 60 ºC temperature setpoint in the tank and 45 ºC temperature at the taps.

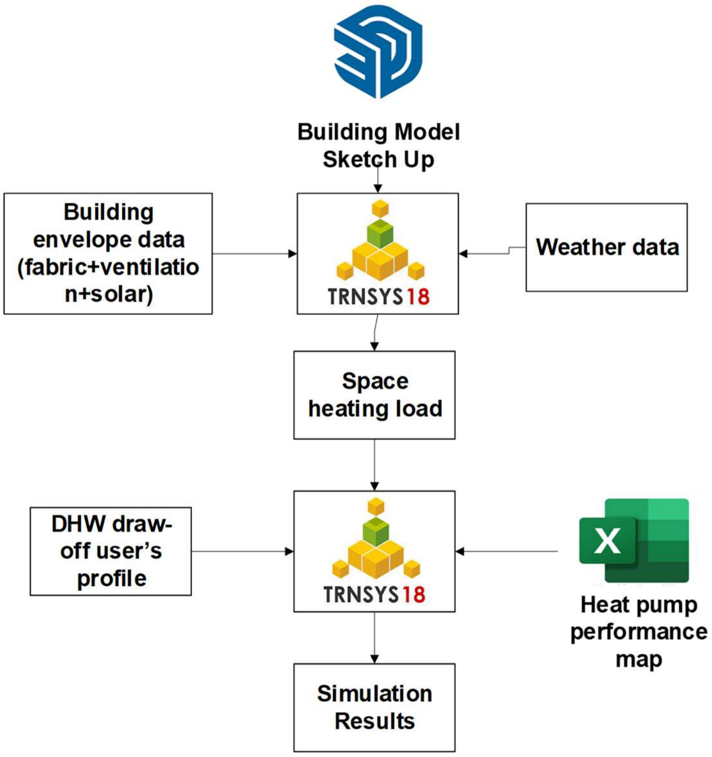

Figure 70. TRNSYS simulation flow chart

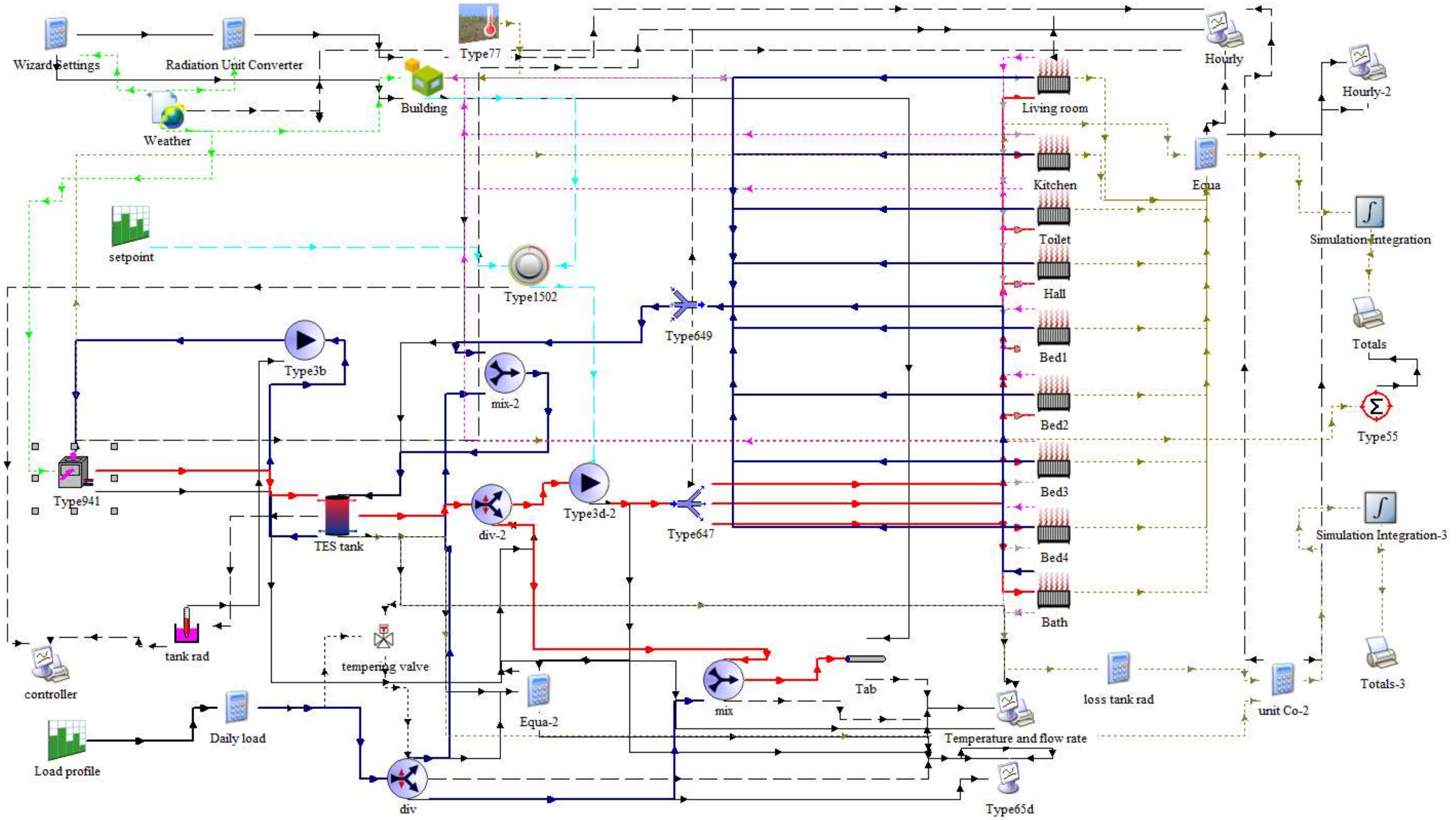

Figure 71. Development of the TRNSYS simulation model

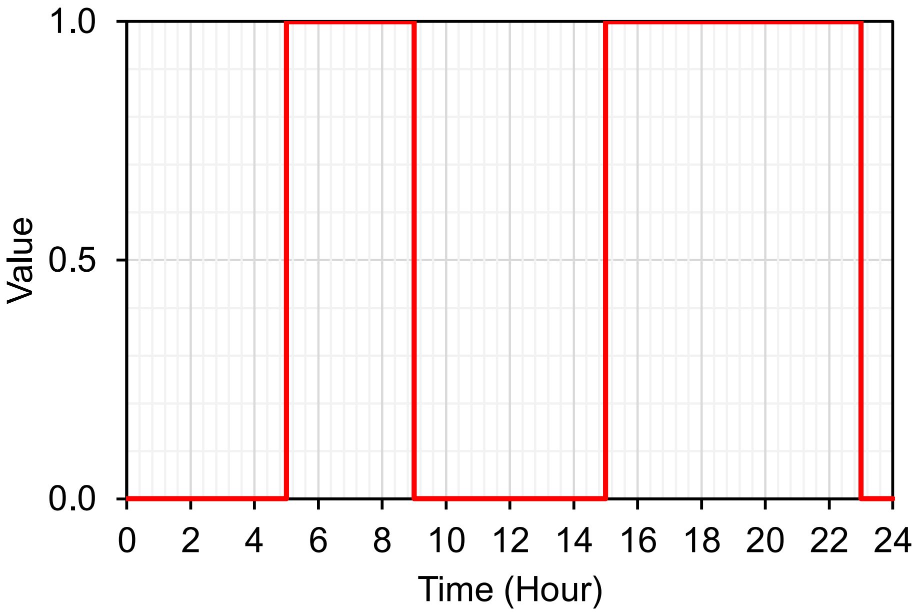

Figure 72. Space heating schedule

Table 20. Design thermal capacity of radiators and hot water storage tank heat exchanger

Room	**Design capacity (W)**
Living room	2300
Kitchen	1300
Hall	530
Bedroom 1	990
Bedroom 2	700
Bedroom 3	900
Bedroom 4	710
Bathroom	510
Toilet	400
Domestic Hot Water Load	2000

4.15.1 Sizing of the thermal energy storage tank

The focus of this analysis was on the investigation of the impact of the thermal energy storage tank size on the performance of the integrated heating system. The storage tank considered was of typical cylindrical construction with 25 mm polyurethane insulation, providing an overall heat transfer coefficient through the wall of 0.83 W/m^2 K.

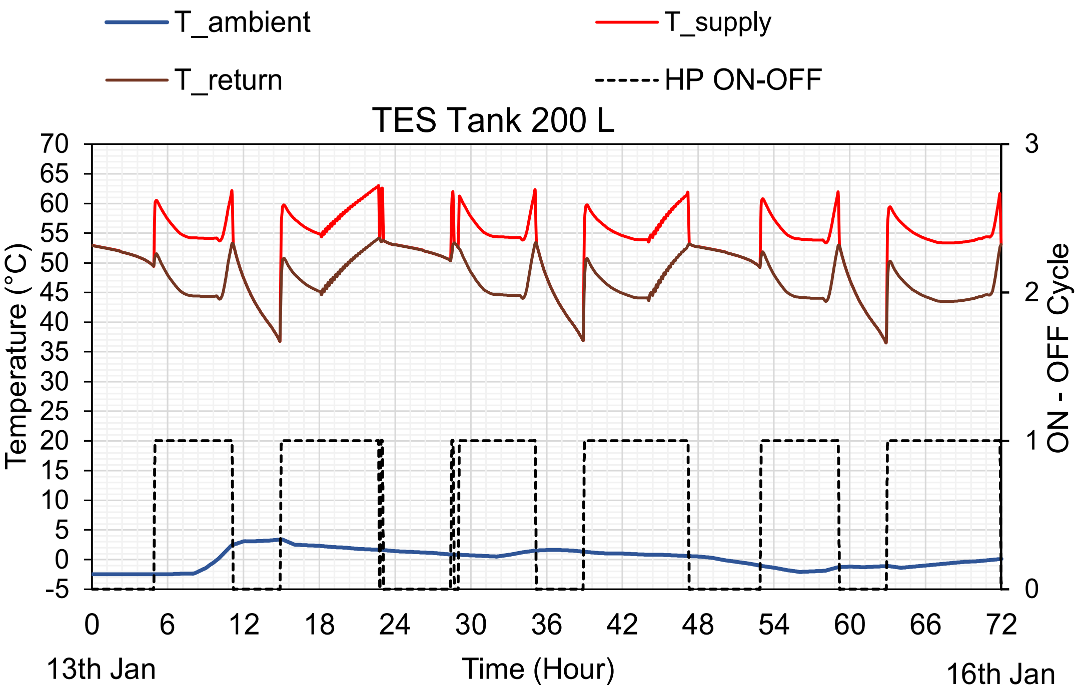

Figure 73. Heat pump operation and supply and return from 200 L storage tank

Figure 74 illustrates the variation in supply and return temperatures within a 200 L thermal energy storage tank for a three-day space heating schedule in January. It can be seen that at the start of the cycle, the supply temperature from the tank to the radiators is approximately 60 ºC and then drops to 55 ºC during the space heating period. At the end of this period, the heat pump continues to run to heat the water in the storage tank to 63 ºC, which is the upper set point of the tank thermostat. The ON period of the heat pump depends not only on the space heating schedule but also on the time that will be required to charge the storage tank to its full capacity after the schedule controller turns off space heating.

The influence of the thermal storage size on satisfying the temperature in the living room of the dwelling for the reference space heating schedule in Figure 73 was considered using storage volumes of 200 L, 300 L, 400 L and 500 L, for the 10 coldest period of the year, in January. The ambient temperature and variation of the living room temperature for the reference space heating schedule are shown in Figure 75. It can be seen that for ambient temperatures of 5 ºC and above, all storage volumes can provide the required temperature in the living room. For ambient temperatures between -1 ºC and +2 ºC, the storage volumes of 200 L and 300 L struggle to meet the indoor temperature in the morning, with the 300 L tank performing slightly better.

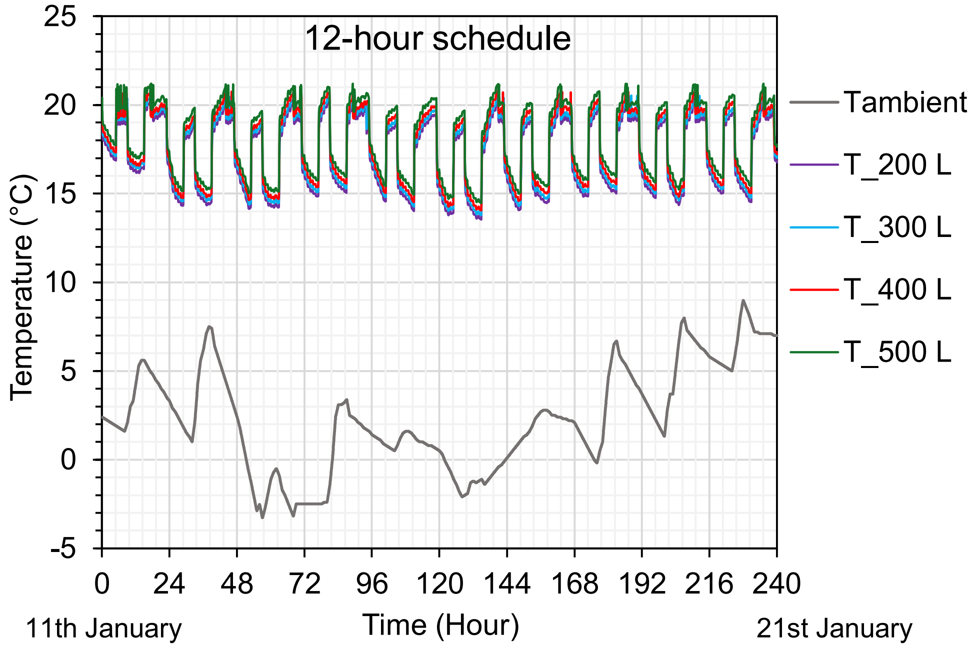

Figure 74. Variation in temperature in the living room for different hot water storage volumes during a 12-hour operating schedule

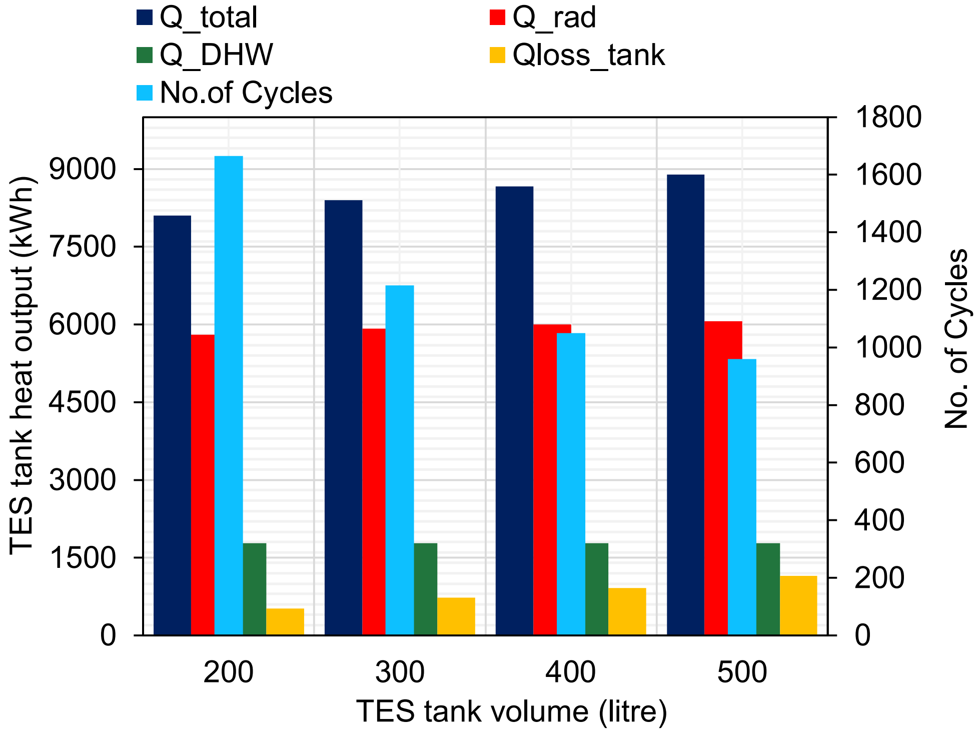

Figure 75. Thermal energy generated and losses for different storage tank sizes

Figure 76 shows the total annual energy consumption of the heat pump, the heat delivered to the radiators, the heat used for domestic hot water, the thermal energy losses from the four storage tank sizes and the number of heat pump on-off cycles for the year. Using the domestic hot water schedule for the building shown in Figure 68 with the assumption of two showers in the morning and two in the evening, the annual thermal energy for domestic hot water was determined to be 1780 kWh per year. The total heat delivered by the heat pump increases from 8100 kWh for the 200 L tank to 8900 for the 500 L tank, whereas the heat delivered to the radiators only increases slightly from 5800 kWh to 6060 kWh. The difference between the total energy delivered by the heat pump for the 200 L and 500 L storage tanks is the higher heat loss from the larger storage tank.

The cycling rate of the heat pump will increase with the smaller storage tank from 960 for the 500 L to 1670 for the 200 L. Although lower cycling rates are preferable for an extended compressor lifetime, an average of 5 cycles per day for the 200 L tank is not expected to have an adverse impact on the lifetime of the heat pump compressor.

4.15.2 Extended heat pump operating period

A way of improving the performance of the heat pump system during low-temperature winter weather conditions is to increase the operating time of the heat pump. The impact of this was investigated by running the simulations with an extended period of operation of one hour in the morning. The results are shown in Figure 77. It can be seen that with this change, the system with the 300 L tank satisfies the internal temperature requirements for the entire period; however, the 200 L tank struggles to meet the required living room temperature when the ambient temperature falls below +3.0 °C. To address this, the operating schedule of the heat pump was extended to 14 hours by starting the heat pump at 4.00 a.m. From the results, it can be observed that with this schedule, all storage tank sizes can satisfy the required temperature in the living room.

Comparing the data in Figures 75, 77 and 78, it can also be observed that increasing the period of operation of the heat pump increases the minimum temperature in the dwelling during the unoccupied period from 13.5 °C for the 12 hour schedule to 16 °C for the 14 hour schedule providing a higher temperature in the dwelling during the unoccupied periods and quicker warm-up when the heating system is switched on.

Figure 79 presents an energy comparison between the 200 L and 300 L storage tanks for extended periods of operation, specifically 13 and 14 hours on cold winter days. The difference in energy consumption between the storage volumes is small, with the larger tank consuming approximately 300 kWh more. Extending the space heating schedule time from 13 hours to 14 hours will only lead to 100 kWh higher energy consumption due to the small number of hours the heat pump will be operating at low ambient temperatures in the winter months.

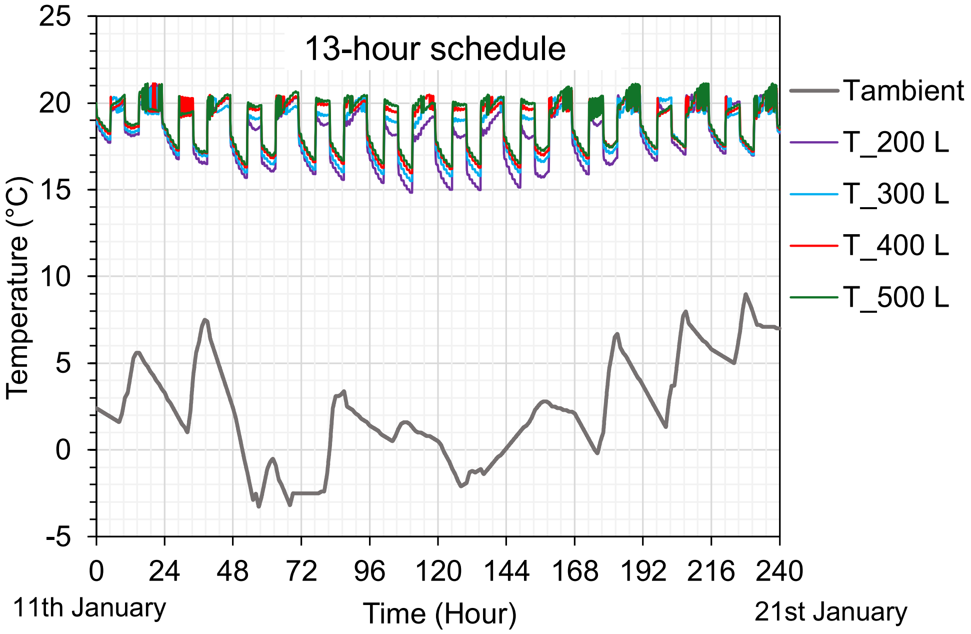

Figure 76. Variation in temperature in the living room for different hot water storage volumes during a 13-hour operating schedule

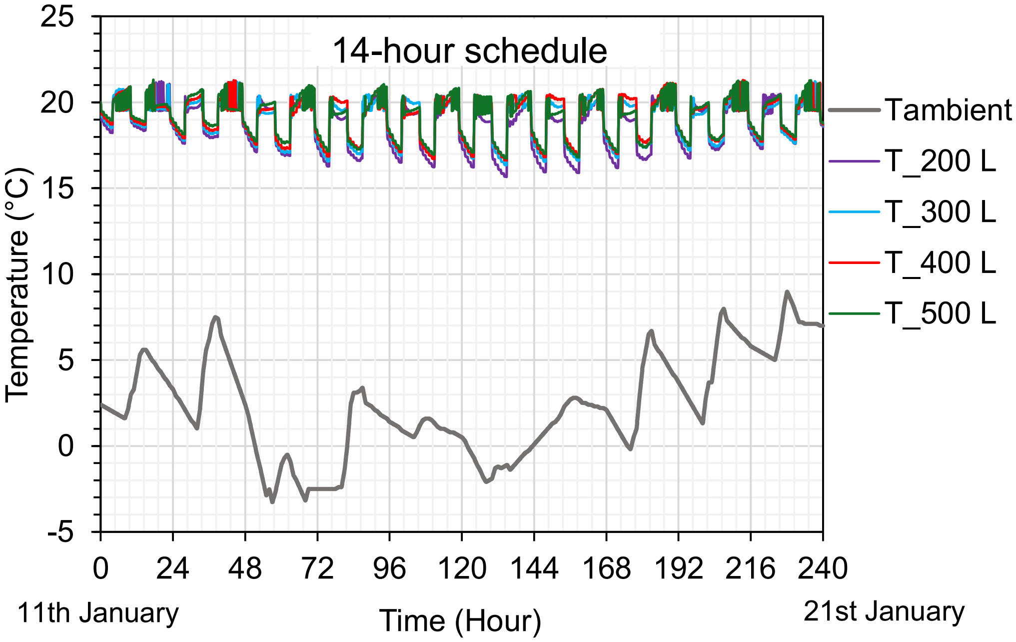

Figure 77. Variation in temperature in the living room for different hot water storage volumes during a 14-hour operating schedule.

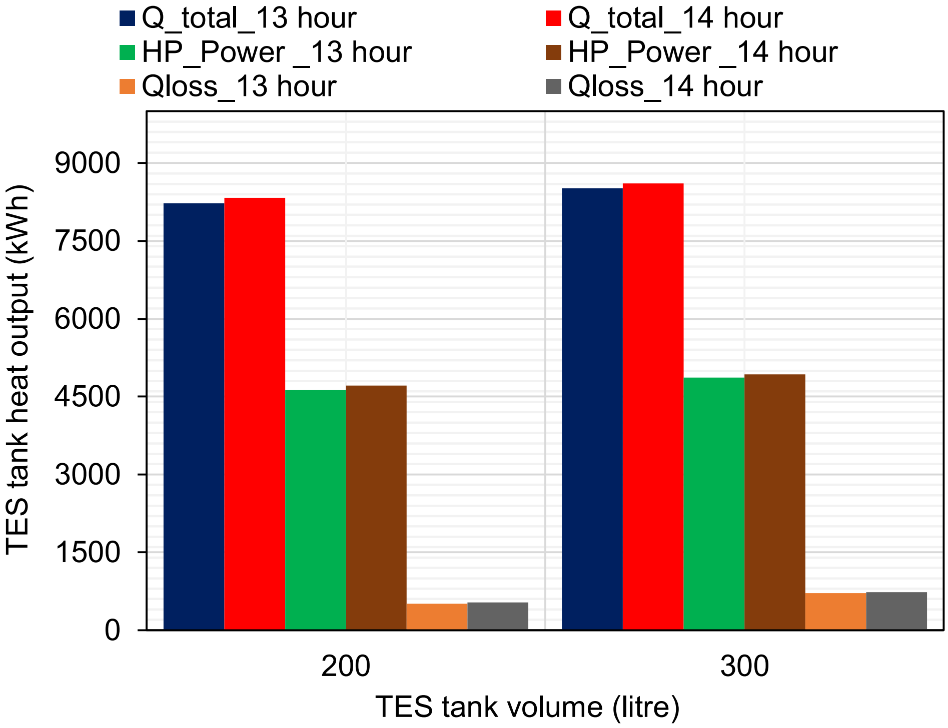

Figure 78. Energy comparison between 200 L and 300 L storage tanks

These results indicate that, by keeping the size of the heat pump constant, a combination of storage tank size and varying space heating schedules can provide the design thermal conditions in the dwelling during occupied periods. The choice of storage tank size will, therefore, depend on space availability and the flexibility that the larger storage tank will provide in the use of domestic hot water, particularly for showers and bathing.

4.16 Comparison of heat pumps and gas boilers in domestic dwellings

The attractiveness of the heat pump as an alternative heating technology to gas boilers will depend on the capital and operating costs and environmental impacts of the two technologies. For the well-insulated domestic dwelling investigated, the data presented in Tables 27 and 28 correspond to the 14-hour space heating schedule. These results were utilised for subsequent analysis and discussion of the system's performance.

Table 21. Energy and environmental impacts of heat pump system for two storage tank sizes

Storage tank size (Litres)	**200**	**300**
Thermal load (kWh)	8330	8610
Heat pump electrical Energy input (kWh)	4706	4920
Heat pump seasonal COP (total thermal energy delivered/total electrical power input)	1.77	1.75
Capital cost of heat pump	£4500	£4500
Capital cost of storage tank	£1000	£1300
Installation cost of heat pump system	£3000	£3000
Unit cost of electricity (includes standing charge and 5% VAT, p/kWh) (Rob, 2025)	29.94	29.94
Emission factor for electricity $kgCO_2e/kWh$ (generation and distribution) (Department for Energy Security and Net Zero, 2025)	0.207	0.207
Total installed cost (£)	7500	7800
Annual running cost (£)	1408	1473
Annual emissions ($kgCO_2e$)	974	1018

The capital and installation costs of a 4.5 kW thermal capacity heat pump at an ambient temperature of 7 °C and hot water delivery temperature of 60 °C and a 12 kW system gas boiler as well as the cost of the two thermal storage tanks are average costs obtained from manufacturers. The results show that the use of the 300 L storage tank will lead to a slightly higher capital cost of approximately £300 and slightly higher seasonal energy consumption in the case of both the heat pump and the gas boiler. However, it will provide higher flexibility in the use of domestic hot water for showers and better temperature control in the space, especially in colder winter conditions. Therefore, the main determinant in the choice of storage tank will be the availability of space to accommodate a 300 L tank. Another option is to use a combination gas boiler rather than a system boiler, which will eliminate the need for a storage tank but will necessitate the use of a higher capacity boiler of the order of 24 or 28 kW to satisfy the domestic hot water flow requirements of the dwelling. The total capital cost of such a system may be lower by approximately £500, but the control of hot water flow for showers will be affected by the other simultaneous hot water use in the dwelling.

The cost of radiators and piping has not been included in the analysis as it has been assumed to be the same for the CO_2 heat pump that will be able to deliver hot water at 60 °C and the gas boiler.

The 60 °C delivery temperature is considered satisfactory for well-insulated dwellings for both heat pumps and gas boilers. The latest Part L regulations recommend a flow temperature of 55 °C (Flexiheat UK, 2025).

4.17 Thermoeconomic analysis of heat pumps and gas boilers

It is now universally accepted that heat pumps will play a significant role in the decarbonisation of space heating in domestic dwellings. Heat pump technology is now becoming available that can provide water flow temperatures similar to those of gas boilers and, therefore, can be used as a direct replacement of gas boilers without the need to replace existing radiators. The COP of the heat pump, though, reduces as the hot water supply temperature is increased.

A heat pump will require a thermal storage tank to satisfy the domestic hot water requirements and supplement the heat pump output when there is a simultaneous demand for space and domestic hot water heating. Thermal storage can also enable the heat pump to be switched off during periods of maximum grid demand, thus enabling the provision of demand services to the grid.

Table 22. Energy and environmental impacts of gas boiler system for two storage tank Sizes

Storage tank size (Litres)	**200**	**300**
Thermal load (kWh)	8330	8610
Condensing system boiler efficiency (Galliers, 2025)	0.91	0.91
Boiler energy input (kWh)	9153	9462
Capital cost of boiler (£)	1500	1500
Capital cost of storage tank (£)	1000	1300
Installation cost of boiler (£)	1200	1200
Unit cost of gas p/kWh (Rob, 2025)	8.05	8.05
Emission factor for gas (kgCO_2e)	0.181	0.181
Total installed cost (£)	3700	4000
Annual running cost (£)	737	762
Annual emissions (kgCO_2e)	1656	1712

Even though many small domestic dwellings nowadays use combination boilers that do not require thermal storage external to the boiler, better thermal comfort and management of domestic hot water usage for larger dwellings can be achieved through the use of ‘system’ boilers that require thermal storage if space is available for the installation of the storage tank.

As the market and skilled personnel for the installation of heat pumps increase, their installed cost is expected to decrease. Experience with their use will also increase the confidence of prospective users of the technology. The current government grant of £7,500 for the installation of heat pumps reduces the cost below that of boilers for new installations in well-insulated dwellings. In the UK, however, 80% of the dwellings that will be in use in 2050 have already been built. The decarbonisation of these dwellings presents a significant challenge due to the high cost of retrofitting to enable low-temperature heat pumps that deliver heat up to 55 °C to be effective.

The CO_2 heat pump developed at Brunel University of London has been demonstrated to be able to deliver hot water temperatures up to 80 °C, which is equivalent to that of domestic boilers. Their use will enable the retrofit of heat pumps in existing dwellings without the need for extensive and costly retrofit and the replacement of radiators in the near term. The results of tests at high temperatures and the use of Phase Change Material storage, which halves the volume of storage required compared to hot water storage, will be presented in a follow-up chapter. 4.18 Conclusions

In this chapter, a study of a transcritical CO_2 air-to-water heat pump heating system integrated with a hot water thermal energy storage tank to satisfy the heat demand of a well-insulated 4-bedroom semi-detached dwelling in the London area (UK) is presented. The heat pump performance characteristics were obtained from controlled tests in environmental test chambers at Brunel University, and the performance of the integrated heating system was modelled using the TRNSYS simulation software. The following are the key outcomes of the study.

The transcritical CO_2 air-to-water heat pump, developed and constructed in the laboratories of Brunel University, was demonstrated to deliver hot water temperatures of up to 80 °C, comparable to those achieved by conventional gas boilers. The results presented in this study correspond to flow temperatures in the range of 55 and 60 °C, which are recommended for well-insulated domestic dwellings.

It has been shown that hot water storage tanks between 200 and 300 Litres can provide the required thermal environment in the domestic dwelling during the occupied periods. The smaller storage tank will struggle to maintain the indoor temperature during outdoor ambient temperature below 3 °C. This shortcoming can be addressed by running the heat pump longer during the morning period. The smaller storage tank may also have limitations if more than two dwelling occupants decide to have a shower at the same time. The 300 L storage tank offers more flexibility but at slightly higher capital and running costs for the system. The higher running cost arises from the higher thermal losses from the tank. The choice between the two tanks will mainly be based on space availability for the larger tank and the flexibility in temperature control for space and domestic hot water heating it provides.

For the heat pump tested and current domestic electricity and gas prices and emission factors, the annual running cost of the heat pump was found to be approximately double that of the gas boiler but offering 40% reduction in CO_2 emissions.

The ability of the CO_2 heat pump to provide water flow temperature at different levels depending on the thermal load and heat distribution system makes it suitable for a wide range of applications. Further work will focus on the design and control optimisation of the integrated heat pump-based heating system for domestic applications with both hot water and PCM thermal energy storage.

Chapter 5 Transcritical CO_2 Heat Pump Numerical Modelling

5.1 Overview of the modelling approach

The heat pump system investigated in this study comprises four interdependent components: the compressor, gas cooler, expansion valve, and evaporator, as illustrated in Figure 80. A simulation of this heat pump system should account for the interdependent behavior of these components, as well as the relevant methodologies to predict component-specific parameter values.

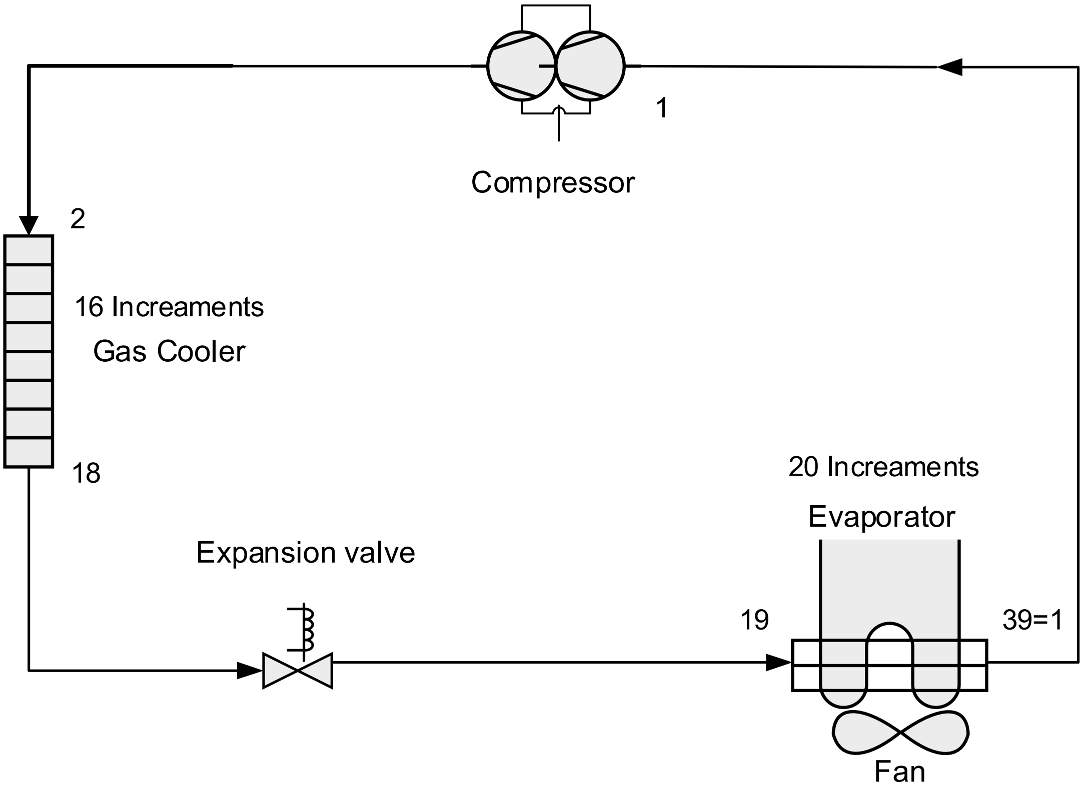

Figure 79. Schematic of Transcritical CO2 AWHP cycle

The operational process is started at cycle point (1) shown in Figure 81. Initially, the low-pressure and low-temperature superheated CO_2 gas is compressed by the compressor, raising its pressure and temperature at cycle point (2). The high-temperature, high-pressure supercritical CO_2 gas then undergoes cooling in the gas cooler, where it transfers heat to the return water at cycle point (18). For the brazed plate gas cooler, the heat exchanger is divided into 18 increments (or segments) along the refrigerant flow direction. Each increment represents a small control volume in which energy balance equations are solved independently. Within each segment, local values of temperature, pressure, enthalpy, and heat transfer coefficient are calculated. This discretisation is particularly important in a transcritical CO_2 system, because the refrigerant experiences strong property variations near the pseudo-critical region. The specific heat, density, and heat transfer coefficients change rapidly along the gas cooler length. By dividing the gas cooler into 18 increments, the model can:

- Accurately track temperature glide of CO_2
- Capture rapid property changes near the pseudo-critical temperature
- Improve prediction of heat rejection and outlet conditions

- Enhance numerical stability

Thus, “18 increments” means the gas cooler is divided into 18 computational segments for detailed heat transfer analysis.

Subsequently, the high-pressure CO_2 gas flows through the EEV, where it undergoes isenthalpic expansion, resulting in a low-pressure, low-temperature CO_2 gas-liquid mixture at cycle point (19). This mixture then absorbs heat from the ambient air in the evaporator at the cycle point (39). Similarly, the evaporator is divided into 20 increments along the refrigerant flow path. In the evaporator, CO_2 undergoes phase change (two-phase region), where heat transfer characteristics differ significantly between liquid, two-phase, and superheated regions. The superheated CO_2 gas then re-enters the compressor to complete the cycle at cycle point (1).

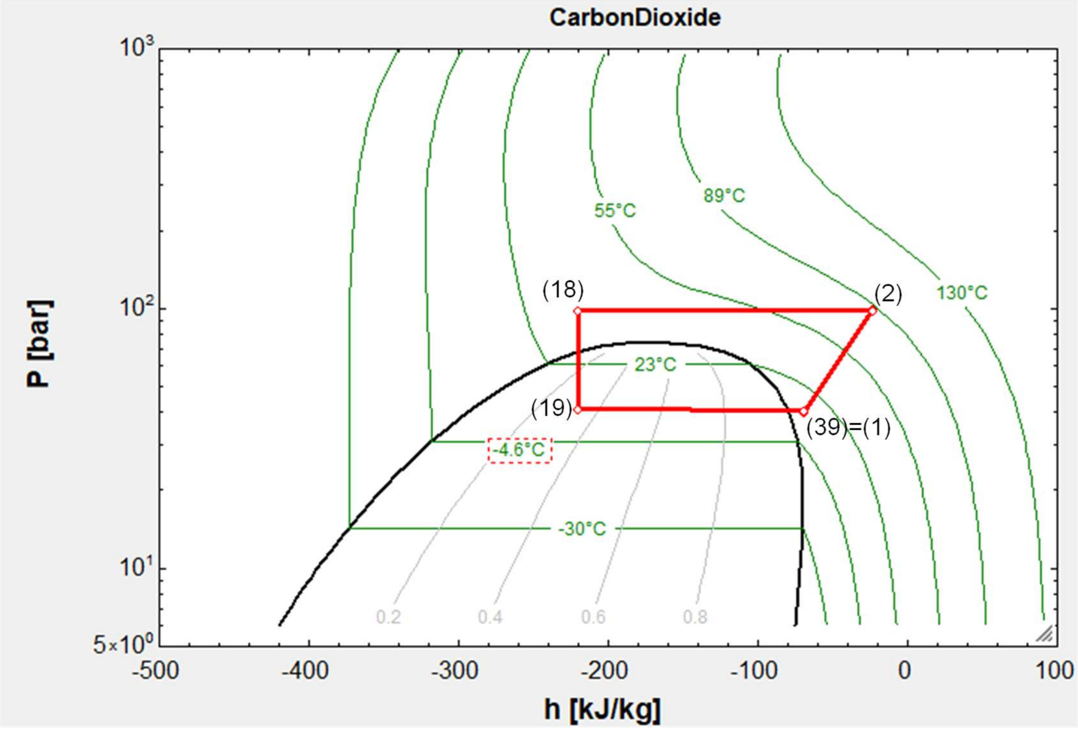

Figure 80. Transcritical CO_2 AWHP p-h diagram

5.2 Modeling of transcritical CO_2 heat pump

Transcritical CO_2 heat pump systems are modeled using thermodynamic analysis that incorporates the transport properties of both the refrigerant and the secondary fluids, typically water and air. The system is represented through conservation equations derived from the energy balance of its individual components. To account for variations along the length of the system, all heat exchangers are discretized, and momentum and energy conservation equations are applied to each segment.

This study's numerical model will be implemented utilising the Engineering Equation Solver (EES) simulation program. This program is considered appropriate because of its inherent thermodynamic and transport property functionalities, together with its integrated numerical solver, which can do both straightforward and iterative computations.

5.3 Modeling of individual components

The components of the heat pump cycle will be modelled in the sections that follow. There are two types of inputs that can be considered while analysing the component models: fixed and non-fixed. Although the geometry and material of the heat exchanger are considered fixed inputs, the boundary conditions of the CO_2 and secondary fluids (water and air) are considered non-fixed inputs. These parameters can change based on the operating conditions of the cycle and the interdependence of its components.

The following are examples of simplified assumptions included in this model:

- The system is functioning at a steady state
- The changes in potential and kinetic energy are considered negligible
- Compression is an adiabatic process
- The heat exchangers (gas cooler and evaporator) are operated adiabatically
- No heat is lost through the pipes
- No pressure loss in the water pipes
- No pressure drop in the air side
- The refrigerant does not contain any oil
- Expansion is an isenthalpic process

5.3.1 Compressor model

The adiabatic compressor model, which disregarded the influence of the specific internal configuration, was formulated based on the principle of efficiency. The CO_2 mass flow rate, outlet specific enthalpy, and compressor power consumption were eventually calculated as follows:

$$W_{comp} = m_r(h_2 - h_1)$$

$$m_r = \rho \gamma_v V_{com} n_{com}$$

(1)

$$h_2 = h_1 + \frac{h_{2,is} - h_1}{\gamma_{is}} \qquad (2)$$

where h_2, is (kJ·Kg^{-1}) denotes the specific enthalpy of the compressor outlet through the isentropic compression. The volumetric efficiency (γ_v) and the isentropic efficiency (γ_{is}) both were assumed to be 0.9.

5.3.2 Gas-Cooler model

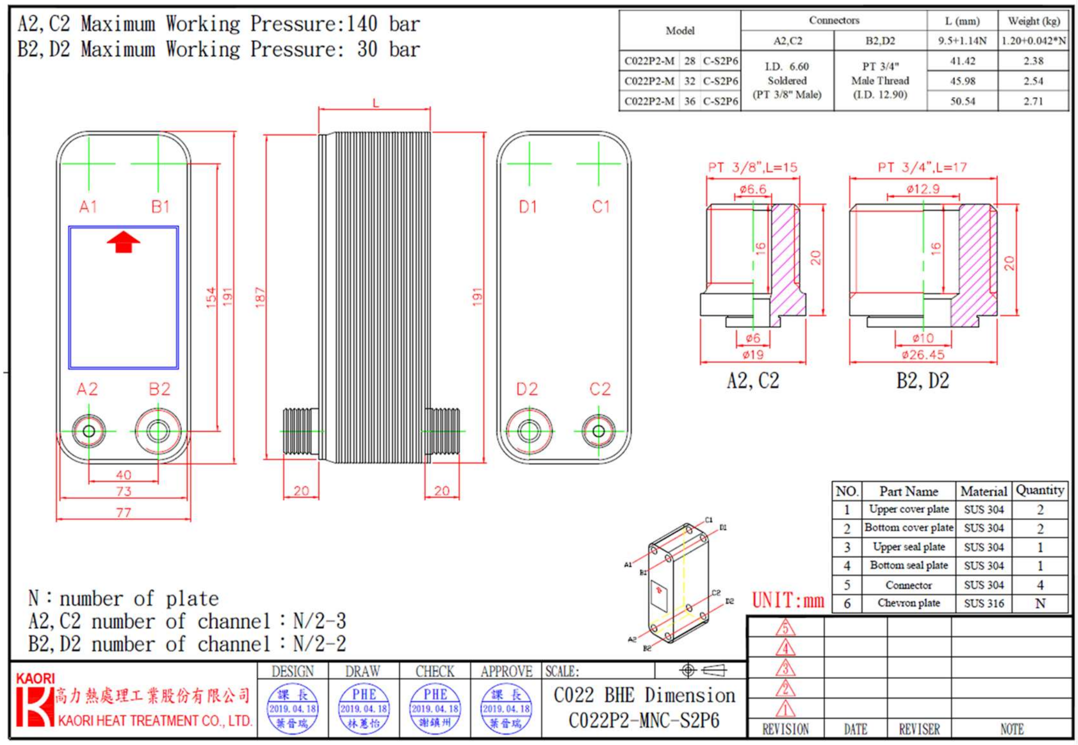

Model			Connectors		L (mm)	Weight (kg)
			A2,C2	B2,D2	9.5+1.14N	1.20+0.042*N
C022P2-M	28	C-S2P6	I.D. 6.60 Soldered (PT 3/8" Male)	PT 3/4" Male Thread (I.D. 12.90)	41.42	2.38
C022P2-M	32	C-S2P6			45.98	2.54
C022P2-M	36	C-S2P6			50.54	2.71

NO.	Part Name	Material	Quantity
1	Upper cover plate	SUS 304	2
2	Bottom cover plate	SUS 304	2
3	Upper seal plate	SUS 304	1
4	Bottom seal plate	SUS 304	1
5	Connector	SUS 304	4
6	Chevron plate	SUS 316	N

Figure 81. Specification of Brazed plate heat exchangers

Table 23. Design/selection of gas cooler for 4.5 kW heat pump

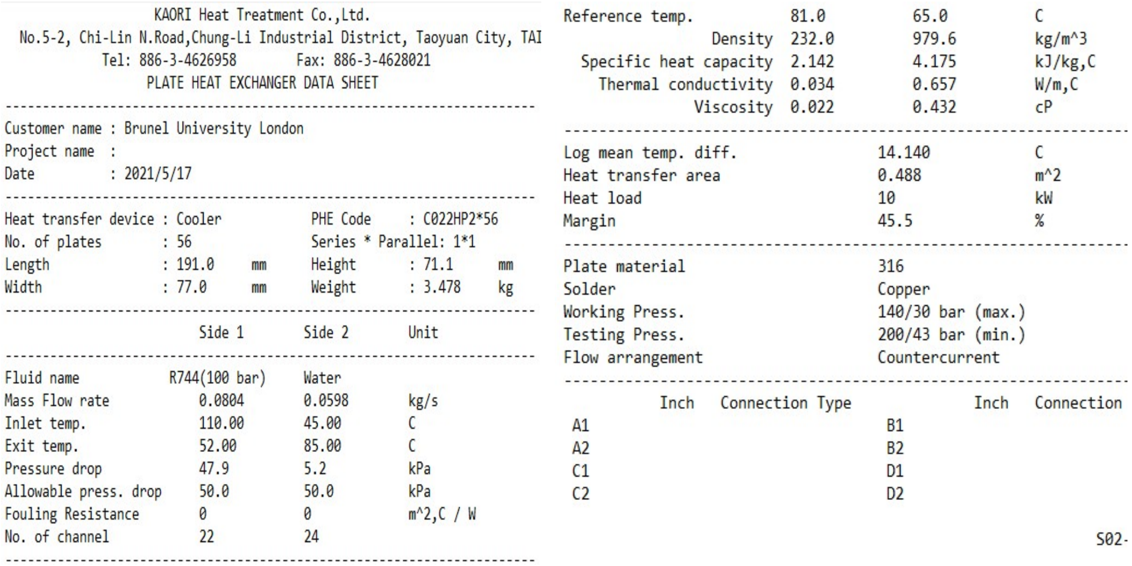

```
              KAORI Heat Treatment Co.,Ltd.
  No.5-2, Chi-Lin N.Road,Chung-Li Industrial District, Taoyuan City, TAI
            Tel: 886-3-4626958        Fax: 886-3-4628021
                 PLATE HEAT EXCHANGER DATA SHEET
-----------------------------------------------------------------
Customer name : Brunel University London
Project name  :
Date          : 2021/5/17
-----------------------------------------------------------------
Heat transfer device : Cooler          PHE Code      : C022HP2*56
No. of plates        : 56              Series * Parallel: 1*1
Length               : 191.0    mm     Height        : 71.1      mm
Width                : 77.0     mm     Weight        : 3.478     kg
-----------------------------------------------------------------
                        Side 1        Side 2        Unit
-----------------------------------------------------------------
Fluid name          R744(100 bar)     Water
Mass Flow rate          0.0804        0.0598        kg/s
Inlet temp.             110.00        45.00         C
Exit temp.              52.00         85.00         C
Pressure drop           47.9          5.2           kPa
Allowable press. drop   50.0          50.0          kPa
Fouling Resistance      0             0             m^2,C / W
No. of channel          22            24
-----------------------------------------------------------------
```

```
Reference temp.              81.0         65.0          C
               Density       232.0        979.6         kg/m^3
  Specific heat capacity     2.142        4.175         kJ/kg,C
    Thermal conductivity     0.034        0.657         W/m,C
               Viscosity     0.022        0.432         cP
-----------------------------------------------------------------
Log mean temp. diff.                   14.140           C
Heat transfer area                     0.488            m^2
Heat load                              10               kW
Margin                                 45.5             %
-----------------------------------------------------------------
Plate material                         316
Solder                                 Copper
Working Press.                         140/30 bar (max.)
Testing Press.                         200/43 bar (min.)
Flow arrangement                       Countercurrent
-----------------------------------------------------------------
            Inch   Connection Type              Inch   Connection
 A1                                     B1
 A2                                     B2
 C1                                     D1
 C2                                     D2

                                                                S02-
```

In this model, the gas cooler is represented as a counterflow brazed plate heat exchanger. For the transcritical CO_2 system, a brazed plate gas cooler was selected and modelled using Engineering Equation Solver (EES). The brazed plate configuration was chosen due to its compact structure, high heat transfer efficiency, and suitability for high-pressure CO_2 applications. In transcritical operation, the gas cooler plays a critical role in rejecting heat at pressures above the critical point, where no distinct phase change occurs and significant property variations are observed near the pseudo-critical region. To accurately represent this behaviour, the gas cooler was modelled in EES using a discretised approach, enabling detailed calculation of local heat transfer, temperature variation, and pressure drop along the flow path. The geometric dimensions of the brazed plate gas cooler are presented in Figure 82, while its technical specifications, including heat transfer area, number of plates, and design parameters, are summarised in Table 29. This modelling framework allows precise prediction of gas cooler performance under transcritical operating conditions.The finite element method is employed to simulate the behavior of the gas cooler. For each finite element within the gas cooler, the Effectiveness-Number of Transfer Unit (ε-NTU) method is applied to compute the heat transfer between the CO_2 refrigerant and the secondary fluid (water), based on the known inlet conditions of both fluids. This approach incorporates the geometry of the heat exchanger and the heat capacity rates of the two fluid streams to determine the actual heat transfer occurring within the exchanger. The resulting heat transfer is then compared to the maximum heat transfer rate, which corresponds to the ideal scenario in which the heat exchanger operates at 100% efficiency. The maximum achievable heat transfer for a single finite element is defined as:

$$Q_{max} = C_{min} \cdot (T_{hot,i} - T_{cold,i}) \tag{3}$$

$$Q_{act} = \varepsilon \cdot C_{min} \cdot \left(T_{hot,i} - T_{cold,i}\right) \quad (4)$$

The effectiveness, ε, is defined as the ratio of the actual heat transfer to the maximum possible heat transfer.

$$\varepsilon = \frac{Q_{act}}{Q_{max}} \quad (5)$$

The effectiveness is a function of the NTU and heat capacity ratio, C_r.

The number of transfer units, NTU, is expressed by Eq. (6) below

$$NTU = \frac{UA}{C_{min}} \quad (6)$$

$$C_r = \frac{C_{min}}{C_{max}} \quad (7)$$

The overall heat transfer coefficient, UA, is calculated based on the thermal resistance between the two fluids.

$$\frac{1}{U} = \frac{1}{h_{CO_2}} + \frac{1}{h_{water}} + \frac{t}{k_{wall}} \quad (8)$$

$$\varepsilon = \frac{1-e^{-NTU(1-C_r)}}{1-C_r e^{-NTU(1-C_r)}} \quad (9)$$

Once the heat transfer rate in the gas cooler is determined, the outlet temperature of the heated water can be calculated using the equation below:

$$T_{water,out} = \frac{Q_{act}}{m_{water}C_{p,water}} + T_{water,in} \quad (10)$$

Where m_{water} is the water mass flow rate $\left({}^{kg}/_{s}\right)$; $C_{p,water}$ is the specific heat of water $\left({}^{kJ}/_{Kg \cdot K}\right)$; $T_{water,out}$ and $T_{water,in}$ are the water outlet and inlet temperatures (°C) of the heat exchangers. The properties of water and CO_2 are determined by using REFPROP in EES software.

The total heat transfer coefficient (h_{total}) is calculated based on the averaged heat transfer rate $\left(Q_{avg}\right)$ the heat transfer area (A) and the actual mean temperature difference (ΔT):

$$h_{total} = \frac{Q_{avg}}{A\Delta T} \quad (11)$$

The heat transfer area (A) of the brazed plate heat exchangers can be calculated as (Shon et al., 2018).

$$A_{tot} = \emptyset W L_p N_{plate} \tag{12}$$

where $\emptyset$ is the area enlargement factor that accounts for the increase in area due to the corrugation of the plates; W, L and N_p represent the width, port-to-port length, and the number of heat exchange plates, respectively. The area enlargement factor is defined as:

$$\emptyset \approx \frac{1}{6}\left(1 + \sqrt{1 + X^2} + 4\sqrt{1 + \frac{X^2}{2}}\right) \tag{13}$$

Where

$$X = \frac{\pi b}{p} \tag{14}$$

Similarly, due to the variations in specific heat, the CO_2 temperature changes nonlinearly during the heat transfer process. Consequently, the commonly used concept of bulk temperature, which is the average of the inlet and outlet temperatures, does not adequately represent the required thermodynamic properties. Instead, the concept of CO_2 mean temperature (T_m) is adopted (Liu et al., 2014).

The total heat transfer coefficient comprises the heat transfer coefficients for the CO_2 and water sides, as well as the wall thermal resistance. It can also be expressed as:

$$\frac{1}{U} = \frac{1}{h_{CO_2}} + \frac{1}{h_{water}} + \frac{t}{k_{wall}} \tag{15}$$

Where $h_{CO_2}$and h_{water} are the heat transfer coefficients in the CO_2 and water sides; t is the thickness of the plate; k_{wall} is the thermal conductivity of the wall. h_{water} is calculated by applying the correlation of Longo (2008) because the plate geometry and the range of Reynolds numbers are similar to those of the studied heat exchanger.

$$Nu_{water} = 0.277 {Re_{water}}^{0.766} {Pr_{water}}^{0.33} \tag{16}$$

$5 < Pr_{water} < 10$ and $200 < Re_{water} < 1200$

$$h_{water} = \frac{Nu_{water} k_{water}}{D} \tag{17}$$

The hydraulic diameter (D) can be defined as:

$$D = \frac{2b}{\emptyset}$$

(18)

where b is the corrugation depth of the plate. The Reynolds number (Re) can be calculated as:

$$Re = \frac{\rho v D}{\mu} \tag{19}$$

where v is the flow velocity of fluid and is defined as:

$$v = \frac{V}{bWN_{ch}} \tag{20}$$

Where ρ and μ are the density and dynamic viscosity of the fluid; V is the volumetric flow rate, N_{ch} is the number of the channels for fluid.

$$Pr = \frac{C_p \mu}{k} \tag{21}$$

5.3.4 Expansion valve model

Because the simulation process of the expansion valve is under adiabatic conditions, its expansion process is isenthalpic.

$$h_{18} = h_{19} \tag{22}$$

5.3.5 Evaporator model

For the transcritical CO_2 system, the evaporator was modelled as a cross-flow fin-and-tube heat exchanger, as illustrated in Figure 83. The detailed specifications and geometric dimensions of the evaporator are provided in Table 30. In the modelling approach, the evaporator was divided into distinct regions to accurately capture the thermodynamic behaviour of CO_2 during evaporation. As shown in Figures 84 and 85, the geometry was discretised into two primary sections: the two-phase region, where phase change occurs and vapour quality varies along the flow path, and the superheated region, where the refrigerant is fully vaporised and undergoes sensible heating. This division allows for more precise calculation of local heat transfer coefficients, pressure drop, and temperature distribution. Furthermore, the evaporator incorporates an A-frame sine-wave fin geometry, depicted from the top and side views in Figures 84 and 85, respectively. The sine-wave fin design enhances air-side turbulence and increases the effective heat transfer area, thereby improving overall heat exchange performance. This detailed geometric representation within the model ensures accurate simulation of the evaporator's thermal behaviour under transcritical CO_2 operating conditions.Due to the phase change of CO_2 and air dehumidification during evaporation, a steady-state distributed-parameter model was employed for the evaporator. The model was divided into several micro-units according to uniform specific enthalpy variations on the air side.

The computations for each micro-unit were streamlined based on the following fundamental assumptions:

i. The flow process was assumed to follow a reverse flow pattern.
ii. The pressure drops on both the CO_2 side and the air side were considered negligible.
iii. The thermophysical properties and local heat transfer coefficients on both the air side and the CO_2 side were assumed to be uniform.
iv. The thermal resistance of the tube wall was considered negligible.
v. The micro-units were assumed to be either completely dry or fully wet.

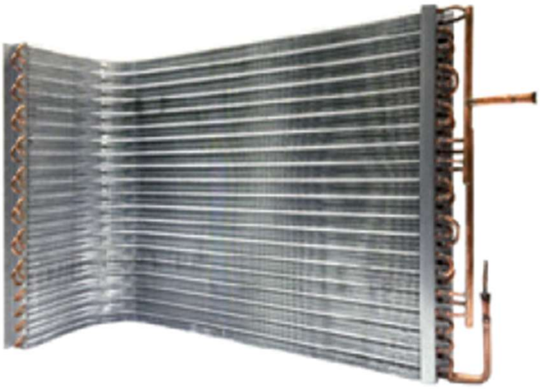

Figure 82. Evaporator coil 5 mm tube diameter from CIG

Table 24. Design/selection of evaporator for 4.5 kW heat pump

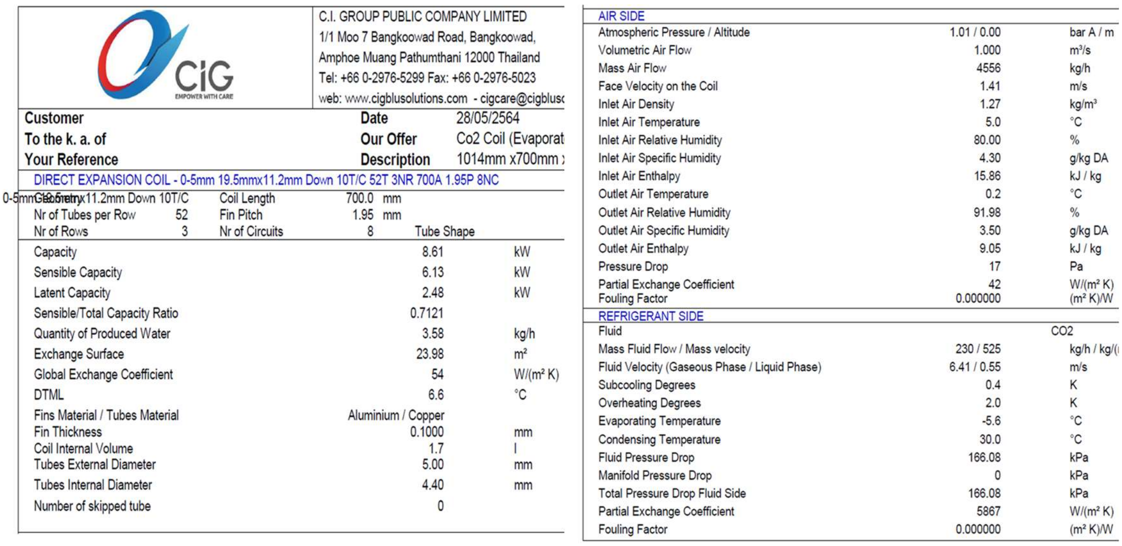

C.I. GROUP PUBLIC COMPANY LIMITED
1/1 Moo 7 Bangkoowad Road, Bangkoowad,
Amphoe Muang Pathumthani 12000 Thailand
Tel: +66 0-2976-5299 Fax: +66 0-2976-5023
web: www.cigblusolutions.com - cigcare@cigblus

Customer		**Date**	28/05/2564
To the k. a. of		**Our Offer**	Co2 Coil (Evaporat
Your Reference		**Description**	1014mm x700mm

DIRECT EXPANSION COIL - 0-5mm 19.5mmx11.2mm Down 10T/C 52T 3NR 700A 1.95P 8NC

Geometry	0-5mm 19.5mmx11.2mm Down 10T/C	Coil Length	700.0	mm
Nr of Tubes per Row	52	Fin Pitch	1.95	mm
Nr of Rows	3	Nr of Circuits	8	Tube Shape

Capacity	8.61	kW
Sensible Capacity	6.13	kW
Latent Capacity	2.48	kW
Sensible/Total Capacity Ratio	0.7121	
Quantity of Produced Water	3.58	kg/h
Exchange Surface	23.98	m²
Global Exchange Coefficient	54	W/(m² K)
DTML	6.6	°C
Fins Material / Tubes Material	Aluminium / Copper	
Fin Thickness	0.1000	mm
Coil Internal Volume	1.7	l
Tubes External Diameter	5.00	mm
Tubes Internal Diameter	4.40	mm
Number of skipped tube	0	

AIR SIDE		
Atmospheric Pressure / Altitude	1.01 / 0.00	bar A / m
Volumetric Air Flow	1.000	m³/s
Mass Air Flow	4556	kg/h
Face Velocity on the Coil	1.41	m/s
Inlet Air Density	1.27	kg/m³
Inlet Air Temperature	5.0	°C
Inlet Air Relative Humidity	80.00	%
Inlet Air Specific Humidity	4.30	g/kg DA
Inlet Air Enthalpy	15.86	kJ / kg
Outlet Air Temperature	0.2	°C
Outlet Air Relative Humidity	91.98	%
Outlet Air Specific Humidity	3.50	g/kg DA
Outlet Air Enthalpy	9.05	kJ / kg
Pressure Drop	17	Pa
Partial Exchange Coefficient	42	W/(m² K)
Fouling Factor	0.000000	(m² K)/W

REFRIGERANT SIDE		
Fluid		CO2
Mass Fluid Flow / Mass velocity	230 / 525	kg/h / kg/(
Fluid Velocity (Gaseous Phase / Liquid Phase)	6.41 / 0.55	m/s
Subcooling Degrees	0.4	K
Overheating Degrees	2.0	K
Evaporating Temperature	-5.6	°C
Condensing Temperature	30.0	°C
Fluid Pressure Drop	166.08	kPa
Manifold Pressure Drop	0	kPa
Total Pressure Drop Fluid Side	166.08	kPa
Partial Exchange Coefficient	5867	W/(m² K)
Fouling Factor	0.000000	(m² K)/W

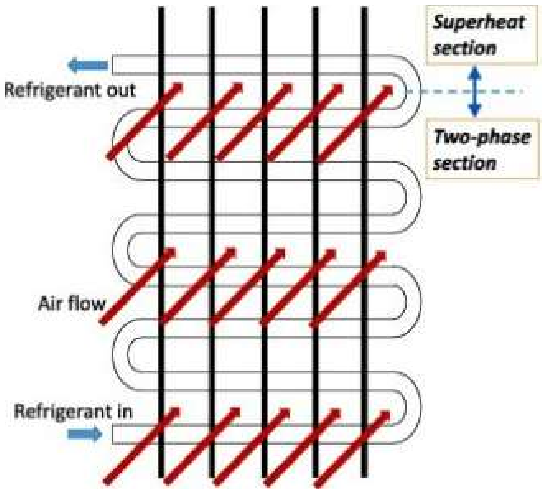

Figure 83. Geometry division between two-phase and superheated sections

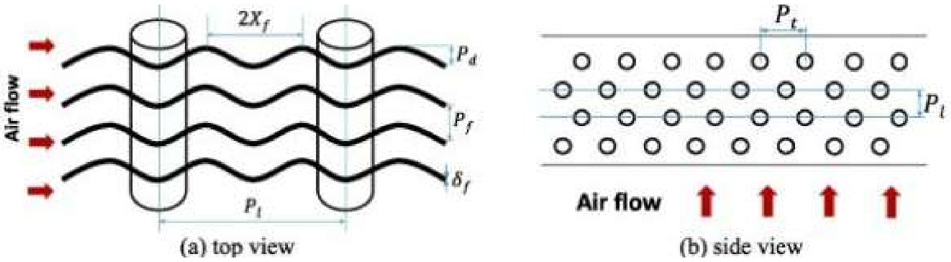

Figure 84. Geometry of the A-frame sine-wave finned-tube heat exchanger

For finned-tube heat exchangers, it is more convenient to work with an overall heat transfer coefficient:

$$Q_{ev} = UA\Delta T \tag{23}$$

where U is the overall heat transfer coefficient, A is the heat transfer area and ΔT is the temperature difference between the fluid streams.

The overall heat transfer coefficient is

$$\frac{1}{UA} = \frac{1}{h_{c,r}A_i} + \frac{\ln\left(\frac{D_o}{D_i}\right)}{2\pi kL} + \frac{1}{\gamma_o h_{c,a}A_o} \tag{24}$$

with $h_{c,a}$ being the air side convection heat transfer coefficient, γ_o the overall surface efficiency and A_o the total outside heat transfer area. The following sections provide details on the determination of the convection heat transfer coefficients. The calculation of γ_o for a finned surface is assumed to be 0.9.

5.3.6 Single phase heat transfer

The heat transfer coefficient is calculated using the Nusselt number. The Nusselt number (Nu) is a dimensionless quantity that represents the ratio of convective to conductive heat transfer and is defined as:

$$N_u = \frac{h_c D_h}{k} \tag{25}$$

Where the Nusselt number is a function of the non-dimensional Reynolds (Re) and Prandtl (Pr) numbers. The Re number is defined by equation (19) and is the heat transfer coefficient. The Pr number provides a measure of the ratio of momentum and thermal diffusivities and is defined as by equation (21)

For the refrigerant side, the single-phase heat transfer coefficient is calculated by the Gnielinski's correlation (Gnielinski, 1976). This correlation is developed for the turbulent flow in a circular tube.

$$Nu_D = \frac{\left(\frac{f}{8}\right)(Re_D - 1000)P_r}{1 + 12.7\left(\frac{f}{8}\right)^{0.5}\left({P_r}^{0.66} - 1\right)} \tag{26}$$

where f is the friction factor as defined below. The friction factor, Reynolds number and Prandtl number are evaluated at the average fluid temperature.

The friction factor is calculated using the recently developed Ghanbari, Farshad and Rieke correlation (Ghanbari et al. 2011)

$$f = \left(-1.52 log\left(\left(\frac{e/D_h}{7.21}\right)^{1.042} + \left(\frac{2.731}{R_e}\right)^{0.915}\right)\right)^{-2.169} \tag{27}$$

e is the relative roughness of the tube wall and Re is the Reynolds number. This equation is applicable for the range 2100 < Re < 108 and 0 < e < 0.05. The Reynolds number provides an indication of the ratio of inertia to viscous forces. A higher Reynolds number indicates that inertial forces dominate over viscous forces, leading to turbulent flow behaviour, whereas lower values indicate laminar flow conditions.

5.3.7 Two phase heat transfer

For two-phase flow, the heat transfer equation of Wattelet et al. (1994) was chosen. They define the heat transfer correlation for pure refrigerant as follows:

$$h_{tp} = h_{nbc} + h_{cec} = N \cdot h_{SA} + F_p \cdot h_{lo} \tag{28}$$

Where N, h_{SA},F_p and h_{lo} are defined in equations below. N is a factor due to the nucleate boiling effect as is represented using the dimensionless Martinelli parameter (X_{tt}) and the boiling number (B_o).

$$N = 4048{X_{tt}}^{1.22}{B_o}^{1.13} \tag{29}$$

The Martinelli parameter is obtained from the following equation, as used by Jung et al. (1989)

$$X_{tt} = \left(\frac{1-x}{x}\right)^{0.9}\left(\frac{\rho_v}{\rho_l}\right)^{0.5}\left(\frac{\mu_l}{\mu_v}\right)^{0.1} \tag{30}$$

The Boiling number is given by:

$$B_o = \frac{\dot{Q}}{Gh_{lv}} \tag{31}$$

Where h_{lv} is the latent heat of vaporization of the refrigerant.

h_{SA} is the pool boiling heat transfer and the correlation of Stephan and Abdelsalam:

$$h_{SA} = 207\frac{k_l}{bd}\left(\frac{\dot{Q}bd}{k_lT_s}\right)^{0.745}\left(\frac{\rho_v}{\rho_l}\right)^{0.581}Pr^{0.533} \tag{32}$$

Where bd is

$$bd = 0.0146\beta\left(\frac{2\sigma}{g(\rho_l-\rho_v)}\right)^{0.5} \tag{33}$$

And the contact angle β=35°

The F factor, as used, has the following correlation for $X_{tt} < 1$

$$F_p = 2.37\left(0.29+\frac{1}{X_{tt}}\right)^{0.85} \tag{34}$$

And for $1 < X_{tt} < 5$ (Oh & Son 2011)

$$F_p = 2 - 0.1(X_{tt})^{-0.28}(B_o)^{-0.33} \tag{35}$$

And lastly h_l is determined using the Dittus-Boelter equation

$$h_l = 0.023\frac{k_l}{D_h}{Re_l}^{0.8}Pr^{0.4} \tag{36}$$

5.3.8 Air side heat transfer correlations

The fin-side heat transfer is typically calculated using Colburn j-factor correlations. The Nusselt number is a function of the Colburn j-factor, the Reynolds number and the Prandtl number as shown by ROUSSEAU and VAN ELDIK (2011)

$$Nu = jRePr^{0.33} \tag{37}$$

The heat transfer coefficient then be calculated using equation (23). For the fin side, under dry surface conditions the Colburn j-factor correlation of Wang et al. (2000) is used.

$$j = \frac{1.2}{[ln(Re_{Dc}{}^{\sigma})]^{2.92}} \tag{38}$$

Where N is the number of tube rows, Re_{Dc} is the Reynolds number for the collar diameter with $D_c = D + 2\delta_f$ and σ is defined as:

$$\sigma = \frac{A_{ff}}{A_{fr}} \tag{39}$$

For a totally wet surface condition the Colburn j-factor correlation proposed by Wang et al. (2000) is used:

$$j = 0.17 \left(\frac{A_{total}}{A_{tube}}\right)^{0.377N} Re_{Dc}{}^{(-0.0142N-0.478)} \left(\frac{S_p}{D_c}\right)^{(0.00412N-0.0217)} \left(\frac{A_{total}}{A_{tube}}\right)^{(-0.114N+\ .440)} \tag{40}$$

On the air side, the thermophysical properties were obtained from the ASHRAE HANDBOOK (2017). The correlations of Li et al. (2018) were selected to calculate the local heat transfer coefficient. On the CO_2 side, the local heat transfer coefficient for the single-phase region was predicted by the Dittus-Boelter correlation (Dittus and Boelter, 1985). The local heat transfer coefficient for the two-phase region was estimated by the correlations of Cheng et al. (2008). However, the flow boiling heat transfer patterns were simplified based on the quality of the vapor-liquid mixture in this paper as follows (S. Wang, Tuo, et al., 2013b):

$x \leq x_{IA}$ gives intermittent flow regime;

$x_{IA} < x \leq x_{di}$ gives annular flow regime;

$x_{di} < x \leq x_{de}$ gives dryout region;

$x_{de} \leq x$ gives mist flow regime.

The evaporator model incorporates known variables such as the air inlet dry-bulb and wet-bulb temperatures (humidity ratio), volume flow rate, CO_2 inlet enthalpy, and CO_2 mass flow rate. Given that there are two rows in the evaporator, at the air side, the air outlet variables of the first row are assumed to be equal to the air inlet variables of the second row for every infinitesimal length of the heat exchanger tube. Based on the energy balance and heat transfer rate equations, and accounting for the discrepancy between the calculated outlet pressure of the evaporator and the set value, the outlet variables are obtained through multiple iterations of variable inputs and calculations.

5.3.9 Evaporator model correlations

Two-phase correlation

The critical quality value, which defines the transition from intermittent to annular flow patterns, is calculated using the correlations proposed by Cheng et al. (2006):

$$x_{IA} = \left(1.8^{1/0.875}\left(\frac{\rho_v}{\rho_l}\right)^{-1/1.75}\left(\frac{\mu_v}{\mu_l}\right)^{-1/7} + 1\right)^{-1} \tag{41}$$

Where:

$\mu: Dynamic\ viscosity\ \left({}^{kg}/_{m.s}\right)$

Note that the subscripts $'l'$ and $'v'$ denote the saturated liquid and vapor state of the CO₂, respectively. For transition between the annular to dryout flow pattern, the critical quality value, also known as the dryout inception quality, is determined with (Wojtan et al., 2005)

$$x_{di} = 0.58exp\left(0.52 - 0.236{We_v}^{0.17}{Fr_{v,Mori}}^{0.17}\left(\frac{\rho_v}{\rho_l}\right)^{0.25}\left(\frac{q}{q_{crit}}\right)^{0.27}\right) \tag{42}$$

Where $We_v\ and\ Fr_{v,Mori}$ represent the vapor Weber number and Froude number, respectively.

These two numbers are equated as follows (MORI et al., 2000):

$$We_v = \frac{G^2 D_i}{{\rho_v}^{\sigma}}$$

(43)

$$Fr_{v,Mori} = \frac{G^2}{\rho_v(\rho_l - \rho_v)gD_i} \tag{44}$$

Where:

$D_i: Innner\ tube\ diameter\ [m^2]$

$G: Mass\ flux\ [kg/m^2]$

$\sigma: Surface\ tension\ [N/m]$

$g{:}\,Gravitational\ constant\ [m/s^2]$

And q_{crit}, the critical heat flux, which is calculated with (Kutateladze, 1948):

$$q_{crit} = 0.131{\rho_v}^{0.5} h_{lv} [g\sigma(\rho_l - \rho_v)]^{0.25}$$

Where:

$h_{lv}{:}\,Latent\ heat\ of\ vaporisation[m^2]$

$q{:}\,Heat\ flux\ \left[{}^{W}\!/_{m^2}\right]$

The dryout region to mist flow transition boundary is calculated with the new criterion developed in this study based on the dryout completion data for CO_2:

$$x_{de} = 0.61exp\left(0.57 - 0.502{We_v}^{0.16}{Fr_{v,Mori}}^{0.15}\left(\frac{\rho_v}{\rho_l}\right)^{-0.09}\left(\frac{q}{q_{crit}}\right)^{0.72}\right) \tag{45}$$

Intermittent flow pattern

The intermittent flow pattern is present when $x \leq x_{l-A}$, where x is the vapor quality of the CO_2 under investigation.

5.4 4.5 kW CO_2 heat pump modelling flow chart

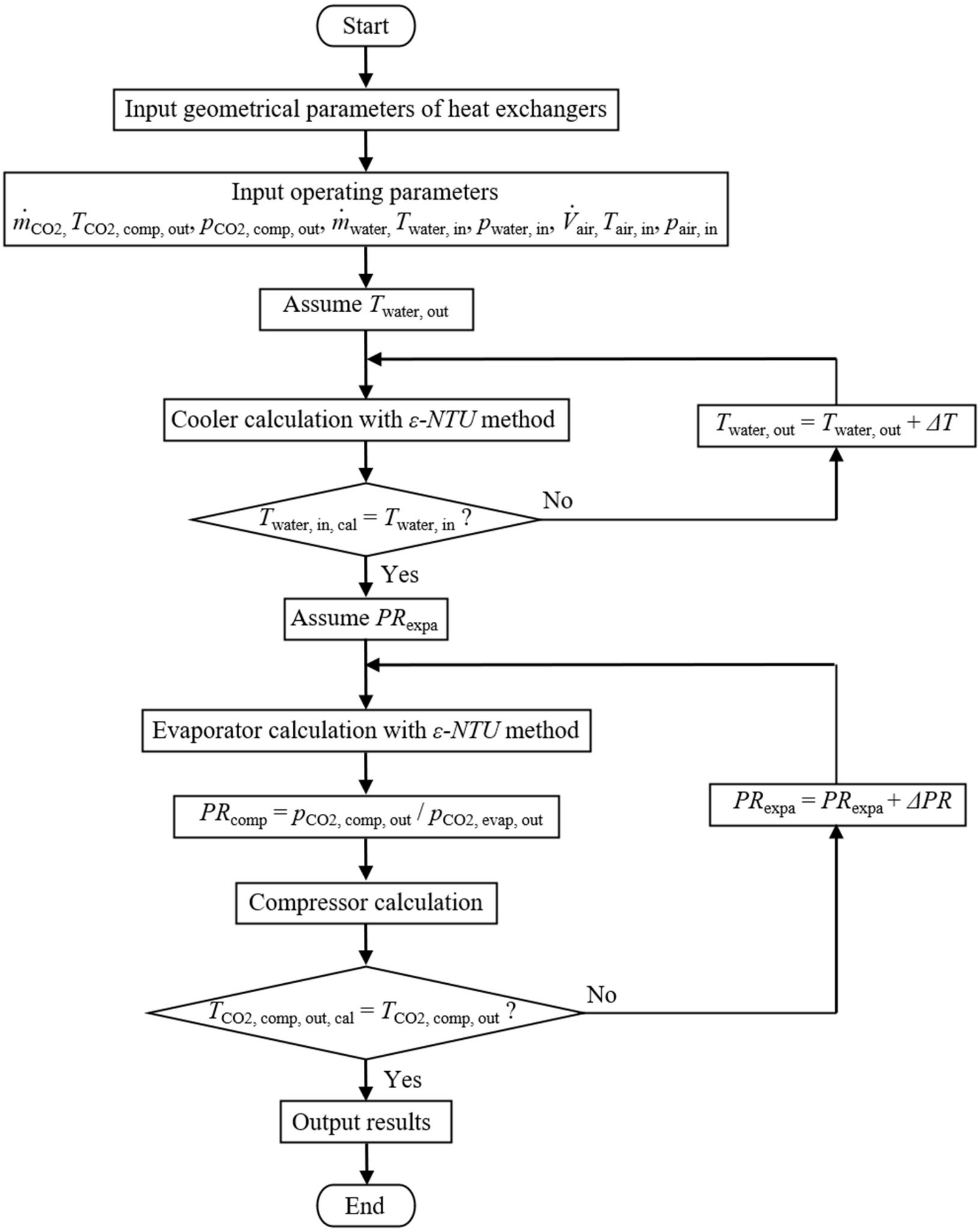

Figure 85. CO_2 heat pump modelling flow chart

5.5 Model validation with experimental results

The experimental results obtained for the 4.5 kW CO_2 air-to-water heat pump (AWHP) under various operating conditions were compared with the corresponding simulated results generated in EES at the same working points in order to validate the model.. This section shows the P-h diagram associated with the working point defined by the input parameters. Figure 87 and Figure 88 show the experimental results and modelling results overlaid on the same P-h diagram.

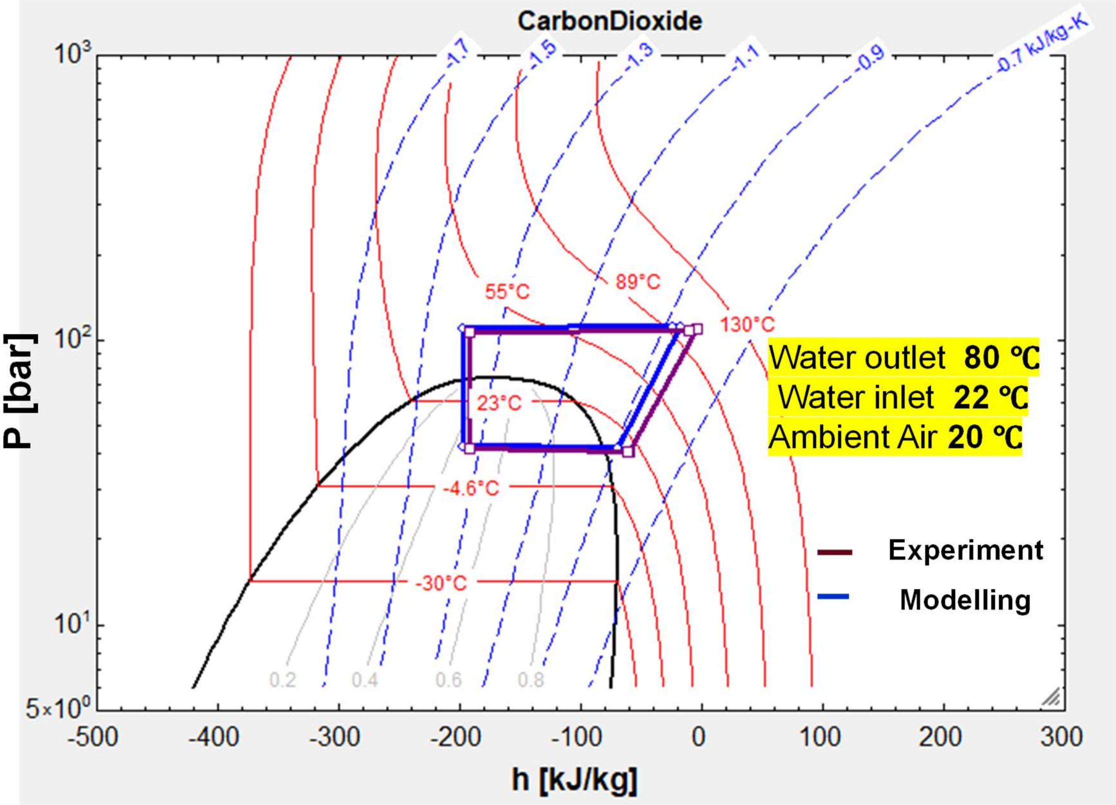

Figure 86. P-h diagram with overlaid experimental and simulated refrigerant cycle

Table 31 illustrates the percent deviation between the modelling and experimental results values for the working point. The experimental results are taken as the reference for the modelling. The accuracy of the modelling is dependent on the accuracy of the measuring equipment used on the experimental system.

Table 25. Measured experimental values vs modelling values

Parameter	Experimental value	Modelling value	Percent deviation
Q_{gc}	5.25	5.33	1.5%
W_c	2.45	2.21	9.8%

COP	2.14	2.41	11.2%

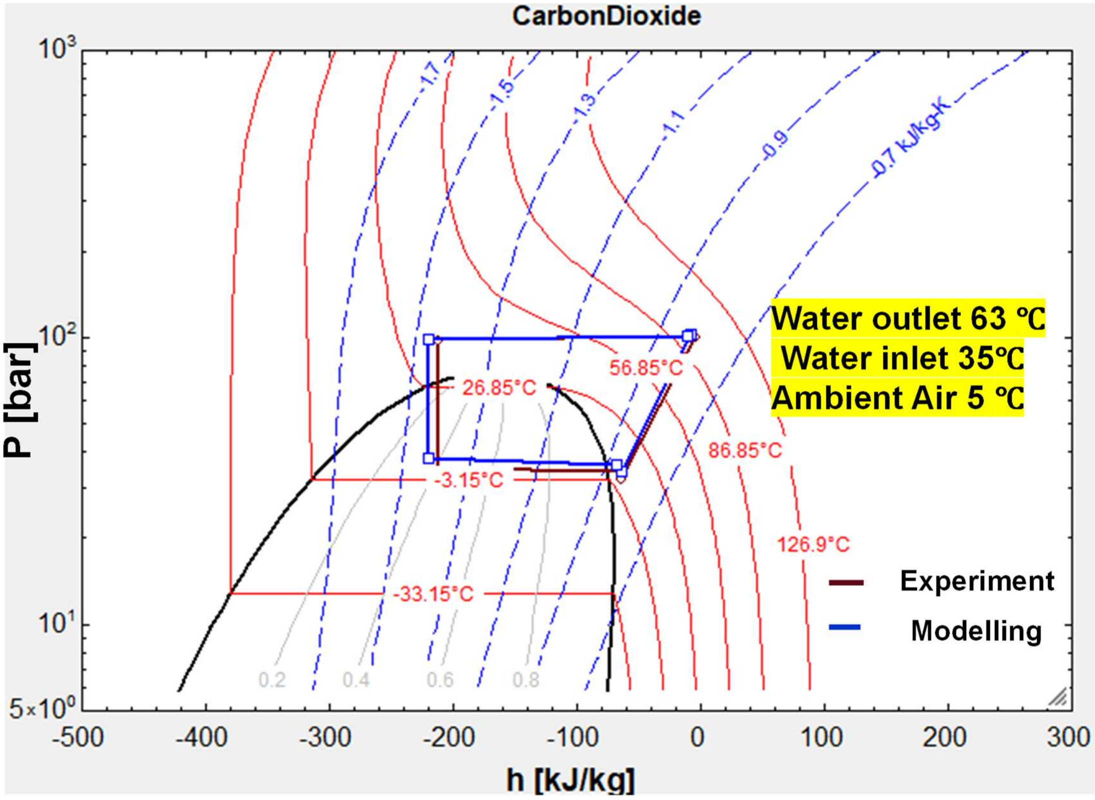

Figure 87. P-h diagram with overlaid experimental and simulated refrigerant cycle

Table 26. Measured experimental values vs modelling values

Parameter	**Experimental value**	**Modelling value**	**Percent deviation**
Q_{gc}	5.25	5.33	1.5%
W_c	2.45	2.21	9.8%
COP	2.14	2.41	11.2%

Chapter 6 Integration of Heat Pump with Thermal Energy Storage System

6.1 Introduction

Thermal energy storage (TES) is essential for facilitating the transition to low-carbon heating and cooling systems. The solution effectively addresses the disparity between energy production and consumption, which can occur across various dimensions, including power, location, time, and temperature. TES facilitates the storage and release of thermal energy, thereby enhancing the sustainability and efficiency of energy systems through the balancing of supply and demand (Raul et al., 2020). TES is a crucial technology for integrating renewable energy sources and heat pumps into modern energy systems. This system enables the effective capture, storage, and release of thermal energy for subsequent utilisation, thus decreasing reliance on fossil fuels and enhancing sustainability. Latent heat thermal energy storage (LHTES) has gained significant interest in recent years within the spectrum of thermal storage technologies. LHTES operates by utilising phase change materials (PCMs) as the medium for storage. These materials can sustain a stable heat release around their phase change temperatures, such as during melting or solidification, and they exhibit a high heat storage capacity. This distinctive characteristic significantly enhances the overall efficacy of thermal energy storage systems (H. Gu et al., 2023).

An air-to-water heat pump (AWHP) is often used in conjunction with a heat storage tank to address the discrepancy between energy supply and heat demand in various applications. This combination also helps reduce operational costs by shifting the charging process from on-peak to off-peak hours, thereby enhancing cost efficiency and optimising energy consumption (Y. Li et al., 2018). This method facilitates grid equilibrium and reduces power expenses for households by enabling them to transition their energy purchases from high-cost to low-cost periods. The integration of PCMs in storage tanks has become increasingly prevalent, as it effectively decreases the necessary volume of the tank or amplifies the quantity of heat stored, thereby enhancing the overall efficiency of thermal energy storage (Zou et al., 2017). An AWHP extracts thermal energy from the ambient air at lower temperatures and transfers it to a water tank at higher temperatures. A storage tank, as an integral part of the AWHP system, is usually employed to store hot water at the desired temperature for end-use applications. Traditional heat pump water heaters, utilising water as the thermal storage medium, have benefits, including a simple design, high heat transfer efficiency and affordability. Nevertheless, their heat storage density is limited due to the reliance on sensible heat storage. In recent years, there has been an increasing interest in AWHP systems that utilise PCMs as a storage medium to overcome this issue (Pardiñas et al., 2017).

Carbon dioxide (CO_2) serves as an environmentally benign refrigerant, characterised by a minimal global warming potential (GWP) and a zero-ozone depletion potential (ODP). There is a growing endorsement for its use as a natural refrigerant to substitute chlorofluorocarbons (CFCs) and hydrochlorofluorocarbons (HCFCs) in vapour compression systems. Limited research exists in the literature regarding the performance of high-temperature CO_2 heat pumps integrated with thermal storage tanks utilising high-temperature phase change materials. Furthermore, there is a significant deficiency in empirical correlations for the coefficient of performance (COP) of heat pumps that are integrated with thermal storage, which impedes the optimisation of these systems. This study aims to experimentally investigate the performance of a transcritical CO_2 absorption working heat pump (AWHP) integrated with a high-temperature thermal energy storage tank for space heating and domestic hot water production. This study aims to assess whether the storage tank can deliver an adequate volume of domestic hot water at suitable mass flow rates and temperatures for residential use.

6.2 PCM Selection

Organic PCMs are ideally suited for building TES systems due to their extensive range of permissible melting temperatures, elevated latent heat of fusion, negligible supercooling, remarkable chemical stability, and non-corrosive properties. The characteristics of organic PCMs significantly improve the performance and longevity of TES systems in building applications (Nair et al., 2022).

The CO_2 heat pump functions with a water supply temperature exceeding 70°C, necessitating the use of a high-temperature phase change material for the experiments. The chosen phase change material for this application was the commercial RT70-HC, provided by Rubitherm, Germany. Table 33 presents the primary properties of the PCM. The phase transition temperature of the PCM was selected to be marginally above the heating system's operating temperature in the building under investigation, thereby ensuring effective management of potential thermal losses while sustaining optimal performance.

Table 27. Physical characteristics of Rubitherm RT70-HC PCM

Parameter	**Value**	**Units**
Melting temperature range	69-71	ºC
Solidification temperature range	71-69	ºC
Heat storage capacity (combination of sensible and latent heat in temperature range 62-77 ºC)	260 72	kJ/kg Wh/kg
Specific heat capacity	2	kJ/kg k
Density (solid) at 15 ºC	0.88	kg/lt
Density (liquid) at 80 ºC	0.77	kg/lt
Thermal conductivity (both phases)	0.2	W/m K
Volume expansion	12.5 %	
Flash point	227	ºC
Maximum operating temperature	100	ºC

6.3 Methodology

This section outlines the methodology of the experiment. The first part details the experimental setup and the instrumentation used, while the second part describes the procedure followed during the experiments.

6.3.1 Experimental test facility

A thermal energy storage tank that uses a PCM with an immersed heat exchanger was used to evaluate the performance of a domestic hot water (DHW), space heating and LHTES system. The finned-tube heat exchanger, which comprises aluminum fins and copper pipes, facilitates efficient heat transfer. Hot and cold water flows were utilised as heat transfer fluids (HTFs) for the PCM charging and discharging processes, respectively. The system was designed to operate under conditions that closely replicate real-world scenarios when connected to an AWHP. It is worth noting that the experimental conditions for the DHW differed from those for space heating. The entire CO_2 AWHP was located in an environmental chamber. The environmental chamber is designed to replicate external conditions, specifically temperature and humidity, for evaluating the performance of heat pumps. The ambient temperature can be adjusted between 0 °C and 30 °C, while the relative humidity remains stable, ranging from 20% to 90%.

The facility, designed and built at the Centre for Sustainable Energy Future (CSEF) at Brunel University London, was used to experimentally test the performance of a CO_2 AWHP with PCM thermal storage. The test rig, built at a real scale, consists of three main components:

1. Heating System: This system features a 4.5 kW nominal capacity CO_2 AWHP, which heats the heat transfer fluid (HTF) and serves as the primary heating energy source during the charging process, thereby simulating real-world installation conditions.

2. Cooling System: A 4 kW_{th} cold water to HTF heat exchanger is used, which drops the temperature to 30 °C coming from the PCM TES tank.

3. Storage System: A black steel PCM TES tank stores thermal energy during the charging process and releases it during the discharging process.

Figure 89 presents an overview of the pilot plant facility, while Figure 90 illustrates the experimental test system. The three systems are linked via a 22 mm polyethylene piping system that facilitates the distribution of the heat transfer fluid (HTF). Furthermore, a 50 mm layer of polyurethane insulation is utilised for the PCM TES tank, while 13 mm of Foamglas insulation is employed on the piping to reduce heat losses to the environment.

To conduct a precise analysis of the thermal behaviour of the PCM and obtain an accurate temperature map during the charging and discharging processes, twelve T-type thermocouples, with a temperature range of −40 °C to +375 °C and an accuracy of ±0.5 °C, were systematically affixed to the finned-tube heat exchanger in a grid configuration. The configuration encompassed the entire PCM volume, with thermocouples subsequently inserted into the powdered PCM within the tank as shown in Figure 91 (c). Figure 91 (a) illustrates the configuration of the sensors, with four sensors aligned along the central vertical axis (H0 to H3), four along the central axial direction (L0 to L3), and four along the central radial direction (W0 to W3). Two Pt-100 class B temperature sensors, with an accuracy of ±0.3 °C, were installed at the inlet and outlet of the heat exchanger's HTF tubes to measure the HTF inlet and outlet temperatures. Two volumetric flow meters, exhibiting a full-scale accuracy of ±3%, were employed to quantify the flow rates of the hot and cold circulated water. A power meter with an accuracy of 2.5% was installed to monitor the electrical power consumption of the compressor. The experimental system is comprehensively equipped to evaluate its overall performance as well as the performance of its individual components. This study utilises National Instruments' cDAQ-9133 and LabVIEW software for accurate control and measurement. The NI 9226 module is employed for PT-100 sensors, whereas the NI 9214 module is designated for T-type thermocouples, facilitating precise temperature data acquisition as illustrated in Figure 92.

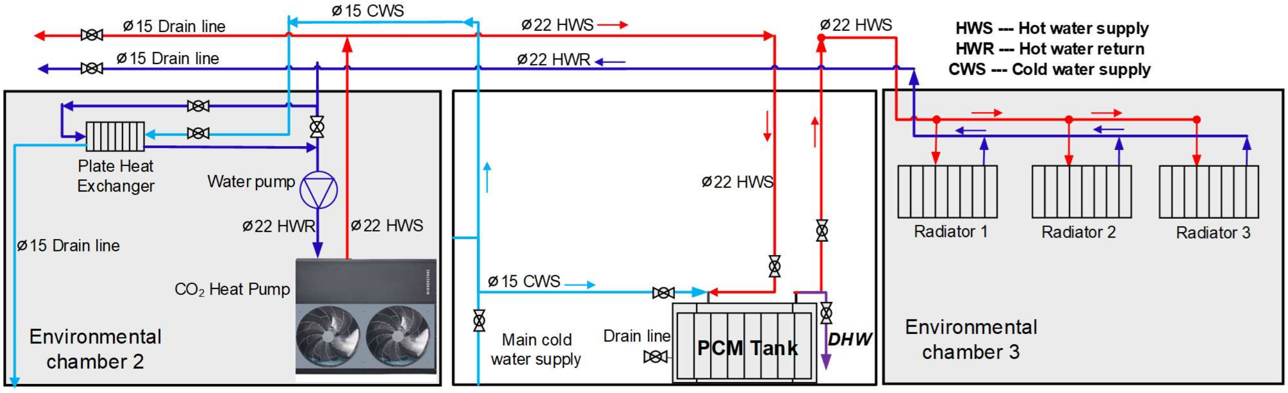

Figure 88. Schematic diagram of the experimental setup

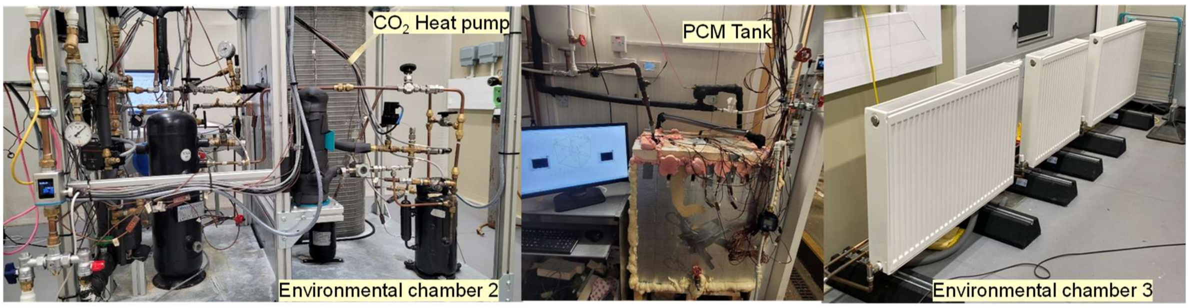

Figure 89. Picture of experiment setup

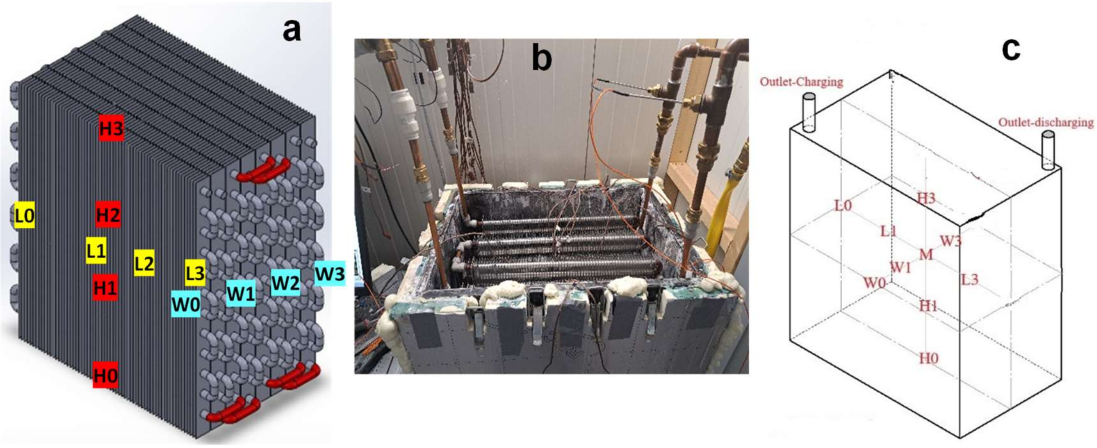

Figure 90. (a) Drawing of heat exchanger, (b) PCM storage tank with heat exchanger and instrumentation, (c) Thermocouples locations in the tank

Figure 91. Data Acquisition system

6.3.2 Experimental procedure

The experimental procedure involved both charging and discharging processes, as illustrated in Figure 93. The CO_2 AWHP was used to charge the PCM storage tank. Initially, the CO_2 in the evaporator absorbed heat from the ambient air. The CO_2 then underwent a typical transcritical refrigeration cycle in the compressor, where it was compressed at high temperatures and pressures. Following this, the CO_2 transferred heat to water in the gas cooler, which was subsequently directed to the PCM tank. Water was circulated between the gas cooler, the PCM storage tank, and the radiators using a circulation pump. The hot water that exited the gas cooler was directed into the PCM storage tank, where it released its energy. The water then flowed to the radiators, where it dissipated heat before returning to the gas cooler. If the water temperature was too high, it passed through a heat exchanger, where it transferred heat to the cold water. The cooled water was then returned to the gas cooler. Throughout the charging process, the PCM absorbed thermal energy directly from the heated water. During the discharge phase, the PCM released its stored energy to the cold water, hence diminishing the temperature differential in the heat transfer. The melting experiments began at room temperature, with the paraffin in its solid phase. The initial state was considered to be reached when all thermocouples inside the paraffin recorded the same temperature.

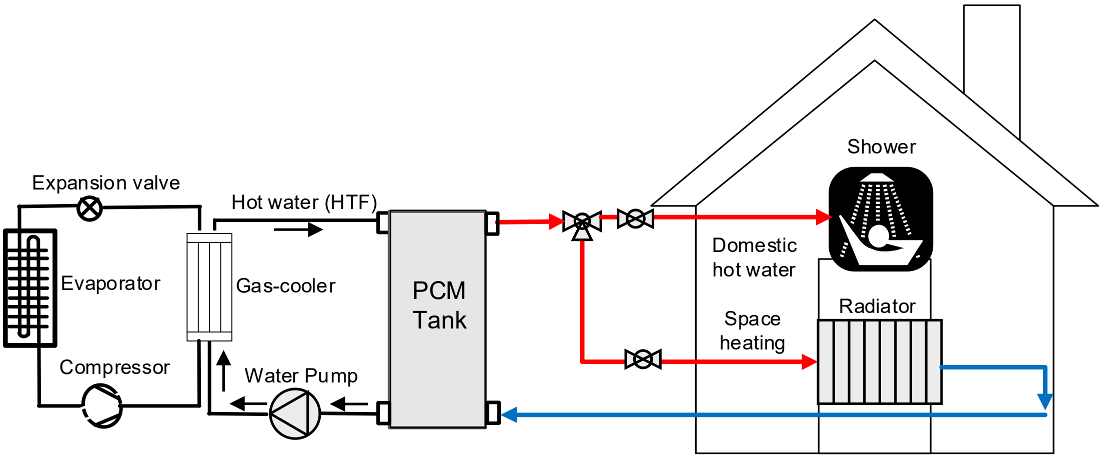

Figure 92. Schematic for CO_2 AWHP to charge PCM storage tank for domestic use.

The closed-loop charging process is initiated, during which the PCM absorbs heat and stores it as it melts. The melting behaviour and properties of the PCM are monitored through temperature distribution, which is recorded by the data acquisition system. The experiments continued until the temperatures at all test points stabilized. The charging process is considered complete when the outlet hot water (HTF) temperature from the PCM tank approaches the temperature of the incoming hot water.

Once the charging process concludes, cold water is pumped to the heat exchanger, where it transfers heat to the heat transfer fluid (HTF). This process enables the HTF to absorb heat from the energy stored in the PCM tank, thereby initiating the discharging protocol. During the discharging process, the PCM undergoes solidification, releasing stored heat, which is then absorbed by the cold water, causing a temperature increase. This simulates domestic hot water consumption. For space heating, heat is transferred from the ambient room temperature to the HTF via radiators.

The analysis of the PCM system was based on its experimental capacity to store and release thermal energy. The intensity of energy discharging plays a crucial role in determining the heat energy usage for end-users, providing a dynamic performance analysis of the thermal energy storage (TES) system. Therefore, it was essential to evaluate the system's performance. To achieve this, the energy released over a 360-minute period was accumulated and averaged to calculate the energy-releasing intensity. The following parameters were measured and compared during the charging and discharging processes of the PCM-based storage TES tank: PCM temperature, HTF temperature, heat transfer rate, the quantities of heat absorbed and released, energy storage rate, and the volume of domestic hot water (DHW). These variables were determined experimentally to evaluate the thermal performance of the system.

6.4 Experimental uncertainty analysis

In this experiment, the primary sources of uncertainty arise from the measurement of temperature (T), circulating water flow rate ($\dot{V}$) and AWHP input power (P). The uncertainties in heating capacity and COP were determined using a standard error analysis in Engineering Equation Solver (EES) software (Klein and Alvarado, 2004), applying the Taylor Series Method (TSM) (Taylor, 1997) based on the uncertainties of individual measurements. The accuracy of various measurement instruments was obtained from manufacturer specifications, as shown in Table 34. Using the TSM method, the overall errors in the heat pump's heating capacity and COP were estimated to be 4.2% and 6%, respectively.

Table 28. Accuracy of experimental devices

Item	Manufacturer	Type	Accuracy	Function
Power meter	Fluke Co. Ltd	345	±2.5%	Measure the power consumption
Thermocouple	TC direct	Pt-100 Class B	±0.3%	Measure temperature
Flowmeter	Ifm	Magnetic Inductive SM 7000	±3.0%	Read the water flow rate

6.5 Performance evaluation of heat pump based PCM TES system

The heating capacity of the PCM tank can be calculated from the water temperatures at the inlet and outlet of the storage tank. The rate of heat released from the water at each time during the charging process and the rate of heat gained by water during the discharging can be calculated as:

$$\dot{Q} = \rho \dot{V} C_p (T_{out} - T_{in}) \qquad \text{Eq. (1)}$$

So, the total amount of heat energy released from or gained by the water can be calculated as:

$$Q = \int_0^{t_{charge}} \rho \dot{V} \, C_p (T_{out} - T_{in}) dt \qquad \text{Eq. (2)}$$

The maximum theoretical heating energy of the storage unit is the summation of sensible and latent heat of the PCM as follows:

$$E_{theo} = m_{PCM}(c_s\,(T_l - T_i) + \Delta H + c_l(T_e - T_s)) \qquad \text{Eq. (3)}$$

The total electric power of the heat pump as follows:

$$W_{Total} = W_{comp} + W_{fan} \qquad \text{Eq. (4)}$$

The average performance coefficient of the heat pump during this operation is derived by dividing the total thermal energy supplied by the heat pump by the total energy consumed by the compressor over the same period. The following is one way to express this ratio using an energy efficiency index:

$$COP = \frac{Q_{th}}{W_{Total}} \qquad \text{Eq. (5)}$$

Where $\dot{Q}$ is the heating capacity of the PCM TES system (kW), C_p is the specific heat of water (kJ· $\text{kg}^{-1} \cdot \text{K}^{-1}$), ρ is the density of water (kg· m^{-3}), T_{out} and T_{in} are the outlet and inlet temperature of PCM tank (°C), Q is the charging thermal energy (kWh), t_{charge} is the total charging time in (h), E_{theor} is the theoretical stored thermal energy (kWh), m_{PCM} is the weight of PCM (kg), c_s is the specific heat of solid PCM (kJ· $\text{kg}^{-1} \cdot \text{K}^{-1}$), T_e is the temperature of the PCM at the ending of the charging process and T_i is the initial temperature. T_l and T_s are the liquidus and solidus temperatures, respectively. c_l is the specific heat of liquid PCM (kJ· $\text{kg}^{-1} \cdot \text{K}^{-1}$), W_{Total} is the total electric power of the compressor and water pump (kW).

6.6 Results and discussion

6.6.1 PCM during the charging

In the initial heat charging operation, the PCM tank's room temperature was recorded at approximately 20°C throughout the test duration. As a result, the PCM in the heat exchanger sustained a temperature consistent with the room, thus remaining in its solid form. Figures 94 (a), (b), and (c) illustrate the temperature progression of the PCM during the charging process at a flow rate of 1.4 L/min across twelve positions within the PCM TES tank. The charging process is comprised of three phases: sensible heat storage of the solid PCM through heat conduction, latent heat storage resulting from the solid-liquid phase transition of the PCM, and sensible heat storage of the liquid PCM through heat conduction and natural convection. The temperature of the hot water supplied by the CO_2 AWHP is consistently maintained at 78°C, taking into account both the phase change temperature and the thermal transfer temperature differential.

Solid sensible heating is the first step and it involves the solid PCM absorbing sensible heat from the hot water, resulting in a rapid temperature rise over a 120-minute period. During this phase, a phase change has not occurred, and the PCM solely retains sensible heat. The initial temperature differentials ΔT_1 (between the intake and output water) and ΔT_2 (between the outlet water and the PCM) are 25 °C and 10 °C, respectively. The temperature differentials gradually decrease throughout the heating process as the heat exchange temperature gradient reduces.

In the second stage, which lasts 120 to 240 minutes, the temperature reaches the melting point of the phase change material (PCM) and increases at a nearly constant rate until complete liquefaction occurs, with the PCM absorbing energy as latent heat. The rate of temperature increase decreases as the temperature approaches the phase transition temperature, attributed to the latent heat of the phase change material (PCM) being significantly higher than its sensible heat in the prior stage. The temperature differentials ΔT_1 and ΔT_2 decrease and stabilise during the solid-liquid phase transition, oscillating between 3 °C and 5 °C. The efficient thermal exchange between the heat transfer fluid and the paraffin phase change material within the TES tank is suggested by the minimal temperature differentials. The temperature range for phase change during charging is 70 °C to 71 °C.

In the third stage, after 240 minutes, the PCM has fully melted, and the liquid PCM continues to absorb sensible heat, resulting in a further temperature increase due to natural convection between the PCM and the water. The rate of temperature increase diminishes compared to the initial stage, which is attributed to the reduction in the temperature gradient for heat transfer. The PCM and outlet water temperatures progressively converge towards the AWHP temperature of 78°C. By the end of the third stage, the temperature differences, ΔT_1 and ΔT_2,decrease to below 5°C.

Figures 94 (a), (b), and (c) provide a comprehensive comparison of temperature fluctuations across varying heights, lengths, and widths. The temperature sensors at location H2 display a similar trend to those at L2 and W2, as these locations are positioned at the center of the heat exchanger and have experienced the same heating effect.

The primary finding of the analysis is that the thermocouples located at the far end of the tank were affected by their proximity to the HTF inlet and outlet. Thermocouples at H0, H1, H2, H3, L1, L2, W1, and W2, which are situated in close proximity to the HTF inlet, exhibited faster melting times than those on the opposing side (L0, L3, W0, and W3). This implies that the position of thermocouples in the middle and lower regions of the tank is significantly influenced by their proximity to the HTF inlet/outlet. Conduction is more significant in these regions, as the PCM remains stable for an extended period.

To begin, Figure 94 (a) clearly shows a temperature gradient in the vertical direction, with a faster melting rate at H0 compared to H1, H2, and H3. Theoretically, heat transfer during the phase change of the PCM is predominantly facilitated by natural convection, which is instigated by density gradients arising from temperature variations. This induces internal recirculation due to buoyancy forces. Consequently, the temperature in the lower region melts more rapidly than in the top section of the system.

Secondly, in the horizontal direction, the melting rates at L1 and L2 surpass those at L0 and L3. As the HTF flows through the pipes, the water progressively cools, diminishing the temperature differential between the PCM and the hot water. Consequently, the driving force for heat transfer diminishes, resulting in the lowest melting rate of the material at the sides of the PCM.

Third, in the radial direction, the tendency follows that of the horizontal direction. The melting rates at W1 and W2 exceed those of W0 and W3. The primary reason for this is the decreased charging rate at W0 and W3, which is a consequence of their distance from the charging flow channel. The material's minimal thermal conductivity further restricts the heating rate in these regions.

Figure 94 (d) depicts the fluctuation of inlet and outlet hot water temperatures (HTFs) within the PCM tank throughout the charging cycle. Initially, a considerable temperature disparity exists between the inlet and outlet HTFs during the charging process. The inlet HTF's temperature rises quickly from 30 °C to 78 °C within 60 minutes during the initial period. At the same time, the PCM temperature increases progressively from 20 °C to 68 °C, with a gradual decrease in the rate of increase. The outlet HTF temperature is closely correlated with the PCM temperatures. In the second stage, the inlet HTF temperature is maintained within a narrow range. During the phase transition from 68 °C to 71 °C, the PCM absorbs a substantial amount of heat and its temperature increases at a remarkably slow pace. Additionally, the outlet HTF temperature increases progressively from 65 °C to 73 °C, indicating that the heat dissipated by the HTF is predominantly transferred to the PCM.

When the PCM's temperature approaches its melting point at various measuring points, the curves flatten out. As the PCM's temperature rises only slightly, heat is absorbed, indicating the presence of a phase transition. When the PCM temperature exceeds 70 °C to 71 °C (in the liquid phase), a more pronounced increase in temperature occurs, indicating the absorption of latent heat, with subsequent heat accumulation relying on sensible heat. The recorded start and end times of the phase change are influenced by the placement of the thermocouples within the tank, underscoring the importance of carefully evaluating how various measurement locations affect the average temperature of the PCM. The PCM has been fully melted after approximately 180 minutes. The temperature of the PCM, as well as the inlet and outlet HTF, increases at a faster rate than that of the first stage, from 71°C to 74-75°C. This phenomenon is due to heat transfer from the HTF to the melted PCM through natural convection and conduction in the third stage. In contrast, in the first stage, heat transfer to the thick solid PCM layer is predominantly facilitated by conduction.

Moreover, the AWHP consumes an average of 13.08 kWh of electricity during the 360 minute charging process, which occurs at an ambient temperature of 18 °C in Environmental Chamber 2. Therefore, the heating capacity throughout the charging procedure is 2.18 kW. The following variables were measured and compared during the charging and discharging procedures of the PCM TES tank: PCM and HTF temperatures, heat transfer rate, quantities of absorbed and released heat, energy storage rate, and volume of DHW, as determined through experiments.

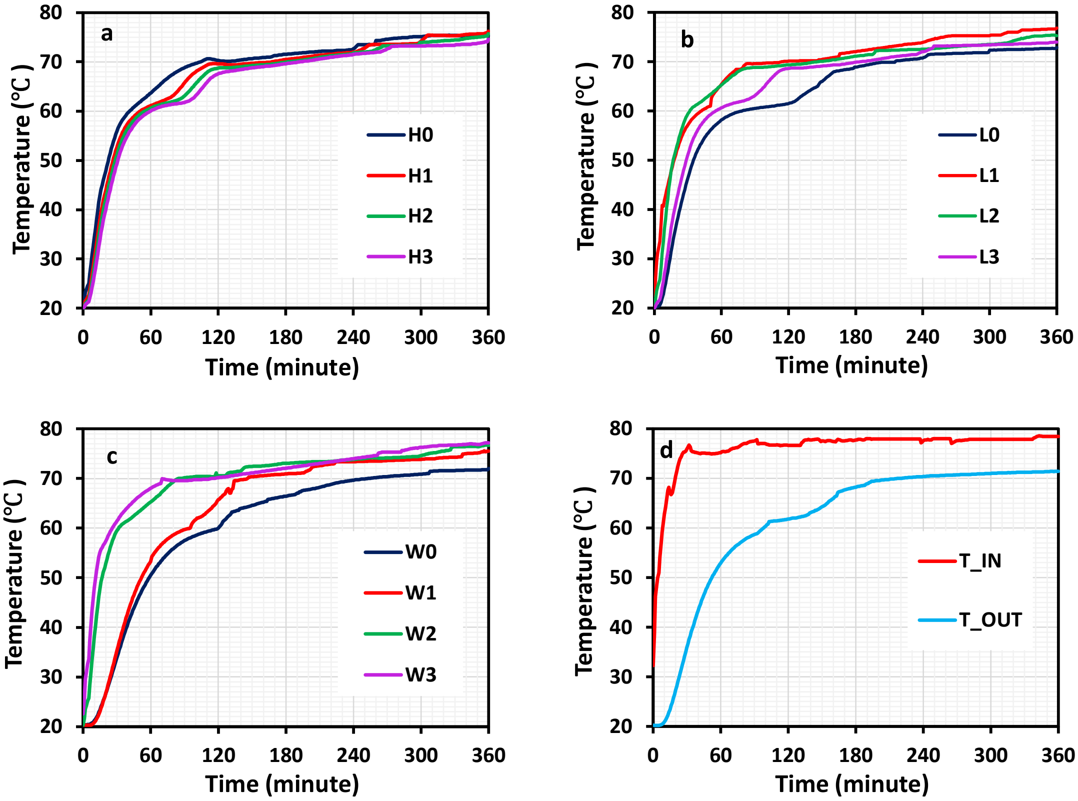

Figure 93. PCM temperature distribution of RT 70 HC inside tank

6.7 Discharge process

6.7.1 Production of DHW

Figure 95 presents a schematic representation of domestic hot water (DHW) production during the discharge process of the PCM-based thermal energy storage tank. During this process, the cold water supply (CWS) enters the system through Gate Valve 1 and flows through the immersed heat exchanger within the PCM tank. As the PCM releases its stored latent heat, thermal energy is transferred to the incoming cold water due to the temperature difference between the PCM and the water, thereby increasing the water temperature. The heated water then exits the tank and passes through Flow Meter 1, at which point it is considered hot water. Subsequently, this hot water is directed to a thermostatic mixing valve, where it is blended with additional cold water supplied through Gate Valve 5. The purpose of this mixing process is to regulate the outlet temperature. As a result, the final water delivered from the mixing valve maintains a controlled supply temperature of 40 ± 2 °C, ensuring safe and consistent domestic hot water delivery. Figures 96 and 97 show the distribution of PCM temperature within the tank, as well as the inlet and outlet cold water temperatures and the mixed water temperature. Figure 98 depicts the heat transfer rate and the thermal energy emitted from the PCM TES tank during the discharge process. In the PCM discharge process, the average inlet temperature of the cold water is 15.4 °C, the volumetric flow rate varies from 3 L/min to 4 L/min, and the thermostatic mixing valve (TMV) regulates the mixed water temperature at 40 ± 2 °C. The mixed water flow rate was determined based on the peak hot water consumption profile for showers in the UK, which is 8 L/min and 6 L/min (EST, 2008).

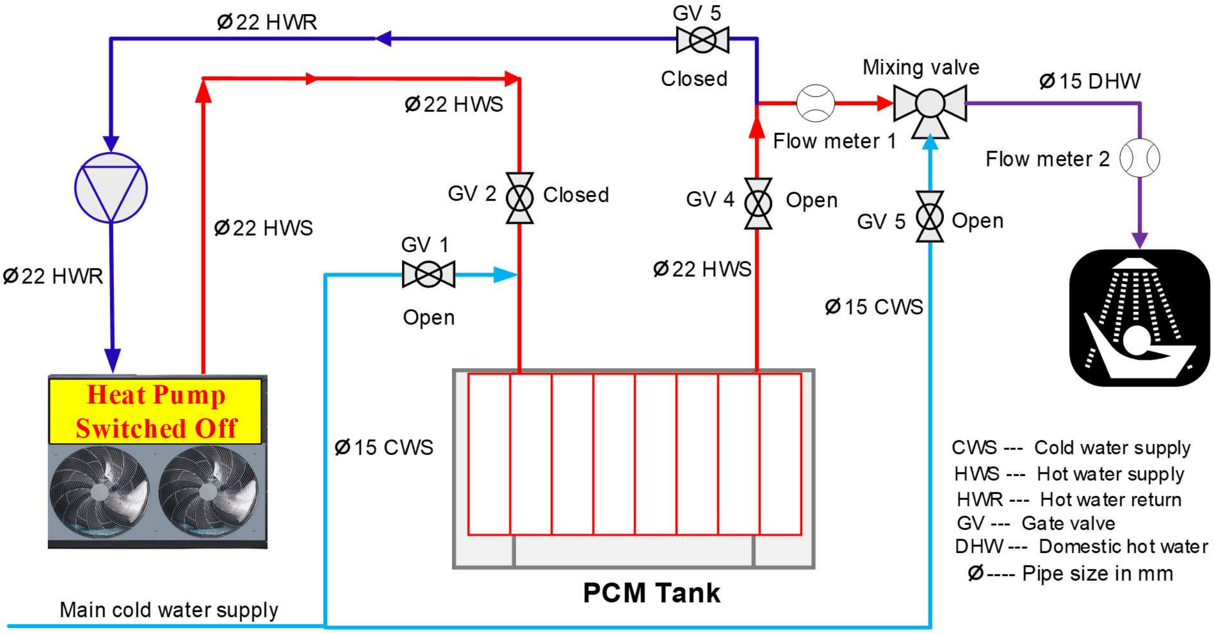

Figure 94. Schematic of DHW discharging

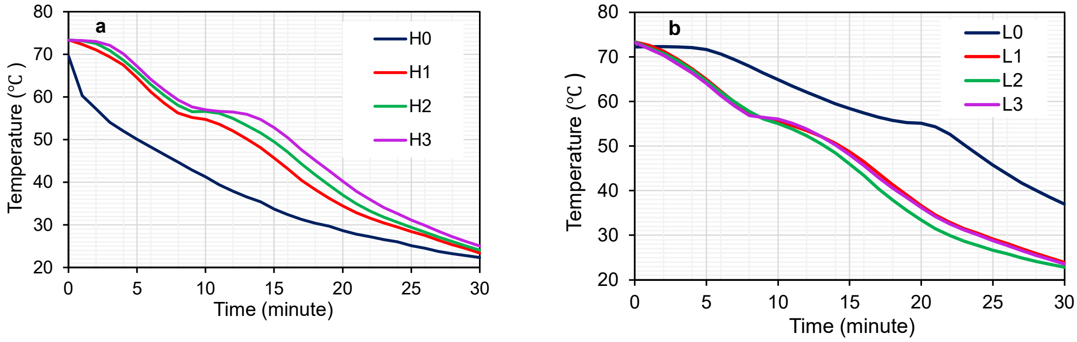

Figure 95. Temperature distribution inside the PCM TES tank during the discharging (solidification) process

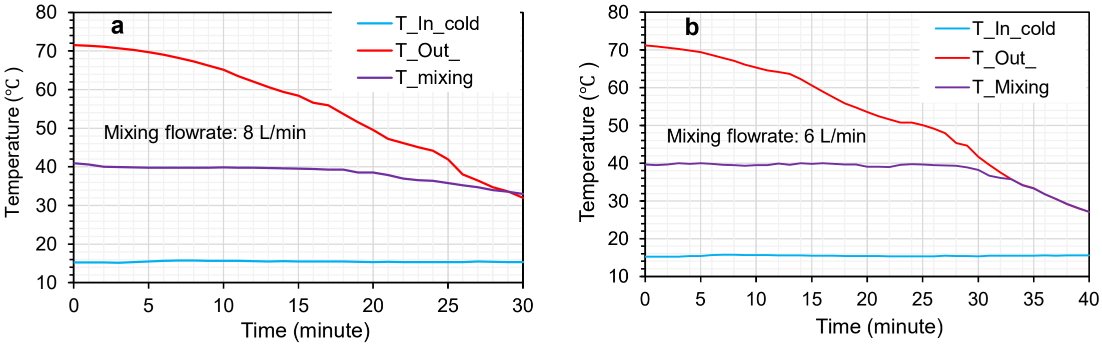

Figure 96. Temperature distribution of cold and mixed water during the discharging process at (a) 8 L/min and (b) 6 L/min.

Figure 96 demonstrates that, throughout the experiment, the temperature curves enter the phase transition range of 69 °C to 70 °C. A more pronounced temperature change occurs within the range of 69 °C to 68 °C. The temperature profile obtained from this study closely corresponds with the theoretical model, indicating minimal temperature changes during the phase transition as a result of latent heat release. A slight temperature fluctuation is observed at the measurement point during the discharging phase, similar to the process of charging the PCM. This indicates that this portion of the PCM is not being efficiently employed during discharge, as there is minimal or no heat exchange occurring. The illustration indicates that the temperature at this site rises during the initial 10 minutes of the PCM discharging operation. This increase in temperature signifies thermal inertia. The temperature of the PCM ultimately converges with the original temperature at the onset of the process, although this transpires only after the process has been completed. This occurs after 30 minutes for elevated flow rates and 40 minutes for diminished flow rates.

Figures 97 (a) and (b) demonstrate that the average temperature at the commencement of the PCM discharging process (71°C) is similar to the average temperature at the conclusion of the charging process (73°C). The elevated temperature differential between the inlet cold water and the PCM results in a more rapid discharging process compared to the charging process. The initial temperature during the charging procedure was 20°C. Under these conditions, discharging 8 L/min of usable mixed hot water at a temperature of 40 ± 2°C requires 20 minutes, whereas a flow rate of 6 L/min necessitates 30 minutes. At a higher flow rate of 8 L/min, a greater mass of water passes through the heat exchanger per unit time. As defined by Equation (1), the rate of heat transfer is directly proportional to the mass flow rate. Therefore, an increase in mass flow rate leads to a higher instantaneous rate of heat extraction from the PCM. Consequently, the stored thermal energy is depleted more rapidly, limiting the supply of usable hot water at 40 ± 2 °C to approximately 20 minutes. In contrast, at a lower flow rate of 6 L/min, the reduced mass flow rate decreases the rate of heat extraction. As a result, the stored energy is released more gradually, extending the duration of usable hot water delivery to approximately 30 minutes. Figures 97 (a) and (b) illustrate that the heat exchange between the PCM and the HTF remains vigorous, and the released thermal energy continues to escalate. The discharging process is prolonged, lasting 30 minutes at 8 L/min and 40 minutes at 6 L/min, as the outlet HTF and PCM temperatures converge with the inlet HTF temperature.

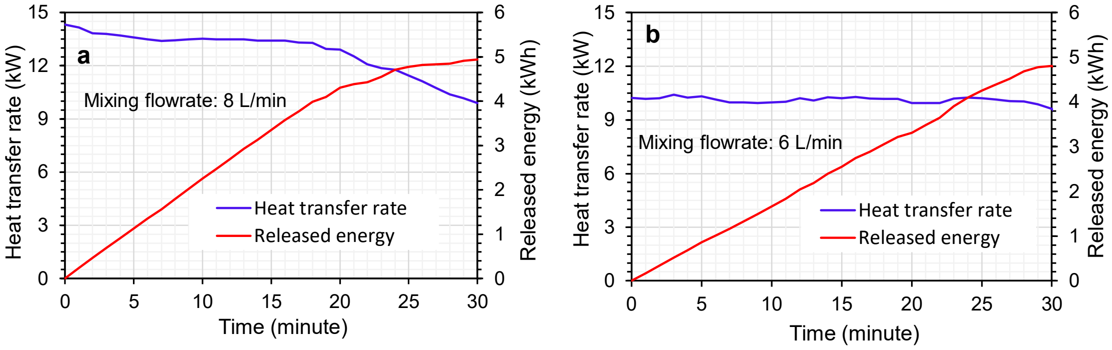

Figure 97. Variation of heat transfer rate and released energy during the discharging process of the PCM TES (a) 8 L/min and (b) 6 L/min.

Figures 98 (a) and (b) illustrate the variation in heat transfer rate and energy released as a function of discharge time for outlet mixing water flow rates of 8 L/min and 6 L/min, respectively. The energy released during the discharging process has a power function connection with time, signifying that the heat transfer rate is maximal at the onset of discharging and thereafter diminishes. The energy release capacity can reach 5 kWh after 30 minutes in both cases. As shown in Figure 10(a), for an 8 L/min mixing flow rate, the heat transfer rate decreases from 14 kW to 9.9 kW, with an average value of 12.8 kW during the discharging process. For a mixing flow rate of 6 L/min, during the discharging process, the heat transfer rate drops from 10.3 kW to 9.6 kW, with an average value of 10 kW after 30 minutes. This is mainly because the inlet cold water temperature of the PCM TES tank remains stable during the discharging operation, whereas the outlet water temperature continuously declines. Therefore, in the system's actual operation, the volumetric flow rate of the water should be adjusted periodically to maintain a consistent temperature difference between the inlet and outlet, thereby ensuring that the heat release power remains relatively stable

6.7.2 Energy required for hot water production

By assessing the useful temperature range depicted in Figures 98 (a) and 98 (b), the energy required to generate mixed hot water is determined. Utilisable heat is the energy content of the heated (mixed) water, which is measured in kWh and supplied at a temperature exceeding 38°C, as determined through experimentation. The effective heat at the designated temperature of 40 ± 2°C is determined by adding the total heat released within the temperature range under investigation. The energy rate represents the proportion of effective heat required to raise a specified volume of water to the target temperature.

Figure 99 illustrates that the thermal energy imparted to the water decreases as the flow rate increases. The heat transfer rate during solidification exceeds that of melting and diminishes when the residual heat in the tank is exhausted. The figure additionally displays the experimental heat transfer rates during the solidification process. Figure 99 again shows the opposite relationship between the heat transfer rate and the amount of heat released. Consequently, the hot water production period is prolonged, and heat transfer to the water is improved due to a reduced outlet water consumption rate. For mixed outlet flow rates of 8 L/min and 6 L/min, with a mixed water temperature of 40 ± 2°C, the total energy consumption for an average cold water inlet temperature of 15.4°C is 4.5 kWh and 5 kWh, respectively. The total volume of mixed water supplied is 180 L at an outlet flow rate of 6 L/min and 160 L at an outlet flow rate of 8 L/min. The heat exchanger's ability to transfer heat to succeeding layers is reduced as a solid phase change material (PCM) layer forms on the surface at a slower rate. It is necessary to transfer the heat produced by the PCM's solidification to the heat exchanger via the growing solid layer during the discharge operation. Natural convection has less impact on the heat transfer coefficient than the thermal conductivity of the solid phase change materials. A portion of the latent heat is not utilised because not all of the PCM solidifies due to the rapid solidification process. Compared to the theoretical values, which solely take latent heat into consideration, the measured values, which encompass both sensible and latent heat, are lower. The storage system is able to dissipate extra heat after reaching thermal equilibrium, which occurs after a predetermined amount of time has passed.

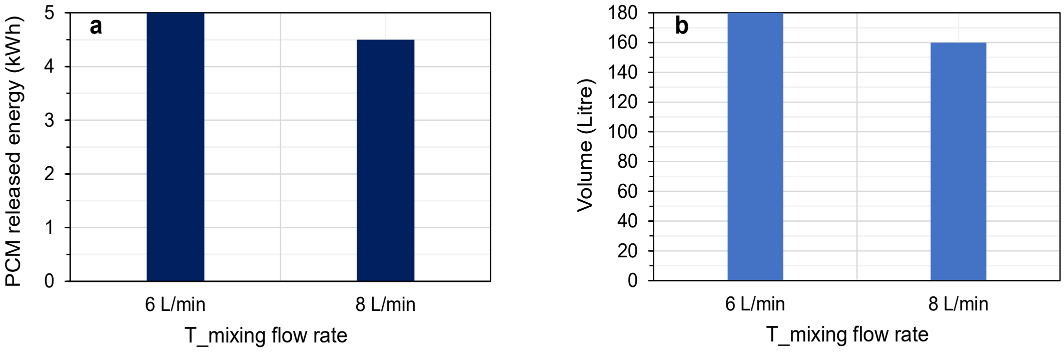

Figure 98. Energy and volume distribution depending on the mixing water flow rate

6.8 Space heating

6.8.1 Performance analysis of TES prototype for space heating mode

An environmental chamber at Brunel University London's CSEF laboratory was used to evaluate the PCM TES system's performance for space heating applications. At 3.5 meters in height, the chamber has a floor space of 24 m^2. The radiators were installed in Chamber 3, which is an environmental test chamber designed to control and maintain specific temperature and humidity conditions. This controlled environment allowed accurate evaluation of the space heating performance under steady and repeatable boundary conditions. In contrast, the PCM-based thermal energy storage (TES) tank was installed in the pump room, where the hydraulic components of the system were located. Positioning the TES tank in the pump room ensured proper integration with the circulation pumps and pipework, while allowing independent monitoring of charging and discharging processes without interference from the environmental chamber conditions. Indoor and outdoor air temperatures, as well as the inlet and outlet water temperatures of the radiators, were monitored using a variety of temperature sensors. Controlling and varying the circulating water flow rate was the primary operational parameter during the discharging process. Under nominal conditions, which entailed an external temperature of -3 °C, an internal room temperature of 20 ± 1 °C, and an air change rate of 0.5 ACH (air changes per hour), the chamber's heating load was determined to be 2 kW.

6.8.2 Discharging process

As shown in Figure 100, the discharging process for space heating begins with the CO_2 AWHP being switched off while only the circulating pump remains active, circulating hot water from the PCM tank to the radiators. A thermostat placed in the chamber maintains a temperature range of 20 ± 1 °C. When the room temperature falls below 19°C, the thermostat sends a signal to start the circulating pump, allowing the hot water to flow through the PCM and radiators, releasing the stored thermal energy to heat the room. Once the room temperature reaches 21°C, the thermostat sends an "off" signal to the circulating pump, stopping the water flow and preventing overheating. This process effectively maintains the desired room temperature by utilising the thermal energy stored in the PCM tank.

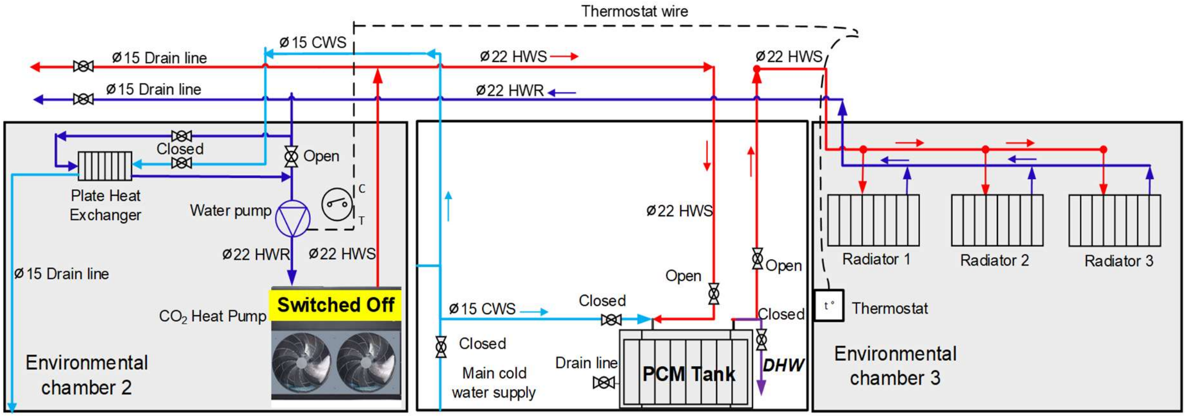

Figure 99. Space heating discharging process

Figures 101 (a) and (b) illustrate the temperature changes of the PCM at various locations within the TES tank throughout the discharging process. The lower-temperature flowing water from the radiators enters the TES tank and first passes the upper layer of the PCM. The lower-temperature fluid subsequently enters the middle and bottom layers of the PCM prior to entering the tank. Upon entering the TES tank, the lower-temperature water rapidly increases in temperature as it absorbs heat from the PCM during the initial cycles. The PCM temperatures, arranged from top to bottom (H1 to H0) and from left to right (L0 to L1), show a gradual decrease to 65°C in both directions during the first hour, as sensible heat is transferred to the working fluid.

The phase transition process in the upper layer of the PCM occurs more quickly than in the middle and lower layers, as the circulating water first extracts the maximum latent heat from the PCM at the bottom (H0). After approximately 60 minutes, the PCM in the tank has fully solidified, as reflected by the temperature variations from H0 to H1 and from L0 to L1, while the outlet water temperature gradually declines. Upon completion of the phase transition, the sensible heat released by the solidified PCM is then utilized, together with the reduced temperature differential, to produce the required heat. The sensible and latent heat released from the TES tank is employed for space heating on a single floor via circulating water. The temperature differential between the inlet and outlet water gradually diminishes, eventually falling below 10°C.

The thermal energy accumulated in the tank during charging is subsequently released during discharging and dissipated via the radiators. The discharging process concludes when the outlet water temperature attains 45°C after 360 minutes; nonetheless, not all stored heat is expended. The amount of heat (in kWh) transferred from the PCM to the cold water during the discharging phase is termed discharged heat.

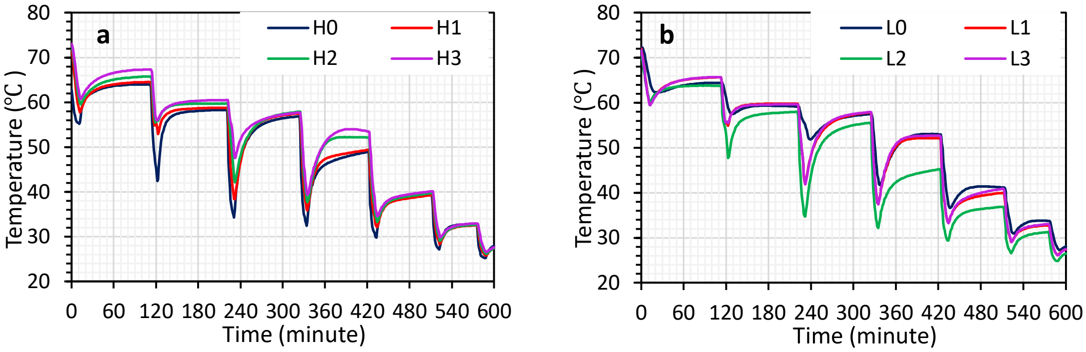

Figure 100. Thermal performance pf the TES-PCM for space heating

Figure 102 presents the thermal performance of the TES-PCM system at a water flow rate of 2 L/min during the discharge process. The TES device delivers continuous space heating for approximately 360 minutes, maintaining a room temperature of 20 ± 1°C. The supply water temperature to the radiators remains above 45 °C from the PCM tank throughout the experiment, even as outdoor air temperatures vary between 13 °C and 10 °C during the autumn season (30th November). As time progresses, maintaining room temperature becomes unfeasible due to a diminishing temperature differential between the inlet and outlet water from the phase change material (PCM). The heating duration of the experimental system is prolonged, primarily due to the small floor area of the room (28 m²), the restricted window area (less than 2 m²), the well-insulated walls, and the airtightness.

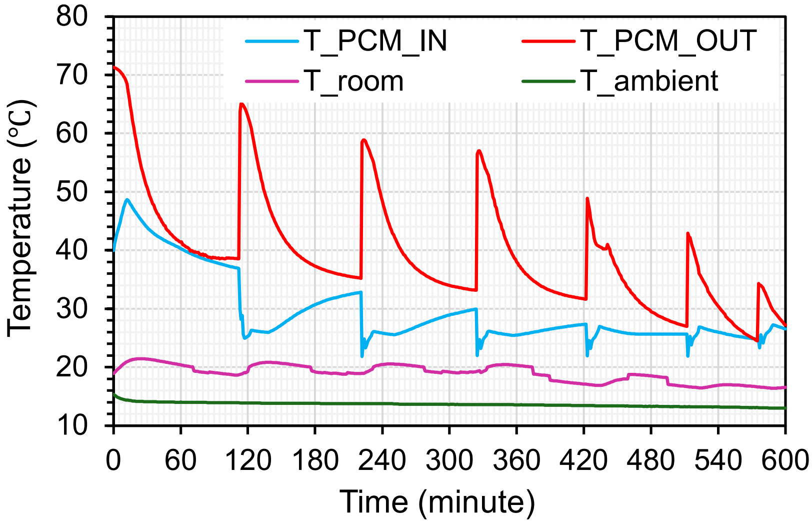

Figure 101. Temperature differences of the HP-PCM thermal storage system during the discharging process

Figure 102 illustrates an area where the temperature curve stabilises for both the inlet and exit water temperatures of the PCM. This behaviour is ascribed to the thermostat setting, as the room temperature equilibrates, resulting in the cessation of the flow rate supply. The regionally averaged PCM exit temperature is consistently greater than the inlet water temperature throughout the entire process. This indicates that some regions inside the PCM mass have not entirely solidified within the designated discharge period, hindering the full exploitation of the latent heat.

Figure 103 illustrates the heat transfer rate of the PCM TES tank equipped with radiators. The variations in the heat transfer rate of the PCM TES tank follow the same trend as the temperature changes of the PCM, as depicted in Figure 101. The heating power of the PCM TES device gradually decreases throughout the cycle. Specifically, it fluctuates between 0 and 7.0 kW during the discharging phase. Additionally, the heating power increases when the thermostat activates the water pump, while it decreases when the pump is turned off. This fluctuation occurs due to the thermostat's role in maintaining the room temperature at a steady 20 ± 1°C.

Additionally, it is noted that the heating power of the PCM TES tank initially declines rapidly before undergoing a sharp increase when the circulating water begins to flow. Subsequently, the heating power stabilises and progressively diminishes at a reduced rate when the flow attains its minimum.

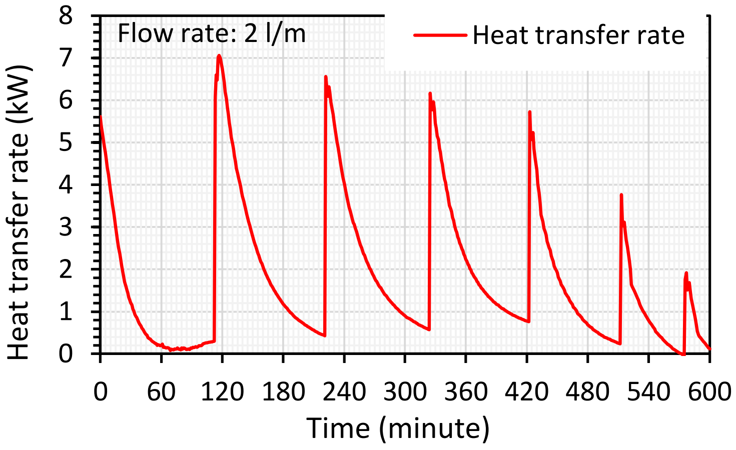

Figure 102. Heat transfer rate of the PCM TES tank for space heating during the discharging process.

6.9 Analysis of the AWHP COP

The COP of AWHP is directly correlated with environmental temperature. This study investigates the impact of ambient temperature on the heating performance of the proposed system, with a constant flow rate of 2 L/min maintained and water outlet and inlet temperatures set at 78°C and 25°C, respectively. The experiments were conducted twice under identical conditions, except for a change in ambient temperature from 18°C to 12°C. Table 35 presents the compressor's power consumption, heating power and COP. The average COP decreased from 2.56 to 2.18, reflecting a 17.4% reduction. The reduction in ambient temperature results in decreased evaporating pressure and an increased compression ratio, thereby impacting the heating performance of the system. Nonetheless, the system can achieve a competitive COP when operating in a low-temperature environment.

Table 29. CO_2 AWHP performance

Ambient Temperature (°C)	Power (kW)	Heating capacity (kW)	COP
18	2.18	4.4	2.01
12	2.56	4.4	1.7

6.10 Performance comparison between water tank and PCM TES tank

Phase Change Materials (PCMs) provide an effective approach for latent heat thermal energy storage (LHTES), facilitating a notable decrease in storage volume relative to traditional sensible heat storage techniques, while preserving a high energy density. One significant challenge associated with phase change materials (PCMs) is their low thermal conductivity, which restricts the rate of energy extraction and delivery, consequently impacting overall system performance.

In domestic hot water and space heating applications, small-scale heat pump systems generally include a hot water storage capacity of about 200 litres. Given that the necessary temperature for effective hot water in both space heating and domestic hot water applications is 40°C, and the maximum temperature in the storage tank is 77°C, the total energy stored in the 200 L (0.2 m^3) storage tank can be determined as follows:

$$Q_w = m\,c_p\,(t_i - t_f)/3600 = 200 \times 4.185 \times (77\text{-}40)/3600 = 8.6\ kWh$$

The PCM storage system developed has a volume 0.1 m^3 and PCM mass of 100 kg. The capacity of the PCM TES tank is determined in accordance with Equation (3). This equation is used to quantify the total amount of thermal energy that can be stored within the PCM, taking into account both sensible and latent heat contributions. By applying Equation (3), the storage capacity can be accurately evaluated based on the thermophysical properties of the PCM, its mass, and the operating temperature range of the system:

$$Q_{PCM} = m\,c_p\frac{(70-40)}{3600} + m\,h_{fg} + m\,c_p\frac{(77-71)}{3600}$$

$$Q_{PCM} = 100\ \times\ 2.0\ \times\frac{22}{3600} + 100\ \times\ 0.072 + 100\ \times\ 2.0\ \times\frac{6}{3600} =\ 9.2\ kWh$$

It can be seen from the above that the PCM storage developed can provide a similar thermal energy storage to water storage in half the volume, significantly reducing the space required for storage in domestic dwellings.

6.11 Conclusions

A PCM TES tank was designed, constructed and evaluated for DHW and space heating applications, integrated with a CO_2 air-to-water heat pump. The findings of the study are summarised below: The PCM TES tank consumed 13 kWh of energy to fully charge in 360 minutes at a constant temperature of 78°C, supplied by the heat pump. During discharging process, the amount of hot water produced, with a temperature of 40 ± 2°C, ranges from 160 litres with an energy consumption of 4.5 kWh to 180 litreswith an energy consumption of 5 kWh, at flow rates of 8 L/min and 6 L/min, respectively, for an average cold water inlet temperature of 15.4°C.In space heating mode, the PCM TES tank provides continuous heating for approximately 360 minutes, maintaining a room temperature of 20 ± 1°C. The supply water temperature to the radiators remains above 45°C throughout the experiment, even as outdoor air temperatures fluctuate between 13°C and 10°C.The PCM storage system, with a volume of 0.1 m^3 and mass of

100 kg, can store thermal energy equivalent to the 200 L (0.2 m^3) water storage while occupying half the space. This offers a space-saving solution for residential thermal energy storage.

Chapter 7 Conclusions and further work

7.1 Conclusions

This thesis focuses on the investigation of the performance of heat pumps in domestic dwellings in the UK using CO_2 as refrigerant. One of the heat pumps was a single stage commercially available system supplied with a 500 litres hot water storage tank and designed to provide hot water temperature at approximately 60 ºC to the tank. The other heat pump was designed and built at Brunel University utilising a two-stage compressor and able to deliver hot water temperature up to 80 ºC. The following main conclusions can be drawn from the work.

i. Carbon dioxide (CO_2) is a natural refrigerant that has excellent thermophysical properties, enabling high heat transfer rates in heat exchangers. Furthermore, CO_2 is environmentally friendly, with a zero Ozone Depletion Potential (ODP) and a negligible Global Warming Potential, (GWP) of 1.0. CO_2 has a low critical temperature which makes the heat pump cycle supercritical, as the critical temperature of CO_2 is only 31.1 ºC and the critical pressure is 73.8 bar. The high critical pressure presents challenges in component design but these, to a large extent, have now been addressed by the refrigeration manufacturing industry. Even though CO_2 has now become a common refrigerant in refrigeration applications it has not been utilised extensively in domestic heat pump applications. This thesis through extensive experimental investigations and modelling contributes to this field by providing useful information and insights on the performance of CO_2 heat pumps that can be used by other researchers and industry for the further development of this technology.

ii. Firstly, a commercially available 2.3 kW heating capacity transcritical CO_2 Air to Water Heat Pump (AWHP) was used to gather experimental data and create a performance map covering ambient temperatures between 0 °C and 20 °C and inlet water temperatures from 20 °C to 50 °C to enable a model to be developed to assess the performance of the system if installed in a 2-bedroom domestic dwelling. The experimental uncertainty was calculated to range from ±6% to ±15%. Results revealed that the coefficient of performance (COP) increased by 20% at a gas cooler inlet water temperature of 50 °C, as the ambient temperature increased from 0 °C to 10 °C. The performance map was used in a TRNSYS simulation model of the house to investigate the seasonal performance of the heat pump coupled to a water thermal storage tank. The results indicated that a tank with a capacity between 150 to 200 litres was optimal for a the house and a thermal load of approximately 7,797 kWh. It was also found that on an annual basis the CO_2 AWHP would result in a 44% reduction with a natural gas boiler under the same operating conditions. It was found that on a seasonal basis, the CO_2 of the AWHP would be reduced by 44% compared to those of the gas boiler.

iii. The test results and knowledge gained from the 2.3 kW CO_2 heat pump were used to design a two-stage CO_2 heat pump of a larger capacity, approximately 4.5 kW at an ambient temperature of a 7 °C and the ability to provide hot water temperatures up to 80 °C. Most of the original design work was carried out by post-doctoral colleagues working in the CSEF Centre. My main contribution was in the assembly and testing of the system, including modifications to accommodate different test requirements.

iv. A Comprehensive series of experiments were conducted on the 2.3 kW CO_2 AWHP, with and without an internal heat exchanger (IHX), varying compressor speeds, and ambient temperatures from 2 °C to 18 °C, alongside return water temperatures from 25 °C to 50 °C. Experimental uncertainty was calculated to range from ±4% to ±8%. The results showed a 34% increase in COP at an inlet temperature of 50 °C when the ambient temperature increased from 2 °C to 12 °C. Additionally, the heating capacity and COP increased by 10% with the inclusion of the IHX. However, it was observed that higher compressor speeds resulted in a decrease in COP, with a 30% reduction when the compressor speed increased from 2400 RPM to 4500 RPM.

v. A TRNSYS dynamic building simulation model for a 4-bedroom semi-detached house with 4 occupants incorporating a performance map of the 4.5 kW heat pump was developed using the same methodology as the modelling of the 2-bedroom house. This analysis assumed the use of water as thermal energy storage. Analysis indicated that storage volumes between 200 litres and 300 litres could meet space temperature control requirements with a 4.5 kW heat pump, operating at a 7 °C ambient temperature and 60 °C water flow temperature. A comparison with a gas boiler revealed that with current gas and electricity prices, the heat pump's running costs would be 91% higher and its CO_2 emissions 40% lower than those of the gas boiler. Further optimisation of the heat pump's design and control is expected to reduce both its running costs and CO_2 emissions.

vi. A numerical simulation model of the 4.5 kW transcritical CO_2 AWHP for hot water applications was developed using the Engineering Equation Solver (EES). The model incorporates simulations of different heat pump components, such as rotary compressors, brazed plate gas coolers, and fin-and-tube evaporators. It was validated against experimental results and was found to provide a good degree of accuracy with a maximum deviation of 5%. The purpose is to be used for component and overall system design and control optimisation studies.

vii. To compare hot water and PCM thermal energy storage for the 4.5 kW heat pump system, tests were performed on a 100 litres PCM storage tank developed at Brunel with a finned tube heat exchanger for charging and discharging. The heat transfer medium used was water and the PCM used in the tests was Rubitherm RT70HC. Tests showed that using the CO_2 heat pump to charging the PCM storage tank for 6 hours during off-peak periods allowed the system to supply 160 litres of domestic hot water at a temperature of 40 ± 1°C. In space heating mode, the system was able to maintain the desired temperature within an environmental chamber measuring 24 m^2 in area and 3.3 meters in height at 20 ± 1 °C when the outdoor temperature ranged from 10 °C to 14 °C without operation of the heat pump. The PCM provided the same storage capacity as hot water storage of double the volume, which is an advantage in the use of heat pumps where there is limited space for the installation of large storage tanks. Another advantage of using PCM storage is to eliminate the risk of legionella formation which is the case with water storage at temperatures below 55 °C.

viii. Overall, the work shows that there is significant potential in the further development of CO_2 heat pumps and their optimum integration with thermal energy storage for domestic space heating and domestic hot water applications.

7.2 Recommendations for further work

i. The heat pump simulation model developed after more extensive validation can be used to optimise the design of components and controls to maximise the heat output and reduce the power consumption over a wide range of conditions. Another parameter that needs further investigation and design modifications is a way of reducing the return water temperature to the heat pump as the lower the water temperature entering the gas cooler, the higher the heat transfer in the gas cooler and the heat output of the heat pump. A number of different approaches can be investigated through modelling and experimentation, such as heating of mains water directly rather than from the thermal store and using the return water to preheat air entering the evaporator.

ii. The control of the heat pump during the tests was carried out manually. An important step will be the development of automatic controls to control the discharge pressure and the compressor speed in response to the heat demand.

iii. Work can also be performed on the optimisation of the performance of the PCM thermal store and its integration with the heat pump. The PCM storage currently developed can operate in charging or discharging mode. Redesign of the storage system to operate in charging and discharging modes simultaneously will enable investigation of the flexibility the latter option can provide against the increase in complexity and cost.

iv. While the present study focuses on the performance of the transcritical CO_2 air-to-water heat pump (AWHP) for space heating and domestic hot water (DHW) applications, future work should extend the analysis to include cooling operation. Investigating the system under summer conditions would enable a comprehensive year-round performance assessment and provide insight into its feasibility for reversible heating and cooling applications in well-insulated UK dwellings.

References

Abas, N., Kalair, A. R., Khan, N., Haider, A., Saleem, Z., & Saleem, M. S. (2018). Natural and synthetic refrigerants, global warming: A review. In *Renewable and Sustainable Energy Reviews* (Vol. 90, pp. 557–569). Elsevier Ltd. https://doi.org/10.1016/j.rser.2018.03.099

Ahmed, R. (2023, September 22). *Central Heating Installation Costs in the UK: 2023 Guide*. https://householdquotes.co.uk/how-much-to-install-central-heating

AHRI. (2022, September 28). *Central Air Conditioners and Air-Source Heat Pumps*. https://www.ahrinet.org/analytics/statistics//historical-data/central-air-conditioners-and-air-source-heat-pumps

Amer, M., & Wang, C. C. (2017). Review of defrosting methods. *Renewable and Sustainable Energy Reviews*, *73*(January), 53–74. https://doi.org/10.1016/j.rser.2017.01.120

Approved Document F Volume 1, 2023. (n.d.). *The building regulations, Volume 1 in England 2023*. Retrieved 8 March 2025, from https://assets.publishing.service.gov.uk/media/61deba42d3bf7f054fcc243d/ADF1.pdf

Arteconi, A., Hewitt, N. J., & Polonara, F. (2012). State of the art of thermal storage for demand-side management. *Applied Energy*, *93*, 371–389. https://doi.org/10.1016/j.apenergy.2011.12.045

Austin, B. T., & Sumathy, K. (2011). Transcritical carbon dioxide heat pump systems: A review. *Renewable and Sustainable Energy Reviews*, *15*(8), 4013–4029. https://doi.org/10.1016/j.rser.2011.07.021

Baek, J. S., Groll, E. A., & Lawless, P. B. (2005). Theoretical performance of transcritical carbon dioxide cycle with two-stage compression and intercooling. *Proceedings of the Institution of*

Mechanical Engineers, Part E: Journal of Process Mechanical Engineering, *219*(2), 187–195. https://doi.org/10.1243/095440805X7080

Bartram, J. (2007). *Legionella and the prevention of legionellosis*. World Health Organization.

BEIS. (2021a). *Annual Fuel Poverty Statistics Report, 2021 (2019 data)* (Vol. 2020, Issue March). https://assets.publishing.service.gov.uk/government/uploads/system/uploads/attachment_data/file/882404/annual-fuel-poverty-statistics-report-2020-2018-data.pdf

BEIS. (2021b). *Heat and buildings strategy*. Department for Business, Energy & Industrial Strategy London, UK.

Bellos, E., & Tzivanidis, C. (2019). A comparative study of CO2 refrigeration systems. *Energy Conversion and Management: X*, *1*(December 2018), 100002. https://doi.org/10.1016/j.ecmx.2018.100002

Besagni, G., Mereu, R., & Inzoli, F. (2016). Ejector refrigeration: A comprehensive review. *Renewable and Sustainable Energy Reviews*, *53*, 373–407. https://doi.org/10.1016/j.rser.2015.08.059

Bramwell, R., Brown, P., Galatioto, F., Ingledew, D., Karagianni, E., Maccarthy, J., Mullen, P., Walker, C., Willis, D., Wong, J., Energy, R., & Harris, B. (2023). *2023 Government Greenhouse Gas Conversion Factors for Company Reporting Methodology Paper for Conversion Factors Final Report 2*. www.nationalarchives.gov.uk/doc/open-government-licence/

Branford, Z., & Roberts, J. (2022). *The installer skills gap in the UK heat pump sector and the impacts on a just transition to net-zero*.

Bre, S. A. P. (2012). The government's standard assessment procedure for energy rating of dwellings. *Building Research Establishment, Watford, UK*.

Broad, O., Hawker, G., & Dodds, P. E. (2020). Decarbonising the UK residential sector: The dependence of national abatement on flexible and local views of the future. *Energy Policy*, *140*(January), 111321. https://doi.org/10.1016/j.enpol.2020.111321

Brodal, E., & Eiksund, O. (2020). Optimization study of heat pumps using refrigerant blends – Ejector versus expansion valve systems. *International Journal of Refrigeration*, *111*, 136–146. https://doi.org/10.1016/j.ijrefrig.2019.11.015

Burns, F., Strachan, S., & Tessa Clark, C. (2021). *Heat pump use in Scotland: an evidence review*. https://doi.org/10.7488/era/976

Calise, F., Cappiello, F. L., Dentice d'Accadia, M., & Vicidomini, M. (2020). Dynamic simulation, energy and economic comparison between BIPV and BIPVT collectors coupled with micro-wind turbines. *Energy*, *191*. https://doi.org/10.1016/j.energy.2019.116439

Cao, F., Cui, C., Wei, X., Yin, X., Li, M., & Wang, X. (2019). The experimental investigation on a novel transcritical CO2 heat pump combined system for space heating. *International Journal of Refrigeration*, *106*, 539–548. https://doi.org/10.1016/j.ijrefrig.2019.05.004

Cao, F., Wang, Y., & Ye, Z. (2019). Theoretical analysis of internal heat exchanger in transcritical CO2 heat pump systems and its experimental verification. *International Journal of Refrigeration*, *106*, 506–516. https://doi.org/10.1016/j.ijrefrig.2019.05.022

Carroll, P., Chesser, M., & Lyons, P. (2020). Air Source Heat Pumps field studies: A systematic literature review. *Renewable and Sustainable Energy Reviews*, *134*(December 2019). https://doi.org/10.1016/j.rser.2020.110275

Carvalho, S., Andersen, S. O., Brack, D., & Sherman, N. J. (2014). Alternatives to high-GWP hydrofluorocarbons. *UNEP (2011) HFCs: ACritical Link IN Protecting Climate AND THE Ozone Layer–A UNEP Synthesis Report*, 27–33.

Cavallini, A., & Zilio, C. (2007). Carbon dioxide as a natural refrigerant. *International Journal of Low Carbon Technologies*, *2*(3), 225–249. https://doi.org/10.1093/ijlct/2.3.225

CCC. (2021). *Progress in reducing emissions: 2021 Report to Parliament* (Issue June). www.theccc.org.uk/publications%0Ahttps://www.theccc.org.uk/wp-content/uploads/2021/06/Progress-in-reducing-emissions-2021-Report-to-Parliament.pdf

Cecchinato, L., Corradi, M., Cosi, G., Minetto, S., & Rampazzo, M. (2012). A real-time algorithm for the determination of R744 systems optimal high pressure. *International Journal of Refrigeration*, *35*(4), 817–826. https://doi.org/10.1016/j.ijrefrig.2012.01.005

Cecchinato, L., Corradi, M., Fornasieri, E., & Zamboni, L. (2005). Carbon dioxide as refrigerant for tap water heat pumps: A comparison with the traditional solution. *International Journal of Refrigeration*, *28*(8), 1250–1258. https://doi.org/10.1016/j.ijrefrig.2005.05.019

Cecchinato, L., Corradi, M., & Minetto, S. (2010). A critical approach to the determination of optimal heat rejection pressure in transcritical systems. *Applied Thermal Engineering*, *30*(13), 1812–1823. https://doi.org/10.1016/j.applthermaleng.2010.04.015

Chaichana, C., Aye, L., & Charters, W. W. S. (2003). Natural working fluids for solar-boosted heat pumps. *International Journal of Refrigeration*, *26*(6), 637–643. https://doi.org/10.1016/S0140-7007(03)00046-X

Chassein, E., Roser, A., & John, F. (2017). *Using Renewable Energy for Heating and Cooling: Barriers and Drivers at Local Level: an Analysis Based on a Literature Review and Empirical Results from Local Case Studies*.

Chaudry, M., Abeysekera, M., Hosseini, S. H. R., Jenkins, N., & Wu, J. (2015). Uncertainties in decarbonising heat in the UK. *Energy Policy*, *87*, 623–640. https://doi.org/10.1016/j.enpol.2015.07.019

Chen, G. M., Liang, L. X., Tang, L. M., Xu, X. X., Zhu, Z. J., & Chen, Q. (2009). Experimental investigation of an adjustable ejector for CO2 heat pump water heaters. *Journal of Zhejiang University: Science A*, *10*(11), 1678–1682. https://doi.org/10.1631/jzus.A0920116

Chen, J., & Wu, C. (1996). Optimization of a two-stage combined refrigeration system. *Energy Conversion and Management*, *37*(3), 353–358. https://doi.org/10.1016/0196-8904(95)00178-6

Chen, Y. G. (2016a). Considérations de l’analyse de Pinch et de la conception de refroidisseur de gaz au CO2 pour des chauffe-eau à pompe à chaleur. *International Journal of Refrigeration*, *69*, 136–146. https://doi.org/10.1016/j.ijrefrig.2016.05.003

Chen, Y. G. (2016b). Pinch point analysis and design considerations of CO2 gas cooler for heat pump water heaters. *International Journal of Refrigeration*, *69*, 136–146. https://doi.org/10.1016/j.ijrefrig.2016.05.003

Chen, Y. G. (2019). Optimal heat rejection pressure of CO2 heat pump water heaters based on pinch point analysis. *International Journal of Refrigeration*, *106*, 592–603. https://doi.org/10.1016/j.ijrefrig.2019.04.003

Chen, Y., & Gu, J. (2005). The optimum high pressure for CO2 transcritical refrigeration systems with internal heat exchangers. *International Journal of Refrigeration*, *28*(8), 1238–1249. https://doi.org/10.1016/j.ijrefrig.2005.08.009

Cheng, L., Ribatski, G., & Thome, J. R. (2008). New prediction methods for CO2 evaporation inside tubes: Part II—An updated general flow boiling heat transfer model based on flow patterns. *International Journal of Heat and Mass Transfer*, *51*(1–2), 125–135.

Cheng, L., Ribatski, G., Wojtan, L., & Thome, J. R. (2006). New flow boiling heat transfer model and flow pattern map for carbon dioxide evaporating inside horizontal tubes. *International Journal of Heat and Mass Transfer*, *49*(21–22), 4082–4094.

Chesi, A., Esposito, F., Ferrara, G., & Ferrari, L. (2014). Experimental analysis of R744 parallel compression cycle. *Applied Energy*, *135*, 274–285. https://doi.org/10.1016/j.apenergy.2014.08.087

China IOL. (2022, September 28). *China IOL. EN Datacenter*. http://data.chinaiol.com/ecdata/index

Chung, Y., Yoo, J. W., Kim, G. T., & Kim, M. S. (2019). Prediction of the frost growth and performance change of air source heat pump system under various frosting conditions. *Applied Thermal Engineering*, *147*(June 2018), 410–420. https://doi.org/10.1016/j.applthermaleng.2018.10.085

CIBSE. (2019). Guide A: Environmental design (2019). In *Design History: A Students' Handbook* (Issue May). https://www.cibse.org/knowledge/knowledge-items/detail?id=a0q20000008I79JAAS

Conservation of fuel and power: Approved Document L Volume 1. (2023). https://assets.publishing.service.gov.uk/media/662a2e3e55e1582b6ca7e592/Approved_Document_L__Conservation_of_fuel_and_power__Volume_1_Dwellings__2021_edition_incorporating_2023_amendments.pdf

Cui, C., Ren, J., Song, Y., Yin, X., Wang, W., Yang, X., & Cao, F. (2021). Multi-variable extreme seeking control for efficient operation of sub-cooler vapor injection trans-critical CO2 heat pump water heater. *Applied Thermal Engineering*, *184*. https://doi.org/10.1016/j.applthermaleng.2020.116261

Da Silva, D. L., Hermes, C. J. L., & Melo, C. (2011). First-principles modeling of frost accumulation on fan-supplied tube-fin evaporators. *Applied Thermal Engineering*, *31*(14–15), 2616–2621. https://doi.org/10.1016/j.applthermaleng.2011.04.029

Dai, B., Liu, S., Sun, Z., & Ma, Y. (2017). Thermodynamic Performance Analysis of CO2 Transcritical Refrigeration Cycle Assisted with Mechanical Subcooling. *Energy Procedia*, *105*, 2033–2038. https://doi.org/10.1016/j.egypro.2017.03.579

Danfoss. (2018). Refrigerant options now and in the future. In *Achieving sustainable HVAC/R through intelligent solutions, energy efficiency and low GWP refrigerants* (Issue April). www.refrigerants.danfoss.com

Department for Energy Security and Net Zero. (2025, March 4). *Greenhouse gas reporting: conversion factors 2024*. https://www.gov.uk/government/publications/greenhouse-gas-reporting-conversion-factors-2024

Dittus, F. W., & Boelter, L. M. K. (1985). Heat transfer in automobile radiators of the tubular type. *International Communications in Heat and Mass Transfer*, *12*(1), 3–22.

Eames, P., Loveday, D., Haines, V. and Romanos, P. (2014). *The Future Role of Thermal Energy Storage in the UK Energy System: An Assessment of the Technical Feasibility and Factors Influencing Adoption - Research Report (UKERC: London)*. *UKERC/RR/ED/2014/001*, 1–52.

Ed Vineyard & Van Baxter. (2021, September 28). *US Heat Pump Market – 2021 Update*. https://heatpumpingtechnologies.org/wp-content/uploads/2021/09/mcr-iea-hpt-presentation-us-20210907.pdf

EHPA. (2022, September 28). *European Heat Pump Association. European Heat Pump Market Statistics*. https://stats.ehpa.org/home/

Elbel, S., & Lawrence, N. (2016). Review of recent developments in advanced ejector technology. *International Journal of Refrigeration*, *62*, 1–18. https://doi.org/10.1016/j.ijrefrig.2015.10.031

Elkins, J. W. (1999). *Chlorofluorocarbons (CFCs)*. Springer Netherlands. https://doi.org/10.1007/1-4020-4494-1_55

Emerson. (2016). *Emerson Climate Technologies, "CO2 as a Refrigerant — Properties of R744*. https://emersonclimateconversations.com/

EST. (2008). Measurement of domestic hot water consumption in dwellings. *Energy Savings Trust*, 1–62. https://www.gov.uk/government/uploads/system/uploads/attachment_data/file/48188/3147-measure-domestic-hot-water-consump.pdf

Fawcett, T., Eyre, N., & Layberry, R. (2015). *Heat pumps and global residential heating*.

Fernandez, N., Hwang, Y., & Radermacher, R. (2010). Comparison of CO2 heat pump water heater performance with baseline cycle and two high COP cycles. *International Journal of Refrigeration*, *33*(3), 635–644. https://doi.org/10.1016/j.ijrefrig.2009.12.008

Ferrara, G., Ferrari, L., Fiaschi, D., Galoppi, G., Karellas, S., Secchi, R., & Tempesti, D. (2016). Récupération d'énergie aux moyens d'un détendeur à piston radial dans un système frigorifique au CO2. *International Journal of Refrigeration*, *72*, 147–155. https://doi.org/10.1016/j.ijrefrig.2016.07.014

Fischer, D., & Madani, H. (2017). On heat pumps in smart grids: A review. In *Renewable and Sustainable Energy Reviews* (Vol. 70, pp. 342–357). Elsevier Ltd. https://doi.org/10.1016/j.rser.2016.11.182

Flexiheat UK. (2025, March 4). *Boiler flow temperature for central heating regulations Part L June 2023*. https://www.flexiheatuk.com/boiler-flow-temperature-for-central-heating-regulations-part-l-june-2023-for-condensing-boilers-and-heat-pumps/

Fronk, B. M., & Garimella, S. (2011a). Water-coupled carbon dioxide microchannel gas cooler for heat pump water heaters: Part i - Experiments. *International Journal of Refrigeration*, *34*(1), 7–16. https://doi.org/10.1016/j.ijrefrig.2010.05.004

Fronk, B. M., & Garimella, S. (2011b). Water-coupled carbon dioxide microchannel gas cooler for heat pump water heaters: Part II - Model development and validation. *International Journal of Refrigeration*, *34*(1), 17–28. https://doi.org/10.1016/j.ijrefrig.2010.05.012

Gaigalis, V., Skema, R., Marcinauskas, K., & Korsakiene, I. (2016). A review on Heat Pumps implementation in Lithuania in compliance with the National Energy Strategy and EU policy. In *Renewable and Sustainable Energy Reviews* (Vol. 53, pp. 841–858). Elsevier Ltd. https://doi.org/10.1016/j.rser.2015.09.029

Galliers, L. (2025, March 4). *Boiler energy efficiency explained*. https://www.which.co.uk/reviews/boilers/article/boiler-energy-efficiency-aCgnH9h8JJP9

Ge, T. S., Weng, Z. C., Huang, R., Hu, B., Eikevik, T. M., & Dai, Y. J. (2023). High temperature transcritical CO2 heat pump with optimized tube-in-tube heat exchanger. *Energy*, *283*, 129223.

Gnielinski, V. (1976). New equations for heat and mass transfer in turbulent pipe and channel flow. *International Chemical Engineering*, *16*(2), 359–367.

Goyal, R., England, M. H., Sen Gupta, A., & Jucker, M. (2019). Reduction in surface climate change achieved by the 1987 Montreal Protocol. *Environmental Research Letters*, *14*(12). https://doi.org/10.1088/1748-9326/ab4874

Gu, H., Chen, Y., Yao, X., Huang, L., & Zou, D. (2023). Review on heat pump (HP) coupled with phase change material (PCM) for thermal energy storage. *Chemical Engineering Journal*, *455*, 140701.

Gu, L., Min, J., Wu, X., & Yang, L. (2017). Airside heat transfer and pressure loss characteristics of bare and finned tube heat exchangers used for aero engine cooling considering variable air properties. *International Journal of Heat and Mass Transfer*, *108*, 1839–1849. https://doi.org/10.1016/j.ijheatmasstransfer.2017.01.047

Gupta, S., Karanam, N. K., Konijeti, R., & Dasore, A. (2018). Thermodynamic Analysis and Effects of Replacing HFC by Fourth-Generation Refrigerants in VCR Systems. *International Journal of Air-Conditioning and Refrigeration*, *26*(2). https://doi.org/10.1142/S201013251850013X

Hafner, A. (2019). The advantages of natural working fluids. *Refrigeration Science and Technology*, *2019-Augus*(2018), 2456–2464. https://doi.org/10.18462/iir.icr.2019.1030

Hamilton, I., Rapf, O., Kockat, D. J., Zuhaib, D. S., Abergel, T., Oppermann, M., Otto, M., Loran, S., Fagotto, I., & Steurer, N. (2020). Global status report for buildings and construction. *United Nations Environmental Programme: Nairobi, Kenya*.

Han, Y. M., Wang, R. Z., & Dai, Y. J. (2009). Thermal stratification within the water tank. *Renewable and Sustainable Energy Reviews*, *13*(5), 1014–1026. https://doi.org/10.1016/j.rser.2008.03.001

He, Y. J., Liang, X. Y., Cheng, J. H., Shao, L. L., & Zhang, C. L. (2020). Approaching optimum COP by refrigerant charge management in transcritical CO2 heat pump water heater. *International Journal of Refrigeration*, *118*, 161–172. https://doi.org/10.1016/j.ijrefrig.2020.06.011

Hendron, B., Burch, J., & Barker, G. (2010). *Tool for generating realistic residential hot water event schedules*. National Renewable Energy Lab.(NREL), Golden, CO (United States).

Hu, B., Li, Y., Cao, F., & Xing, Z. (2015). Extremum seeking control of COP optimization for air-source transcritical CO2 heat pump water heater system. *Applied Energy*, *147*, 361–372. https://doi.org/10.1016/j.apenergy.2015.03.010

Huang, J. M., Hsieh, W. C., Ke, X. J., & Wang, C. C. (2008). The effects of frost thickness on the heat transfer of finned tube heat exchanger subject to the combined influence of fan types. *Applied Thermal Engineering*, *28*(7), 728–737. https://doi.org/10.1016/j.applthermaleng.2007.06.020

Hughes, P. (2008). *Geothermal (ground-source) heat pumps: Market status, barriers to adoption, and actions to overcome barriers*. Oak Ridge National Lab.(ORNL), Oak Ridge, TN (United States).

Hundy, G. H., Trott, Albert Runcorn, Welch, T. (2016). *Refrigeration, Air Conditioning and Heat Pumps,* (Fifth Edit). Butterworth-Heinemann.

Hyysalo, S., Juntunen, J. K., & Martiskainen, M. (2018). Energy Internet forums as acceleration phase transition intermediaries. *Research Policy*, *47*(5), 872–885. https://doi.org/10.1016/j.respol.2018.02.012

IEA. (2021). *Net Zero by 2050 A Roadmap for the*. https://iea.blob.core.windows.net/assets/deebef5d-0c34-4539-9d0c-10b13d840027/NetZeroby2050-ARoadmapfortheGlobalEnergySector_CORR.pdf

Ituna-Yudonago, J. F., Belman-Flores, J. M., Elizalde-Blancas, F., & García-Valladares, O. (2017). Numerical investigation of CO2 behavior in the internal heat exchanger under variable boundary conditions of the transcritical refrigeration system. *Applied Thermal Engineering*, *115*, 1063–1078. https://doi.org/10.1016/j.applthermaleng.2017.01.042

Jang, J. Y., Bae, H. H., Lee, S. J., & Ha, M. Y. (2013). Continuous heating of an air-source heat pump during defrosting and improvement of energy efficiency. *Applied Energy*, *110*, 9–16. https://doi.org/10.1016/j.apenergy.2013.04.030

Kelly, N. J., Tuohy, P. G., & Hawkes, A. D. (2014). Performance assessment of tariff-based air source heat pump load shifting in a UK detached dwelling featuring phase change-enhanced buffering. *Applied Thermal Engineering*, *71*(2), 809–820. https://doi.org/10.1016/j.applthermaleng.2013.12.019

Khan, J. U. R., & Zubair, S. M. (1998). Design and rating of a two-stage vapor-compression refrigeration system. *Energy*, *23*(10), 867–878. https://doi.org/10.1016/S0360-5442(98)00024-3

Kim, D., Jeon, Y., Jang, D. S., & Kim, Y. (2018). Performance comparison among two-phase, liquid, and vapor injection heat pumps with a scroll compressor using R410A. *Applied Thermal Engineering*, *137*(September 2017), 193–202. https://doi.org/10.1016/j.applthermaleng.2018.03.086

Kim, M. H., Pettersen, J., & Bullard, C. W. (2004). Fundamental process and system design issues in CO2 vapor compression systems. In *Progress in Energy and Combustion Science* (Vol. 30, Issue 2). https://doi.org/10.1016/j.pecs.2003.09.002

Kim, M. S., Kang, D. H., Kim, M. S., & Kim, M. (2017). Étude de la régulation optimale de la pression du refroidisseur de gaz pour un système frigorifique au CO2 avec un échangeur de chaleur interne. *International Journal of Refrigeration*, *77*, 48–59. https://doi.org/10.1016/j.ijrefrig.2017.03.002

Klein, S. A., & Alvarado, F. L. (2004). Engineering Equation Solver (EES) Software. *Department of Mechanical Engineering, University of Wisconsin—Madison*.

Klein, S. A., Beckman, W. A., Mitchell, J. W., Duffie, J. A., Duffie, N. A., Freeman, T. L., Mitchell, J. C., Braun, J. E., Evans, B. L., & Kummer, J. P. (2010). TRNSYS 17: A transient system simulation program, solar energy laboratory. *Madison, Madison, USA: University of Wisconsin*.

Kutateladze, S. S. (1948). On the transition to film boiling under natural convection. *Kotloturbostroenie*, *3*, 10.

Lawton, P., & Abeysinghe, S. (2022). *Neighbourhood Green Work Package 1 Report*.

Lee, K. S., Jhee, S., & Yang, D. K. (2003). Prediction of the frost formation on a cold flat surface. *International Journal of Heat and Mass Transfer*, *46*(20), 3789–3796. https://doi.org/10.1016/S0017-9310(03)00195-9

Lee, S. (2018). An overview of the European technical guidelines for the prevention, control and investigation of infections caused by Legionella species. *Perspectives in Public Health*, *138*(5), 241–247.

Leoni, A., Mondot, M., Durier, F., Revellin, R., & Haberschill, P. (2017). Frost formation and development on flat plate: Experimental investigation and comparison to predictive methods. *Experimental Thermal and Fluid Science*, *88*, 220–233. https://doi.org/10.1016/j.expthermflusci.2017.06.005

Li, X.-Y., Li, Z.-H., & Tao, W.-Q. (2018). Experimental study on heat transfer and pressure drop characteristics of fin-and-tube surface with four convex-strips around each tube. *International Journal of Heat and Mass Transfer*, *116*, 1085–1095.

Li, Y., Huang, G., Xu, T., Liu, X., & Wu, H. (2018). Optimal design of PCM thermal storage tank and its application for winter available open-air swimming pool. *Applied Energy*, *209*, 224–235.

Liang, S., Wang, W., Sun, Y., Li, Z., Zhao, J., Lin, Y., & Deng, S. (2020). A novel design method for ASHPs considering output heating capacity and frosting suppression. *Energy and Buildings*, *224*, 110099. https://doi.org/10.1016/j.enbuild.2020.110099

Liao, S. M., & Zhao, T. S. (2002). Measurements of heat transfer coefficients from supercritical carbon dioxide flowing in horizontal mini/micro channels. *Journal of Heat Transfer*, *124*(3), 413–420. https://doi.org/10.1115/1.1423906

Liu, F., Groll, E. A., & Ren, J. (2016). Comprehensive experimental performance analyses of an ejector expansion transcritical CO2 system. *Applied Thermal Engineering*, *98*, 1061–1069. https://doi.org/10.1016/j.applthermaleng.2015.12.017

Liu, F., Zhu, W., & Zhao, J. (2018). Model-based dynamic optimal control of a CO2 heat pump coupled with hot and cold thermal storages. *Applied Thermal Engineering*, *128*, 1116–1125. https://doi.org/10.1016/j.applthermaleng.2017.09.098

Liu, F., Zhu, W., Zhao, J., Ren, J., Groll, E. A., & Cai, Y. (2017). A new method for optimal control of a dual-mode CO2 heat pump with thermal storage. *Applied Thermal Engineering*, *125*, 1123–1132. https://doi.org/10.1016/j.applthermaleng.2017.07.068

Liu, H., Gu, Z., & Li, Y. (2002). *Simulation of NH3 / CO2 Two-Stage Low Temperature Refrigeration System*.

Liu, Z., Fan, P., Wang, Q., Chi, Y., Zhao, Z., & Chi, Y. (2018). Air source heat pump with water heater based on a bypass-cycle defrosting system using compressor casing thermal storage. *Applied Thermal Engineering*, *128*, 1420–1429. https://doi.org/10.1016/j.applthermaleng.2017.09.131

Liu, Z.-B., He, Y.-L., Yang, Y.-F., & Fei, J.-Y. (2014). Experimental study on heat transfer and pressure drop of supercritical CO2 cooled in a large tube. *Applied Thermal Engineering*, *70*(1), 307–315.

Llopis, R., Nebot-Andrés, L., Sánchez, D., Catalán-Gil, J., & Cabello, R. (2018). Subcooling methods for CO2 refrigeration cycles: A review. *International Journal of Refrigeration*, *93*, 85–107. https://doi.org/10.1016/j.ijrefrig.2018.06.010

Longo, G. A. (2008). Refrigerant R134a condensation heat transfer and pressure drop inside a small brazed plate heat exchanger. *International Journal of Refrigeration*, *31*(5), 780–789.

Lorentzen, G., & Pettersen, J. (1993). A new, efficient and environmentally benign system for car air-conditioning. *International Journal of Refrigeration*, *16*(1), 4–12. https://doi.org/10.1016/0140-7007(93)90014-Y

Love, J., Smith, A. Z. P., Watson, S., Oikonomou, E., Summerfield, A., Gleeson, C., Biddulph, P., Chiu, L. F., Wingfield, J., & Martin, C. (2017). The addition of heat pump electricity load profiles to GB electricity demand: Evidence from a heat pump field trial. *Applied Energy*, *204*, 332–342.

Lowe, R., Chiu, L. F., Oikonomou, E., Gleeson, C., Love, J., Wingfield, J., & Biddulph, P. (n.d.). *ANALYSIS OF DATA FROM HEAT PUMPS INSTALLED VIA THE RENEWABLE HEAT PREMIUM PAYMENT (RHPP) SCHEME*.

Lowe, T. (2017, June 28). *UK 'signifcantly off track' its heat pump targets, CCC report warns*. https://assets.publishing.service.gov.uk/government/uploads/system/uploads/attachment_data/file/607085/DECC_RHPP_161214_Case_Studies_v15_from_docx_.pdf

Lowes, R., Woodman, B., & Speirs, J. (2020). Heating in Great Britain: An incumbent discourse coalition resists an electrifying future. *Environmental Innovation and Societal Transitions*, *37*, 1–17. https://doi.org/10.1016/j.eist.2020.07.007

Ma, Q., Wu, X., Chu, F., & Zhu, B. (2018). Experimental and numerical investigations of frost formation on wavy plates. *Applied Thermal Engineering*, *138*(April), 627–632. https://doi.org/10.1016/j.applthermaleng.2018.04.098

Ma, Y., Liu, Z., & Tian, H. (2013). A review of transcritical carbon dioxide heat pump and refrigeration cycles. *Energy*, *55*(2013), 156–172. https://doi.org/10.1016/j.energy.2013.03.030

Marini, D., Buswell, R. A., & Hopfe, C. J. (2019). Sizing domestic air-source heat pump systems with thermal storage under varying electrical load shifting strategies. *Applied Energy*, *255*. https://doi.org/10.1016/j.apenergy.2019.113811

Mastrowski, M., Smolka, J., Hafner, A., Haida, M., Palacz, M., & Banasiak, K. (2019). Experimental study of the heat transfer problem in expansion devices in CO2 refrigeration systems. *Energy*, *173*, 586–597. https://doi.org/10.1016/j.energy.2019.02.097

Mazzeo, D., Matera, N., Cornaro, C., Oliveti, G., Romagnoni, P., & De Santoli, L. (2020). EnergyPlus, IDA ICE and TRNSYS predictive simulation accuracy for building thermal behaviour evaluation by using an experimental campaign in solar test boxes with and without a PCM module. *Energy and Buildings*, *212*. https://doi.org/10.1016/j.enbuild.2020.109812

McMillan, T. (2022, August 25). *Heat pumps: why is the UK falling short?*

MCS. (2020). The heat pump Standard. In *Europhysics News* (Vol. 8, Issue 9). https://doi.org/10.1051/epn/19770809004

Minetto, S. (2011). Theoretical and experimental analysis of a CO2 heat pump for domestic hot water. *International Journal of Refrigeration*, *34*(3), 742–751. https://doi.org/10.1016/j.ijrefrig.2010.12.018

Minetto, S., Brignoli, R., Banasiak, K., Hafner, A., & Zilio, C. (2013). Performance assessment of an off-the-shelf R744 heat pump equipped with an ejector. *Applied Thermal Engineering*, *59*(1–2), 568–575. https://doi.org/10.1016/j.applthermaleng.2013.06.032

MORI, H., YOSHIDA, S., OHISHI, K., & KAKIMOTO, Y. (2000). Dryout quality and post-dryout heat transfer coefficient in horizontal evaporator tubes. *3rd European Thermal Sciences Conference (Heidelberg, 10-13 September 2000)*, 839–844.

Nair, A. M., Wilson, C., Huang, M. J., Griffiths, P., & Hewitt, N. (2022). Phase change materials in building integrated space heating and domestic hot water applications: A review. *Journal of Energy Storage*, *54*, 105227.

Nastasi, B., Markovska, N., Puksec, T., Duić, N., & Foley, A. (2022). Renewable and sustainable energy challenges to face for the achievement of Sustainable Development Goals. In *Renewable and Sustainable Energy Reviews* (Vol. 157). Elsevier Ltd. https://doi.org/10.1016/j.rser.2022.112071

ofgem. (2023, October 2). *Boiler Upgrade Scheme (BUS)*. https://www.ofgem.gov.uk/environmental-and-social-schemes/boiler-upgrade-scheme-bus#:~:text=Grant%20level%20change&text=From%20Monday%2023%20October%202023,biomass%20boilers%3A%20%C2%A35%2C000

Owen, A., Middlemiss, L., Brown, D., Davis, M., Hall, S., Bookbinder, R., Brisbois, M. C., Cairns, I., Hannon, M., & Mininni, G. (2023). Who applies for energy grants? In *Energy Research and Social Science* (Vol. 101). Elsevier Ltd. https://doi.org/10.1016/j.erss.2023.103123

Ozgener, O., & Hepbasli, A. (2005). Experimental performance analysis of a solar assisted ground-source heat pump greenhouse heating system. *Energy and Buildings*, *37*(1), 101–110. https://doi.org/10.1016/j.enbuild.2004.06.003

Padhmanabhan, S. K., Fisher, D. E., Cremaschi, L., & Moallem, E. (2011). Modeling non-uniform frost growth on a fin-and-tube heat exchanger. *International Journal of Refrigeration*, *34*(8), 2018–2030. https://doi.org/10.1016/j.ijrefrig.2011.06.005

Pardiñas, Á. Á., Alonso, M. J., Diz, R., Kvalsvik, K. H., & Fernández-Seara, J. (2017). State-of-the-art for the use of phase-change materials in tanks coupled with heat pumps. *Energy and Buildings*, *140*, 28–41.

Patil, M. S., Seo, J. H., & Lee, M. Y. (2017). Heat transfer characteristics of the heat exchangers for refrigeration, air conditioning and heap pump systems under frosting, defrosting and dry/wet conditions—A review. *Applied Thermal Engineering*, *113*, 1071–1087. https://doi.org/10.1016/j.applthermaleng.2016.11.107

Peñarrocha, I., Llopis, R., Tárrega, L., Sánchez, D., & Cabello, R. (2014). A new approach to optimize the energy efficiency of CO2 transcritical refrigeration plants. *Applied Thermal Engineering*, *67*(1–2), 137–146. https://doi.org/10.1016/j.applthermaleng.2014.03.004

Peng, X., Wang, D., Wang, G., Yang, Y., & Xiang, S. (2020). Numerical investigation on the heating performance of a transcritical CO2 vapor-injection heat pump system. *Applied Thermal Engineering*, *166*(100), 114656. https://doi.org/10.1016/j.applthermaleng.2019.114656

Pereira da Cunha, J., & Eames, P. (2016). Thermal energy storage for low and medium temperature applications using phase change materials - A review. *Applied Energy*, *177*, 227–238. https://doi.org/10.1016/j.apenergy.2016.05.097

Pinel, P., Cruickshank, C. A., Beausoleil-Morrison, I., & Wills, A. (2011). A review of available methods for seasonal storage of solar thermal energy in residential applications. *Renewable and Sustainable Energy Reviews*, *15*(7), 3341–3359. https://doi.org/10.1016/j.rser.2011.04.013

Poongavanam, G., Sivalingam, V., Prabakaran, R., Salman, M., & Kim, S. C. (2021). Selection of the best refrigerant for replacing R134a in automobile air conditioning system using different MCDM methods: A comparative study. *Case Studies in Thermal Engineering*, *27*(August), 101344. https://doi.org/10.1016/j.csite.2021.101344

Protopapadaki, C., & Saelens, D. (2017). Heat pump and PV impact on residential low-voltage distribution grids as a function of building and district properties. *Applied Energy*, *192*, 268–281.

Qiao, H., Aute, V., & Radermacher, R. (2018). Modeling of transient characteristics of an air source heat pump with vapor injection during reverse-cycle defrosting. *International Journal of Refrigeration*, *88*, 24–34. https://doi.org/10.1016/j.ijrefrig.2017.12.017

Qu, M., Tang, Y., Zhang, T., Li, Z., & Chen, J. (2019). Experimental investigation on the multi-mode heat discharge process of a PCM heat exchanger during TES based reverse cycle defrosting using in cascade air source heat pumps. *Applied Thermal Engineering*, *151*(January), 154–162. https://doi.org/10.1016/j.applthermaleng.2019.02.003

Rahman, M. A., & Jacobi, A. M. (2012). Drainage of frost melt water from vertical brass surfaces with parallel microgrooves. *International Journal of Heat and Mass Transfer*, *55*(5–6), 1596–1605. https://doi.org/10.1016/j.ijheatmasstransfer.2011.11.015

Rampazzo, M., Cervato, A., Corazzol, C., Mattiello, L., Beghi, A., Cecchinato, L., & Virzi, A. (2019). Energy-efficient operation of transcritical and subcritical CO2 inverse cycles via Extremum Seeking Control. *Journal of Process Control*, *81*, 87–97. https://doi.org/10.1016/j.jprocont.2019.06.008

Raul, A., Saha, S. K., & Jain, M. (2020). Transient performance analysis of concentrating solar thermal power plant with finned latent heat thermal energy storage. *Renewable Energy*, *145*, 1957–1971.

Razzaq, M. E. A., Ahamed, J. U., Abu, M., & Hossain, M. (907). *A REVIEW ON HYDROCARBON (HCs) AS AN ALTERNATIVE REFRIGERANT: BASED ON THERMODYNAMIC AND ENVIRONMENTAL APPROACH EXPERIMENTAL ANALYSIS OF HEAT TRANSFER ENHANCEMENT IN A CIRCULAR TUBE USING PERFORATED TRIANGULAR WAVY TAPE INSERT View project Heat Transfer Vi*. *11*(March), 86–96. https://www.researchgate.net/publication/332785950

Remund, J., Mueller, S., Kunz, S., & Schilter, C. (2020). Meteonorm handbook, part II: theory. In *Bern, Switzerland, Meteotest* (7.3.4). https://meteonorm.com/assets/downloads/mn73_theory.pdf

Renaldi, R., Kiprakis, A., & Friedrich, D. (2017). An optimisation framework for thermal energy storage integration in a residential heat pump heating system. *Applied Energy*, *186*, 520–529. https://doi.org/10.1016/j.apenergy.2016.02.067

Rob. (2025, March 4). *Average Gas & Electricity Prices per kWh (2025)*. https://www.energy-review.co.uk/guides/gas-electricity-prices-per-kwh/

Robinson, D. M., & Groll, E. A. (1998). Efficiencies of transcritical CO2 cycles with and without an expansion turbine. *International Journal of Refrigeration*, *21*(7), 577–589. https://doi.org/10.1016/S0140-7007(98)00024-3

Rosenow, J., Lowes, R., Broad, O., Hawker, G., Wu, J., Qadrdan, M., & Gross, R. (2020). The pathway to net zero heating in the UK. In *Ukerc*. https://doi.org/10.5286/ukerc.edc.000941

ROUSSEAU, P. G., & VAN ELDIK, M. (2011). Thermal-Fluid Sytems Modelling I-Lecture Notes. *Potchefstroom: North-West University*.

Sánchez, D., Cabello, R., Llopis, R., & Torrella, E. (2012). Development and validation of a finite element model for water - CO2 coaxial gas-coolers. *Applied Energy*, *93*, 637–647. https://doi.org/10.1016/j.apenergy.2011.12.100

Sarkar, J. (2008). Optimization of ejector-expansion transcritical CO2 heat pump cycle. *Energy*, *33*(9), 1399–1406. https://doi.org/10.1016/j.energy.2008.04.007

Sarkar, J. (2010). Review on cycle modifications of transcritical CO2 refrigeration and heat pump systems. *Journal of Advanced Research in Mechanical Engineering*, *1*(1), 22–29.

Sarkar, J., & Agrawal, N. (2010). Performance optimization of transcritical CO2 cycle with parallel compression economization. *International Journal of Thermal Sciences*, *49*(5), 838–843. https://doi.org/10.1016/j.ijthermalsci.2009.12.001

Sarkar, J., Bhattacharyya, S., & Gopal, M. R. (2004). Optimization of a transcritical CO2 heat pump cycle for simultaneous cooling and heating applications. *International Journal of Refrigeration*, *27*(8), 830–838. https://doi.org/10.1016/j.ijrefrig.2004.03.006

Sarkar, J., Bhattacharyya, S., & Gopal, M. R. (2006). Simulation of a transcritical CO2 heat pump cycle for simultaneous cooling and heating applications. *International Journal of Refrigeration*, *29*(5), 735–743. https://doi.org/10.1016/j.ijrefrig.2005.12.006

Scamman, D., Solano-Rodríguez, B., Pye, S., Chiu, L. F., Smith, A. Z. P., Cassarino, T. G., Barrett, M., & Lowe, R. (2020). Heat decarbonisation modelling approaches in the UK: An energy system architecture perspective. *Energies*, *13*(8). https://doi.org/10.3390/en13081869

Shao, L. L., Zhang, Z. Y., & Zhang, C. L. (2018). Constrained optimal high pressure equation of CO2 transcritical cycle. *Applied Thermal Engineering*, *128*, 173–178. https://doi.org/10.1016/j.applthermaleng.2017.09.023

Shon, B. H., Jung, C. W., Kwon, O. J., Choi, C. K., & Kang, Y. T. (2018). Characteristics on condensation heat transfer and pressure drop for a low GWP refrigerant in brazed plate heat exchanger. *International Journal of Heat and Mass Transfer*, *122*, 1272–1282.

Song, M., & Dang, C. (2018). Review on the measurement and calculation of frost characteristics. *International Journal of Heat and Mass Transfer*, *124*, 586–614. https://doi.org/10.1016/j.ijheatmasstransfer.2018.03.094

Song, M., Deng, S., Dang, C., Mao, N., & Wang, Z. (2018). Review on improvement for air source heat pump units during frosting and defrosting. *Applied Energy*, *211*(June 2017), 1150–1170. https://doi.org/10.1016/j.apenergy.2017.12.022

Song, M., Xie, G., Pekař, L., Mao, N., & Qu, M. (2020). A modeling study on the revere cycle defrosting of an air source heat pump with the melted frost downwards flowing away and local drainage. *Energy and Buildings*, *226*, 1–14. https://doi.org/10.1016/j.enbuild.2020.110257

Song, X., Lu, D., Lei, Q., Wang, D., Yu, B., Shi, J., & Chen, J. (2021). Energy and exergy analyses of a transcritical CO2 air conditioning system for an electric bus. *Applied Thermal Engineering*, *190*(September 2020), 116819. https://doi.org/10.1016/j.applthermaleng.2021.116819

Song, Y., & Cao, F. (2018). The evaluation of optimal discharge pressure in a water-precooler-based transcritical CO2 heat pump system. *Applied Thermal Engineering*, *131*, 8–18. https://doi.org/10.1016/j.applthermaleng.2017.11.092

Song, Y., Cui, C., Yin, X., & Cao, F. (2022). Advanced development and application of transcritical CO2 refrigeration and heat pump technology—A review. In *Energy Reports* (Vol. 8, pp. 7840–7869). Elsevier Ltd. https://doi.org/10.1016/j.egyr.2022.05.233

Song, Y., Li, D., Yang, D., Jin, L., Cao, F., & Wang, X. (2017). Comparaison de performances entre une pompe à chaleur combinée au R134a/CO2 et une pompe à chaleur en cascade au R134a/CO2 pour chauffage de locaux. *International Journal of Refrigeration*, *74*, 590–603. https://doi.org/10.1016/j.ijrefrig.2016.12.001

Song, Y., Yang, D., Li, M., & Cao, F. (2019). Investigations on optimal discharge pressure in CO2 heat pumps using the GMDH and PSO-BP type neural network—part B: Experimental study. *International Journal of Refrigeration*, *106*, 248–257. https://doi.org/10.1016/j.ijrefrig.2019.06.008

Stene, J. (2005). Residential CO2 heat pump system for combined space heating and hot water heating. *International Journal of Refrigeration*, *28*(8), 1259–1265. https://doi.org/10.1016/j.ijrefrig.2005.07.006

Sweetnam, T., Fell, M., Oikonomou, E., & Oreszczyn, T. (2019). Domestic demand-side response with heat pumps: controls and tariffs. *Building Research and Information*, *47*(4), 344–361. https://doi.org/10.1080/09613218.2018.1442775

Tang, J., Hu, X., Herman, C., & Gong, G. (2020). Computational modeling and prediction of the performance of air source heat pumps under frost prevention and retardation conditions. *Energy and Buildings*, *224*, 110264. https://doi.org/10.1016/j.enbuild.2020.110264

Tao, Y. B., He, Y. L., Tao, W. Q., & Wu, Z. G. (2010). Experimental study on the performance of CO2 residential air-conditioning system with an internal heat exchanger. *Energy Conversion and Management*, *51*(1), 64–70. https://doi.org/10.1016/j.enconman.2009.08.024

Taylor, J. R. (1997). An introduction to error analysis, 327 pp. *Univ. Sci. Books, Sausalito, Calif.*

Thonon, B. (2007). *Transcritical R744 (CO2) heat pumps*. *744*(October 2007).

Tian, H., Ma, Y., Li, M., & Wang, W. (2010). Study on expansion power recovery in CO2 trans-critical cycle. *Energy Conversion and Management*, *51*(12), 2516–2522. https://doi.org/10.1016/j.enconman.2010.05.016

Toke, D. (2022, December 2). *UK heat pump sales are the lowest in Europe – why?*

UNEP. (2020). 2020 Global Status Report for Buildings and Construction. In *Global Status Report*. www.iea.org

Vekony, T. A. (2023, October 3). *Total Cost of Heat Pumps in the UK 2023*. https://www.greenmatch.co.uk/blog/2014/08/the-running-costs-of-heat-pumps

Vutukuru, R., Pegallapati, A. S., & Maddali, R. (2019). Thermodynamic studies on a solar assisted transcritical CO2 based tri-generation system with an ejector for dairy applications. *International Journal of Refrigeration*, *108*, 113–123. https://doi.org/10.1016/j.ijrefrig.2019.08.031

Wang, B., Shi, W., Li, X., & Yan, Q. (2008). Numerical research on the scroll compressor with refrigeration injection. *Applied Thermal Engineering*, *28*(5–6), 440–449. https://doi.org/10.1016/j.applthermaleng.2007.05.012

Wang, C.-C., Chi, K.-Y., & Chang, C.-J. (2000). Heat transfer and friction characteristics of plain fin-and-tube heat exchangers, part II: Correlation. *International Journal of Heat and Mass Transfer*, *43*(15), 2693–2700.

Wang, D., Tao, T., Xu, G., Luo, A., & Kang, S. (2012). Experimental study on frosting suppression for a finned-tube evaporator using ultrasonic vibration. *Experimental Thermal and Fluid Science*, *36*, 1–11. https://doi.org/10.1016/j.expthermflusci.2011.03.002

Wang, G. B., & Zhang, X. R. (2019). Thermoeconomic optimization and comparison of the simple single-stage transcritical carbon dioxide vapor compression cycle with different subcooling methods for district heating and cooling. *Energy Conversion and Management*, *185*(February), 740–757. https://doi.org/10.1016/j.enconman.2019.02.024

Wang, J., Zhong, H., Yang, Z., Wang, M., Kammen, D. M., Liu, Z., Ma, Z., Xia, Q., & Kang, C. (2020). Exploring the trade-offs between electric heating policy and carbon mitigation in China. *Nature Communications*, *11*(1), 6054.

Wang, S., He, Y., Tuo, H., Cao, F., & Xing, Z. (2013). Effect of heat transfer area and refrigerant mass flux in a gas cooler on heating performance of air-source transcritical CO 2 heat pump water heater system. *Energy & Buildings*, *67*, 1–10. https://doi.org/10.1016/j.enbuild.2013.07.078

Wang, S., Tuo, H., Cao, F., & Xing, Z. (2013a). Experimental investigation on air-source transcritical CO2 heat pump water heater system at a fixed water inlet temperature. *International Journal of Refrigeration*, *36*(3), 701–716. https://doi.org/10.1016/j.ijrefrig.2012.10.011

Wang, S., Tuo, H., Cao, F., & Xing, Z. (2013b). Experimental investigation on air-source transcritical CO2 heat pump water heater system at a fixed water inlet temperature. *International Journal of Refrigeration*, *36*(3), 701–716.

Wang, Y., & He, W. (2021). Temporospatial techno-economic analysis of heat pumps for decarbonising heating in Great Britain. *Energy and Buildings*, *250*, 111198. https://doi.org/10.1016/j.enbuild.2021.111198

Wang, Y., Wang, J., & He, W. (2022). Development of efficient, flexible and affordable heat pumps for supporting heat and power decarbonisation in the UK and beyond: Review and perspectives. *Renewable and Sustainable Energy Reviews*, *154*(October 2021). https://doi.org/10.1016/j.rser.2021.111747

Wang, Z., Li, G., Wang, F., & Zhang, Y. (2021). Performance investigation of a transcritical CO2 heat pump combined with the terminal of radiator and floor radiant coil for space heating in different climates, China. *Journal of Building Engineering*, *44*, 102927. https://doi.org/10.1016/j.jobe.2021.102927

Watson, S. D., Crawley, J., Lomas, K. J., & Buswell, R. A. (2023). Predicting future GB heat pump electricity demand. *Energy and Buildings*, *286*. https://doi.org/10.1016/j.enbuild.2023.112917

Watson, S. D., Lomas, K. J., & Buswell, R. A. (2021). How will heat pumps alter national half-hourly heat demands? Empirical modelling based on GB field trials. *Energy and Buildings*, *238*, 110777. https://doi.org/10.1016/j.enbuild.2021.110777

Wattelet, J. P. (1994). *Heat transfer flow regimes of refrigerants in a horizontal-tube evaporator*. University of Illinois at Urbana-Champaign.

Wojtan, L., Ursenbacher, T., & Thome, J. R. (2005). Investigation of flow boiling in horizontal tubes: Part I—A new diabatic two-phase flow pattern map. *International Journal of Heat and Mass Transfer*, *48*(14), 2955–2969.

Wookey, R., Bone, A., Carmichael, C., & Crossley, A. (2014). Minimum home temperature thresholds for health in winter–a systematic literature review. *Public Health England, London*.

Xiao, X., Ming, G., Ming, L., & Jiang, Z. (2012). Experimental investigation on performance of transcritical CO 2 heat pump system with ejector under optimum high-side pressure. *EGY*, *44*(1), 870–877. https://doi.org/10.1016/j.energy.2012.04.062

Yang, J. L., Ma, Y. T., Li, M. X., & Guan, H. Q. (2005). Exergy analysis of transcritical carbon dioxide refrigeration cycle with an expander. *Energy*, *30*(7), 1162–1175. https://doi.org/10.1016/j.energy.2004.08.007

Yang Lingyan & Xu Wei. (2021, September 28). *The Development of Heat Pump Technology in China*. https://heatpumpingtechnologies.org/wp-content/uploads/2021/07/the-development-of-heat-pump-technology-in-china.pdf

Yang, Y., Li, M., Wang, K., & Ma, Y. (2016a). Study of multi-twisted-tube gas cooler for CO2 heat pump water heaters. *Applied Thermal Engineering*, *102*, 204–212. https://doi.org/10.1016/j.applthermaleng.2016.03.123

Yang, Y., Li, M., Wang, K., & Ma, Y. (2016b). Study of multi-twisted-tube gas cooler for CO2 heat pump water heaters. *Applied Thermal Engineering*, *102*, 204–212. https://doi.org/10.1016/j.applthermaleng.2016.03.123

Yao, Y., Jiang, Y., Deng, S., & Ma, Z. (2004). A study on the performance of the airside heat exchanger under frosting in an air source heat pump water heater/chiller unit. *International Journal of Heat and Mass Transfer*, *47*(17–18), 3745–3756. https://doi.org/10.1016/j.ijheatmasstransfer.2004.03.013

Ye, H. Y., & Lee, K. S. (2013). Performance prediction of a fin-and-tube heat exchanger considering air-flow reduction due to the frost accumulation. *International Journal of Heat and Mass Transfer*, *67*, 225–233. https://doi.org/10.1016/j.ijheatmasstransfer.2013.08.026

Yin, X., Cao, F., Wang, J., Li, M., & Wang, X. (2019). Investigations on optimal discharge pressure in CO2 heat pumps using the GMDH and PSO-BP type neural network—Part A: Theoretical modeling. *International Journal of Refrigeration*, *106*, 549–557. https://doi.org/10.1016/j.ijrefrig.2019.04.027

Yıldız, A., & Yıldırım, R. (2021). Investigation of using R134a, R1234yf and R513A as refrigerant in a heat pump. *International Journal of Environmental Science and Technology*, *18*(5), 1201–1210. https://doi.org/10.1007/s13762-020-02857-z

Yu, B., Yang, J., Wang, D., Shi, J., & Chen, J. (2019). An updated review of recent advances on modified technologies in transcritical CO2 refrigeration cycle. *Energy*, *189*, 116147. https://doi.org/10.1016/j.energy.2019.116147

Yu, P. Y., Lin, W. K., & Wang, C. C. (2014). Performance evaluation of a tube-in-tube CO2 gas cooler used in a heat pump water heater. *Experimental Thermal and Fluid Science*, *54*, 304–312. https://doi.org/10.1016/j.expthermflusci.2014.01.007

Yu, Z., Tao, L., Huang, L., & Wang, D. (2020). Numerical investigation on cooling heat transfer and flow characteristic of supercritical CO2 in spirally fluted tubes. *International Journal of Heat and Mass Transfer*, *163*. https://doi.org/10.1016/j.ijheatmasstransfer.2020.120399

Zhang, F., Zhu, Y., Li, C., & Jiang, P. (2018). Thermodynamic optimization of heat transfer process in thermal systems using CO2 as the working fluid based on temperature glide matching. *Energy*, *151*, 376–386. https://doi.org/10.1016/j.energy.2018.03.009

Zhang, L., Jiang, Y., Dong, J., & Yao, Y. (2018). Advances in vapor compression air source heat pump system in cold regions: A review. *Renewable and Sustainable Energy Reviews*, *81*(August 2017), 353–365. https://doi.org/10.1016/j.rser.2017.08.009

Zhang, L., Jiang, Y., Dong, J., Yao, Y., & Deng, S. (2018). An experimental study of frost distribution and growth on finned tube heat exchangers used in air source heat pump units. *Applied Thermal Engineering*, *132*, 38–51. https://doi.org/10.1016/j.applthermaleng.2017.12.047

Zhang, W. J., & Zhang, C. L. (2011). A correlation-free on-line optimal control method of heat rejection pressures in CO2 transcritical systems. *International Journal of Refrigeration*, *34*(4), 844–850. https://doi.org/10.1016/j.ijrefrig.2011.01.014

Zhang, Z., Hou, Y., & Kulacki, F. A. (2018). Theoretical analysis of a transcritical double-stage nitrous oxide refrigeration cycle with an internal heat exchanger. *Applied Thermal Engineering*, *140*(April), 147–157. https://doi.org/10.1016/j.applthermaleng.2018.05.053

Zhou, M., Liu, H., Peng, L., Qin, Y., Chen, D., Zhang, L., & Mauzerall, D. L. (2022). Environmental benefits and household costs of clean heating options in northern China. *Nature Sustainability*, *5*(4), 329–338.

Zhu, Y., Huang, Y., Li, C., Zhang, F., & Jiang, P. X. (2018). Experimental investigation on the performance of transcritical CO2 ejector-expansion heat pump water heater system. *Energy Conversion and Management*, *167*(April), 147–155. https://doi.org/10.1016/j.enconman.2018.04.081

Zhu, Y., Huang, Y., Lin, S., Li, C., & Jiang, P. (2019). Study of convection heat transfer of CO2 at supercritical pressures during cooling in fluted tube-in-tube heat exchangers. *International Journal of Refrigeration*, *104*, 161–170. https://doi.org/10.1016/j.ijrefrig.2019.03.033

Zou, D., Ma, X., Liu, X., Zheng, P., Cai, B., Huang, J., Guo, J., & Liu, M. (2017). Experimental research of an air-source heat pump water heater using water-PCM for heat storage. *Applied Energy*, *206*, 784–792.